UNIVERSITÀ DEGLI STUDI DI PADOVA

DIPARTIMENTO DI SCIENZE CHIMICHE

CORSO DI LAUREA MAGISTRALE IN SCIENZA DEI MATERIALI

TESI DI LAUREA MAGISTRALE IN SCIENZA DEI MATERIALI

Evaluation of the stabilizing effect of CeO_2 on the electrochemical performance of $Pt/CeO_2/C$ as a catalyst for the oxygen reduction reaction in the cathodic compartment of proton exchange membrane fuel cells

RELATORE: CH.MO PROF. Christian Durante
CONTRORELATORE: CH.MO PROF. Denis Badocco

LAUREANDO: Giovanni Zuccante

Anno Accademico 2021/2022

SUMMARY

Abstract

Proton Exchange Membrane Fuel Cells are the best candidates for replacing the traditional combustion engines used in the automotive sector. The most widespread catalysts implemented in these systems rely on platinum, which is nanosized and supported on high surface area carbons. The main hindrances of PEM Fuel Cells commercialization lie firstly on the high costs of platinum, secondly on the sluggish oxygen reduction reaction (ORR) at platinum-based cathode and finally on the short-term durability associated with degradative mechanisms, which cause the loss of cell performance during its working. Carbon corrosion, due to an oxidative process caused by the operating conditions of PEMFCs, is maybe the worst since it accelerates further degradative phenomena such as sintering and detachment of platinum nanoparticles. Therefore, research has investigated on supports capable of guaranteeing a long-term durability throughout the operating conditions of PEM. Metal oxides have been demonstrated as promising supports as they manifest an elevated corrosion resistance and avoid the migration and detachment of platinum nanoparticles owing to the strong metal-support interaction created at the interface. It has been found that this effect can have an impact on the catalytic activity, as well since electron transfer phenomena can occur at the interface between the metal and metal oxide. Nevertheless, metal oxides taken alone does not afford a sufficient electron conductivity, which is the main requirement of an electrode. Therefore, metal oxide-carbon hybrid supports have been developed in the last few years to achieve an appreciable electrical conductivity. Among the most promising metal oxide ceria, CeO_2, utilized in a wide variety of industrial applications, is rated as an interesting compound due to its intriguing feature of easily switching from Ce^{4+} to Ce^{3+} and its high oxygen storage capacity. These unique peculiarities have led scientists to study the effects of its presence on the cathodic compartment of PEM fuel cell. It has been proven that its capability of easily changing the oxidation states promotes the quenching of aggressive radicals that can destroy the proton conductive membrane (Nafion®) over time. Furthemore, the addition of ceria to Pt/C catalysts has been found to be helpful for improving the CO tolerance in the oxidation of methanol in direct methanol fuel cells and for enhancing the ORR catalytic activity and durability of Pt/C catalysts thanks to the oxygen spillover and the strong metal support interaction. In this thesis ceria was deposited together with platinum by one pot or two-step approach on a commercial carbon, Vulcan XC72 and on home-made biomass-based carbon supports. Home-made carbons were prepared via a pyrolysis treatment of cheap carbon precursor, namely agarose and chitosan, mixed with a template, Pluronic F127 and a graphitizing agent, iron, which was selectively removed from the carbon matrix through an acid washing leaving intact the morphology of carbon. The best performing catalyst of this thesis Pt_3h/CeO_2_750_15/CC was synthesized by

firstly depositing ceria at 750 °C for 15 min and afterwards platinum at 300 °C for 3 h on a highly graphitized chitosan-based carbon. The final catalyst contains up to 5 wt% of CeO_2 and 25 wt% of platinum loading. By performing a linear sweep voltammetry at 1600 rpm and 50 mV s^{-1} on a rotating disk electrode, its catalytic activity surpassed that of standard Pt/C (with 30 wt% of Pt) showing a mass activity 2.7 times higher and a half-wave potential shift of 30 mV towards more positive compared to Pt/C standard. In gas diffusion electrode the best performance in terms of activity and stability was obtained by using the same conditions but depositing on carbon VulcanXC72.

Riassunto

Le celle a combustibile con membrana a scambio protonico sono i migliori candidati per rimpiazzare i tradizionali motori a combustibile impiegati nel settore automobilistico. I catalizzatori più diffusi implementati in questo sistema fanno affidamento al platino, che viene nanostrutturato e supportato su carboni ad elevata area superficiale. I principali ostacoli che impediscono la commercializzazione delle celle a combustibile con membrana a scambio protonico riguardano in primo luogo gli elevati costi del platino, in secondo luogo la cinetica lenta della riduzione dell'ossigeno (ORR) nel catodo a base di platino, ed infine la durabilità a breve termine associata a meccanismi di degradazione che causano perdite di prestazioni di cella durante il suo funzionamento. La corrosione del carbone, dovuta ad un processo ossidativo causato dalle condizioni operative della cella, è forse il peggiore poiché accelera ulteriori fenomeni di degradazione come il *sintering* e il distacco delle nanoparticelle di platino. Perciò, la ricerca ha investigato su supporti in grado di garantire una durabilità a lungo termine durante il funzionamento delle PEM. Gli ossidi metallici si sono dimostrati supporti promettenti dal momento che manifestano un'elevata resistenza alla corrosione e impediscono la migrazione e il distacco delle nanoparticelle a causa di un'elevata interazione metallo-supporto all'interfaccia tra il metallo e l'ossido. Nonostante ciò, gli ossidi metallici presi singolarmente non permettono una sufficiente conducibilità elettronica, che è il requisito principale di un elettrodo. Perciò, supporti ibridi metallo-ossido sono stati sviluppati negli ultimi anni per raggiungere una conducibilità elettronica apprezzabile. Tra i più promettenti ossidi metallici, la ceria (CeO_2) utilizzata in una ampia varietà di applicazioni industriali, è ritenuta come un interessante composto data la sua intrigante caratteristica nel passare facilmente da Ce^{4+} to Ce^{3+} e la sua elevata abilità nell'immagazzinare ossigeno. Queste uniche peculiarità hanno spinto gli scienziati a studiare gli effetti della sua presenza nel compartimento catodi delle PEM. È stato dimostrato che la sua capacità nel variare facilmente lo stato di ossidazione promuove la rimozione di radicali aggressivi che possono distruggere la membrana a conducibilità protonica (Nafion®) nel tempo. Inoltre, l'aggiunta di ceria a catalizzatori Pt/C si è dimostrata di grande ausilio per migliorare la tolleranza nei confronti di CO nell'ossidazione del metanolo nelle celle a combustibile a metanolo diretto e per aumentare l'attività catalitica verso la riduzione dell'ossigeno di catalizzatori Pt/C grazie allo *spillover* di ossigeno e l'elevata interazione metallo-supporto. In questa tesi la ceria è stata depositata assieme al platino tramite un approccio *one-pot* o due *step* su un carbone commerciale, VulcanXC72, e su supporti di carbone provenienti da biomassa. I carboni sono stati preparati con trattamento per pirolisi di precursori a basso costo, cioè agarosio e chitosano, mescolati con un templante, Pluronic F127 e un agente grafitizzante, il ferro, che è stato successivamente rimosso dalla matrice carboniosa tramite

un lavaggio acido lasciando intatta la morfologia del carbone. Il catalizzatore più performante di questa tesi è Pt_3h/CeO_2_750_15/CC, che è stato sintetizzato prima depositando la ceria a 750 °C per 15 min e successivamente il platino a 300° per 3 h su un supporto altamente grafitizzato proveniente da chitosano. Il catalizzatore finale contiene fino a un 5 wt% di CeO_2 e 25 wt% di Pt. Eseguendo una voltammetria lineare a 1600 rpm e 50 mV s^{-1} su un elettrodo a disco rotante la sua attività catalitica sorpassa quella dello standard Pt/C (contenente un 30 wt% di Pt), mostrando una *mass activity* 2.7 volte maggiore e uno *shift* del potenziale di mezz'onda di 30 mV verso valori più positivi rispetto allo standard Pt/C. Con l'elettrodo a diffusione di gas, le migliori prestazioni in termini di attività e stabilità sono state ottenute usando le stesse condizioni ma depositando sul carbon Vulcan XC72.

Acknowledgements

Before moving to the discussion of my thesis I would like to thank all of people who have given an important contribution during my educational path and my happiest and warmest moment throughout my life.

A special thank should be given to my thesis supervisor, assistant professor Christian Durante, who has been a kind, witty, well-organized and patient person. He provided me useful suggestions during the critical moments of my thesis and I have always executed all his requests with great pleasure. I would like to thank my co-supervisor Denis Badocco for his wittiness and his helpful suggestions.

A warm acknowledgement should be given to people who assisted me during this hard but satisfying thesis, especially Riccardo and Mattia who provide me tremendous help above all in the last months. They taught me to become a well-organized person and not to waste my time in useless things. I would like to express gratitude to Giorgia Daniel, who firstly assisted me in the first month in the laboratory and helped me to use the main instruments for the carbon support synthesis.

I would like to give great thanks to all my friends who I met during the years at the university. I spent a delightful period with them especially before the pandemic broke out. They were funny, sociable in the funniest moment, and helpful when I studied with them. I really wish to meet them again in the future.

Finally, I would like to thank my family, which has always supported me during my studies and give me the opportunity of growing in comfortable and lovely environment.

1 INTRODUCTION

Despite the unprecedented drop in 2020, the year of the beginning of the pandemic, CO_2 emissions, which are responsible for global warming, have rapidly rebounded in 2021 reaching almost the same values of 2019 because of the global economy recovering [1]. The most updated previsions of Climate Action Tracker foresee a global temperature rising of about 2.7 °C above the preindustrial levels at the end of this century by adopting the current environmental policies (https://climateactiontracker.org/global/temperatures/). Some agreements, such as Kyoto Protocol (in 1997) and Paris agreement (in 2015) were developed to tackle the problem of climate change by reducing carbon dioxide emissions [2]. In addition, the recent conference COP26 in Glasgow has encouraged nations to discuss and agree on possible solutions to fight climate change and fix a date to completely abandon the exploitation of coal and fossil fuels as sources of energy. In fact, these are currently the largest contributors to world energy demand. On the other hand, they are rated as the most CO_2 emitters, and they are exhaustible sources of energy. In the last few decades, the research community has explored several alternative environmental-friendly and renewable sources such as thermal, solar, wind, ocean, biomass and geothermal energy. Although they fulfill the environmental requirements, their intermittent production of energy hinders their widespread usage in the global society. Fuel cells (FCs), which are devices capable of converting the chemical energy of reactants (i.e. fuel and comburent) into electrical energy, have grasped the attention of several researchers since they can be used to produce clean energy without pollutant emissions even though they are not renewable sources. Moreover, they have numerous advantages that make them so appealing and competitive with pollutant energetical sources, e.g. fossil fuels [3]. Some important pros are here mentioned:

- High yield of the electrical energy (up to 60 % in some cases) which can overtake the ideal thermodynamic limit represented by the Carnot's cycle, i.e. 52%
- Versatility of the fuel used, including hydrogen, methane, methanol and ethanol
- Lack of noise while the device is working
- Use of air as possible comburent instead of pure oxygen
- Modularity, which allows increasing power by connecting different cells in series
- Lack of the emission of hazardous gases

Thanks to their modularity FCs have already been introduced in a broad number of applications. These include stationary plant plants, among which The Ballard Generation Systems is currently the biggest one, submarines, ammonia and iron production, small portable devices and transport vehicles. Among them, the latter is maybe the sector that more exploit this technology by developing Fuel cell

vehicles or implementing fuel cells in hybrid vehicles, FCVs. Some notable brands which have recently developed FCVs are Toyota, Hunday, Audi, Volvo and Daimler-Chrysler [3].

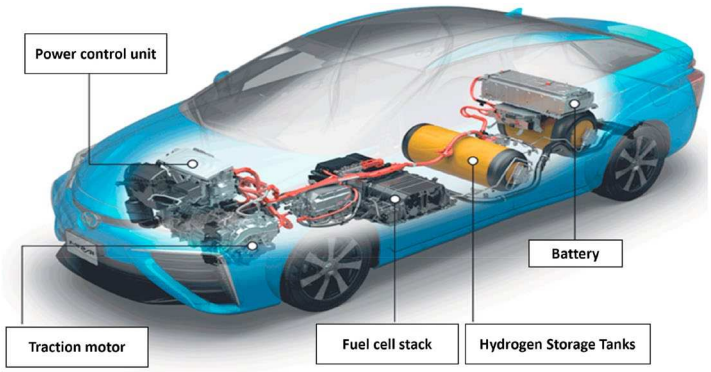

Figure 1. Toyota Mirai, an example of commercialized fuel cell vehicle [3].

The breakthrough of fuel cells took place in 1839 by Sir Thomas Groove, who came up with a device capable of producing electricity by exploiting the reversing the electrolysis of water. He immersed two platinum electrodes on one end in an electrolyte solution of sulfuric acid and the other two ends were separately sealed in containers of oxygen and hydrogen. He observed that water was produced in the sealed containers as a constant current flowed between the electrodes. Subsequently, he tried to combine pairs of electrodes connected in series to raise the potential drop, thus creating the first fuel cell [4]. Further advancements were made when Francis Bacon built the first fully-operational fuel cell in 1932, which contains an alkaline electrolyte. Thanks to the help of his colleagues, he implemented that fuel cell into a 5 kW device in 1959. In the same period, NASA started to investigate on this technology for the purpose of developing a compact electricity generator for spacecraft and in the Gemini program employed the early proton exchange membrane fuel cell. This kind of fuel cell was utilized until the ’90s when NASA in conjunction with the University of South California developed the direct methanol fuel cell [4].

So far, six different types of commercial-available fuel cells are distinguished according to their electrolyte:

- Solid oxide fuel cells SOFC
- Molten fused carbonate fuel cells MFCF
- Phosphoric acid fuel cells PAFC
- Alkaline fuel cells AFC
- Direct methanol fuel cell DMFC
- Proton exchange membrane fuel cell PEMFC

Another distinction is based on the working temperature. In fact, SOFC and MCFC require high temperatures to work (up to 800-1000 °C), PAFC intermediate temperatures (i.e. 200-300 °C) and the remaining FCs low temperatures (around 100 °C).

1.1 PROTON EXCHANGE MEMBRANE FUEL CELLS

Among the already listed cells, PEMFCs are the most suitable candidate for FCVs owing to their lightness and compactness. They operate at low temperatures (70-90°C at most) while pressure is still kept around 1-2 bar [3]. Each cell has a maximum output of around 1/1.1 V in DC. The connection in series of cells gives rise to a stacked structure that exhibits a higher output depending on the final application. The common structure of a PEM fuel cell includes the anode, cathode, electrolyte all layered between two bipolar plates, which allow the transport of the reactant gases through serpentines, and two current collectors. The layered structure of a typical PEMFC is shown in Figure 2.

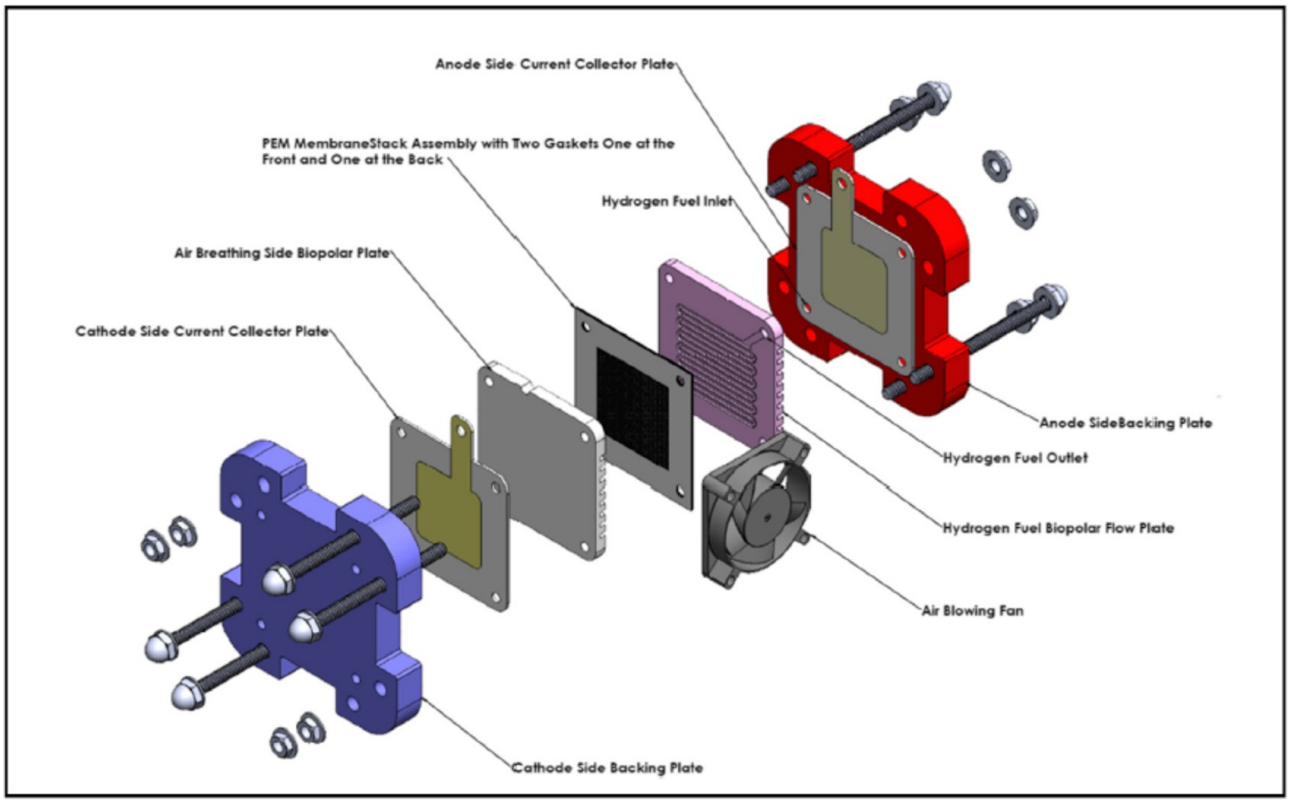

Figure 2. PEMFC planar diagrams illustrating the main components [5].

The anode, the cathode and the electrolyte of a single cell form the so-called membrane assembled electrode (MEA). The overall mechanism of a single cell is depicted in Figure 3. At the anodic compartment hydrogen H_2 is oxidized to proton H^+ according to the following reaction:

$$H_2 \rightleftharpoons 2H^+ + 2e^- \qquad E^\circ = 0\ V \qquad (1.1)$$

The generated electrons are injected into the external circuits through which they flow towards the cathode. The protons, instead, pass through the electrolyte, made of a proton conductive material, to reach the cathode. Here, electrons and protons react with oxygen to give water according to the following reduction reaction:

$$O_2 + 4H^+ + 4e^- \rightleftharpoons 2H_2O \qquad E^\circ = 1.23\,V \qquad (1.2)$$

Therefore, the overall reaction is:

$$2H_2 + O_2 \rightleftharpoons \ 2H_2O \qquad \Delta E^\circ = 1.23\,V \qquad (1.3)$$

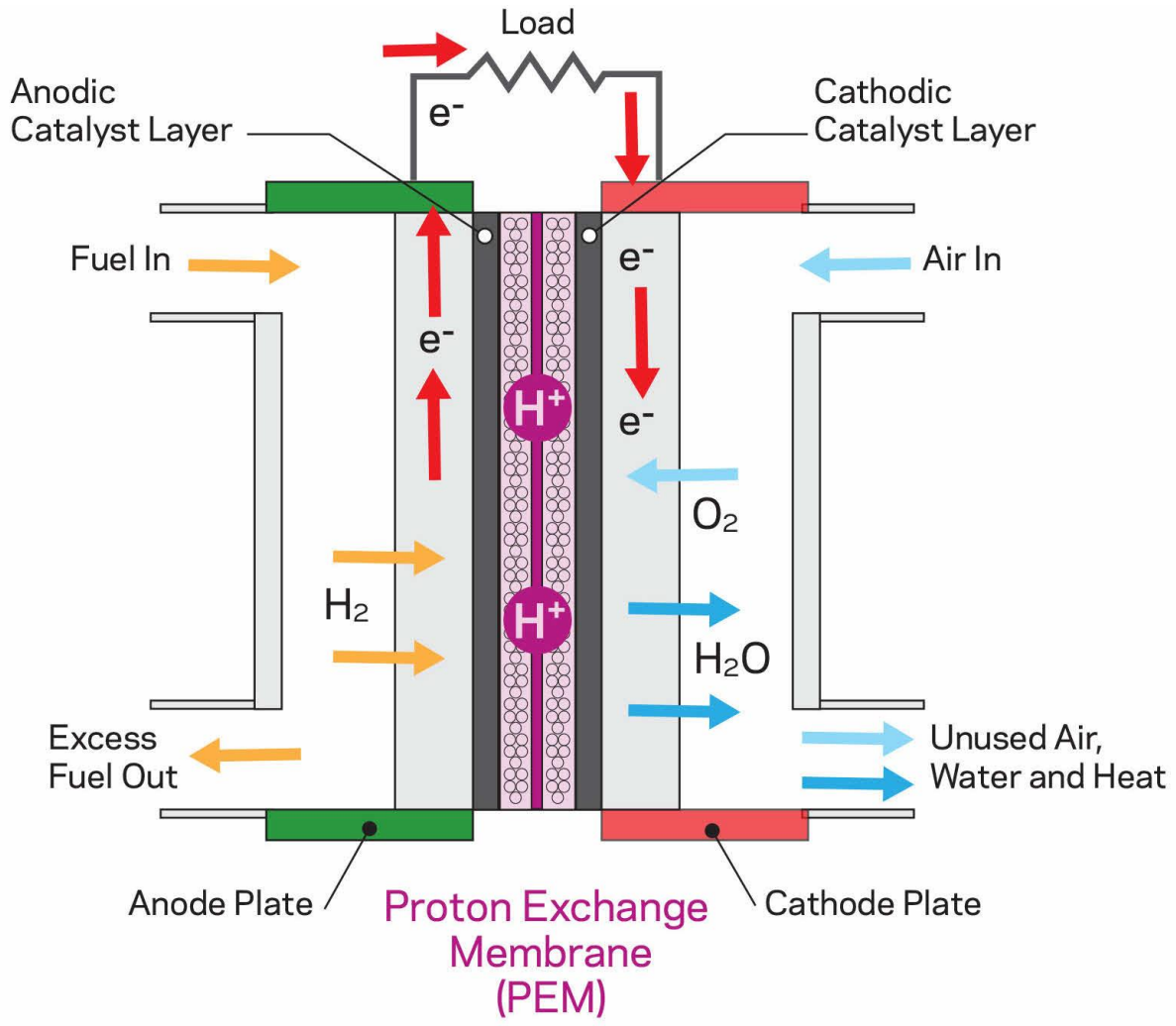

Proton Exchange Membrane (PEM)

Figure 3. Single cell compartment working principle.

The membrane, which is crossed by protons, is made of a polymeric material, polyperfluorosulfonic acid, known as Nafion®, a polymer deriving from Teflon and permeable to protons. However, the membrane must be sufficiently hydrated to guarantee the transport of protons. Unlike Teflon, which is totally hydrophobic, Nafion® can be considered as a bifunctional polymer since it has a hydrophobic behavior given by the perfluorinated backbone chains and hydrophilic behavior due to the sulfonated groups attached on the side chains. Figure 4A shows the polymeric structure of the Nafion® highlighting the hydrophobic and hydrophilic domains given by the sulphonate group,

which assists in the transport of H^+ occurring mainly by means of Grotthus' mechanism which is depicted in Figure 4B. Basically, this mechanism can be seen as an exchange of a hydrogen atom between the hydronium ion and a water molecule which interacts by means of a hydrogen bond. The presence of water also explains why this cell must work below 120 °C otherwise the solvent evaporates thus leaving an anhydrous membrane incapable of conveying protons [5].

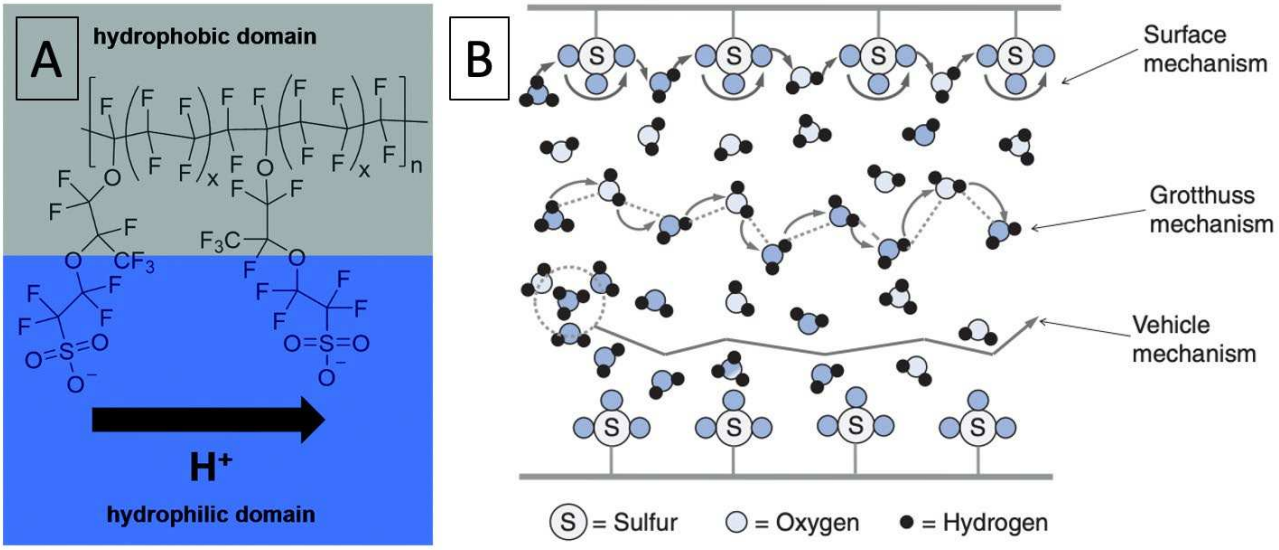

Figure 4. A) Structure of polyperfluorosulfonic acid and B) schematic representation of transport mechanisms occurring inside the Nafion membrane.

By looking inside the electrode structure depicted in Figure 5, two main layers must be distinguished: a gas diffusion layer (GDL) and a catalyst layer. The former is designed with the aim of:

- conveying a copious amount of reactants back to the catalyst layer;
- expelling the water in excess to avoid the electrode flooding;
- transporting electrons.

Carbon paper, which is made of carbon fibers, satisfies all these criteria. In fact, it is highly porous, highly electronically conductive and can also be impregnated with polytetrafluoroethylene particles to increase the hydrophobic behavior and thus easily remove water. However, this impregnation can decrease the electronic conductivity [6]. Similar requirements are needed for the catalyst layer with the addition of a catalyst that must be active towards the hydrogen oxidation reaction HOR or the oxygen reduction reaction ORR at the anodic and cathodic compartment respectively.

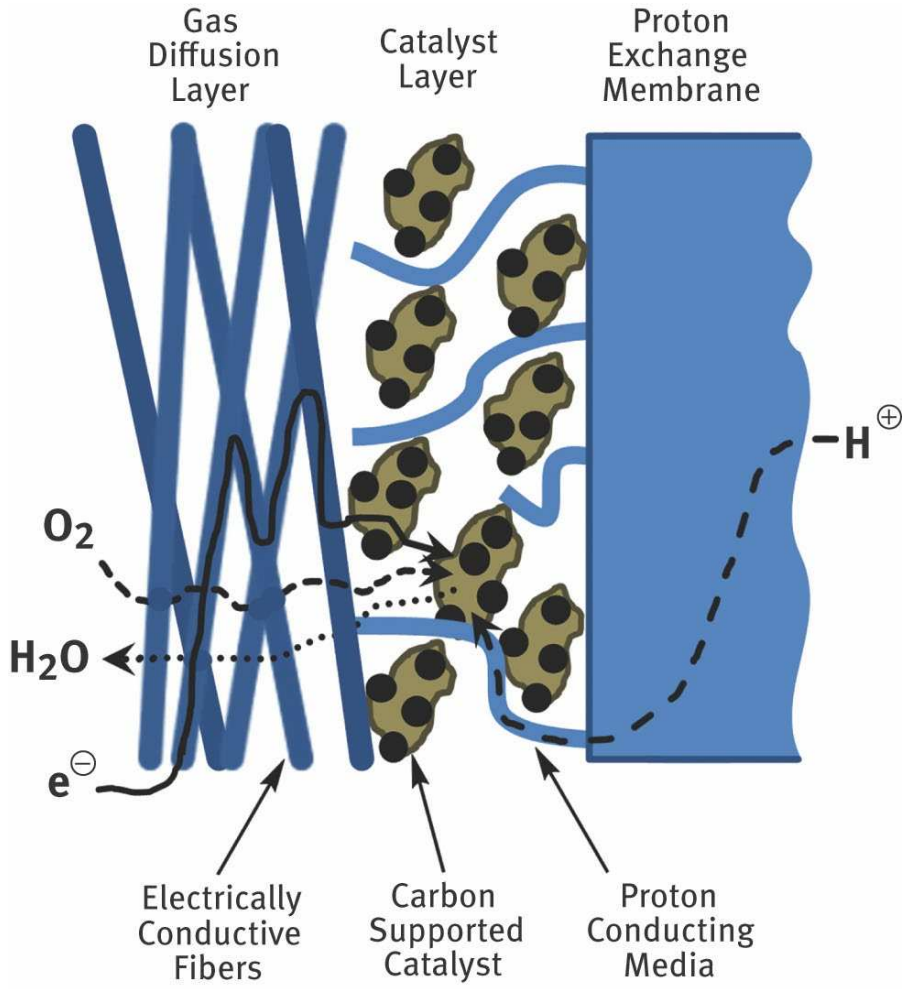

Figure 5. Internal structure of the cathodic electrode of PEMFC.

The introduction of the catalyst is necessary since PEMFCs work at low temperatures. Currently, the most employed catalysts are based on platinum nanoparticles supported on porous carbon. The nanostructuring of platinum and the porosity of the support provide a high active area. In this way, numerous active sites are exposed for the adsorption of hydrogen and oxygen molecules.

Theoretically, a single fuel is expected to produce 1.23 V in an open circuit. However, when it is connected to a load the potential drops to 0.6-0.7 V. This voltage loss is mainly due to three factors: electrode polarization caused by slow kinetics of electrochemical reactions occurring at the two different electrodes, mass transport polarization due to reactant concentration gradient inside the electrode as they are rapidly consumed within the catalyst layer and ohmic loss owing to the internal resistance of the cell. As regards the first loss it is well-known that the oxygen reduction reaction has a sluggish kinetic with respect to that of the hydrogen oxidation reaction. This kinetic bottleneck is one of the main factors that hinders the widespread of PEMFC in the market. In the following section will be reported the main steps the general mechanism for this reaction by discussing the state of art of the mainly used catalyst.

1.2 OXYGEN REDUCTION REACTION

The kinetics of the hydrogen oxidation reaction and oxygen reduction reaction is quite different. The kinetic of ORR is six orders of magnitude slower than that of HOR and implies a higher amount of catalyst in the cathodic compartment to boost this sluggish reaction. Platinum is currently known as the most active catalyst for both reactions, but the research is more focused on the development of platinum catalysts for boosting the ORR and thus lowering the kinetic losses in low-temperature fuel cells. Furthermore, the use of an alkaline or an acidic electrolyte can strongly affect the pathway of the reaction and therefore the kinetic which is lower in an acidic environment. In both media, i.e. acidic and alkaline, oxygen can be reduced according to a four or two electrons pathway. The former leads to water, H_2O in acidic media or OH^- in alkaline media whereas the latter brings to hydrogen peroxide, H_2O_2, in acidic media and OH_2^- in basic media. Moreover, the ORR can occur through an associative or a dissociative mechanism [7]. As regards the associative mechanism occurring on a metal surface such as Pt in alkaline media, ORR starts with the adsorption of O_2 molecule and the whole mechanism can be summarized as reported below (* represents the active site and O_2^* refers to an adsorbed species):

$$O_2 + * \leftrightharpoons O_2^* \quad (1.4)$$

$$O_2^* + 2H_2O + e^- \leftrightharpoons OOH^* + OH^- \quad (1.5)$$

$$OOH^* + e^- \leftrightharpoons O^* + OH^- \quad (1.6)$$

$$O^* + H_2O + e^- \leftrightharpoons OH^* + OH^- \quad (1.7)$$

$$OH^* + e^- \leftrightharpoons * + OH^- \quad (1.8)$$

Overall, four electrons are accepted by O_2 thus resulting in 4 OH^- ions. Alternatively, if the rupture of O-O is not energetically favored reasons the reaction (1.6) leads to the formation of a peroxide ion according to the reaction (1.9):

$$OOH^* + e^- \leftrightharpoons * + OOH^- \quad (1.9)$$

In this case, a two electrons pathway is followed. According to the dissociative mechanism the oxygen molecule splits into two atoms which adsorbs on two different active sites and the 4 electrons pathway proceeds following the steps (1.7) and (1.8):

$$\frac{1}{2}O_2 + * \leftrightharpoons O^* \quad (1.10)$$

Meanwhile, in an acidic environment the associative mechanism occurs in the presence of protons as follows:

$$O_2 + H^+ + e^- \leftrightharpoons OOH^* \quad (1.11)$$

$$OOH^* + H^+ + e^- \leftrightharpoons O^* + H_2O \quad (1.12)$$

$$O^* + H^+ + e^- \leftrightharpoons OH^* \quad (1.13)$$

$$OH^* + H^+ + e^- \leftrightharpoons H_2O + * \qquad (1.14)$$

The dissociative mechanism takes place in the alkaline environment by following the step (1.10) and proceeding with the steps (1.13) and (1.14). A fast cleavage of the O-O in the OOH^* species is required to form a water molecule. Conversely, if the rupture of this bond takes long time to occur on the catalyst surface due to energetic reasons the reaction (1.12) involves the formation of H_2O_2 according to the reaction (1.15):

$$OOH^* + H^+ + e^- \leftrightharpoons H_2O_2 + * \qquad (1.15)$$

Hydrogen peroxide can easily degrade by producing OH radicals which can attack the C-O-C bond of the Nafion® membrane thus leading to its degradation [8]. This results in a decrease of the ionic conductivity and therefore in a loss of cell performances. Hence, the two electrons pathway must be avoided as much as possible.

To achieve appreciable performances ORR should occur at potentials as close as possible to the ideally thermodynamic potential, i.e. 1.23 V if water is released in liquid form [9]. In any fuel cell ORR is the slowest reaction. The primary thermodynamic reason associated to that is the high bond energy of the oxygen molecule, which is estimated by the enthalpy ΔH^0 needed to break the O=O bond of an oxygen molecule and thus generating two atoms in gas form:

$$O_2\,(g) \rightarrow 2O(g) \qquad \Delta H^0 = 498\ kj\ mol^{-1} \qquad (1.16)$$

This value is higher to that associated to H-H bond, i.e. 436 kj mol^{-1} [10]. The entropy variation of O_2 dissociation is positive. Therefore, the variation of Gibbs free energy of the oxygen dissociation is given by the following relationship:

$$\Delta G = \Delta H - T\Delta S \qquad (1.17)$$

where ΔH and ΔS are the enthalpy and entropy variation of the oxygen dissociation. Since the entropy change associated to the dissociation is positive, as the temperature increases the ΔG decreases and thus the oxygen cleavage is favored at high temperatures. Despite that, the ΔS associated to the oxygen reduction to water is negative. Consequently, as the temperature rises, ΔG increases (it becomes less negative) leading to a decrease of the thermodynamic Gibbs efficiency which is defined according to the following equation [9]:

$$\eta = \frac{\Delta G}{\Delta H} \qquad (1.18)$$

where η represents the thermodynamic Gibbs efficiency, whereas ΔG and ΔH are the Gibbs free energy and the enthalpy of the oxygen reduction to water.

1.3 PLATINUM-BASED CATALYSTS FOR ORR

As deduced from above, catalysts for ORR must exhibit a high selectivity towards the water production by utilizing the protons which come from the anodic side and permeate through the membrane. Platinum-based materials are the most active, selective, stable and durable catalysts toward ORR. On the other hand, the low occurrence of platinum in the earth crust makes it very expensive, about $1,000 per ounce. This has exhorted to reduce the platinum content by over one order of magnitude in a PEMFC stack, from about 4 mg cm^{-2} to < 0.1 mg cm^{-2} in the last three decades [11]. However, the catalyst cost still contributes to 41% of the total cell cost compared to the other components such as the membrane, gas diffusion layer and bipolar plate [3].

One of the reasons explaining the high activity of platinum towards the ORR is the strong binding with O_2 [12]. Three ways of oxygen adsorption on platinum catalysts have been classified so far, as reported in Figure 6.

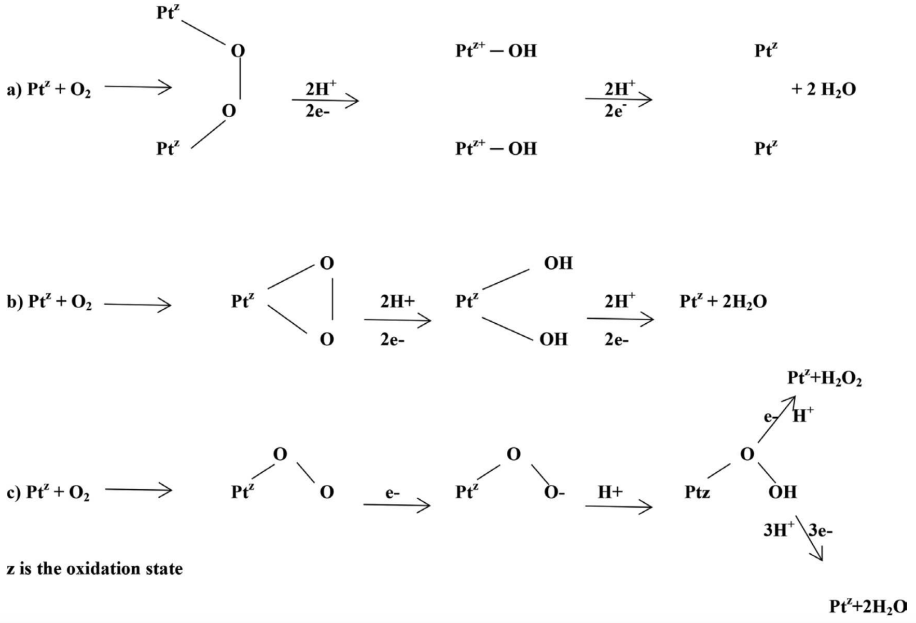

Figure 6. Oxygen reduction reaction on Pt from the a) bridge, b) Griffiths and c) Pauling model [12].

The first type is a single site adsorption called Gripphits model where the two oxygen atoms are both bond to one metal atom. The Pauling model is another single site adsorption where only one of the two oxygen atoms is bond to a metal atom. Bridge model is instead a dual site adsorption since the two oxygen atoms are bond to two different metal atoms. The Pauling model is suitable for the two electrons pathway whereas the other two models are related to the four electrons pathway [12,13]. As shown in section 1.2, the most important intermediates are OOH*, O*, OH* in the acidic environment. Their binding free energies are reported in Figure where it is possible to deduce that the rate determining step for the four electrons pathway is the reaction which involve the rupture of O-O bond of OOH*, i.e. the reaction (1.12) in the section 1.2. It was found that the binding free energies

of the three species are linearly related to each other [14]. In fact, the OH* binding free energy is given by:

$$\Delta G_{OH} = \frac{1}{2}\Delta G_O \qquad (1.19)$$

$$\Delta G_{OH} = \Delta G_{OOH} - 3.2 \qquad (1.20)$$

Therefore, ΔG_{OH} can be used as a descriptor to evaluate the ORR catalysts performance. According to the Sabatier principle the interaction between the atoms of catalyst surface and the adsorbed species must be neither too weak nor too strong, thus individuating an optimum in the catalytic activity. Therefore, on top of the volcano plot lays the best performing catalyst whose overpotential for the examined reaction is minimum. As shown in Figure 7A, which reports the activity as a function of ΔG_{OH}, platinum is the best candidate for the ORR. In the case of metals that bind oxygen-containing species too strongly, the formation of H_2O from the further reduction of OH* controls the pace of the reaction (i.e. represents the rate determining step). Meanwhile, for metals binding the oxygen-containing species too weakly, the ORR performance is related to the dissociation of oxygen and reduction of OOH* to O* [14].

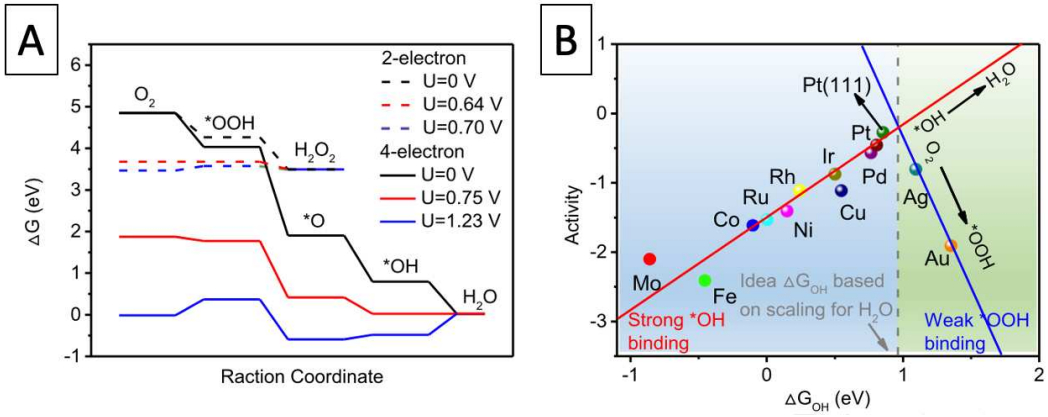

Figure 7. A) Free energy diagrams for the four-electron associative pathway of ORR on Pt (111) (solid lines) and two-electron pathway of ORR on PtHg4 (dashed lines) at different potentials with respect to the reversible hydrogen electrode: 0 V (black lines), equilibrium potential (blue lines) and the thermodynamic limiting potential (red lines). B) Volcano plot representing the ORR activity of different metals as a function of OH free binding energy (ΔG_{OH}), depicting the ideal ΔG_{OH} based on scaling of water and the limiting step with either too strong OH* binding or too weak OOH* binding.*

Therefore, the conclusion of volcano plot shown in Figure 7B is that Platinum is the catalyst that binds OH species more weakly than the other metals on its left and OOH more strongly than the species observable on its right. Another important feature of platinum-based catalysts is that H_2O_2 is thermodynamically unstable on (111), (110) and (100) as proven by ab-initio calculations. In fact, H_2O_2 it is immediately dissociate to OH, unless the cleavage of O-O is inhibited by adsorbed spectator species [15]. This is a huge benefit for Nafion membrane and explains why platinum catalysts are so widely used PEM fuel cells.

1.3.1 Strategies for improving activity of platinum-based catalysts

Since platinum seems to be insuperable form the catalytic point of view, the two ways to enhance the electrochemical activity of platinum: changing its surface structure and increasing the active sites [16]. The studies related to platinum surface reveal that the electronic structure of the metal is influenced by the exposed crystallographic facets since each facet has a different arrangement of atoms. It is experimentally proven that, for instance, the ORR activity of pure Pt surface in 0.1 M solution of $HClO_4$ follows this trend: (110) > (111) > (100) [16]. Additionally, DFT studies show that the intermediates formed during the ORR depend on platinum surface arrangements [16]. For example, the Raman Spectroscopy experiment of Dong et al. demonstrated that the ORR pathway on the Pt(111) surface occurs through OOH* intermediate whereas via OH* formation on the Pt(110) and Pt(100) [17].

The second way to improve the ORR catalytic activity of Platinum based catalysts, i.e. increasing the number of active sites, can be performed via reducing the metal size (i.e. obtaining nanoparticles) and improving its dispersion. Many studies have so far emphasized the effect of the nanoparticle size and shape on catalytic activity suggesting that the highest performance can be reached by approaching very small dimension, i.e. up to 2 nm [18–21]. A suitable dispersion can be fulfilled by using supporting materials which are used to anchor small nanoparticles and thus improving their stability through the so-called metal-support interaction. This phenomenon is a consequence of two effects: 1) electronic effect and 2) geometric effect [22,23]. The former arises from the energy difference between a metal and the support giving rise to an electron transfer form metal to a support or viceversa in order to achieve an equilibrium at the interface. According to the metal-semiconductor boundary theory, when two components come in contact a thermodynamic equilibrium is achieved when the Fermi energy level (E_f) of the electrons of the two components are the same at the interface. This equalization of E_f gives rise to an electron transfer across the interface. If the E_f level of the electrons in the metal is higher than that of the support, electron transfer occurs from the metal to the support until the equilibration of the Fermi level and vice versa, as shown in Figure 8. The electron transfer can be connected to the electronic structure of the support and the size of metal nanoparticles [22].

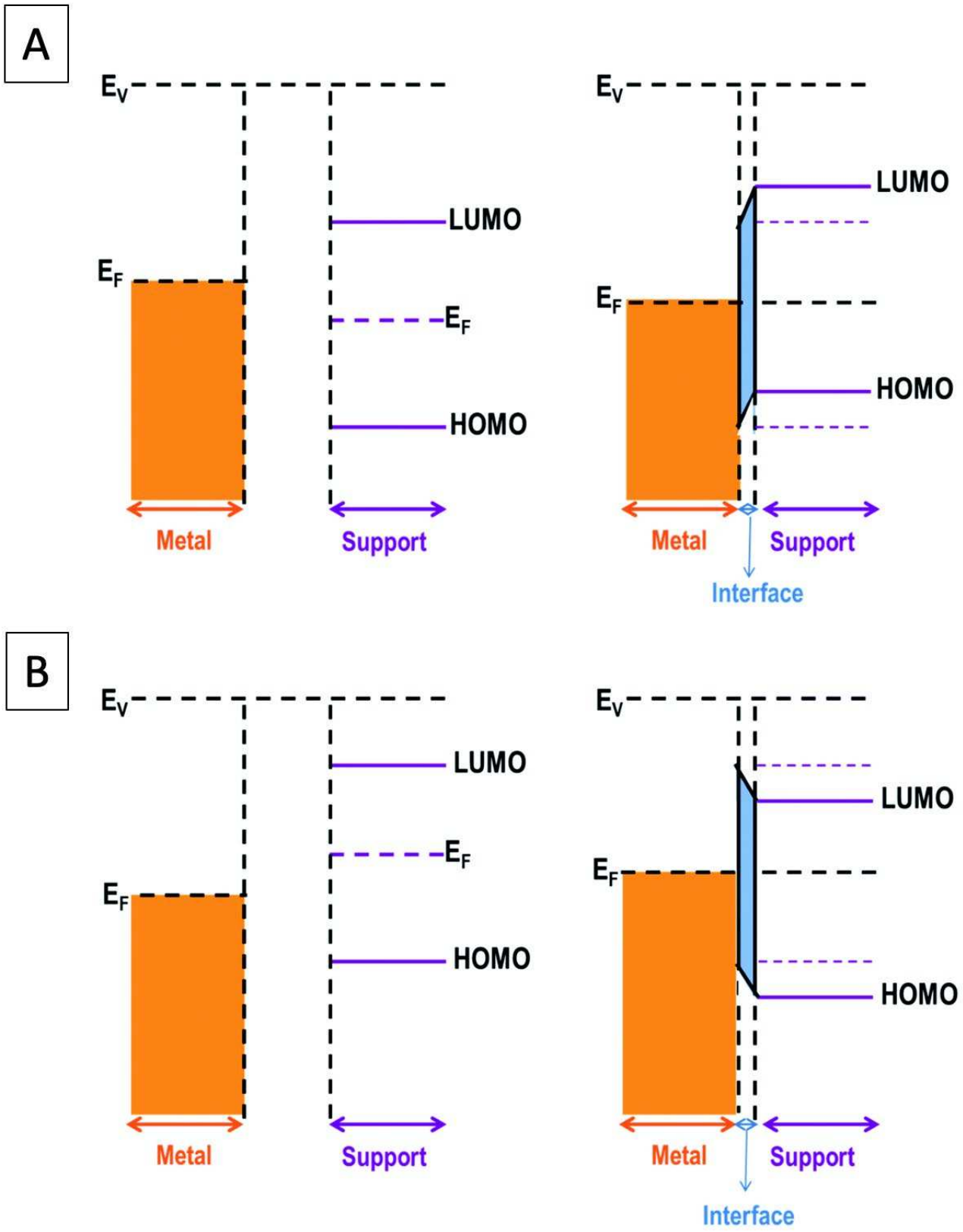

Figure 8. Electronic effect induced at the metal-support interaction from metal to support (a) and vice versa (b) [22].

The geometric effect is governed by the lattice mismatch between metal particles and their support, and it brings about the change the morphology of metal particles enhancing the interaction between the metal and support. Hence, the resulting exposed crystallographic facets and coordination number of metal atoms affect the catalytic activity. In fact, the activation energy of a catalytic reaction can be lowered when the metal nanoparticles possess plane with a lower coordination number of atoms exposed on the surface. Electronic and geometric effects are intimately related to each other as they both affect the activity and stability.

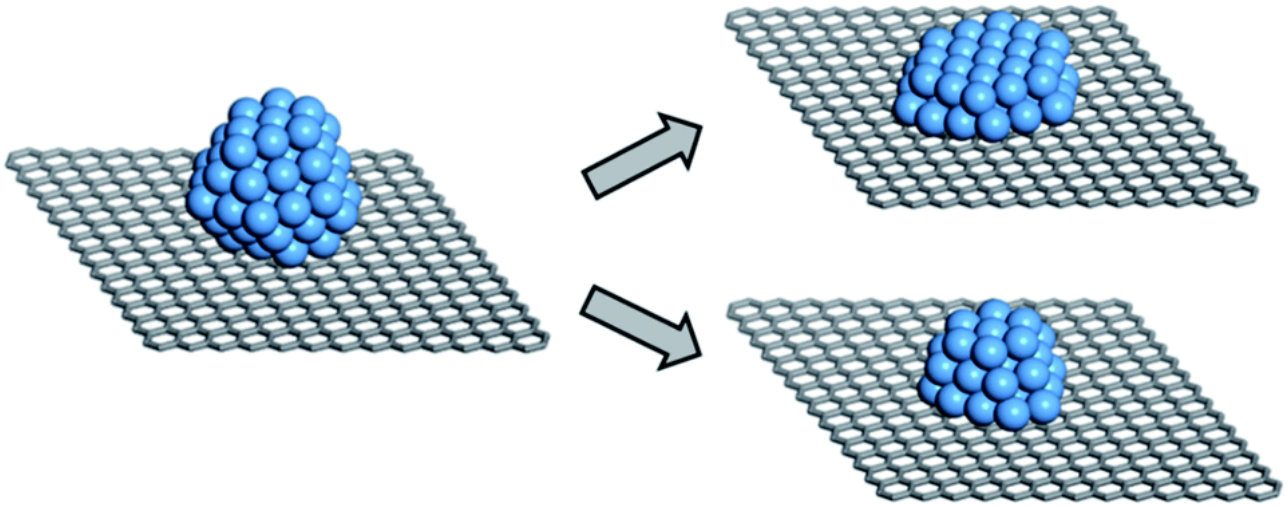

Figure 9. Illustration representing the geometric effect in metal-support interaction [22].

Among the most used supports, carbon-based materials are the most employed due to their excellent electronic conductivity, large surface area and low cost [24]. In this case a strong metal-support interaction arises from the overlap between d-band and the π-orbitals of the carbon support, thus allowing an electron transfer from the platinum to the carbon support, which can enhance the electrochemical activity and stability. In fact, the binding energy of the reactant that adsorbs on platinum nanoparticle decreases when the electron density on Pt drops because of an electron transfer from Pt to the support (downshift of the d-band energy level) and therefore gives rise to a better electrocatalytic activity [22]. Moreover, their modification with heteroatoms doping such as nitrogen or sulfur can increase the electrocatalytic activity because of the tuning of the electronic structure of platinum. DFT and experimental studies show a superior electrochemical activity for platinum supported on nitrogen-doped graphene-based materials with respect to platinum on graphene and this is associated to the shifting of a d-band center position of platinum, i.e. changing the electronical properties [25,26].

1.3.2 Platinum alloys

As well as improving the surface feature of the platinum itself or its dispersion on supporting materials, alloying platinum is an effective method to enhance the catalytic performances and also reduce its content which is of great interest.

Great efforts have demonstrated up to now that decreasing the d-band center of platinum is an effective method for improving the activity towards the ORR [27] . This can be performed by alloying platinum with metals of the fourth period of the periodic table elements such and Ni, Co [28]. The allowing composition which gives the best results is Pt_3M [27]. The enhancement in ORR activity is due to a change in the electronic structure of platinum, i.e. the shifting of the d-band center as displayed in the Figure 10 where the volcano plot demonstrate a linear relationship between the ORR activity measured with the kinetic current at 0.9 V and the d-band center. Here Pt_3Fe and Pt_3Co are the most promising candidates to replace conventional Pt/C catalysts in PEM fuel cell [29].

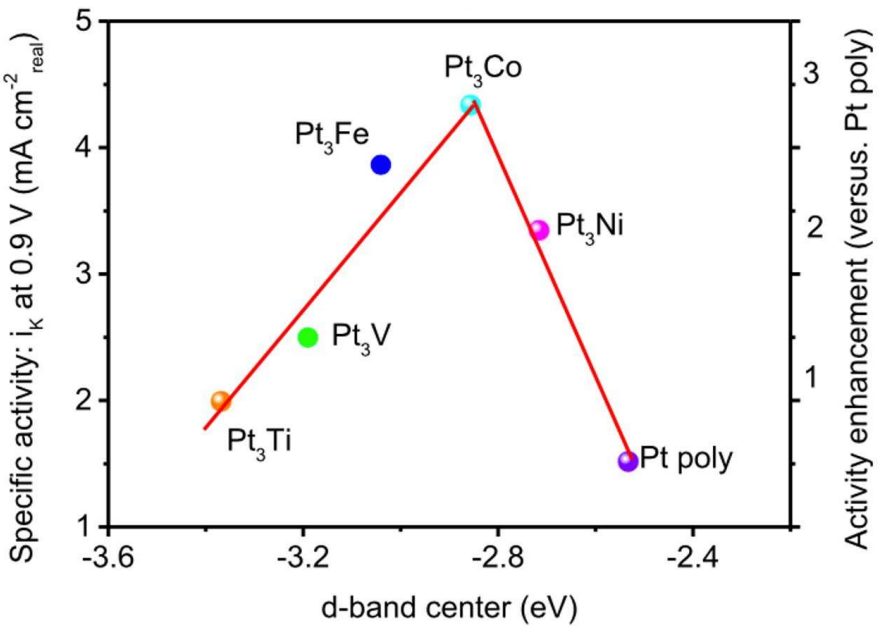

Figure 10. A volcano plot showing the best active Pt alloying catalysts compared to polycrystalline platinum [29].

A change in the electronic structure of platinum alloys can be mainly induced by two effects strain and ligand effect. The strain effect is related to a deformation caused by a lattice mismatch. This can occur when a heteroatom is introduced in the lattice structure or when a film of such a material having a certain lattice parameter is deposited on a substrate that possesses another lattice parameter.

Therefore, the change of atomic bond distances due to the lattice mismatch modifies the overlap between the atomic orbitals and consequently the electronic d-band structure. As an example, a tensile stress can be induced when a Ni atom is inserted in the platinum lattice or if Ni atoms are deposited on a platinum substrate. In this case the Ni d-band center upshifts and the d-band width narrows. The opposite occurs when a compressive strain is introduced in the lattice. It is accepted in literature that

compressive strain downshift the d-band center thus bringing to a weakened interaction between the adsorbed specie whereas the tensile stress upshift the d-band center upshift the d-band center giving rise to a strong interaction.

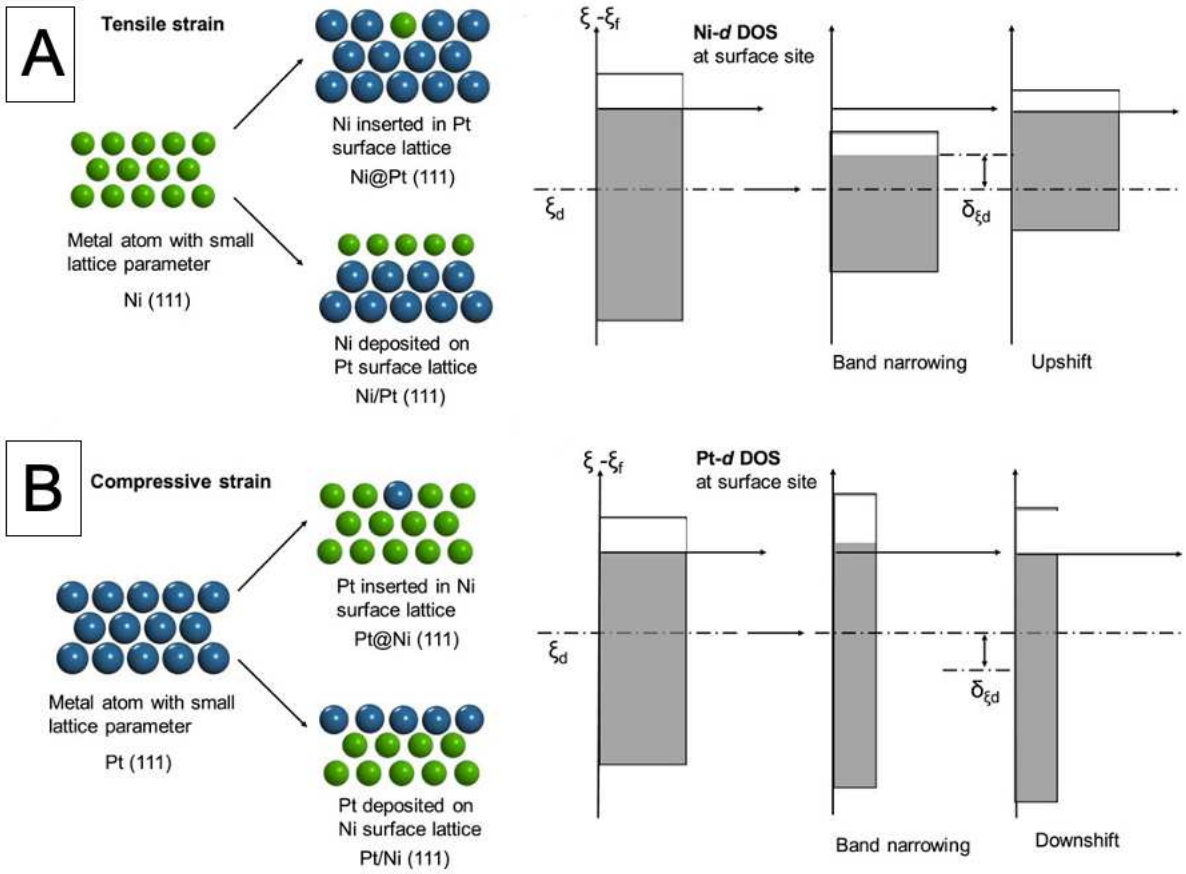

Figure 11. Tensile (A) and compressive strain (B) induced in a PtNi alloy with the respective changes in the electronic d-band structure of Ni and Pt.

The ligand effect occurs on the interface of atoms with different electronegativity (in case of metals different d-band center) which leads to a charge transfer between them. For instance, the alloying of platinum with transition metal such as Ni weakens the d-band center thanks to an electron donation.

1.3.3 Alternatives to Pt: PGM-free catalysts

Alloying platinum with other elements represents one effective way to reduce the platinum content even enhancing the catalytic activity. Notwithstanding, there is also a huge interest of finding cheaper catalysts which can completely replace platinum. Noble metals belonging to the Platinum group metals, such as Pd have been used as cathodic material in PEMFC since they exhibit a catalytic performance close to that of platinum [30]. However, PGM-free catalysts, are considered the cheapest alternative to platinum. The most promising PGMs materials for the ORR in acidic media are transition metals-nitrogen doped carbon materials (TM-N_x) where TM usually denotes Fe or Co or Mn. These catalysts consist of cobalt or iron phthalocyanine complexes embedded within a carbon matrix. Their kinetics follow the four-electron pathway and in some cases, the activity is almost

comparable to Pt supported on carbon catalysts [31]. However, these materials are much less stable than platinum-based catalysts because of carbon corrosion phenomena, active site delamination and metal dissolution acidic environment. Therefore, the activity-stability trade-off represents the major constrain that hinders their employment in commercial fuel cell [31,32].

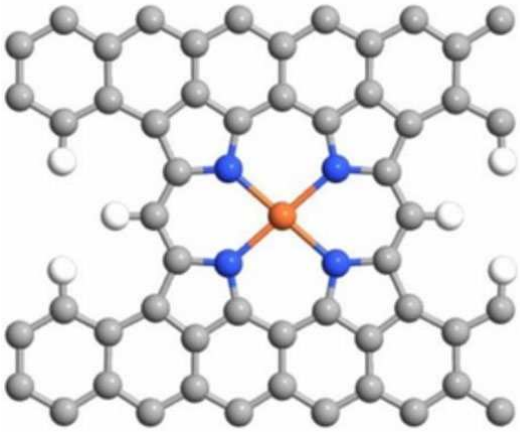

Figure 12. Example of a PGM-free catalysts where iron and nitrogen atoms are in orange and blue respectively whereas carbon and hydrogen are in grey and white respectively [33].

1.4 STABILITY ISSUES REGARDING PLATINUM-BASED MATERIALS

Developing highly durable PEM fuel cells is of great importance since these devices are designed for vehicles. Hence, in addition to activity, another essential requirement for a catalyst is stability. Although platinum catalysts are highly active towards the ORR, their unacceptable durability impedes the commercialization of PEM fuel cells. Consequently, it is worthy to gain a deeper understanding of the degradative mechanisms of these catalysts for designing a reliable cathodic material.

Platinum catalysts undergo structural and morphological changes during the operating conditions of PEM fuel cells which can result in a loss of performance over time.

Degradation mechanisms can be divided into three groups: dissolution of the metal component, growing of nanoparticle sizes and support degradation [34].

1.4.1 Platinum and platinum alloys dissolution

In order to understand the possible platinum dissolution in the PEMFC environment, it is worthy to analyze a Pourbaix diagram, which provides thermodynamic information about the stable equilibrium phases of an aqueous electrochemical system. It is well-established that platinum undergoes a stepwise oxidation process that ends up with the formation of PtO_3 and both the metallic and the oxide are subject to dissolution reactions, as reported below [35]:

Oxidation/reduction:

$$Pt + 4H_2O \rightleftharpoons PtO + 2H^+ + 2e^- \qquad E^\circ(Pt/PtO) = 0.98 - 0.059\,pH \qquad (1.21)$$

$$PtO + H_2O \rightleftharpoons PtO_2 + 2H^+ + 2e^- \qquad E^\circ(PtO/PtO_2) = 1.045 - 0.059\,pH \qquad (1.22)$$

$$PtO_2 + H_2O \rightleftharpoons PtO_3 + 2H^+ + 2e^- \qquad E^\circ(PtO_2/PtO_3) = 2.000 - 0.059\,pH \qquad (1.23)$$

Dissolution/precipitation:

$$PtO + 2H^+ \rightleftharpoons Pt^{2+} + H_2O \qquad E^\circ(Pt/PtO) = -7.06 - 2\,pH \qquad (1.24)$$

$$Pt \rightleftharpoons Pt^{2+} + 2e^- \qquad E^\circ(PtO/PtO_2) = 1.188 + 0.030\,pH \qquad (1.25)$$

$$PtO_2 + 4H^+ + 2e^- \rightleftharpoons Pt^{2+} + 2H_2O \qquad E^\circ(PtO_2/PtO_3) = 0.837 - 0.118pH \qquad (1.26)$$

Figure 13 displays a simplified Pourbaix diagram of platinum in the potential region of 0.8-1.4 V vs. SHE and pH region of -2 and 2. The circled numbers refer to the reactions (1.19), (1.20), (1.22), (1.24) whereas nanomolar and micromolar are the concentration of dissolved Pt^{2+} ions. At the pH of 0, the pH of the acidic environment of PEMFCs, the Pt^0 is subject to a nanomolar Pt^{2+} dissolution at potential between 0.92 and 1.10 V (vs. NHE). These correspond to the typical potentials at the PEMFC cathode during low loads and non-ideal start up/shut down cycles. This observation is highly relevant from the practical point of view [35].

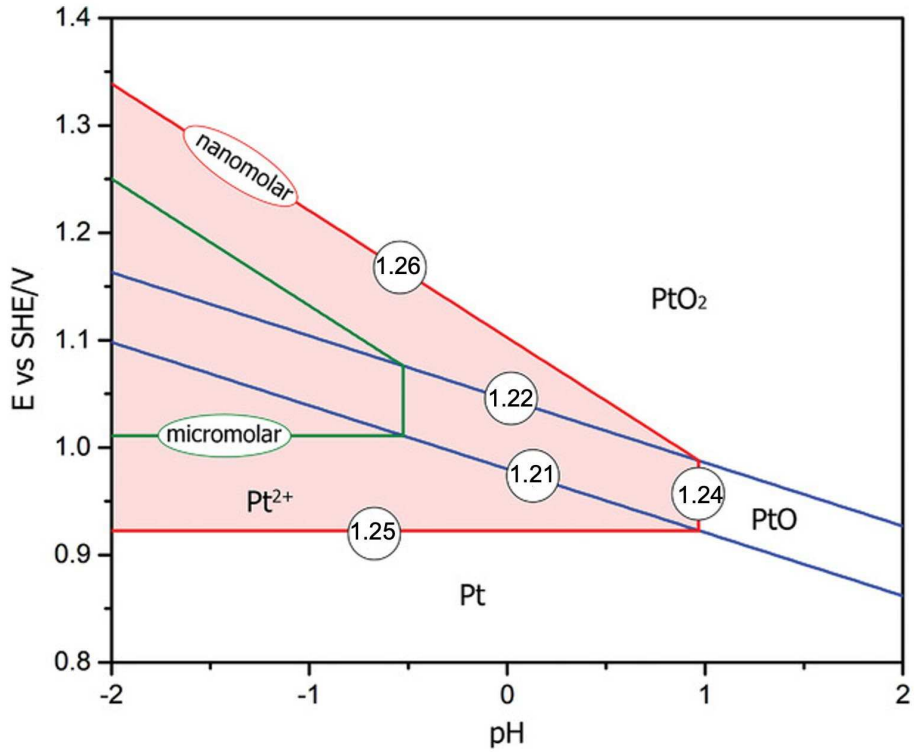

Figure 13. Pourbaix diagram of platinum in the potential region between 0.8-1.4 V vs. SHE and pH region of -2 and 2. The red area enveloped by red lines represents the region where Pt^{2+} is dissolved with nanomolar; the green lines refer to the region where Pt^{2+} is present in micromolar concentrations. The circled numbers refer to the equation reported above [34].

If, on the one hand, alloying platinum with the transition metals reduces the costs of the catalyst and boosts the ORR, on the other hand, their insufficient durability in PEM fuel cell working conditions hinders their practical application. It has been reported that the metals such as Fe, Co, Ni, Cu, having a dissolution potential much lower than that of platinum (-0.5, -0.2, 0.1, 0.3 V respectively vs. 0.8 V for Pt), tend to easily dissolve in the strongly acidic conditions of PEM whereas Pt tends to form a solid oxide rather than soluble ions [34]. The dissolution of the transition metal in Pt alloyed catalysts brings about the loss of cell performances since these metal ions, having a strong affinity for the sulfonic acid of the Nafion membrane, can easily exchange with the proton of the membrane destroying the membrane itself.

1.4.2 Growing of nanoparticle sizes

As the activity is affected by nanoparticle dimension, growing of nanoparticle size is another process which causes a decrease in the catalytic activity. In fact, the enhancing of nanoparticles dimension leads to the decrease of the number of active sites available for the adsorption of the reactants. Growing of nanoparticles comprises a series of phenomena which leads to the increase in nanoparticles size: Ostwald ripening, aggregation, agglomeration and coalescence.

1.4.2.1 Ostwald ripening

Ostwald ripening is a growing process based on the different solubility of nanoparticles with dissimilar chemical potential due to a difference in their surface energy. The atoms of small nanoparticles, which have a higher chemical potential, easily dissolve, and redeposit on larger nanoparticles, which have higher chemical potential. In a fuel cell environment, this process is called *electrochemical Ostwald ripening* because the mass transport is electrochemical rather than diffusive [36]. In fact, the migration of metallic Pt occurs through a process involving the dissolution of Pt in the electrolyte and the transmission of electrons through the substrate. In the case of isolated nanoparticles, the atoms of the smallest nanoparticle easily dissolve in the electrolyte in a cationic form and subsequently deposit on larger nanoparticles due to the difference in the chemical potential. In this case, no electron transmission occurs. The growing process of the largest nanoparticles at the expense of the smallest one stopped when a quasi-equilibrium state is reached. However, if two nanoparticles are supported on a conductive support both ion transportation (through the electrolyte) and electron transport (through the support) take place. In this case, the electrochemical Ostwald ripening keeps going on since it is not able to reach a quasi-equilibrium state. A similar situation occurs when two nanoparticles are in contact since the ions are transported through the electrolyte whereas the electrons pass through the interparticle contact [36].

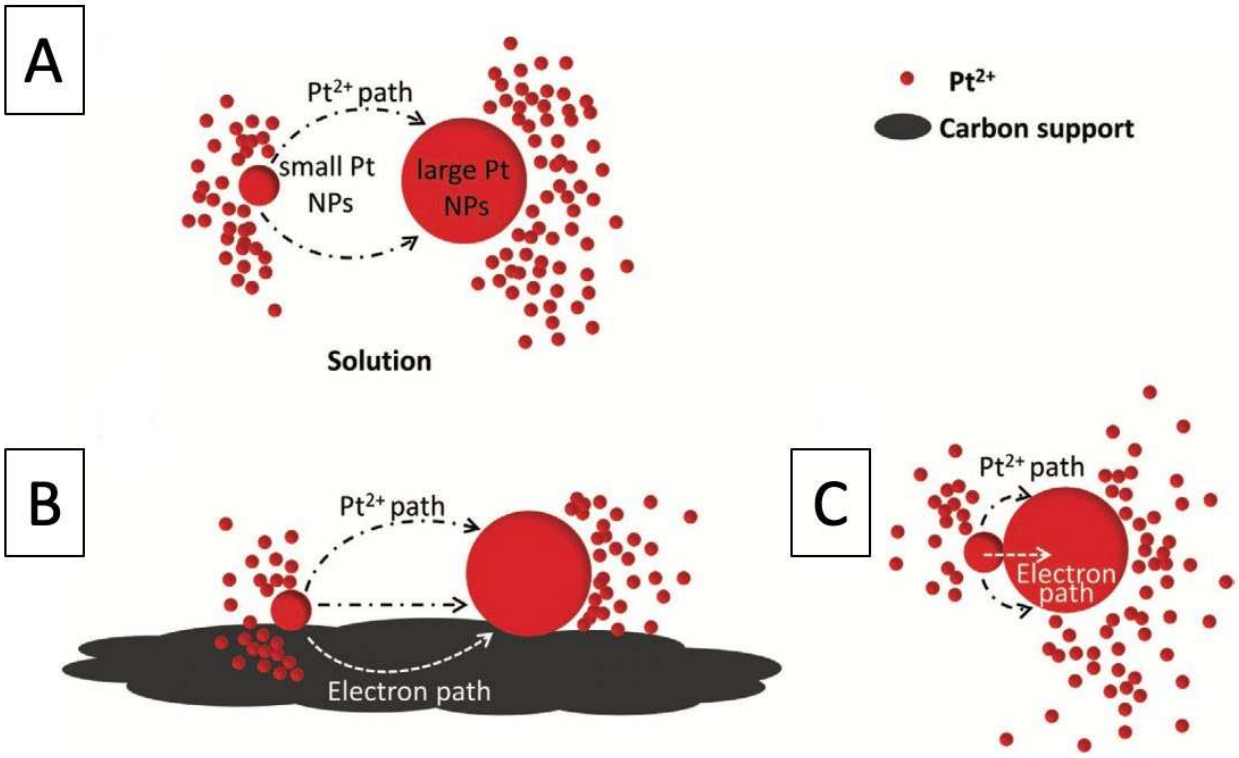

Figure 14. Ostwald ripening phenomenon occuring for isolated A) isolated nanoparticles anchored on a conductive support B), for in contact nanoparticles C).

1.4.2.2 Agglomeration and coalescence

When platinum nanoparticles are weakly bonded to a carbon support they can migrate on support surface and give rise to agglomeration and coalescence. The former leads to the formation of clusters of nanoparticles whereas the latter is, instead, a consequence of the collision of nanoparticles, which fuse together thus forming a larger nanoparticle. Figure 15 shows an example of agglomeration leading to the formation of clusters marked by ellipses.

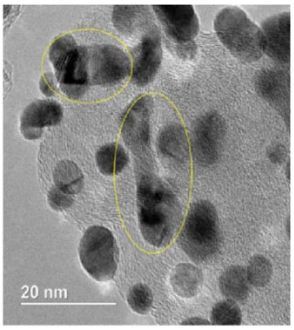

Figure 15. An example of agglomerated platinum nanoparticles.

1.4.3 Carbon support corrosion

Aggregation, agglomeration, coalescence, and particles detachment are very often the result of a further degradation phenomenon which is the support corrosion. In fact, a preferential local corrosion of the support near nanoparticles could ease the migration of particles due to the shrinkage of the support surface. When the corrosion leads to a very weak interaction between the nanoparticles and carbon support particle detachment may occur. Ultimately, a severe carbon support corrosion could bring to a loss of the structure integrity deteriorating the porous channels which are of vital for the reactant transport and dramatically decrease the electrical conductivity, essential to the conduction of electrons [37]. The mechanism of carbon corrosion is substantially attributed to an electrochemical oxidization process which leads firstly to the formation of oxygen-containing functional groups such as phenols, esters, ketones and carboxylic acids and secondly evolve into CO_2. It is believed that the formation of an excessive number of the oxyphilic functional groups can enhance the hydrophilicity facilitating the flooding of the electrode that can hinder the transport of oxygen to the active sites thus causing a loss of performances [38]. Carbon oxidation is made thermodynamically possible in fuel cell operating conditions because the standard potential associated to the redox couple CO_2/C is 0.207 V vs. NHE [39]. A hypothetical corrosion mechanism which severely alters the performance of the catalyst is reported below [34].

$$C^+ + H_2O \leftrightharpoons CO_{surf} + 2H^+ \quad (1.27)$$

$$CO_{surf} + H_2O \leftrightharpoons CO_2 + 2H^+ \quad (1.28)$$

$$CO_{surf} + Pt \leftrightharpoons Pt - CO_{ads} \quad (1.29)$$

$$Pt - CO_{ads} + H_2O \leftrightharpoons CO_2 + 2H^+ + 2e^- \quad (1.30)$$

The first step involves formation of C^+ species which are subsequently hydrolized thus forming carbon surface oxides (CO_{surf}) and further oxidized to CO2. The evolution of CO_2 can also be easily triggered by platinum nanoparticle, acting as catalyst for the CO oxidation [40]. The crystallinity of carbon enormously affects the oxidation rate of carbon support in PEMFC environment and generally the corrosion process of the graphitic ordered domains begins to occur at higher potentials with respect to the amorphous disordered sites [41], as depicted in Figure 16.

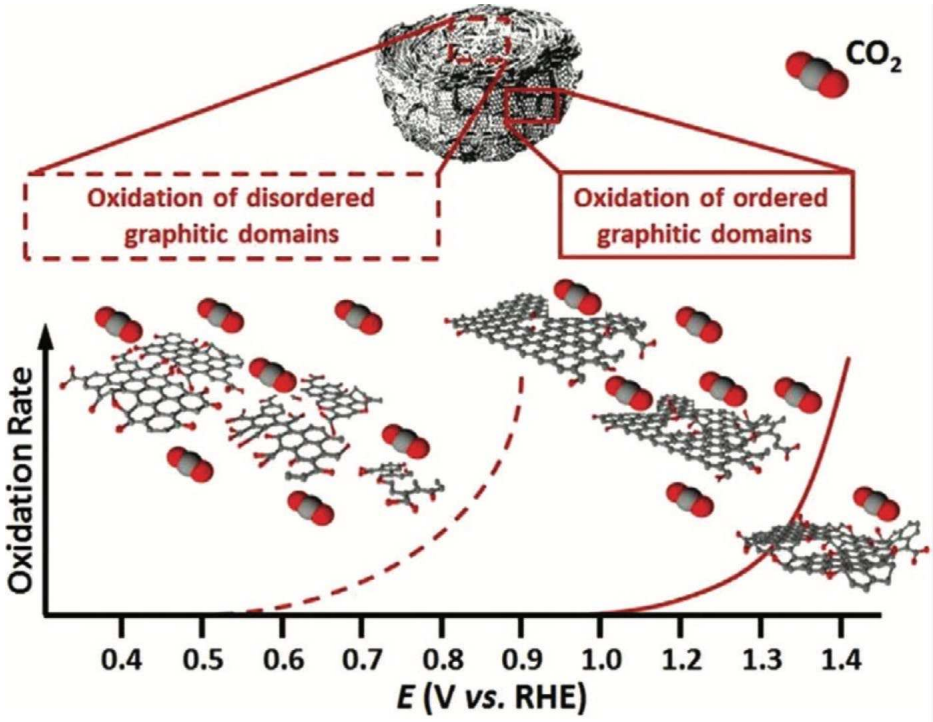

Figure 16. Oxidation rate trend for the disordered graphitic domains at low potentials (0.5 V vs. RHE) and ordered graphitic domains at higher potentials (beyond 1.0 V) [41].

This difference is explained by the fact that amorphous region presents a lot of defects such as dangling bonds which are the starting points of the corrosion. Hence, the graphitization of carbon support was identified as a good strategy to enhance the corrosion resistance and achieve a better electronic conduction. Among the most graphitized carbon support, graphitized mesoporous carbon, reduced graphene oxide and carbon nanotubes have drawn the attention of many scientists as they stabilize well the Pt nanoparticle due to their high corrosion resistance [34,42]. As an example, graphitization of the commercial amorphous carbon support Vulcan XC72 with high thermal treatment increased the corrosion resistance of the support giving better results than no graphitized Vulcan XC72 after accelerated stress test since it better stabilized Pt nanoparticle [43]. Blending of graphitized supports and amorphous carbon black have been used as another strategy to prolong the lifetime of Pt/C catalysts [44].

1.5 PLATINUM SUPPORTED ON CARBON-METAL OXIDE COMPOSITE

In comparison to the highly graphitized carbon materials, noncarbon support have received enormous attention in the last decade since they can completely avoid the electrochemical corrosion during PEM fuel cell long-term operation and repeated start/stop cycles. Among the most explored alternative to carbonaceous support, transition metal oxides are highly attractive owing to their tremendous corrosion resistance in acid medium and strong metal-support interaction (SMSI).

Generally, the metal oxide exhibits a higher stability in acidic medium compared to carbon due to their high corrosion resistance and the strong metal support interaction prevents the migration and detachment of platinum nanoparticles [23,42].

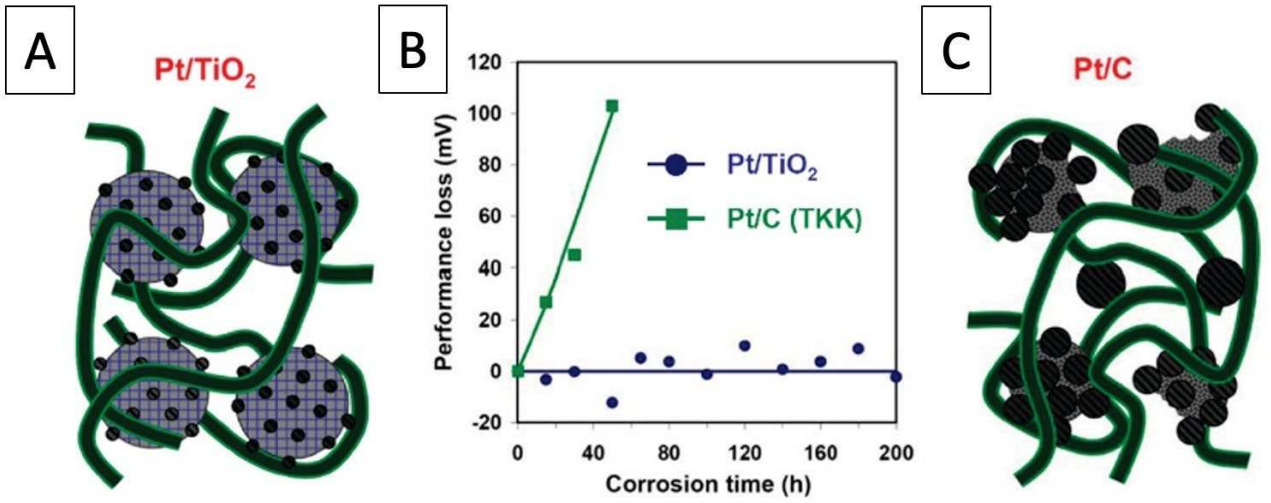

Figure 17. Comparison of durability performance between a Pt/TiO_2 on left and Pt/C on right after an accelerated stress test showed in the middle where a graph reports the performance loss (mV) as a function of the corrosion time (h) [45].

Popov et al. demonstrated the strong stabilizing effect of the TiO_2 mesoporous support with respect to that of carbon during an accelerated stress test performed in a fuel cell system. The results are shown in Figure 17B. By holding a potential 1.2 V for 200 h Pt/TiO_2 does not exhibit any performance loss, whereas Pt/C (TKK) shows an incredible loss of performance after 80 h. This is explained by the degradation phenomena which occurred for Pt/C during fuel cell operating conditions, such as nanoparticle coalescence, detachment and aggregation which are clearly represented in Figure 17C. After 80 h the platinum nanoparticle size changes from 2.5 to 11.5 nm for Pt/C with a rapid decay in the electrochemical surface area (ECSA). On the contrary, for Pt/TiO_2 the nanoparticle dimension varies from 6.2 to 7.8 nm after 80 h with only a slight decrease in the ECSA [45]. In a study, platinum was deposited on six metal oxide supports, TiO_2, MoO_3, SnO_2, Nb_2O_5, Ta_2O_5, WO_3 to develop the most durable catalyst. After 60000 start/stop cycles, Pt/SnO_2 exhibits the best durability as SnO_2 was the most corrosion resistant oxide. Besides, its performance was compared with Pt/C commercial catalyst. Pt/C show a more rapid decrease of the electrochemical surface with respect to Pt/SnO_2 and

this result was due to the highest dissolution of Pt/C compared to Pt/SnO_2, as confirmed by ICP-MS analysis [46].

As already mentioned in section, SMSI effect, which arises whenever nanoparticles are supported, is something that can alter the catalytic activity of a reaction when an electron transfer occurs between the metal and the support. Differently from Pt supported on carbon, fundamental aspects of SMSI between metal and metal oxides such as the interfacial bonds and direction of electron transfer is something that depends on the nature of the used oxide and on the interface between the metal and metal oxide. The importance of the interface between the metal and the metal oxide has been already emphasized in a study where a $Pt/NbO_x/C$ catalyst was synthesized by arc plasma deposition. In that work it was highlighted that the interaction of platinum with the metal cation (of the metal oxide) and/or the O belonging to the metal oxide depends on the composition at the metal-metal oxide interface, which in turn depends on the valence state of the metal oxide. It was found that Pt interact with Nb in a unsaturated (in terms of the number of bonds with O) NbO_x due to the oxygen deficiency in the metal-metal oxide interface while Pt interacts with O in nearly saturated NbO_x as depicted in Figure 18 . EXAFS and XAS analysis revealed that Pt donates electron to NbO_x through Pt-Nb and Pt-O bonds. The presence of Pt-O improves the activity of the catalyst toward the ORR by shortening the Pt-Pt and the electron deficiency of low-coordinated platinum atoms exposed on small nanoparticle surface have a strong effect on catalyst durability [47].

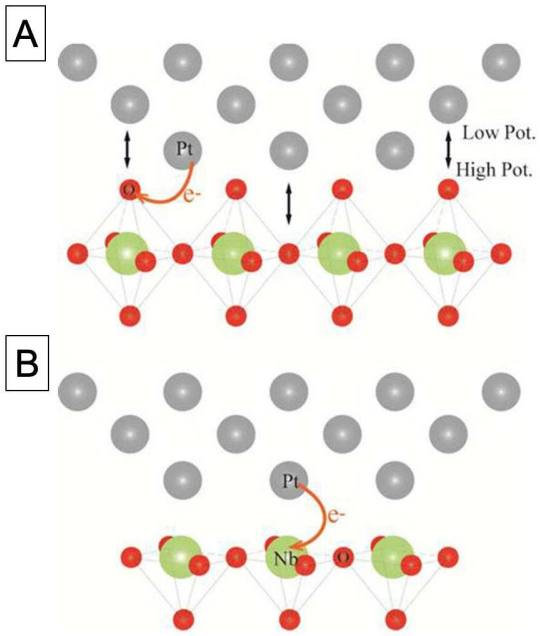

Figure 18. An example of an interaction between platinum and NbO_x oxide at saturated Nb bonds interface A) where an Pt donates electrons to O and unsaturated Nb and at saturated Nb bonds interface B) where an Pt donates electrons to Nb.

However, many metal oxides supports taken alone suffer from an insufficient electrical conductivity and possess a low surface area which make these supports unsuitable for catalytic purposes. One way to tackle this problem is the aliovalent doping of the oxide support so as to enhance the electrical

conductivity. It is well-established that doping with an aliovalent atom alters the electronic structure of oxides by introducing additional electronic states, which can favor the electronic conductivity and change the electronic transfer between the oxide and Pt. It was found that doping TiO_2 with V, Cr and Nb can improve the electrical conductivity of TiO_2 which becomes comparable to the Pt/C used in this study and generates a strong compressive strain of the Pt lattice than TiO_2 by affecting the activity. Moreover the TiO_2 doped catalysts show a durability higher than that of carbon due to their strong metal interaction between the metal and the oxide support [48]. Atanassov et al. synthetized an antimony-doped tin oxide (ATO) aerogel support for anchoring Pt. DFT model demonstrated that the doping with antimony alters the electronic structure of SnO_2 from that of a direct band gap semiconductor to that of a material with a n-type metallic character thus enhancing the electronic conduction. Moreover, the doping of SnO_2 increase the metal support interaction facilitating the charge electron transfer from ATO to Pt. The SMSI affects the durability of Pt/ATO catalyst, as well, making it a more convenient (even from the economic point of view) catalyst for PEMFC fuel cell compared to Pt/C [49].

Fabricating a carbon/metal oxide support is another way to enhance the conductivity compared to Pt/metal oxide composites. This way permits to combine the two main feature of the two materials, i.e. the electrical conductivity of carbon and the chemical and electrochemical corrosion resistance of the oxide. These composite supports have been produced with different architecture in literature. For instance, Tong et al. deposited a thin SiO_2 layer on carbon nanoparticles by using a polysiloxane precursor and subsequently Pt nanoparticles of 2 nm. The hydrophobic oxide thin layer not only provides a higher durability compared to Pt/C but also a better ORR activity which was due to the reducing free energy barrier of the rate determining step of ORR as confirmed by DFT calculations [50]. Nanozirconia-shell were deposited on carbon Vulcan XC72 by isothermal hydrolysis of Pt/C-$ZrOCl_2 \cdot H_2O$ aqueous solution at low temperature, thus developing to a hybrid support with the excellent stability of ceramic support but also the electric conductivity of carbon supports. The deposition of ZrO_2 nanoshell occurred on the surface of carbon black uncoated with Pt nanoparticles. Even though Pt/ZrO_2-C resulted slightly less active than Pt/C, the presence of this shells on the surface enhance the electrochemical corrosion resistance as assessed by an 8 hours chronoamperometric test (see Figure 19A) of the support and prevented the aggregation of Pt nanoparticles, thus leading to a better durable catalyst compared to Pt/C, as displayed in the TEM images in Figure 19C, D, E, F [51].

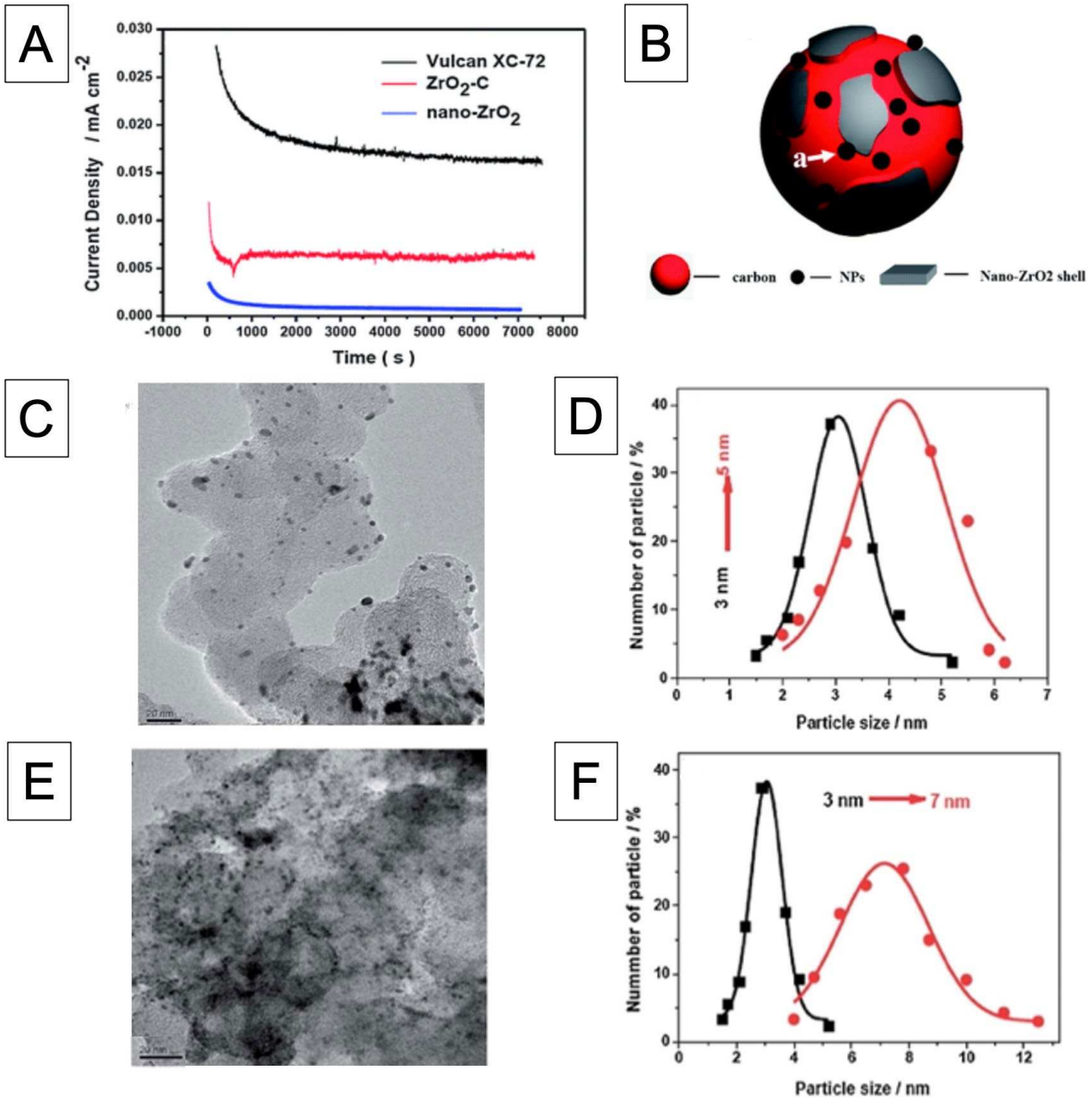

Figure 19. A) chronoamperometric curves after 8 h electrochemical oxidation for Vulcan XC72, nano-zirconia, ZrO_2-C hybrid catalyst demonstrating the high corrosion resistance of ZrO_2 ; (B) hypothetical architecture of Pt/C-ZrO_2 composite synthesized by Shichun Mu et al.; (C) TEM image recorded after accelerated stress test of Pt/C-ZrO_2 with the particle size distribution reported before and after the accelerated stress test (D) and (E) TEM image recorded after accelerated stress test of Pt/C-ZrO_2 with the particle size distribution reported before and after the accelerated stress test (F) .

1.6 CERIUM OXIDE

Among all the commercial-available oxides, cerium oxide (or ceria), CeO_2, is one of the most used compounds in industrial processes ranging from the mechanical processing to catalysis. Fine ceria powders are used as polishing agent in glass and scree manufacturing [52], whereas CeO_2 materials are used as ultraviolet absorbents. It is a promising electrolyte for solid oxide fuel cells since it permits the conduction of O^{2-} ions form the cathode to the anode at temperatures between 800-1000 K [53]. Among the different uses, the most successful application of ceria is its utilization in the wash coat of three-way catalyst for the elimination of the exhausted gases of vehicles. Here, it plays the role of oxygen storage material promoting the catalytic performance [54]. The wide-spread utilization in catalysis is related to the reversible Ce^{3+}/Ce^{4+} redox couple which originates because of its intrinsic defectivity structure [55]. Pure stoichiometric ceria shows a fluoritic structure where atoms are arranged in a face-centered cubic cell, which is depicted in Figure 20A.

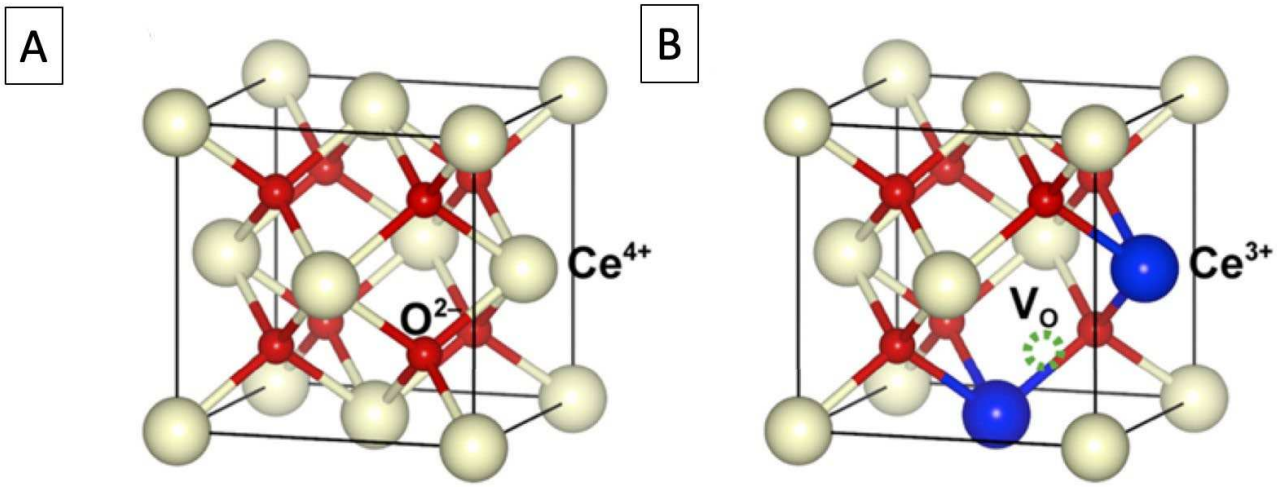

Figure 20. A) Fluoritic structure of the FCC cell of pure CeO_2 and B) after the introduction an oxygen vacancy. Red, pale yellow and blue spheres refer to Ce^{4+}, O^{2-} and Ce^{3+} ions, respectively belonging the crystal lattice of ceria.

The non-stoichiometric ceria is generated by the release of oxygen and consequently the formation of oxygen vacancy inside the crystal structure according to the following mechanism:

$$2Ce_{Ce}^{x} + O_{o}^{x} \rightarrow V_{O}^{\cdot\cdot} + 2Ce_{Ce}^{\prime} + \frac{1}{2}O_2(g) \qquad (1.31)$$

The vacancy formation $V_O^{\cdot\cdot}$ leaves two electrons localized into two cerium cations $Ce_{Ce}^{\prime}$, thus altering the oxidation state from Ce^{4+} to Ce^{3+}. As the size of Ce^{3+} is larger a lattice strain will be introduced in its neighborhood, thereby affecting the local charge distribution. DFT calculations have proven that the formation of vacancies is energetically more favored at the nanoscale rather than in bulk ceria

[56]. For this reason, ceria nanosizing has triggered innumerable applications in catalysis. Actually, controlling the Ce^{3+}/ Ce^{4+} ratio, which is of high importance in catalysis, still remains a challenge.

The presence of the redox couple Ce^{4+}/ Ce^{3+} is a clear indication that ceria can easily switch between releasing and storing oxygen. This is a surface property denominated as oxygen storage capability, OSC, used as quantitative parameter to determine the capability of ceria to release or incorporate oxygen. This is a crucial parameter for TWCs in catalytic converters since a large OSC value promote the oxidation of CO and hydrocarbon and the reduction of NO_x oxides [54].

Recently, ceria has been incorporated in PEM fuel cell of Toyota 2017 Mirai since it can be acts as a radical scavenger during the operating conditions of the device [57]. As briefly mentioned in regarding of the ORR mechanism, in addition to the predominant production of water via the four-electron pathway, small amounts of undesirable products, such as H_2O_2, hydroxyl radical ($HO^{\cdot}$), hydroperoxyl radical ($OOH^{\cdot}$) and hydrogen radical (H) may form. It is well-documented that the degradation of Nafion® is primarily caused by $HO^{\cdot}$. This remarkable issue hinders the widespread of fuel cell and must be resolved as soon as possible. It has been declared that sub-stoichiometric CeO_x, owing to its capability of switching to Ce^{3+} to Ce^{4+} oxidation states, quenches radicals by accepting or donating electrons under aqueous condition according to the following reactions [58]:

$$Ce^{4+} + H_2O_2 \leftrightharpoons Ce^{3+} + HOO^{\cdot} + H^+ \qquad (1.32)$$

$$Ce^{4+} + HOO^{\cdot} \leftrightharpoons Ce^{3+} + O_2 + H^+ \qquad (1.33)$$

$$Ce^{3+} + H^+ + OH^{\cdot} \leftrightharpoons Ce^{4+} + H_2O \qquad (1.34)$$

$$Ce^{3+} + H^+ + HOO^{\cdot} \leftrightharpoons Ce^{4+} + H_2O_2 \qquad (1.35)$$

Ce^{4+} tend to induce the decomposition of hydrogen peroxide and peroxyl radicals whereas Ce^{3+} ease the scavenging of hydroxyl radicals as well as peroxyl radicals. The beneficial scavenging effect of CeO_2 in PEM fuel cell has been recently investigated by using in situ time-resolved nano-XAFS-SEM/EDS technique. The results demonstrated that Ce^{3+} species possess a high mobility inside the Nafion® membrane ranging between 0.38-3.8μm h^{-1} depending on the applied conditions such as the voltage operating conditions, spatial density of Ce, interactions of Ce with Nafion®, thickness and state of the MEA [57].

In addition to this effect ceria has been introduced in the as a co-catalyst together with Pt/C in the anodic and cathodic side of fuel cell working at low temperature. It has been reported that coexistence of ceria and Pt in $Pt/CeO_2/C$ catalyst improve the CO tolerance of platinum during the electrochemical

oxidation of methanol. Many articles have recently introduced ceria in Pt/C for the methanol oxidation reaction (MOR) and that the high CO tolerance of Pt-CeO_2/C is mainly due to the high storage capacity of ceria and thus to its capability of switching between the Ce^{3+} and Ce^{4+}. As a matter of fact, CeO_2 functions as a supplier of oxygen-containing functional groups which are of vital importance for the oxidation of methanol to CO_2 [59]. Li et al. studied the effect of calcined CeO_2 on the CO tolerance/poisoning for Pt-CeO_2/C catalysts employed for the MOR. They found that CeO_2 calcined at 400 °C gives a better dispersion of small Pt nanoparticles giving the best activity and CO tolerance compared the sample where ceria was calcined at higher temperatures. They also proposed a bi-functional mechanism for MOR based on the fact that CeO_2 provide the OH_{ads} species for the oxidation to interact with the carbonaceous intermediates adsorbed (CO_{ads}) by Pt giving rise to CO_2 as a product of MOR [60]:

$$CeO_2 + H_2O \rightarrow CeO_2 - OH_{ads} + H^+ + e^- \quad (1.36)$$

$$Pt - CO_{ads} + CeO_2 - OH_{ads} \rightarrow Pt + CeO_2 + CO_2 + H^+ + e^- \quad (1.37)$$

$$Pt - CeO_2 + xCO \rightarrow Pt - CeO_{2-x} + xCO \quad (1.38)$$

Recently, some works have been introduced CeO_2 in Pt/C catalysts for the ORR of PEM fuel cell. It has been demonstrated that CeO_2 not only has an impact on the stability of the catalyst as it avoids sintering of platinum nanoparticles but also affects the activity of the ORR. It has been reported that the interaction between Pt and CeO_2 can increase the activity compared to Pt/C and this is attributed to the high oxygen storage capacity of ceria and the oxygen spillover from CeO_2 to Pt [61–64]. Xu et al. synthesized Pt/CeO2/C with different content of CeO_2 (10, 20, 30, 40%) by a one-pot wet chemistry approach where Pt and CeO_2 simultaneously nucleate on carbon VulcanXC72. The vacancies of defective CeO_2 acted as site where nucleation of platinum preferentially occurs. XPS analysis revealed that a clear oxygen spillover from CeO_2 to Pt surface occurred for Pt/CeO_2/C catalysts, which is facilitated by the rich Pt-CeO_2 interface. This phenomenon has a strong impact on the ORR activity. As reported by the authors, a high oxygen coverage on Pt surface could decrease the energy barrier associated to formation and dissociation of OOH species in the ORR mechanism. Due to their higher coverage, Pt/10CeO_2/C and Pt/20CeO_2/C resulted more active as well as more stable than Pt/C which was not subject to the oxygen spillover caused by the presence of CeO_2. However, the activity declined in Pt/40CeO_2/C due to the too high oxygen coverage on platinum [65]. The oxygen spillover over from CeO_2 to Pt has been also recently discussed by K.R. Yoon et al. who synthesized nanocomposite catalyst composed of Pt nanoparticle, CeO_2 nanoparticle and CNT functionalized with carboxylic groups by a two-step synthesis approach [66]. In that study XPS highlighted the presence of oxygen spillover effect at the interface between CeO_2 to Pt NPs.

Moreover, EXAFS and DFT calculation reveals that the presence of CeO_2 changes the electronic structure of Pt by filling the d-band vacancies in the Pt nanoparticles and lowering the d-band center of Pt by 0.03 eV compared to the sample without CeO_2. The downshifting of the d-band center may lead to the weakening of the bond between the metal catalysts and the adsorbate, according to the authors. The last observation along with the oxygen spillover should be enough to justify the enhanced activity of Pt@CeO_2@CNT compared to that of Pt@CNT, as declared by the writers. In addition to that, the same authors observed a dissolution of ceria after 2000 cycles of the accelerated stress test in 0.1 M of $HClO_4$. This phenomenon had been already detected in previous studies where in Pt-CeO_2/C catalysts CeO_2 partially dissolve in the acid environment during conditioning treatment, especially in H_2SO_4 solutions, leaving some CeO_x layer attached to Pt nanoparticles [67,68]. At the interface between the remaining CeO_x and Pt the charge transfer keeps occurring and the benefits on the ORR activity are not lost [68]. In the Yoon et al. study the remaining CeO_2 at Pt-CeO_2 interface maintain the aforementioned benefits on the activity and on the stability of Pt NPs avoiding their sintering and detaching. Additionally, the dissolved Ce ions exhibited their scavenging action against the aggressive free radicals generated by an insufficient ORR electrocatalysis during the PEM fuel cell testing and fuel cell lifetime resulted to be prolonged [66]. The Figure 21 displays a hypothetical architecture of Pt@CeO_2@CNT catalysts synthesized by K.R. Yoon showing the path of protons coming from the electrolyte and of electrons through the CNT support. A zoomed insert summarizes the main effects of ceria, which permits the nucleation of small platinum nanoparticles, the oxygen spillover from ceria to platinum, the SMSI, and finally the scavenging of the aggressive $OH^{\cdot}$ radicals.

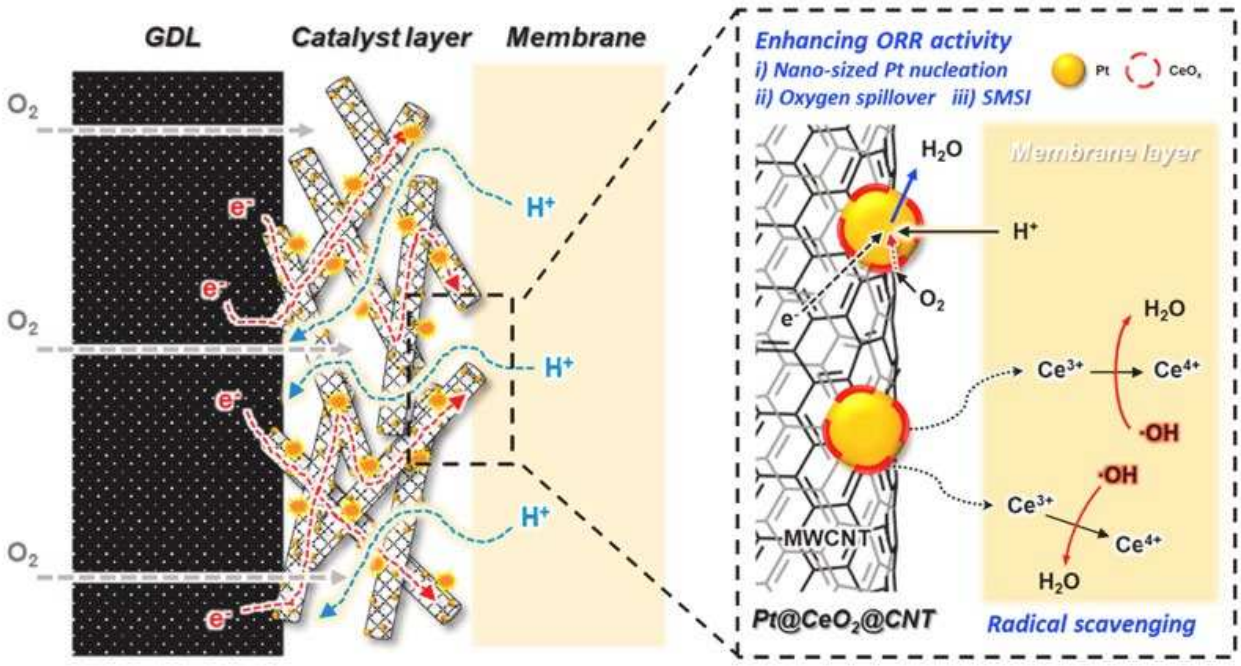

Figure 21. A) Structure of the Pt@CeO_2@CNT composite catalysts in the gas diffusion layer developed by K.R. Yoon et al with the proton and electron path and the benefits of ceria on the catalytic activity, durability and lifetime Nafion membrane.

Taking into account all of the aforementioned extraordinary features of CeO_2, this thesis will investigate on the effect of this oxide on $Pt/CeO_2/C$ electrocatalyst for the ORR. Different synthetic routes were adopted for the deposition of CeO_2 and platinum on commercial-available carbon, Vulcan XC72 and on biomass-derived carbons showing improved morphological properties with respect those of commercial such as the graphitization degree. The activity and above all the stability of $Pt/CeO_2/C$ tested by electrochemical techniques such linear sweep voltammetry on rotating ring disk electrode and gas diffusion electrode will be widely discussed.

2 THEORY EXPLANATION

2.1 THREE-ELECTRODE SYSTEM

All the electrochemical measurements are carried out with a three electrodes system where a working electrode (WE), a counter electrode (CE) and a reference electrode (RE) are connected by a potentiostat and put inside a pirex cell containing the electrolyte and the analyte. The electrolyte is a chemical species that must fit the following requirements:

- inertness
- not hindering the diffusion and the charge transfer on the electrode surface
- having a discharge potential different from that of the analyte (100-200 mA at least)
- possessing an appreciable ionic conductivity to lower the solution resistance

In this work a 0.1 M of $HClO_4$ was used as electrolyte (see section 3.1). An example of a potentiostat is depicted in Figure 22. The WE is the electrode where the potential is varied upon measurements and the semireaction taken in consideration occurs. It is commonly composed of a disk of a conductive material (e.g. glassy carbon) enveloped in a insulant support (e.g. Teflon) traversed by a conductive material which is in contact with the disk. Conversely, the CE, which is made of graphite in this thesis, is the electrode where the opposite semireaction takes place. These two electrodes, i.e. WE and CE, are joined by an amperometric circuit. The RE is the electrode respect to which the potential is measured. In this thesis, a reverse hydrogen electrode (RHE) was used as RE. It consists in a Pt loop wire directly immersed in the electrolyte ($HClO_4$) and it is polarized as a cathode to generate a hydrogen bubble (see section 3.2.3) which is in contact with Pt and the electrolyte. The connection with the WE can be ensured by a potentiometric circuit, i.e. a circuit where the current does not flow or it can be negligible.

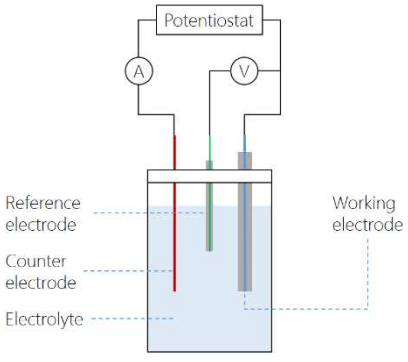

Figure 22. A sketch of a three-electrode system showing the reference, the working electrode, and the counter electrode with the amperometric circuit connecting the counter and the working electrode and the potentiometric circuit connecting the working and the reference electrode.

2.2 CYCLIC VOLTAMMETRY

Cyclic voltammetry is an electrochemical technique which is widely used to characterize electrochemical reactions by recording a current signal under a cyclic voltage variation. It is technique providing notable information on the thermodynamics of redox processes, on the kinetics of heterogeneous electron-transfer reactions and on coupled chemical reactions or adsorption processes. The name *cyclic* is due to the fact that the potential of the working electrode WE, which is measured against the constant potential of the reference electrode RE, is swept from an initial value E_i to a desired one E_λ by setting a scan rate and then reversed back to the beginning, E_i as depicted in Figure 23.

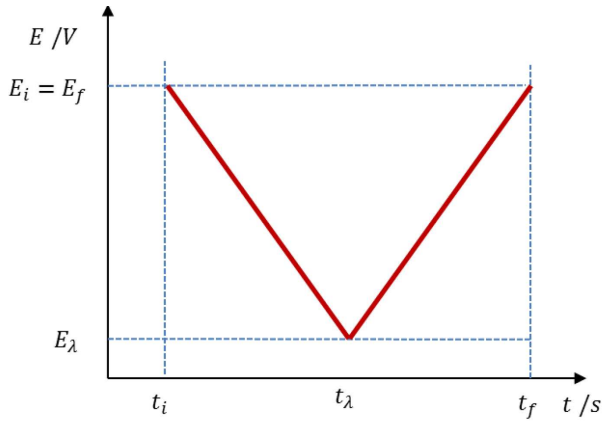

Figure 23. Trend of the potential (E) vs. time (t) during the acquisition of a cyclic voltammetry. E_i is the intial potential corresponding to the final one E_f and E_λ is the potential at the instant t_λ.

A cyclic voltammogram is acquired by measuring a current signal at the WE during the potential scan. In a cyclic voltammetry, an electrochemical process involving an oxidized species O and reduced species R is considered.

Reduction process: $O + e^- \rightarrow R$ (2.1)

Oxidation process: $R + e^- \rightarrow O$ (2.2)

Figure 24 shows a voltammogram of a reversible process (explanation of a *reversible process* will be provided further ahead in the text) with the changes of the concentration profiles of O and R species within the solution upon the potential scan. The numbers indicated in the voltammogram refer to the respective concentration profile.

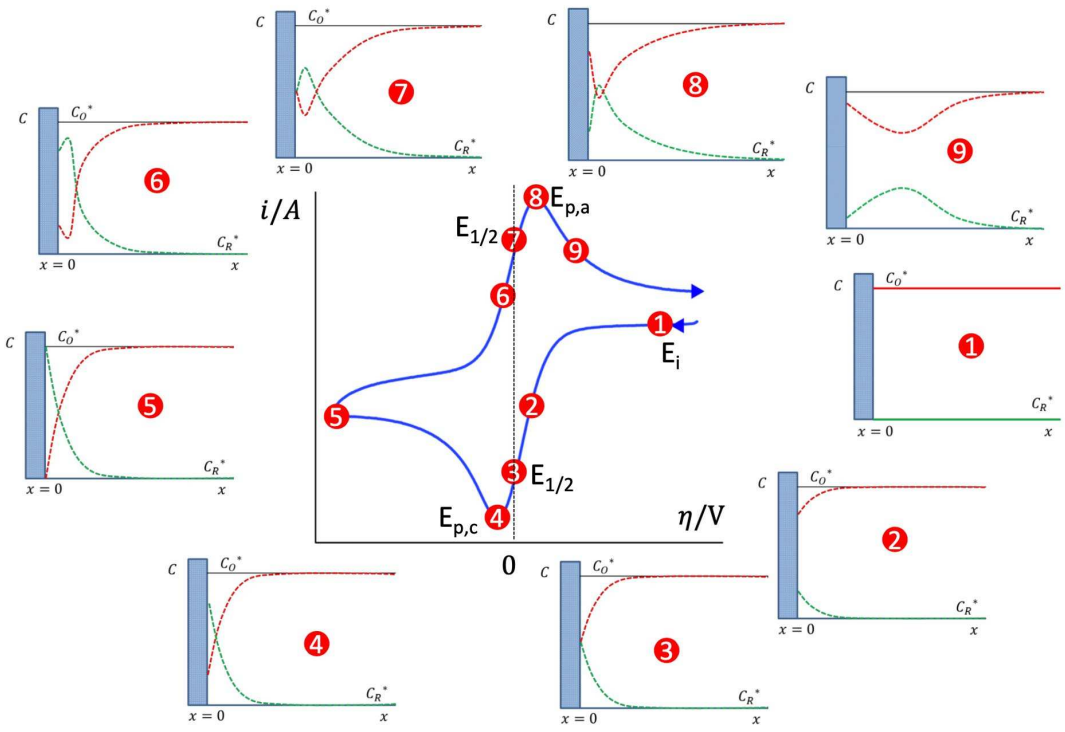

Figure 24. A voltammogram related to a reversible process with the variation of the concentration profile of the oxidized and reduced species in different points of the voltammogram.

The experiment begins at a potential where no electrochemical reactions occurs (E_i) (1). At this point the concentration of the oxidized and of the reduced species at the electrode surface, C_O (x=0) and C_R(x=0) respectively, are equal to those of the bulk, C_O^* and C_R^* respectively. At the beginning it can be assumed, for simiplicity, that the concentration of the oxidized species in the bulk C_O^* is different from 0 whereas C_R^* is equal to 0. By scanning the potential in the cathodic direction, the current remains constant until it begins to grow (in absolute value) at an onset potential, which means that the O starts to be reduced into R (eq. (2.1)). As long as the potential is swept in the cathodic direction, the concentration profile of both species varies in such a way that the O species concentration decreases near the electrode (in the diffusion layer, i.e. the layer where the concentration changes) with respect to the bulk whereas the opposite happens for the R species (2). When the half wave potential $E_{1/2}$ is reached C_O (x=0) and C_R(x=0) are equal (3). The half wave potential is defined as:

$$E_{1/2} = E^\circ - \frac{RT}{nF}\ln\left(\frac{D_O}{D_R}\right)^{2/3} \qquad (2.3)$$

where E° is formal potential, D_o and D_R are the diffusion coefficient of the oxidized and reduced species respectively, n is the number of transferred electrons, F is the faraday constant (i.e. 96485 C/mol), R is the gas constant (i.e. 8,31 J/(mol·K)) and T is the temperature of the system. At the peak potential $E_{p,c}$ the concentration gradient reaches the highest value (4). After overcoming the peak, the current starts to decrease because the concentration gradient decreases (i.e. the diffusion layer widens) due to depletion of the reactants at the interface. In this part, the diffusion control prevails and the

current does not depend on the potential but it decreases exponentially upon time according to the Cottrell equation as depicted in Figure 25.

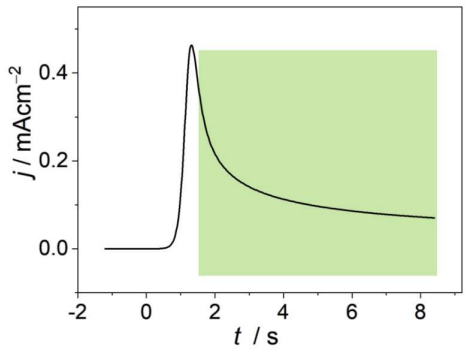

Figure 25. Trend of the current as a function of time provided by the Cottrell equation, which foresees an exponential decay of the current upon time highlighted by the evidenced green square.

At the reverse potential the concentration of the O species on the electrode surface C_O (x=0) approaches to 0 whereas that of the reduced species C_R(x=0) reaches the highest value (5). By inverting the potential and therefore going to more positive potential an oxidation process where R is oxidized to O takes place and therefore the concentration of the oxidized species on the electrode surface C_O (x=0) increased when the reaction starts to occur whereas that of reduced species C_R(x=0) diminishes (6). Once again, at the half wave potential $E_{1/2}$ the concentrations of O and R species become equal (7). At the cathodic potential peak $E_{p,c}$ a $I_{p,c}$ is recorded and the concentration gradient reaches the highest value (8). Beyond the peak the cathodic peak $I_{p,c}$ the concentration profiles decrease exponentially as explained above until the starting point (1) is reached.

The important parameters of a cyclic voltammetry are the anodic and cathodic peak current $I_{p,a}$ and $I_{p,c}$ together with the respective potentials $E_{p,a}$ and $E_{p,c}$, the half peak potential $E_{p/2}$ and the half wave potential $E_{1/2}$. The process represented in the Figure 24 is reversible, which means that the electron transfer ET between the electrochemical species and O and R is fast and the redox system remains in equilibrium throughout the whole scan. This implies that the concentration of O and R species are those obtained by the Nernst equation:

$$E = E^o + \frac{RT}{nF}\ln\frac{C_O^*}{C_R^*} \qquad (2.4)$$

where E° is the standard potential, C_O^* and C_R^* are the concentration of the oxidized and reduced species in the bulk respectively, R is the gas constant (i.e. 8,31 J/(mol·K)), n is the number of the transferred electrons, F is the Faraday constant (i.e. 96485 C/mol) and T is the temperature of the system. There are different diagnostic criteria to individuate a reversible process: the anodic and cathodic current peaks, $I_{p,c}$ and $I_{p,a}$, show a similar intensity and their potential value, $E_{p,c}$ and $E_{p,a}$ respectively, is independent on the scan rate, the couple of peaks is centered at $(E_{p,c} - E_{p,a})/2$, the

difference $E_p - E_{p/2} = 56.5$ mV whereas the difference $E_{p,c} - E_{p,a} = 59$ mV and the peak current follows the Randles-Sevich equation:

$$i_p = 0.4463nFAC_i^* D_i^{\frac{1}{2}} \frac{nF}{RT}^{1/2} v^{1/2} \qquad (2.5)$$

where n is the transferred electrons, F is the Faraday's constant, C_i^* and D_i are respectively the bulk concentration and the diffusion coefficient of the oxidized species or reduced species depending on the considered current peak (anodic or cathodic), A is the geometric area of the electrode (anode or cathode according to the considered peak), R is the constant gas, T is the temperature, ν is the scan rate.

If the electron transfer is slow an irreversible process takes place. In this case the voltammogram changes since the two peaks, i.e. $E_{p,c}$ and $E_{p,a}$, are separated by a high overpotential value. This is clearly visible in Figure 26 where η_c and η_a are the overpotential of the cathodic and the anodic process defined with respect to the standard potential E°. This means that the reverse peak (the cathodic or the anodic depending on the scan direction) could not appear if the potential window of the voltammogram is not large enough. Apart from these important features others diagnostic criteria must be considered for an irreversible process: the two peaks exhibit a different intensity, the peak potential depends on the scan rate, $E_p - E_{p/2}$ is a function of α, which is a kinetic parameter defined as an electron transfer coefficient. In an irreversible process the current peak follows the Randles-Sevich trend with respect to the scan rate, but further parameters must be included:

$$i_p = 0.4958nFAC_i^* D_i^{\frac{1}{2}} \frac{\alpha F}{RT}^{1/2} v^{1/2} \qquad (2.6)$$

where n is the transferred electrons, F is the Faraday's constant, A is the geometric area of the electrode, C_i^* and D_i are respectively the bulk concentration and the diffusion coefficient of the oxidized species or reduced species depending on the considered current peak (anodic or cathodic), R is the constant gas, T is the temperature, ν is the scan rate and α is the electron transfer coefficient.

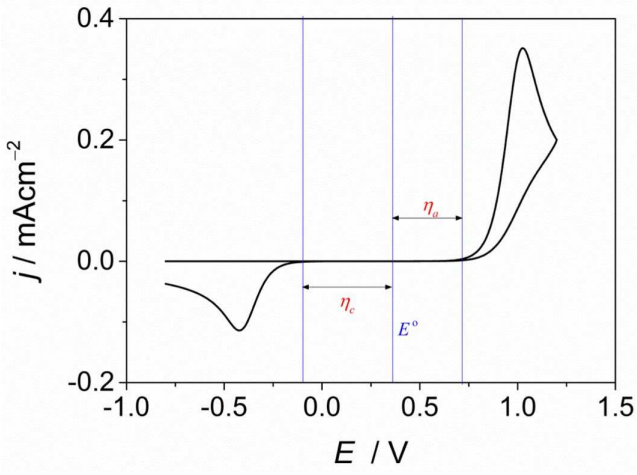

Figure 26. Voltammogram of an irreversible process.

2.3 LINEAR SWEEP VOLTAMMETRY ON A ROTATING DISK ELECTRODE

In linear sweep voltammetry LSV a current signal is recorded under a potential which changes linearly with time by setting a scan rate ν according to the equation:

$$E(t) = E_i + \nu t \qquad (2.7)$$

where E_i is the initial potential (in volts, V), $\nu = \frac{dE}{dt}$ is the scan rate (in V s^{-1}) and t is time (in seconds, s). Unlike cyclic voltammetry, in LSV the potential is swept between an upper and lower limit with only a forward scan, therefore it corresponds with the first half part of a cyclic voltammogram: a no-negligible current is observed when the reaction starts to occur, keeps rising until the peak is reached and beyond the maximum diminishes due to a decrease of the supply of reagent species to the surface of the electrode.

An LSV can be recorded by exploiting a rotating disk electrode (RDE) as working electrode in a three-electrodes set up. In this technique an engine actions the rotation of a shaft the WE is hooked to. This rotation induces a stationary flow of the species in the electrolytic solution so that they can react on the electrode surface giving products which can be subsequently expelled from it by the centrifugal force of the rotating motion. As a consequence, RDE can be considered as an irreversible mass transfer technique. Regarding the concentration of the species, this motion generates the so-called Nernst diffusion layer (δ) (or stagnant layer), a zone near the electrode surface inside where the concentration of the species is controlled only by diffusion and its thickness is controlled by rotation rate (see equation) but it does not overtakes values of 10 μm. Outside the Nernst diffusion layer the concentration does not change with the position (x) since it is not controlled by diffusion and it remains constant upon time (t) due to the effect of the consistent convective motions. As regards the trend of the concentration inside the diffusive layer, the concentration is constant over time and it can be assumed that:

$$\frac{\partial C}{\partial t} = 0 \qquad (2.8)$$

And thus for the second Fick's law:

$$\frac{\partial C}{\partial t} = cost \qquad (2.9)$$

which means that there is a linear variation of the concentration with the distance from the electrode surface.

Thus, the concentration profile generated by the effect of RDE technique, represented in Figure 27, shows a linear trend of the concentration in the diffusive layer whereas the concentration remains constant at C^* outside (in the bulk).

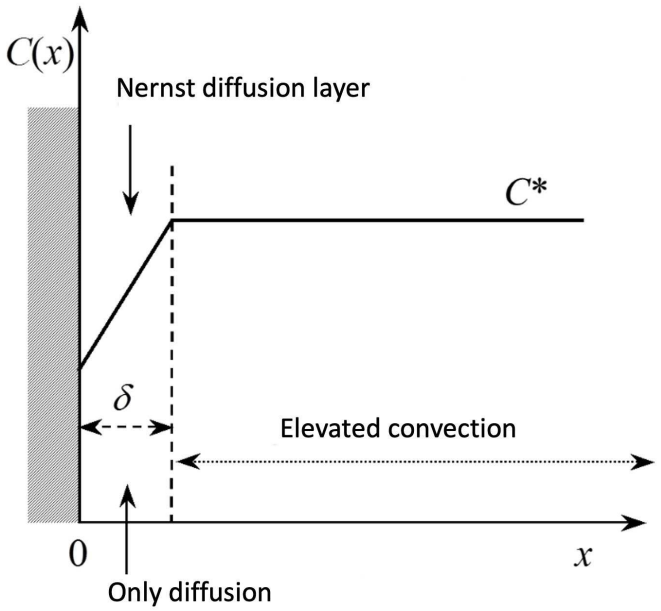

Figure 27. Nernst diffusion layer near the electrode surface and bulk zone where convection takes place.

The wideness of δ can be controlled by the rotation rate according to:

$$\delta = 1.61 D_O^{1/3} \nu^{-1/6} \omega^{-1/2} \qquad (2.10)$$

where D_O is the diffusion coefficient of the reactant O, ν is the kinematic viscosity and ω the rotation rate.

A typical LSV presents a sigmoidal shape where three different zone can be individuated, as depicted in Figure 28C:

- Kinetic zone, which starts from the onset potential (i.e. the potential at which the reaction starts to occur, see section 3.1.2.1) and refers to a process limited by the reaction rate, i.e. the electron transfer occurring between two species.
- Mass transferred controlled zone where the current reaches its highest value in module (the so-called *limiting current,* i_L) and the process is limited by the supply of the reagent on the electrode surface so that the current reaches a plateau (i.e. it remains constant upon varying potential). This is due to the forced convention generated by the motions of rotating disk, which maintains constant the bulk concentration C^* of the reactant at the edge of the stagnant layer (x=δ), thereby impeding an expansion of the diffusive layer during the experiment.
- Kinetic and MT limited zone in the middle of the other two.

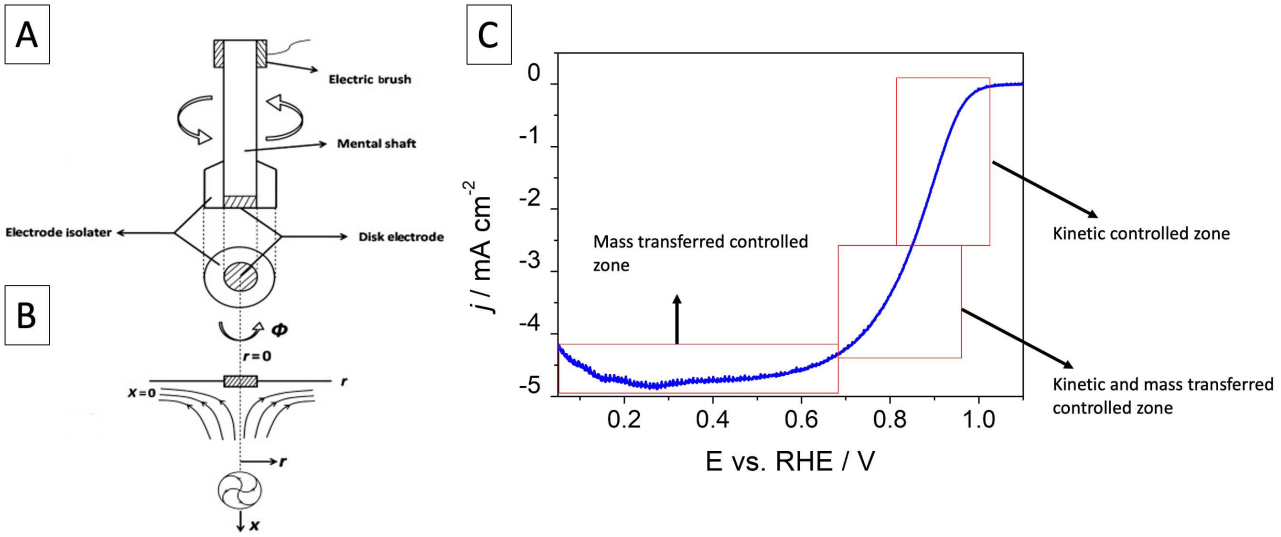

Figure 28. A) Sketch of a rotating disk electrode; B) Mass transport phenomena occurring at the disk surface during its rotation; C) Example of a linear sweep voltammetry showing the different zones (j is the current density, i.e. the current divided by the area of the electrode).

The relationship between the potential E and the current i in a LSV is described by:

$$E = E_{1/2} + \frac{RT}{nF}\ln\frac{i_L - i}{i} \qquad (2.11)$$

Where $E_{1/2}$ is the half wave potential, R is the gas constant, F is the Faraday's constant, n is the electrons transferred during the reaction, i_L is the limiting current. The current i is inversely proportional to the diffusive layer according to:

$$i = nFAD_O\frac{C_o^* - C(0,t)}{\delta} \qquad (2.12)$$

Where C_o^* is the concentration of the reactant O for example, F is the Faradic constant, n is the number of the electrons transferred, D_O is the diffusion coefficient of the reactant O and δ is the Nernst diffusion layer. Therefore, the narrower the stagnant layer the higher is the resultant current. The limiting current is defined by the Levich equation:

$$|i_L| = 0.620nFAD^{2/3}\nu^{-1/6}\omega^{1/2}C_o^* \qquad (2.13)$$

Where n is the transferred electrons, F is the Faraday's constant, D_O and C_o^* are respectively the diffusion coefficient and the bulk concentration of the reactant O species, ν is the kinematic viscosity and ω is rotation rate (rpm). Generally, if the kinetic transfer is so fast that the diffusion process is not able to compete with it and therefore the concentration of the reactant on the electrode surface quickly reaches a value of 0, the limiting currant is proportional to the $\omega^{1/2}$, as reported in Figure 29A. However, the kinetic transfer is very slow, for reaching a concentration equal to 0 on the electrode surface elevated overpotentials are required. In this case, the Levich equation is no longer valid since there is deviation from the linear relationship between i_L and $\omega^{1/2}$. Thus, a more general relationship considering also a kinetic current contribution j_k must be introduced:

$$\frac{1}{j} = \frac{1}{j_k} + \frac{1}{j_L} \qquad (2.14)$$

$$\frac{1}{j} = \frac{1}{j_k} + \frac{1}{0.62\, nFD_O^{\frac{2}{3}}\omega^{\frac{1}{2}}\nu^{-1/6}C_o^*} \qquad (2.15)$$

Where j is the current density, i.e. the current i divided by the area of the electrode A. By rearranging the equation as

$$j^{-1} = \frac{1}{0.62nFD_O^{\frac{2}{3}}\nu^{-1/6}C_o^*}\omega^{-\frac{1}{2}} + \frac{1}{j_k} \qquad (2.16)$$

and by plotting j^{-1} vs. $\omega^{-\frac{1}{2}}$ (as depicted in Figure 29B) it is possible to obtain j_k from the intercept and the number of transferred electrons n from the slope.

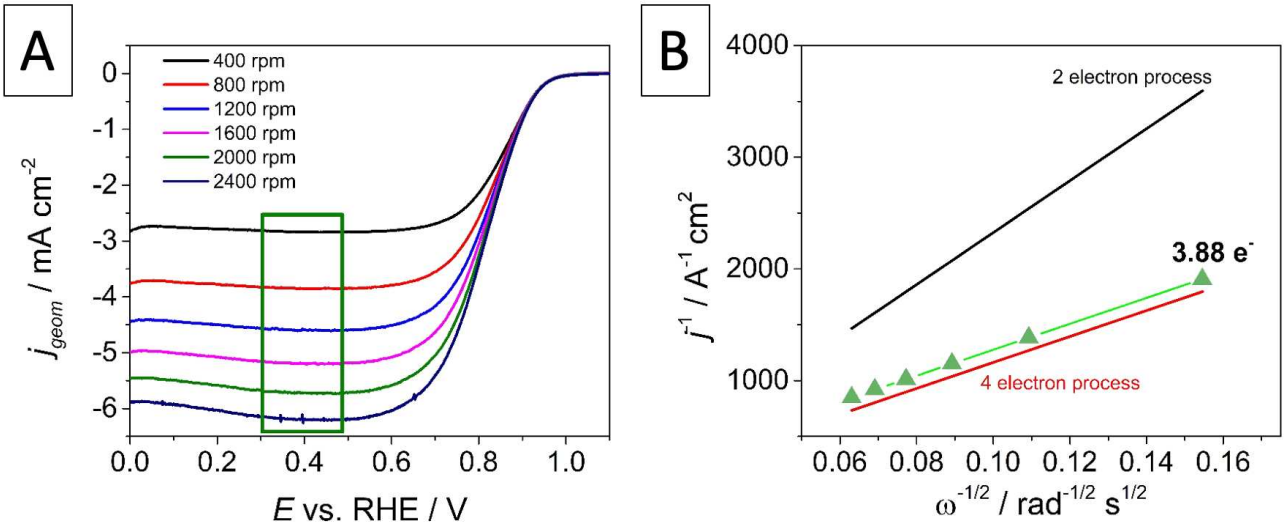

Figure 29. A) Effect of the rotation rate on the limiting current and B) An example of a plot of j^{-1} vs. $\omega^{-\frac{1}{2}}$ showing a process with 2, 3.88, 4 electrons transferred. The plot for the process with 3.88 electrons was obtained from the limiting current and ω reported on figure A).

2.4 GAS DIFFUSION ELECTRODE

RDE technique is one of the best techniques used to determine the catalytic activity of Pt/C catalysts by following well-defined protocols proposed in literature. Nevertheless, the activity of these materials obtained by means of an ideal RDE environment cannot be transferred to (reproduced in) more realistic membrane electrode assemblies (MEAs). The discrepancies between ORR activity performed by RDE or MEA systems are due to the different electrolytes (liquid vs solid) and a non-optimal catalyst layer composition.

RDE does not allow to assess the effects of catalyst layer parameters due to the low current densities developed during measurements associated with low mass transport and the idealized catalyst layers on a solid substrate. MEA experiments should be used for catalyst layer optimization. Notwithstanding, conversely to the cheap and quick analysis provided by RDE, investigations carried out in MEA are time-consuming and expensive (large amounts of catalyst required, complex and extended setup) and do not allow segregated investigation of either cathode or anode catalyst layer. Moreover, the comparison of different MEA experiments could be challenging owing to different processing and operating conditions.

Gas diffusion electrode is a half-cell technique combining the advantages of RDE, i.e. simplicity, rapidity, and comparability, with the more realistic operating conditions of MEA. In other words, GDE represent a tool to bridge the gap between fundamental and applied fuel cell catalyst research, as illustrated in Figure 30. GDE permits to evaluate the catalyst layer performance in terms of activity and durability upon current densities and potential ranges close to those employed in fuel cell (≅ 1 A cm^{-2} , 0.6-0.8 V vs. RHE) without systematic mass-transport limitations [69,70].

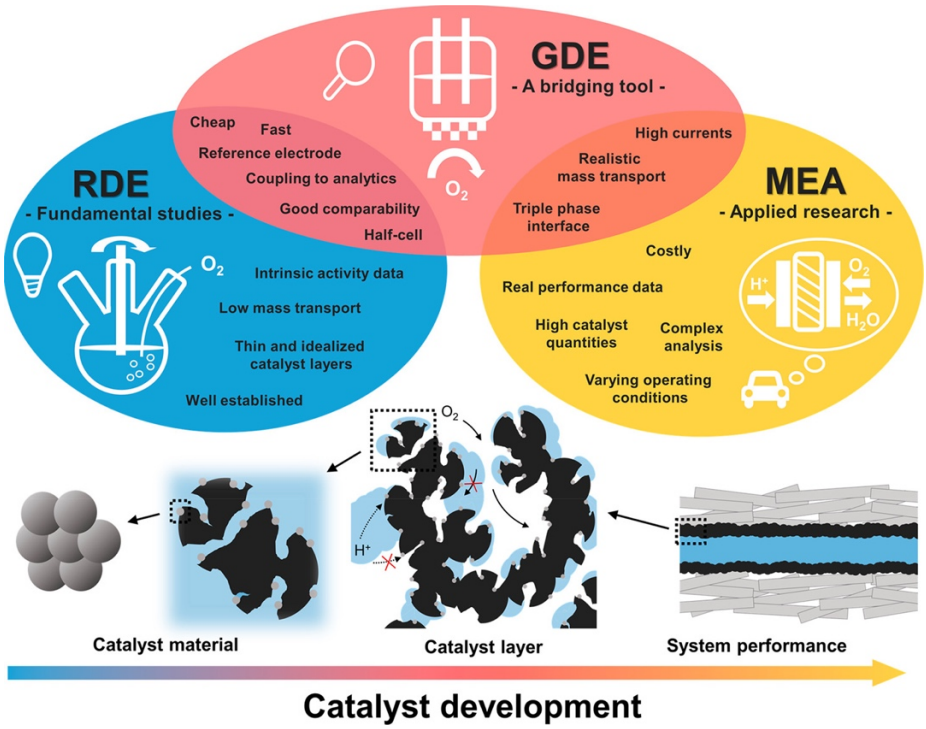

Figure 30. Comparison of different systems used for evaluating the electrocatalytic performance [69].

2.5 X-RAYS DIFFRACTION

X-rays diffraction (XRD) is a technique employed for analyzing the crystallographic properties of materials. The generation of X-rays is provided by a x-rays tube where the electrons emitted by the thermoionic effect of a hot filament (cathode) are accelerated towards a metallic anode target. When they hit the anode, three types of radiations are emitted: K_α, K_β and the Bremsstrahlung. Then a filter eliminates the K_β and the Bremsstralung in order to obtain a monochromatic radiation, which is send to the sample, where the diffraction phenomenon takes place, and finally to a detector collecting the diffracted beam. The diffraction phenomenon occurs whenever a light beam has a wavelength comparable to the dimension of the object hit by the radiation. In x-rays diffraction the wavelength of the incident beam is in the order of angstrom which corresponds with the interplanar distance of crystallographic planes. XRD can be used for both single crystal and powders. In a typical diffractogram the scattered (diffracted) intensity is plotted against the diffraction angle 2θ, which is twice the Bragg angle θ, i.e. the angle generated when the incident beam hits a crystal plane. Each reflection appearing in the spectrum arises from a constructive interference of the rays reflected by a specific family of hkl planes. The constructive interference can be obtained by the Bragg's law:

$$2d_{hkl}sin\theta = n\lambda \qquad (2.17)$$

where d_{hkl} is the interplanar distance of the hkl planes, θ is the Bragg angle, n is the diffraction order, λ is the wavelength of the incoming beam. Figure 31 displays a graphical illustration of the Bragg's law.

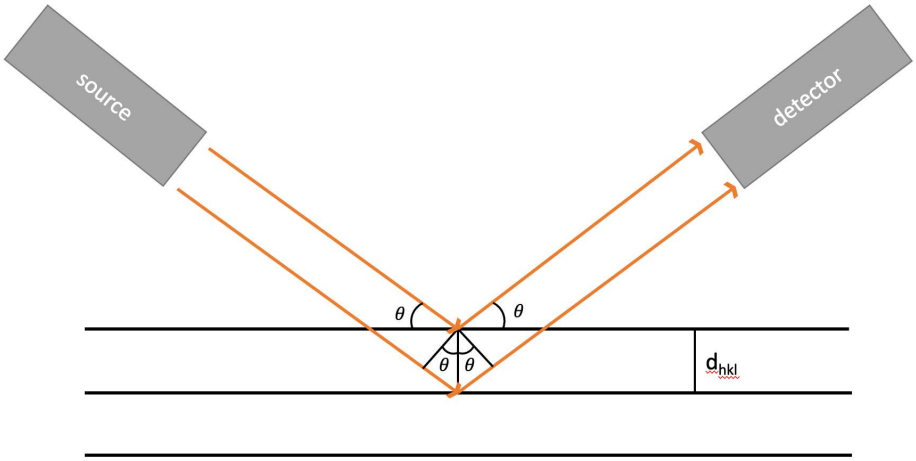

Figure 31: Illustration of the Bragg's law.

For a typical powder sample data are collected in the 2θ range of 5° - 90° and a reflection geometry, called Bragg-Brentano, is employed. The sample surface, the focus of the incident beam and the detector slit lay on the surface of the focusing sphere as shown in Figure 32.

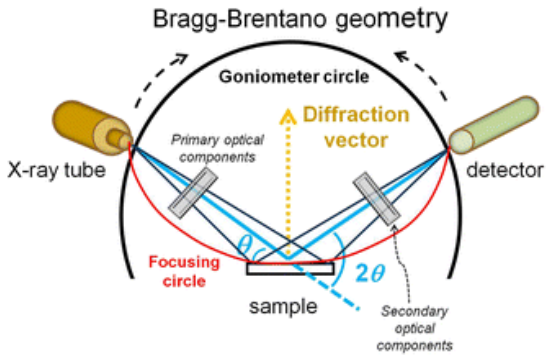

Figure 32. Bragg Brentano geometry applied in reflection x-rays measurements.

XRD technique provides information concerning:

- unit cell dimension
- sample purity
- crystal structure
- grains orientation in polycrystalline sample
- stress and strain effect
- thickness, roughness, and density of film

Thus, in this thesis XRD is used as a technique to detect the presence of ceria and platinum deposited on carbon dimension. Moreover, assuming that the dimension of crystallite coincides with the nanoparticle size, the Debye-Sherrer equation, which is valid only for a cubic system, allows to determine the mean nanoparticle dimension $< D_{hkl} >$ related to a specific reflection at θ:

$$< D_{hkl} >= K \frac{\lambda}{\beta_{hkl} \cos(\theta)} \qquad (2.18)$$

where:

- λ is the incident beam wavelength in angstrom;
- β_{hkl} is the line broadening at the full half width at maximum expressed in radiants (FHWM);
- θ is the Bragg angle;
- K is the dimensionless shape factor, with a value of 0.9 assuming a sphere shape of the crystallite.

The interplanar distance d_{hkl} of a family plane with h, k, l Miller indices is another width which can be easily determined by knowing the Miller indices. In the case of the cubic system, it is given by this simple equation:

$$d_{hkl} = \frac{a}{\sqrt{h^2 + k^2 + l^2}} \qquad (2.19)$$

Where:

- a is the cubic cell parameter;
- h, k, l are the Miller indices of a certain crystallographic plane.

2.6 N_2 ADSORPTION/DESORPTION ANALYSIS

Gas adsorption, more specifically physisorption, represents one of the most important tools for characterizing the textural properties of a porous catalyst. According to IUPAC, pores are classified based on their size into micropores (less than 2 nm), mesopores (2-50 nm) and macropores (more than 50 nm) [71]. Physisorption is a phenomenon involving a chemical species (the adsorptive) from a fluid phase which interacts with a solid surface (the adsorbents) by intermolecular forces. The choice of the adsorptive strictly depends on the pores dimension analyzed sample. For ultramicropores (i.e. pores < 0.7 nm) CO_2 must be used, whereas for micropores larger than 0.7 nm up to mesopores (i.e. pores whose diameter is between 2 and 50 nm) N_2 is employed [72]. Since this thesis deals with carbon supports exhibiting mainly micro and mesopores N_2 was used as adsorbitive gas. The opposite of adsorption is desorption, which leads to the complete detachment of the adsorptive from the surface, i.e. they no longer interact. Both the adsorption and desorption are useful to acquire a curve of the adsorptive called isotherm since it is acquired at a constant temperature. Figure 33 illustrates the seven types of isotherm classified by IUPAC [71].

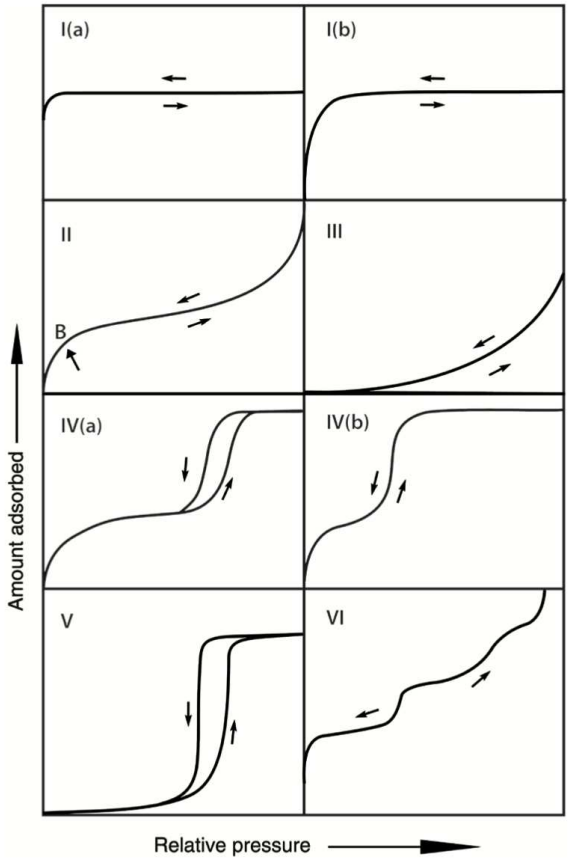

Figure 33. The six types of isotherms according to IUPAC classification [71].

Type I (a) and I(b) can be found for microporous materials and the former even indicates the presence of ultramicropores (i.e. < 0.7 nm, micropores of molecular dimension) which is attributed to the uptake at p/p^o smaller than 0.01. Type II is usually given by non-porous or macroporous samples and the point B (marked by an arrow in Figure 33) represents the complete coverage of the first

monolayer. At higher pressures many layers of the adsorptive deposits on the adsorbent until the maximum pressure where the gas condenses on the surface. This multilayer formation can be identified in type VI, where each step refers to the deposition of one layer of the adsorbate. Type III and V are recorded when the adsorptive-adsorbent interaction is weak, and no point B can be identified and thus no identifiable monolayer formation. Type IV is usually detected in mesoporous materials and the adsorption has the same path of the type II followed by the capillary condensation of the adsorptive inside mesopores. This is responsible for the hysteresis loop which means that the desorption does not follow the same path of the adsorption because the condensation is delayed by the confinement effect. This phenomenon occurs in Type V isotherm, as well. By the way, it is fundamental to consider the further IUPAC classification regarding the hysteresis loops (depicted in Figure 34), which is helpful to provide additional information on the pore sizes, shapes and connectivity. Type H1 hysteresis is dominant in material possessing uniform cylindrical open-ended pores, which can also be interconnected. Type II hysteresis is given by materials exhibiting pore networks with ink-bottle shape pores where the wide body remains filled until the neck evaporates at lower vapor pressure. The main difference between H2(a) and H2(b) is represented by the desorption branch which immediately plummets in (a) whereas gradually declines in (b). This is caused by pore cavitation in (a) and pore blocking in (b), which are illustrated in Figure 35. The latter takes place when pores remained filled, i.e. blocked, until the vapor pressure for the neck is reached (the evaporation is a percolation process) whereas the former is observed if the pore neck is smaller than a certain critical size at a given temperature and adsorptive, e.g. 5 nm for N_2 at 77 K, and the evaporation process occurs via spontaneous nucleation of bubbles inside the pores at $p/p_0 \cong 0.45$ [73]. Cavitation is even present in the desorption branch of type H3 hysteresis, which is observed for aggregates of plate-like particles, but also in systems containing macropores which are not completely filled with adsorbate at atmospheric pressure. Type H4 is quite similar but the part at high pressure increases more gently and it can be found in samples containing micro- and meso- or macroporosity such as hierarchical carbons [71,74]. The last hysteresis loop, i.e. type H5, contains the steep step down due to cavitation, as well. However, this hysteresis can be obtained for materials including both open and partially blocked mesoporosity [71].

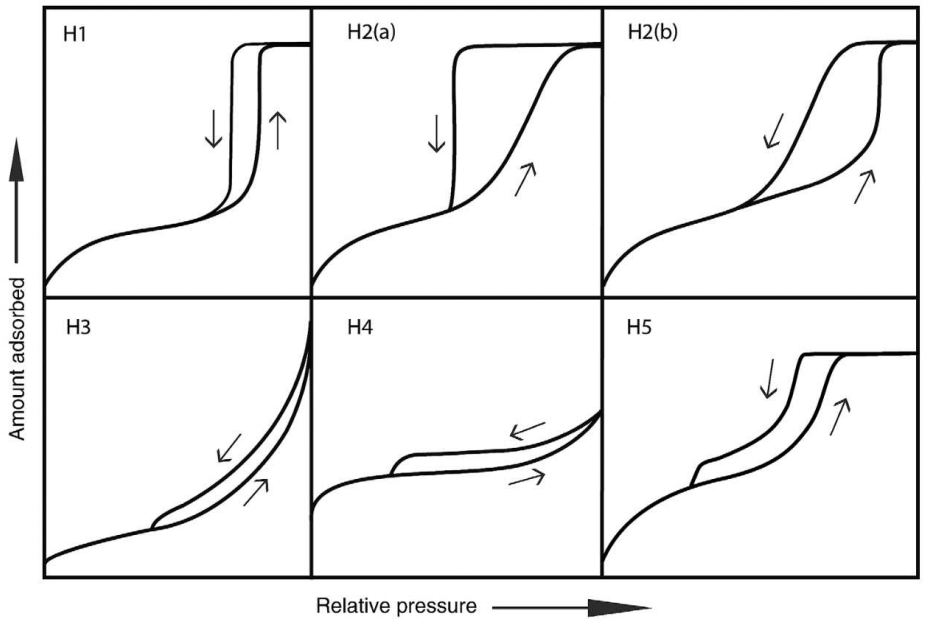

Figure 34. Hysteresis loops classified by IUPAC in 2015.

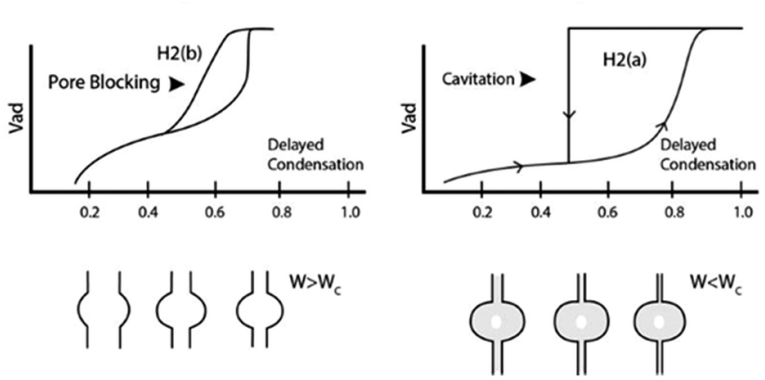

Figure 35. Pore blocking and cavitation effects distinguished by the neck width W with respect to the critial value W_c.

The analysis of the isotherm can be conducted by using different mathematical models with the aim of evaluating the surface area and pore volume. The most rudimental method commonly applied is the BET (Brauner-Emmett-Teller) described by the following equation:

$$\frac{\frac{p}{p_0}}{V\left(1-\frac{p}{p_0}\right)} = \frac{1}{V_m C} + \frac{C-1}{V_m C}\left(\frac{p}{p_0}\right) \qquad (2.20)$$

Where V_m is the specific volume for a monolayer, V is the adsorbed gas volume and C is a quantity proportional to the adsorption energy of a monolayer. If BET method is applied for micropore characterization, an apparent surface area is given since this method does not distinguish between mono-multilayer adsorption and the filling of micropores. Other better methods, including density functional theory (DFT) should be used. Two types of DFT method can be accounted: non-linear DFT (NLDFT) and quenched-solid DFT (QSDFT). This two method have been recently applied to characterize micro- mesoporous carbons [73,75]. Both QSDFT and NLDFT consider that that the distribution of the adsorbate in the pore corresponds to a minimum of the gran potential of the fluid,

$\Omega_f[\rho_f(r)]$ (see equation 2.21). NLDFT does not take into account the roughness of the sample and considers the solid adsorbent as inert and non-deformable. In this case, only the adsorptive can interact with the surface of the sample and not the other way around. The interactions are due to a solid-fluid distributed potential U_{ext} (r), by which the gran potential of the fluid depends (as shown in equation). Unlikely, this method, does not consider the nucleation of bubbles occurring during the cavitation phenomenon [76]. Thus, NLDFT cannot be used when cavitation is observed in the hysteresis loop. The proper alternative is represented by QSDFT, which the adsorbent as a rough solid composed of hardcore spheres interacting with fluid molecules and the latter in turn interact with the surface of the adsorbent. Hence, this result in a biunivocal interaction and the adsorption interaction is expressed as a pairwise attractive potential between the solid adsorbent and the fluid molecules. Additionally, the density of the solid depends in the geometrical hetereogeneity of the pore wall, namely the surface roughness, and that is why the model is called quenched state theory [76]. In the equation (2.22) the final density profile conditions is depicted, $\Omega_f[\rho_s(r), \rho_f(r)]$, where $\rho_s(r)$ is the density of the solid, $F_{ex}[\rho_s(r), \rho_f(r)]$ is the excess repulsion term for both the solid and fluid component, u_{ss}, u_{ff}, u_{sf} are the attractive term of the solid-solid, fluid-fluid and solid-fluid potential respectively whereas μ_s and μ_f refer to the chemical potential of the solid and the fluid.

$$\Omega_f[\rho_f(r)] = F_f[\rho_f(r)] - \int dr\rho_f(r)[\mu_f - U_{ext}(r)] \qquad (2.21)$$

$$\begin{aligned}\Omega_f[\rho_s(r), \rho_f(r)] &= F_{id}[\rho_f(r)] + F_{id}[\rho_s(r)] + F_{ex}[\rho_s(r), \rho_f(r)] \\ &+ \frac{1}{2}\iint dr dr'\, \rho_f(r), \rho_f(r') u_{ff}(|r - r'|) \\ &+ \frac{1}{2}\iint dr dr'\, \rho_s(r), \rho_s(r') u_{ss}(|r - r'|) \\ &+ \iint dr dr'\, \rho_f(r), \rho_s(r') u_{sf}(|r - r'|) \\ &- \mu_f \int dr\rho_f(r) - \mu_s \int dr\rho_s(r)\end{aligned} \qquad (2.22)$$

The application of DFT method was accomplished by using QuadraWin software. Some problems can come out for the interconnected systems of micro- and mesopores throughout the interpretation of the hysteresis loop. When the hysteresis is characterized by pore-blocking effect the pre size distribution can be obtained by both the adsorption and desorption branch. Specifically to desorption branch, when the fluid evaporates at the same time from the body and the neck of pores, the achieved pore size distribution refers to the neck size whereas from the adsorption branch the distribution of body size is obtained. As regards the cavitation, the pore size distribution obtained from the desorption branch does not give information concerning the size of the neck since the neck hinders

the gas to come out. Therefore, when cavitation is observed the adsorption branch is enough for predicting the pore size distribution [77]. The typical porous structure of a catalyst is displayed in Figure 36: isolate closed pores, dead end pores (or blind pores), ink bottle pores, through pores and interconnected pores. Interconnectivity is a desirable feature for catalysts since it favors the mass transport properties of reactants which can affects the electrochemical activity.

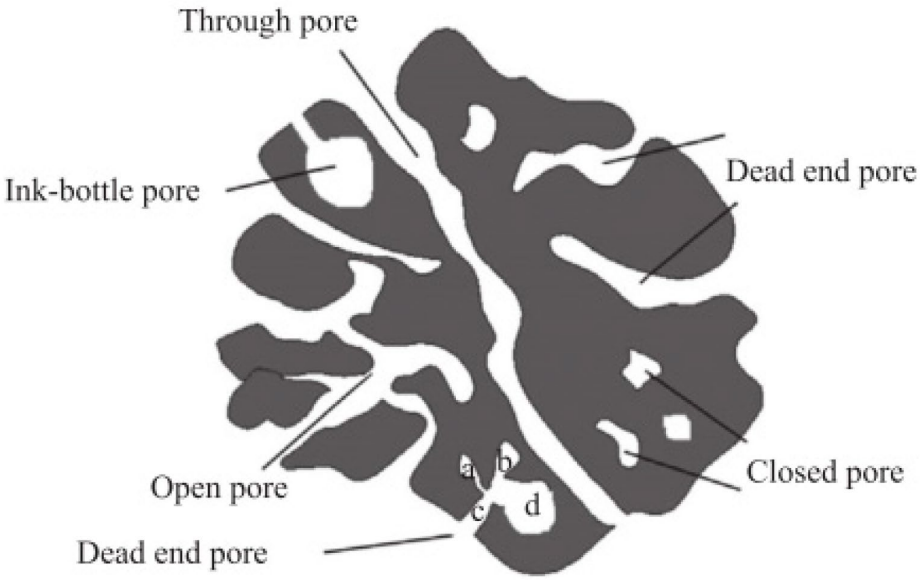

Figure 36. Scheme of the main pore types: closed, open pore with possible interconnectivity, dead end pore, ink-bottle pores [78].

At this purpose, a hierarchical factor (HF) is introduced and it is calculated as follows:

$$HF = \frac{V_{\mu}}{V_{tot}} \cdot \frac{SA_m}{SA_{tot}} \qquad (2.23)$$

Where V_{μ} and V_{tot} are the pore volume of micro and mesopores respectively whereas SA_m and SA_{tot} are the surface area of mesopores and total surface area respectively. This factor was used to characterize hierarchical structure of zeolites but it has been recently introduced for carbons [79], [80]. Microporous materials have HF < 0.1 whereas those mostly mesoporous have HF < 0.05. Materials showing a high relative microporosity and low relative mesoporosity have HF > 0.10 whereas system with spread hierarchical pores have HF > 0.15 [81].

2.7 TRANSMISSION ELECTRON MICROSCOPY (TEM)

TEM is an outstanding technique applied to obtain a hugely magnified image with atomic resolution thanks to an electron beam which interacts with a sample. The Figure 37 reports a sketch representing electron beam path. In the electron source a cathodic tungsten filament emits electrons by means of the thermoionic effect. The electrons are accelerated towards the anode. Afterwards, the beam is collimated by the Whenhelt's cylinder and focused on the sample through condenser electromagnetic lens. The beam hitting the sample has a diameter of 3-5 μm whereas the sample must be thinner than 150 nm to allow the transmission of beam, which then across other lenses before hitting the fluorescent screen.

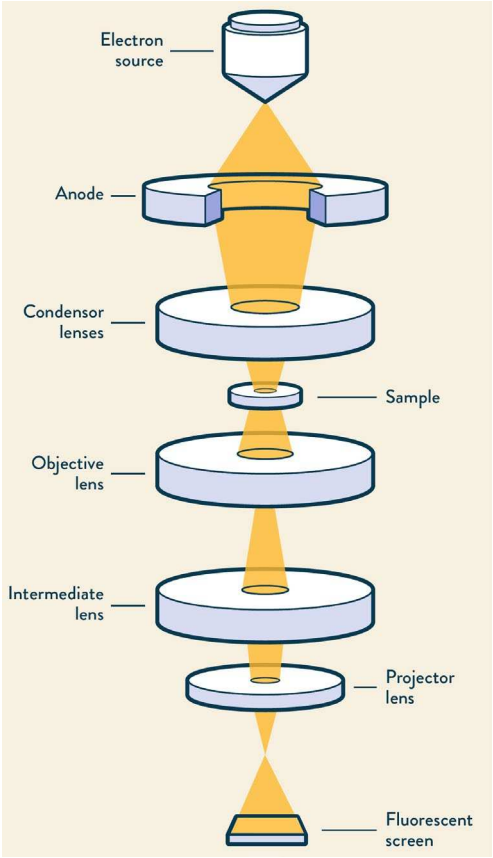

Figure 37. Representation of transmission electron microscope.

The generation of the image on a computer screen depends on the dispersion of electrons produced by the different parts of the sample. When a direct beam is used a bright field image is generated whereas a refracted beam gives rise to a dark field image. The Bragg's diffraction does not produce any image but it is fundamental to achieve a contrast on the image, namely the *diffraction contrast*. In fact, the intensity of the main beam is attenuated by the zones which are correctly oriented to give diffraction. Therefore, by exploiting the rotation of the sample holder it is possible to select some diffractions which helps to evidence a specific detail of the sample.

2.8 ICP-MS

Inductively coupled plasma mass spectroscopy is analytical technique used to detect most elements of the periodic table with very high sensibility (up to nanogram per liters of solution). The mechanism of detection is based on the ionization of the chemical species present in the solution of the sample. To form a plasma the sample must be in gas or aerosol form. Gases can be directly analyzed by the plasma, liquids need to be turned into an aerosol form and solids require a mineralization process, which is performed by an acidic digestion. To determine the concentration of the analyte a calibration curve (a linear regression in most of cases) must be obtained by the standards of known concentration of the analyte. Therefore, the extrapolation of the curve allows to calculate the concentration of the analyte [82].

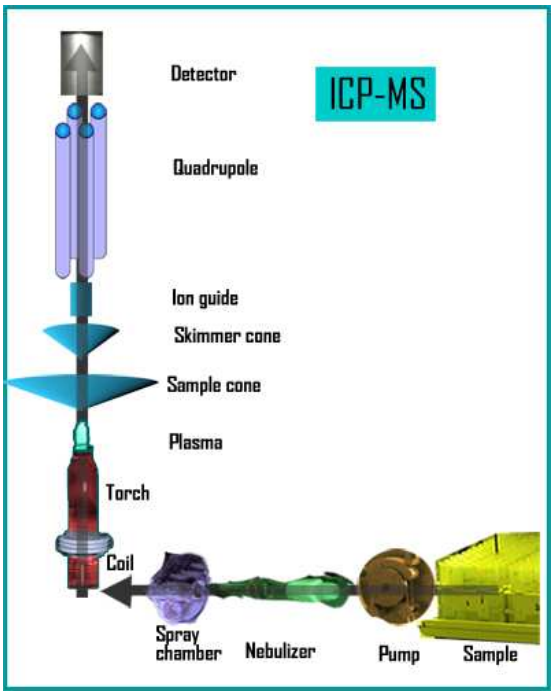

Figure 38. Sketch of ICP-MS technique.

2.9 RAMAN SPECTROSCOPY

Raman is a powerful technique to characterize carbon material, oxides and metals. As regards carbons, Raman provides useful information about their disorder, e.g. density of defects, and order, i.e. the presence of graphite crystallites within a disordered matrix. Consequently, it is possible to evaluate the degree of carbon graphitization. This technique also allows to monitor the changes of carbon support after the deposition of ceria and platinum nanoparticles. Besides, it is possible to identify the amount of defects incorporated in ceria nanoparticles after their deposition, such as the oxygen vacancies.

Raman Spectroscopy is based on anelastic diffusion of a light beam hitting a sample. The Figure 39 represent the possible scattering phenomena arising during the Raman spectroscopy. Considering the vibrational energetic levels of a molecule belonging to the sample, the interaction with the incident radiation leads to a transition from the vibrational ground state of the electronic state of the molecule (S_0) to a virtual level. Afterwards the system (i.e. molecule) can return to its initial state generating the Rayleigh radiation (elastic scattering) or it can relax to an excited vibrational state giving rise to the Stokes Raman radiation (anelastic scattering). Alternatively, if the system in an excited vibrational state is excited to a virtual state and then relaxes to the ground vibrational states an Antistokes Raman radiation is generated. The Raman spectrum reports the intensity on the vertical axis and the *Raman shift* on the horizontal axis [cm^{-1}], which is defined the difference of the wavenumber between the laser radiation and the scattered one.

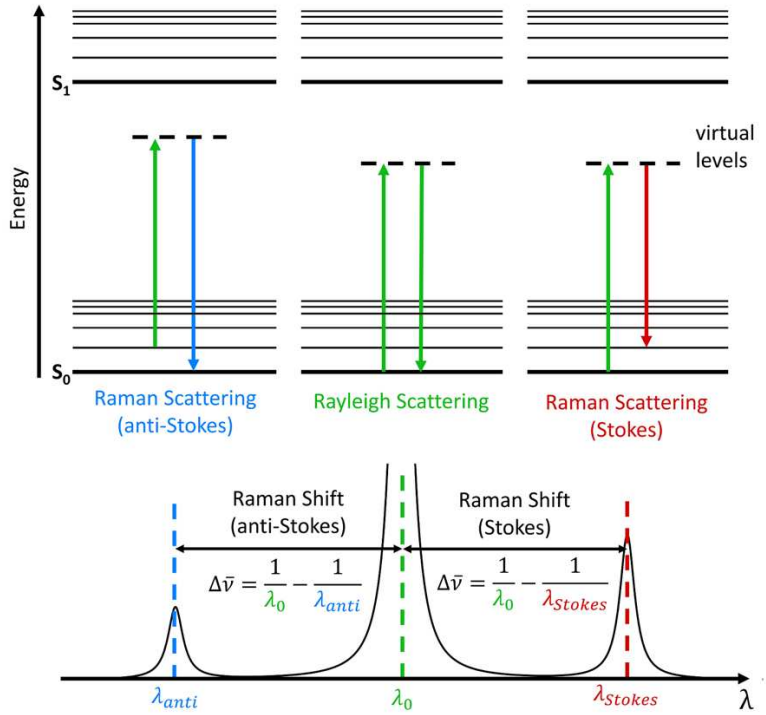

Figure 39. Represenation of the Raman scattering phenomena showing the generation of Raylaigh, stokes and antistokes signals.

In the case of carbon, the first-order spectrum shows two main peaks arising from two active Raman modes: the E_{2g} in-plane bond-stretching of carbon sp^2 atoms which generates the G band and the A_{1g} breathing mode of C atoms in presence of defects which gives rise to the D band. More specifically, the G band is generated from all the sp^2 C atoms whereas the D1 only from those of hexagons. In fact, in highly oriented pyrolytic graphite (HOPG) only the G is observable on the Raman spectrum and when some disorder is introduced the D1 band appears. Generally, the increase of disorder tends to modify the Raman spectrum.

Ferrari et al.[83] introduce the amorphization trajectory described in Figure 40 . It consists in 3 stages:

- Graphite to nanocrystalline graphite where the D1/G intensity ratio follows the Tuinstra and Koening (TK) equation (2.24) [84]; the increase of D1 band is indicative of an enhancing of defects.
- Nanocrystalline graphite to amorphous carbon where the rising of defects decreases the number of ordered rings (hexagons with sp^2 carbon) and D1/G follows another relationship (eq. (2.25))[83]; conversely to the first stage the increase of D1 band correspond to a diminishing of defects.
- Amorphous carbon to tetrahedral amorphous carbon where the degree of disorder is so high that sp^2 sites change gradually from rings to chain and consequently the D1 band disappeared.

$$\frac{I_{D1}}{I_G} = \frac{C(\lambda)}{L_a} \qquad (2.24)$$

$$\frac{I_{D1}}{I_G} = C'(\lambda) \cdot L_a^2 \qquad (2.25)$$

Where $C(\lambda) = -126\ \text{Å} + \lambda_L \cdot 0.033$, $C'(\lambda) = \frac{C(\lambda)}{8}$ [84], L_a is the average graphitic crystalline dimension and $\frac{I_{D1}}{I_G}$ the ratio of the two bands intensity.

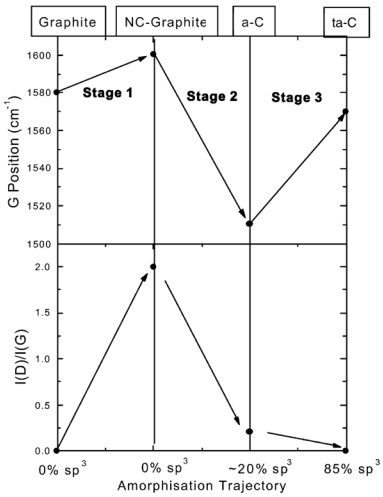

Figure 40. Amorphization trajectory desribed by Ferrari et al.[83].

Recently, some studies have deconvoluted the D and G bands to find out more detailed information about the carbonaceous materials, as depicted in Figure 41A [85,86]. Therefore, the G band at 1600 cm^{-1} could be deconvoluted in the G and D2 band, where the latter could be due to the disorder graphitic lattice on the surface of graphene layers. Moreover, especially in highly disordered carbons the D1 and G bands tend to overlap and another intense band at 1500 cm^{-1} can be detected, namely the D3 band which is related to the amorphous degree of the carbon material. At 1200 cm^{-1} the D1 band could exhibits a shoulder, denominated as D4, which can be attributed to the sp^2-sp^3 carbon bonds or C-C and C=C stretching vibration of polyene-like structures.

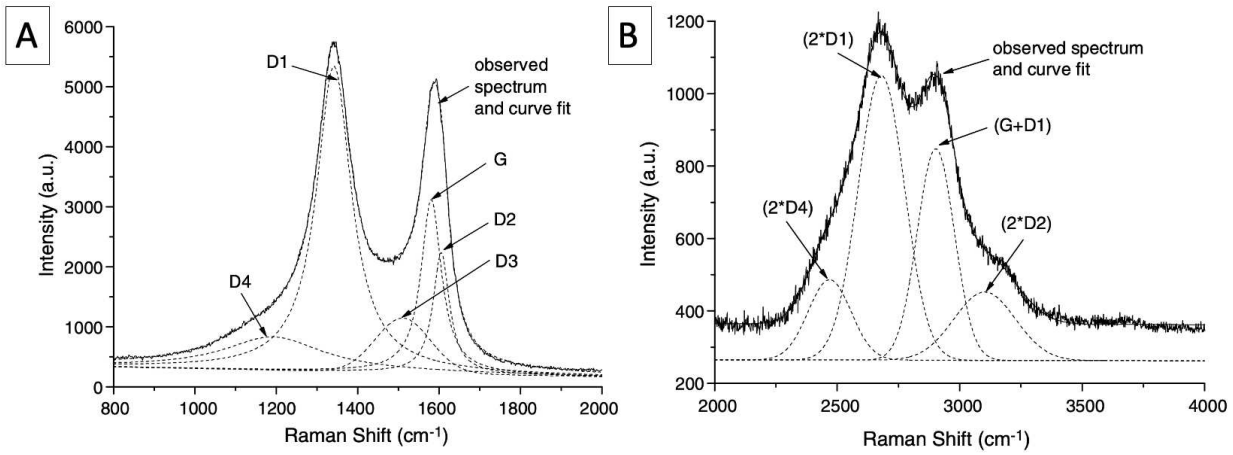

Figure 41. Raman spectra deconvolution of the first order band A) and second order band B)

The second order spectrum shows two peaks at 2700 and 2900 cm^{-1} assigned to the 2D1, an overtone of the D1 band, and G+D1 combination, respectively. The former is the more intense and it is due to the ordered stacking of the graphene layers along the hexagonal ring axis in short or medium ranges whereas the latter is a double resonance induced by defects. Another two less intense peaks could appear at 2480 and 3150 cm^{-1} and they are assigned to 2D4 and 2D2 bands [86].

$$R2 = \frac{I_{D1}}{I_G + I_{D1} + I_{D2}} \qquad (2.26)$$

To sum up, four parameters can be obtained by Raman spectroscopy of carbonaceous material: L_a (i.e. the average graphitic crystalline dimension), $\frac{I_{D1}}{I_G}$ or R2 defined by Beyssac et al. (eq. (2.26)) to obtain information concerning the order degree [87], D3 peak area or the ratio $\frac{I_{D3}}{I_G}$ to obtain the amorphous degree and $\frac{I_{2D}}{I_G}$ ratio which is indicative of high graphitic ordering and crystalline quality [43]. In fact, the two components of carbon, i.e. crystalline and amorphous, could have a different impact both on ceria and platinum nanoparticles and finally affect the electrochemical performances. Generally, a highly graphitized carbon support has a low capacitive current and allows a fast electron transfer towards ceria and platinum NPs enhances the stability in highly acidic environment against degradation [43]. On the other hand, a too graphitized carbon could hinder the growth of ceria and platinum NPs. In fact, the presence of defects within the amorphous fraction, such as heteroatoms, could act as anchoring sites which favor the nucleation of NPs.

As mentioned above, Raman can also be used to confirm the presence ceria nanoparticles supported on carbon [88] . The most intense peak at ca. 460 cm^{-1} (see Figure 42A) is attributed to the F_{2g} Ce-8O symmetric breathing vibration mode of oxygen atoms around Ce^{4+} ions [89]. Generally, a broad and asymmetric peak is indicative of the existence of nanosized CeO_2 particles [90,91]. Particles size as well as carbon interaction and the presence of lattice point defects (i.e. vacancies and Ce^{3+} centers) can influence the position and broadening of this peak [88,89,91]. Graham et al. found an empirical correlation between the half width and the inverse of the nanoparticle dimension, which is reported in Figure 42B. As the size of nanoparticle increases the half width decreases until it converges to ca. 4 cm^{-1} in the case of bulk ceria.

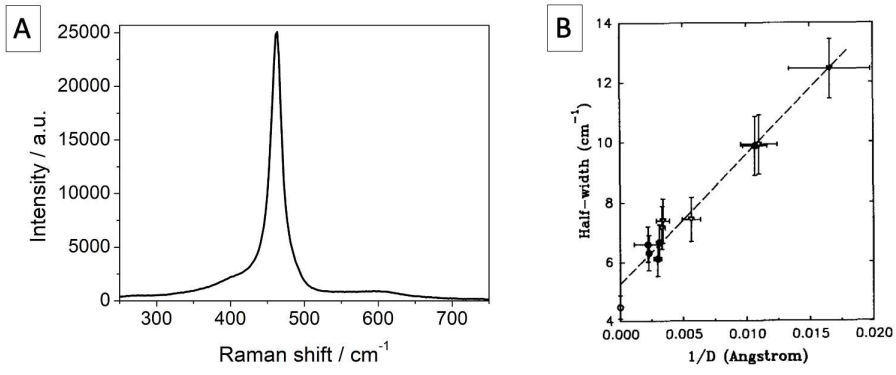

Figure 42. A) An example of Raman spectra of bulk ceria showing the peak at 460 cm^{-1} and the less intense peak at 595 cm^{-1} B)Linear trend of the half-width of the 460 cm^{-1} against the inverse of nanoparticle dimension. The different symbols are defined as mentioned in the article [90] *, whereas the dashed line is a linear fit.*

A further weak peak at 595 cm^{-1} is due to the Frenkel-type oxygen vacancies in the ceria lattice [92] [93]. Since Raman spectroscopy offers only surface information, the oxygen vacancies detected by Raman are those on the surface and therefore by calculating the ratio of the integrated peak areas (A_{595}/A_{460}) it is possible to quantify the relative concentration of oxygen vacancies [92] which can be compared to that calculated by XPS spectroscopy analysis.

3 CHARACTERIZATIONS PROCEDURE

3.1 ELECTROCHEMICAL CHARACTERIZATION FOR PLATINUM-BASED MATERIALS

$Pt/CeO_2/C$ catalysts was characterized similarly to Pt/C catalysts in a conventional electrochemical cell both in argon and oxygen saturated $HClO_4$ electrolyte solution. The electrochemical surface area of the catalyst is measured in a electrolyte solution saturated with Ar inert gas and the electrode is not subject to rotation (static mode). The purpose is to get information concerning the redox activity of the catalyst or the catalyst surface behavior, such as the electrochemical active surface area (ECSA). In oxygen saturated solution kinetic parameters for the ORR was determined, instead.

3.1.1 Information determined by measurement in Ar saturated solution

3.1.1.1 Platinum voltammogram in Ar

A typical platinum on carbon voltammogram recorded in Ar saturated solution is represented in Figure 43A. Two main peaks are clearly visible on the right part (0.6-1.0 V vs. RHE), which refer to the oxidation of Pt to PtO (positive current) and the reverse process, i.e. the reduction of PtO to Pt (negative current). The associated reactions are reported below:

Oxidation of platinum:

$$Pt + H_2O \longrightarrow Pt - OH + H^+ + e^- \qquad (3.1)$$

$$Pt - OH \longrightarrow Pt - O_{ad} + H^+ + e^- \qquad (3.2)$$

Reduction of platinum oxide:

$$Pt - O_{ad} + 2H^+ + 2e^- \longrightarrow Pt + H_2O \qquad (3.3)$$

On the left part (from 0 to 0.3 V vs. RHE) 4 peaks appear at negative current which correspond to the hydrogen adsorption on the (111), (110) and (100) and hydrogen evolution (or hydrogen discharge) and other 2 peaks at positive current related to the desorption of hydrogen from (110) and (100) faces. For example, a possible adsorption mechanism for the Pt (110) in acid electrolyte can be represented by this reaction:

$$Pt(110) + H^+ + e^- \rightleftharpoons Pt(110) - H_{ad} \qquad (3.4)$$

Each Pt faces show a different kinetic rate for the adsorption/desorption and for the same Pt crystallographic face the kinetic rate is different between the adsorption and the desorption. Moreover, each Pt sites show a different H_2 adsorption pathway as depicted in Figure 43B [94].

Furthermore, the perfect alignment between the peak of adsorption and desorption from the same crystallographic face at the low potentials is attributed to a reversible process occurring on the surface. The region placed at middle potential corresponds to the double layer charge which surrounds the

electrode surface. The area of the voltammogram attributed to the double layer must be subtract during the determination of ECSA and EPSA.

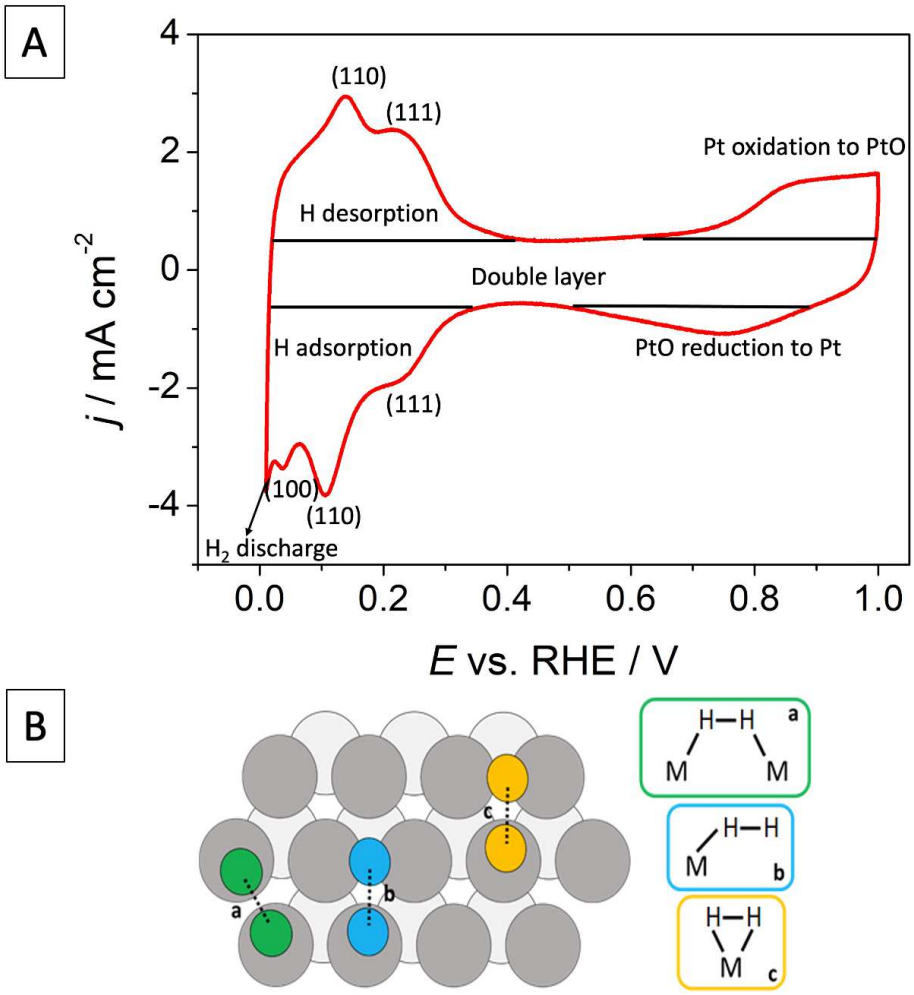

Figure 43. A) Description of cyclic voltammogram of a Pt/C catalyst recorded at 200 mV s^{-1} . B) Different way of adsorption of H_2 on different Pt sites.

3.1.1.2 EPSA and ECSA

EPSA, i.e. *Electrochemical platinum surface area* expressed in cm^2, can be calculated by mediating the EPSA related to the adsorption area of the voltammogram (i.e. the charge of hydrogen adsorbed) and that related to the desorption:

$$EPSA = \frac{EPSA_{ads} + EPSA_{des}}{2} \qquad (3.5)$$

where:

$$EPSA_i = \frac{\frac{A_i}{(v/1000)}}{0{,}210} \qquad (3.6)$$

and where:

- A_i is the adsorption or desorption area expressed in mA·V;
- v is the scan rate expressed in mV/s;

- 0,210 mC/cm^2 is the charge needed to oxidize a monolayer of hydrogen adsorbed on Pt surface.

ECSA, i.e. *Electrochemical surface area*, can be calculated be mediating the ECSA related to the adsorption area of the voltammogram (i.e. the charge of hydrogen adsorbed) and that related to the desorption according to the following equation:

$$ECSA = \frac{ECSA_{ads} + ECSA_{des}}{2} \qquad (3.7)$$

where:

$$ECSA = \frac{EPSA_i \cdot 10^{-4}}{A_{El} \cdot L_{Pt,El} \cdot 10^{-3}} \qquad (3.8)$$

where:

- A_{El} is the area of the electrode expressed in cm^2;
- $L_{Pt,El}$ is the Pt loading on the catalyst layer deposited on the electrode surface;
- $EPSA_i$ refers to the EPSA related to adsorption or desorption area of voltammogram.

EPSA and ECSA are essential parameters to describe the concentration of the active sites on the surface of platinum catalysts.

3.1.2 Information determined by measurement in O_2 saturated solution

Moving to oxygen saturated electrolyte, the kinetic parameters related to ORR can be determined by a linear sweep voltammetry in a rotating disk electrode (RDE). For convention, these parameters are determined by recording a linear sweep voltammetry at 1600 rpm and 50 mV s^{-1}. The main parameters determined from this measurement are the half wave potential, $E_{1/2}$, the onset potential, E_{on}, the limiting current, j_L, the kinetic current (usually determined at 0.9 V vs. RHE), j_k, the mass and specific activity, MA and SA respectively [95,96]. The Figure 44 represents a LSV on RDE recorded at 1600 rpm, 50 mV s^{-1} with the main parameters determined from the voltammogram and listed above.

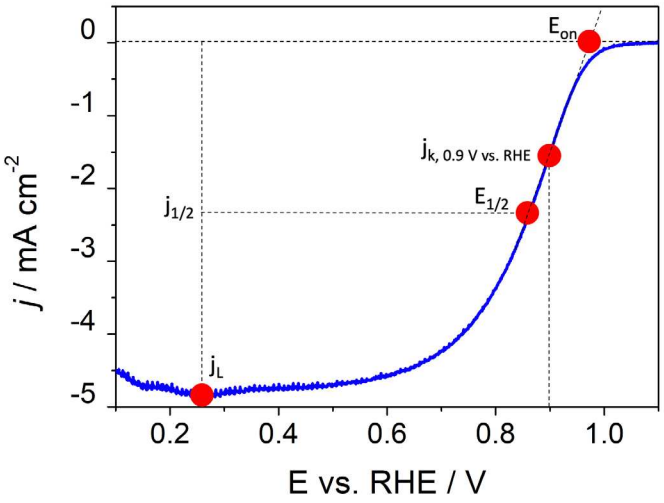

Figure 44. The main parameters determined from a LSV acquired on RDE at 1600 rpm and 50 mV s^{-1}. The current density j was determined diving the current by dividing the geometric area of the electrode.

As a general rule, the electrochemical performances vs. ORR are evaluated graphically using the LSV with RDE recorded at 1600 rpm and 50 mV s^{-1} after the subtraction of the background current recorded in Ar- saturated electrolyte under the same experimental conditions, i.e., scan rate, angular velocity, potential window, and after normalization with respect to the geometrical surface area (0.196 cm^2). This subtraction is fundamental since in this way the capacitive contribution is eliminated from the faradaic one. An example of a subtracted LSV is represented by the blue LSV reported in Figure 45.

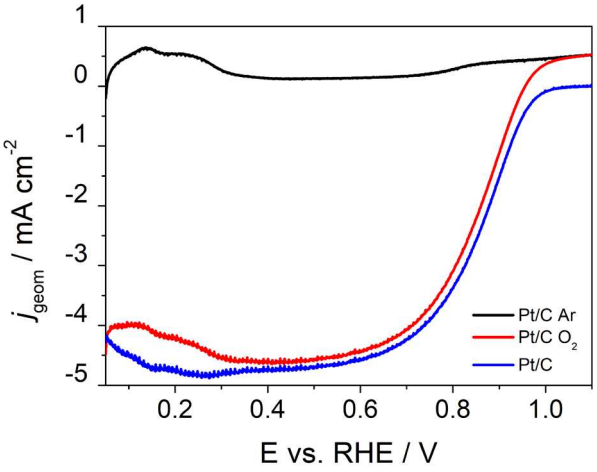

Figure 45.The blue line represents the LSV of a Pt/C catalyst obtained in O_2 saturated solution after subtracting the capacitive contribute (LSV recorded in Ar sat. solution, black line) from the red line (LSV recorded in O_2 saturated solution without any subtraction).

3.1.2.1 Half Wave Potential, Onset Potential

Two important parameters of a LSV are represented by the half wave potential and the onset potential. The first one is the potential corresponding to the half of the limiting current. Another definition can be provided by including the diffusion coefficient of the oxidized and reduced species:

$$E_{1/2} = E^{\circ} - \frac{RT}{nF}\ln\left(\frac{D_O}{D_R}\right)^{2/3} \qquad (3.9)$$

where:

- E° is formal potential
- D_o and D_R are the diffusion coefficient of the oxidized and reduced species respectively
- n is the number of transferred electrons
- F is the faraday constant
- R is the gas constant, i.e. 8,31 J/(mol·K)
- T is temperature

This kind of potential can be used to compare the activity of two different catalysts. However, the 2 potentials must differ by 5 mV at least, otherwise the 2 catalysts are considered equally active.

The onset potential can be defined as the potential at which the reaction starts to occur, i.e. the beginning of the kinetic regime. Its individuation is not simple at all. However, in the case of Pt the assigned value corresponds to potential where the current is around -0.1 mA/cm^2.

3.1.2.2 Kinetic current, mass and Specific Activity

The kinetic current density (expressed in mA cm^{-2}) is the current due to the kinetic electron transfer for the O_2 reduction and it is calculated as follows:

$$i_k = \frac{i_L \cdot i(V)}{i_L - i(V)} \qquad (3.10)$$

where i_L is the limiting current whereas i(V) is the current defined as such a potential V.

The other quantities which depend on j_k are the mass activity and the specific activity.

The mass activity expressed in A/g is the kinetic current developed per unit of catalyst mass:

$$MA = \frac{i_k}{m_{Pt}} \qquad (3.11)$$

Where i_k is the kinetic current obtained by the (3.10) whereas m_{Pt} is the mass of Pt catalyst calculated as $A_{El} \cdot L_{Pt,El}$.

The surface area expressed in A/cm^2 is the kinetic current divided by EPSA:

$$SA = \frac{i_k}{EPSA} \qquad (3.12)$$

Where i_k is the kinetic current obtained by the (3.10) whereas EPSA is the electrochemical surface area calculated according to equation (3.6).

At the purpose of comparing platinum-based catalysts, the kinetic current is determined at 0.9 or 0.95 V vs. RHE and consequently MA and SA are reported at those potentials.

3.1.3 Ohmic compensation (iR compensation)

The electrodes in solution are placed in a triangle configuration that allows to minimize the electrodes distances, i.e. the ohmic drop in the electrolytic solution. However, the resistance, which significantly alter the potential value of a cyclic voltammetry is never completely reduced since it comes from other components of the system such as the electrodes (which are not perfectly conductive), cables and contacts. Therefore, it is possible to define an overall resistance of the system which takes into accounts all of the listed elements (electrolytic solution, cables, contacts, electrodes). The presence of this resistance causes an inconsistency between the controlled electrode potential (Econtrol vs Reference electrode) and the actual electrode potential (E vs Reference electrode):

$$E = E_{control} \pm iR \qquad (3.13)$$

where $\pm$ is used to take care of the current direction. Consequently, it is advisable to make a compensation, which means excluding the contribute of potential affected by the overall ohmic drop. This operation consists in recording an electrochemical impedance spectroscopy (EIS), which permits to obtain the maximum resistance of the entire system. The value can be found by reading the real part of resistance which lays on the x axis of a graph where the imaginary contribute is plotted against the real one. To obtain this graph, the potentiostat makes the system oscillate around the open circuit potential with an amplitude of 5 mV, a range where no possible reactions can take place, and a frequency of 200 kHz. The obtained graph must have a linear relationship between the imaginary and real part of resistance because the examined material is a conductor. The maximum resistance can be determined by the minimum of the linear trend, and it can be read on the real axis, as mentioned above. Hence, compensation was enabled for every measurement by setting the resistance value below the 80 % of its maximum in order to avoid the risk of oscillations. Thus, by making a compensation the potential and the current of a voltammetry are not influenced by the overall resistance of the system.

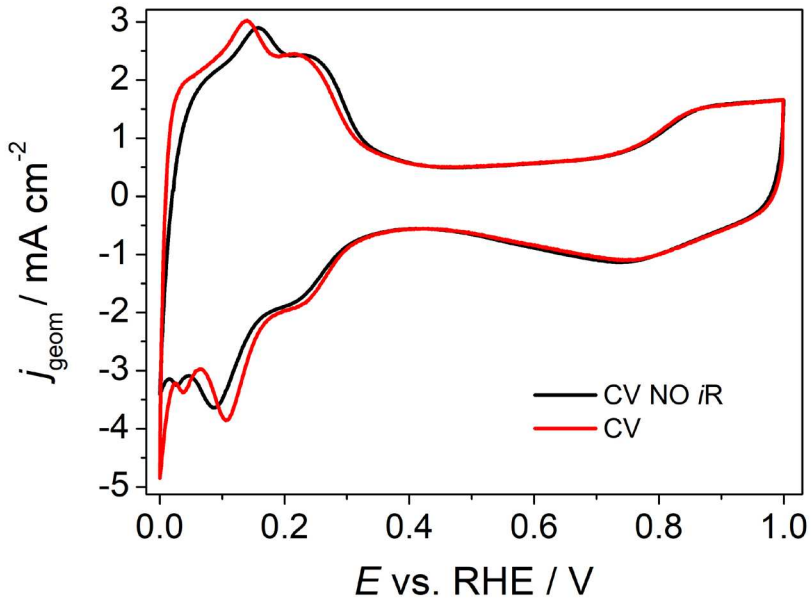

Figure 46. The black and the red lines refer to an uncompensated and a compensated cyclic voltammetry respectively recorded at 200 mV s^{-1} with 1 - 0 V as potential window and 10 Ω as compensation resistance

Figure 46 depicts a comparison between a compensated and no compensated cyclic voltammetry recorded with the same parameters (i.e. 200 mV s^{-1} and 1 - 0 V as scan rate and potential window respectively) and a compensated voltammetry recorded in the same conditions. All the curves follow the same trend in the potential window except for lower potential, which some changes can be observed since the black curve shows an inclination at positive current indicating that the potential is affected by the overall resistance of the system.

3.2 ELECTROCHEMICAL PROCEDURE FOR PLATINUM-BASED MATERIALS

Catalyst testing must be carried out carefully since it strongly depends on the operating conditions adopted. In fact, different factors should be accounted in order to achieve reliable results. The usual procedures for platinum catalysts which catalyze the ORR were discussed in several papers. Hence, it is necessary to accurately follow a certain number of procedures for each step of testing. However, this number must not be too high otherwise the catalyst could be stressed and therefore lose its performance. Consequently, only the essential measurements must be done. In the case of novel platinum catalysts for ORR, such as $Pt/CeO_2/C$, there are no systematic procedures reported for testing them. Therefore, in this thesis a recommended procedure for characterize platinum-ceria carbon supported catalysts was reported and the different efforts (attempts) which led to develop this procedure was widely discussed.

In this thesis the electrochemical cell for making electrochemical measurements is made of three electrodes: a working electrode (glassy carbon, GC) mounted on a rotating disk electrode (RDE), a reference electrode (reverse hydrogen electrode, RHE) and a counter electrode (graphite). Additionally, the cell has a water jacket connected to a water bath to control the temperature which must be around 20 °C. The cell was cleaned for 24 hours in a mixture of H_2SO_4 (Trace Select) and Nocromix and then subject to multiple cycles of heating and rinsing with Milli-Q water (Millipore, 18.2 M cm^{-1}) to remove residual sulphates. All measurements were performed in a 0.1 M $HClO_4$ (Trace Select) solution. All the potentials were referred to the RHE and corrected by iR compensation. In the following the steps of the catalyst testing procedure adopted in this thesis are enumerated:

1. Cleaning the glassware
2. Polishing and cleaning of glassy carbon electrode
3. Fabrication of catalyst ink
4. Catalyst layer deposition
5. Bubbling of Ar as an inert gas in the electrolyte solution for 20 minutes
6. Preparation of RHE in situ
7. Activation of the catalyst
8. Determination of the ohmic resistance by impedance spectroscopy
9. Acquirement of cyclic voltammetries for ECSA and EPSA determination
10. RDE cyclic voltammetry under inert gas condition with the same parameters set in the oxygen saturated solution
11. Bubbling of oxygen for 20 minutes and ORR measurements

3.2.1 Electrodes polishing

A commercial glassy carbon rotating disk electrode (5 mm of diameter and 0.196 cm^2 geometrical surface area) was employed as a working electrode. Before being used, glassy carbon electrodes must be carefully cleaned. As a rule, a diamond paste with 3 μm is spread on the electrode which is scratched on an abrasive paper made of silicon carbide in order to remove the previous superficial deposit. Afterwards, the electrode surface is immersed in a milliQ water and sonicated for 5 minutes so as to eliminate the residues of the cleaning. This procedure is then repeated for diamond pastes with 1 and 0.25 μm. The abrasive paper is essential to obtain a homogeneous surface thus removing any superficial flaws. During the scratching of the electrode, the movement of the cleaner must draw small eights to avoid preferential orientation of flaws on the surface.

3.2.2 Ink formulation

A suspension containing 2.5 mg of catalyst was prepared by successively adding 2 ml of milliQ water, 0.2 ml of isopropanol (IPA) and 5 μl of Nafion® (5 wt% in ethanol solution), which is used as a binder giving the appropriate viscosity, especially for drop casting. Then, the ink was sonicated for 2 hours by setting the temperature below 35 °C to avoid the detachment and sintering of Pt nanoparticles from the carbon support. After sonication ca. 10 μl of the prepared ink was drop casted onto a cleaned glassy carbon electrode (as depicted in Figure 47B) and dried under air all night. The ink was formulated to obtain a platinum loading of 15 mg_{Pt} cm^{-2}.

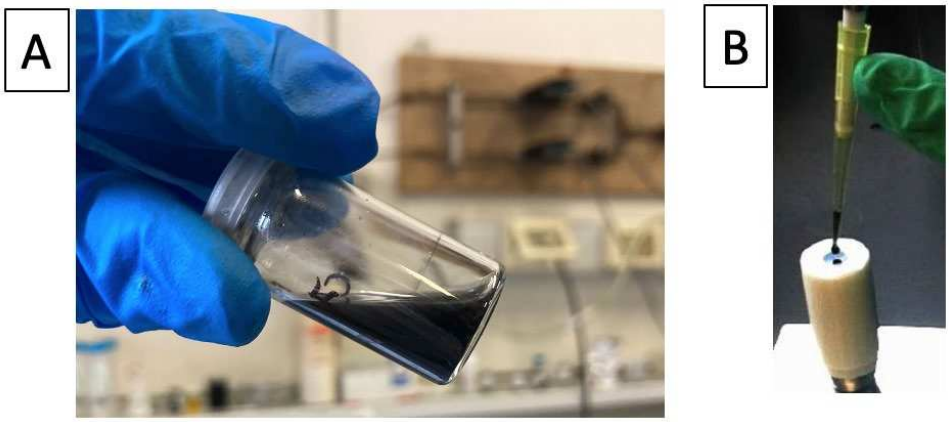

Figure 47: A) An example of ink obtained as described above B) Drop casting technique [22].

The chemicals used for the ink preparation are:

MilliQ water (Millipore, 18.2 M cm^{-1}), Nafion (5 wt%, Sigma-Aldrich,), Isopropanol (MM= , Sigma-Aldrich,), Perchloric acid (MM=100.46 g mol^{-1}, 62 wt%, Trace Select, Sigma-Aldrich,).

3.2.3 Cell preparation and activation

A cell containing a 0.1 M of $HClO_4$ electrolytic solution was degassed with Ar gas for 20 minutes. For the data acquirement the potentiostat (Biologic SP300) and the EC-Lab software were employed. $HClO_4$ as electrolyte is generally used to characterize catalyst since it reduces the possibility of introducing contaminants, unlike other electrolytes such as H_2SO_4, whose sulphate ion can poison Pt surfaces and thus alter electrochemical measurements. Afterwards, a reverse hydrogen electrode (RHE) was prepared by performing two chronopotentiometries, an electrochemical technique which measures a potential exponential decay upon time keeping the current constant at a specific value, -3 mA for 240 s in the examined case. An example of a chronopotentiometry is reported in Figure 48A. The experimental set-up for making an RHE is composed of two electrodes, a cathode and an anode corresponding to the RHE and graphite electrode respectively. The RHE is made of a Pt loop wire immersed in the electrolytic solution (0.1 M $HClO_4$) and a gas hydrogen bubble which can be formed thanks to a chronopotentiometry. Thus, once the chronopotentiometry was completed, a small hydrogen bubble formed inside the Pt loop (wire) and its size doubled after finishing the second chronoamperometry (see Figure 48B)

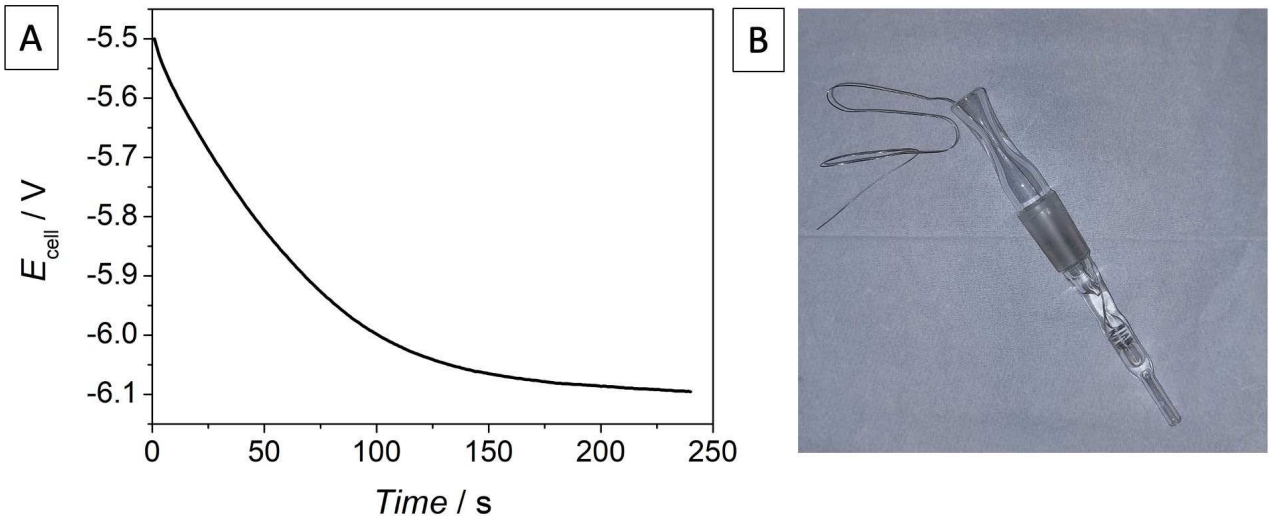

Figure 48. A) Chronopotentiometry for the preparation of the reverse hydrogen electrode; B) Reverse hydrogen electrode (RHE)

The RHE preparation was followed by the catalyst activation which was carried out with a cyclic voltammetry in a three electrodes system where the catalyst, the graphite bar and the RHE were used as working electrode, WE, counter electrode, CE, and reference electrode, RE respectively. A image of the electrochemical cell used in this thesis is reported below in Figure 49.

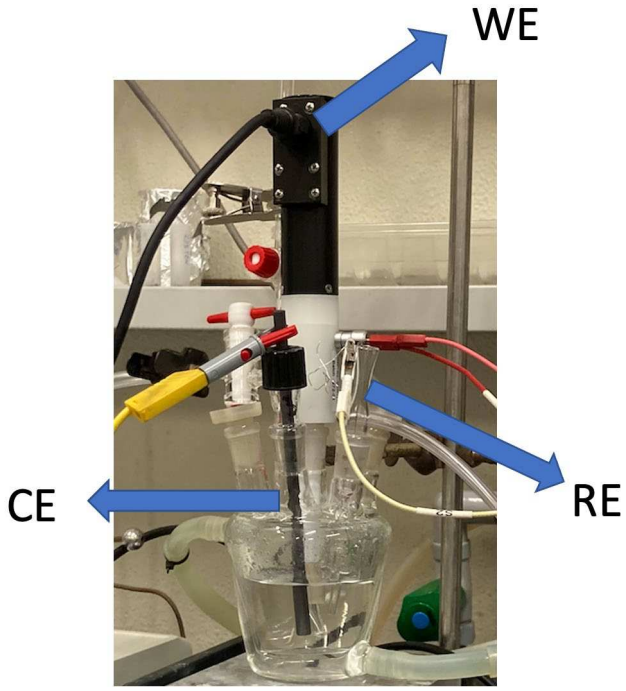

Figure 49. Electrochemical set-up employed for the ORR testing. WE, CE and RE denote the working, counter, and reference electrode respectively.

Activation is an important process consisting in cycling the electrodic material until a stable voltammogram is obtained which means that the last voltammetry must overlap. Hence, during the activation, cyclic voltammetries was performed by setting the following parameters:

- 50 cycles;
- 200 mV/s as scan rate;
- 1.2 V – 0 V vs. RHE as potential range, where 1.2 V was the upper vertex potential and 0 the lower vertex potential.

The choice of this upper vertex potential value (i.e. 1.2 V) was justified by the need of removing the possible oxide layer deposited on platinum whereas 0 V is the potential of hydrogen evolution. An example of an activation is depicted in Figure 50.

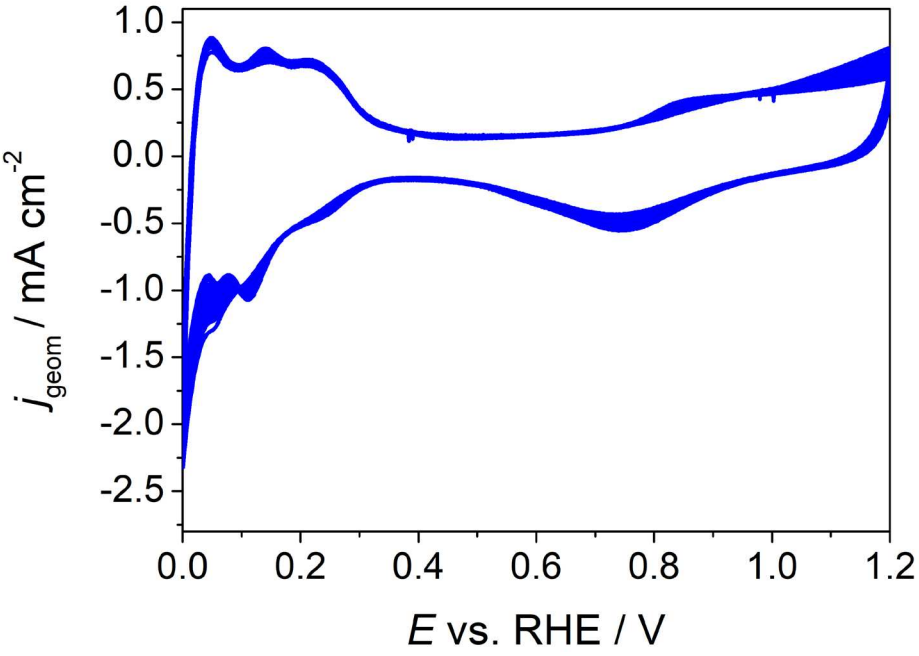

Figure 50. An example of an activation performed on Pt/C catalyst.

During the activation, the peaks of the platinum butterfly (on the left side of the voltammogram) sharpened more and more whereas the peaks at anodic potentials related to the platinum oxide stripping decrease.

Conditions for Impedance spectroscopy:

- Measuring the Open Circuit Potential (OCV)
- Measuring the impedance with a frequency range between 200 kHz and 0.1 Hz and a potential amplitude of 5 mV

Conditions for ORR testing:

In Argon saturated solution:

- Cyclic voltammetry at 200, 100, 50 mV s^{-1} between 1 V and 0.05 V vs. RHE
- LSV at 1600 rpm at 50 mV s^{-1} between 1.05 V and 0.05 V vs. RHE

In Oxygen saturated solution:

- LSV at 1600 rpm at 50 mV s^{-1} between 1.05 V and 0.05 V vs. RHE

3.3 GAS DIFFUSION ELECTRODE (GDE) PROCEDURES AND SET-UP

3.3.1 Gas diffusion electrode setup

In contrast to RDE technique GDE setup allow testing of ORR activity at high current density under realistic mass transport limitations. The GDE setup employed in this thesis is based on Arentz et al. protocol and it consists of two cell components [70]:

- a lower component made of body of stainless steel with a flow field and gas supply,
- an upper cell body of polytetrafluoroethylene (PTFE) with electrolyte and counter electrode (platinum mesh) and reference electrode (reversible hydrogen electrode, RHE).

For cleaning, the Teflon upper part was soaked in mixed acid (H_2SO_4 : HNO_3 = 1:1, v:v) overnight. Subsequently, it was rinsed thoroughly by ultrapure water, and boiled three times

The geometric surface area of the working electrode was 3 mm. The GDE was used with and without membrane between electrolyte and working electrode. When the membrane was used, it was pressed during assembling of the cell to the catalyst layer. For measurements using humidification, the gas was bubbled through a gas humidifier.

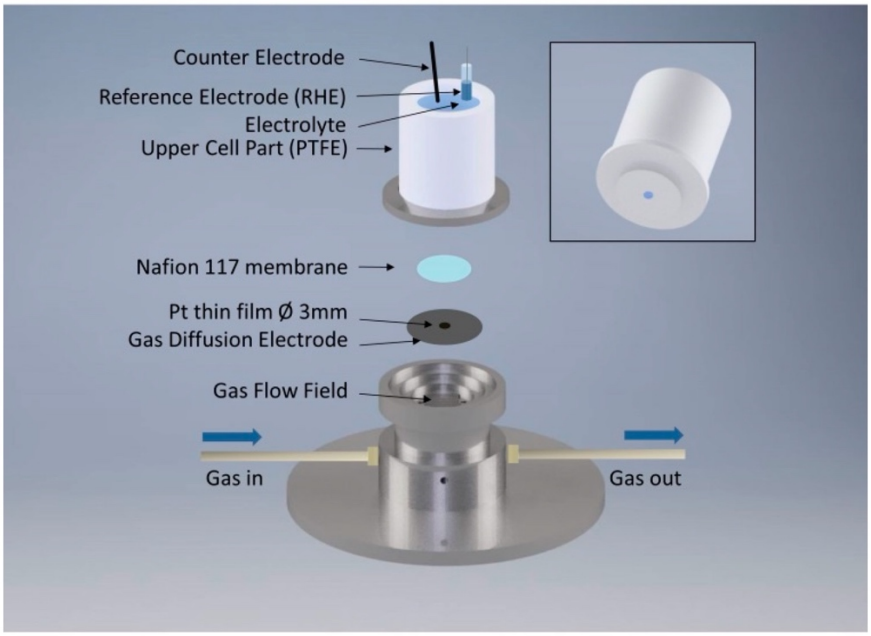

Figure 51. Gas diffusion electrode setup.

3.3.2 Measurements

The electrochemical measurements were performed by using bipotentiostat (Parstat 3000A-DX) and the Versastudio software.

The measurements were performed using 4 M $HClO_4$ aqueous solution at room temperature. The high electrolyte concentrations reduce the solution resistance between working electrode, counter electrode and reference electrode. Before starting the measurements, the working electrode was purged from the backside (through the gas diffusion layer) with O_2 gas and the catalyst was conditioned by potential cycles between 0.1 and 1.0 V RHE at a scan rate of 100 mV s^{-1} until a stable

cyclic voltammogram is obtained. The polarization curves were corrected for the non-faradaic background by subtracting the cyclic voltammograms (CVs) recorded in Ar-purged electrolyte at the identical scan rate. The resistance between the working and reference electrode (~10 Ω) was determined using an AC signal (5 kHz, 5 mV) and then compensated so that the effective resistance was ≤ 1 Ω [70].

To determine the stability of the electrocatalysts accelerated durability test was performed by following a protocol reported in literature [97] which consists of repeating 20 times these steps (reported in Figure 52):

1) A cyclic voltammetry at 10 mV s^{-1} between 1.05 V and 0.05 V for the forward scan and between 0.05 V and 1.1 V for the backward scan;
2) 500 potential cycles, where the electrode potential was modulated with a square wave and stepped between 0.6 and 1.0 V vs. RHE with a holding time of 3 s;
3) 10 potential cycles, where the electrode potential was cycled with a scan rate of 0.5 V s−1 between 1.0 and 1.5 V vs. RHE;
4) Again, 500 potential cycles, where the electrode potential was modulated with a square wave and stepped between 0.6 and 1.0 V vs. RHE with a holding time of 3 s.

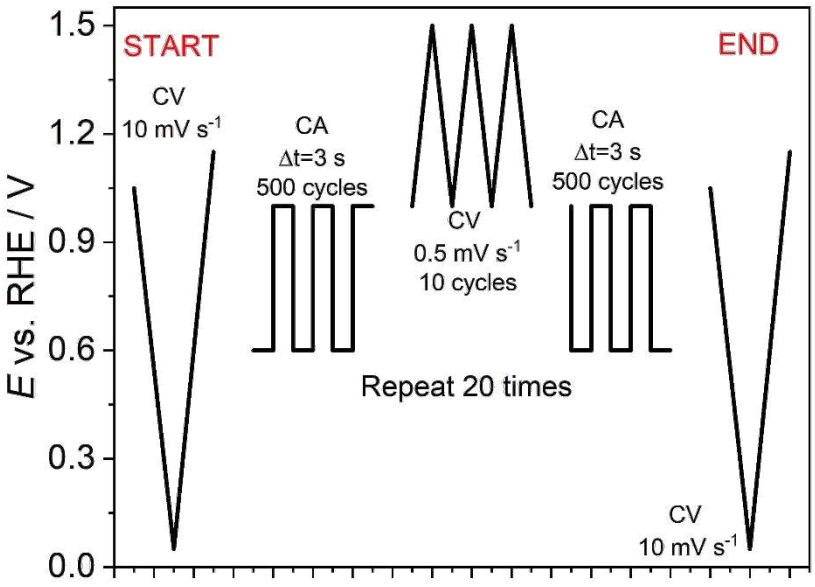

Figure 52. Steps of the GDE procedure adopted in this thesis by following a protocol reported in literature [97]. *The vertical axis refers to the potential E vs. RHE in volts whereas the x-axis represents a sort of timeline where time increasing form left to right.*

3.4 ELEMENTARY ANALYSIS INSTRUMENTATION

The elemental analysis is carried out with the analyzer Flash 200 ThermoScientific. The analysis consists of burning the sample by means of V_2O_5. The sample is placed near a CuO and metallic Cu column, whose setting temperature is 950 °C, even if the internal combustion raises the temperature up to 1900 °C giving H_2O, CO_2, NO_x and SO_x. These generated gases were transported by He, a gas carrier which put them in contact with Cu surface, where reduction reactions occur (i.e. $SO_3 \rightarrow SO_2$ and $NO_x \rightarrow N_2$). A molecular-exclusion chromatographic column operating at 200 °C provides the transportation of gases until a Wheatson bridge, a thermal conducibility detector where they are collected for the analysis.

3.5 RAMAN SPECTROSCOPY INSTRUMENTATION

Raman spectra were acquired by iRaman plus spectrometer with a Ar^+ laser source having 534 nm of wavelength. The software BWSpec was used to visualize the spectra and set all the required parameters. The attenuation of the beam power, provided by a filter, was set to 25 % of the laser emitted by the source. The signal was recorded by setting 90 s as acquisition time and mediated with 12 repetitions. To subtract the environmental noise from the Raman signal, the option *Dark subtraction* was selected.

3.6 N_2 ADSORPTION/DESORPTION ANALYSIS INSTRUMENTATION

Before performing measurements, a sample tube was weighted three times on an analytical scale with four digits. About 100 mg of sample was poured in the tube through a funnel and the loaded tube is weighted again other three times. Then the sample tube was mounted for the analysis, which was carried out with the machine ASAP 2020 Micromeritics depicted in Figure 53 using only N_2 as adsorbitive. The analysis is divided into two steps:

- Degassing: a step performed at 573 K and 1.3 Pa to remove the species adsorbed on the sample surface.
- Analysis: a step for the acquirement of adsorption and desorption branch of the isotherm where the parameters are summarized in the table In the free space module *lower dewar for evacuation* option was selected in order to analyze (quantify) the void inside the sample tube. In dosing option low pressure incremental dose was imposed with an amount of 0.5 mmol g^{-1} and 0.2 h of maximum equilibrium delay.

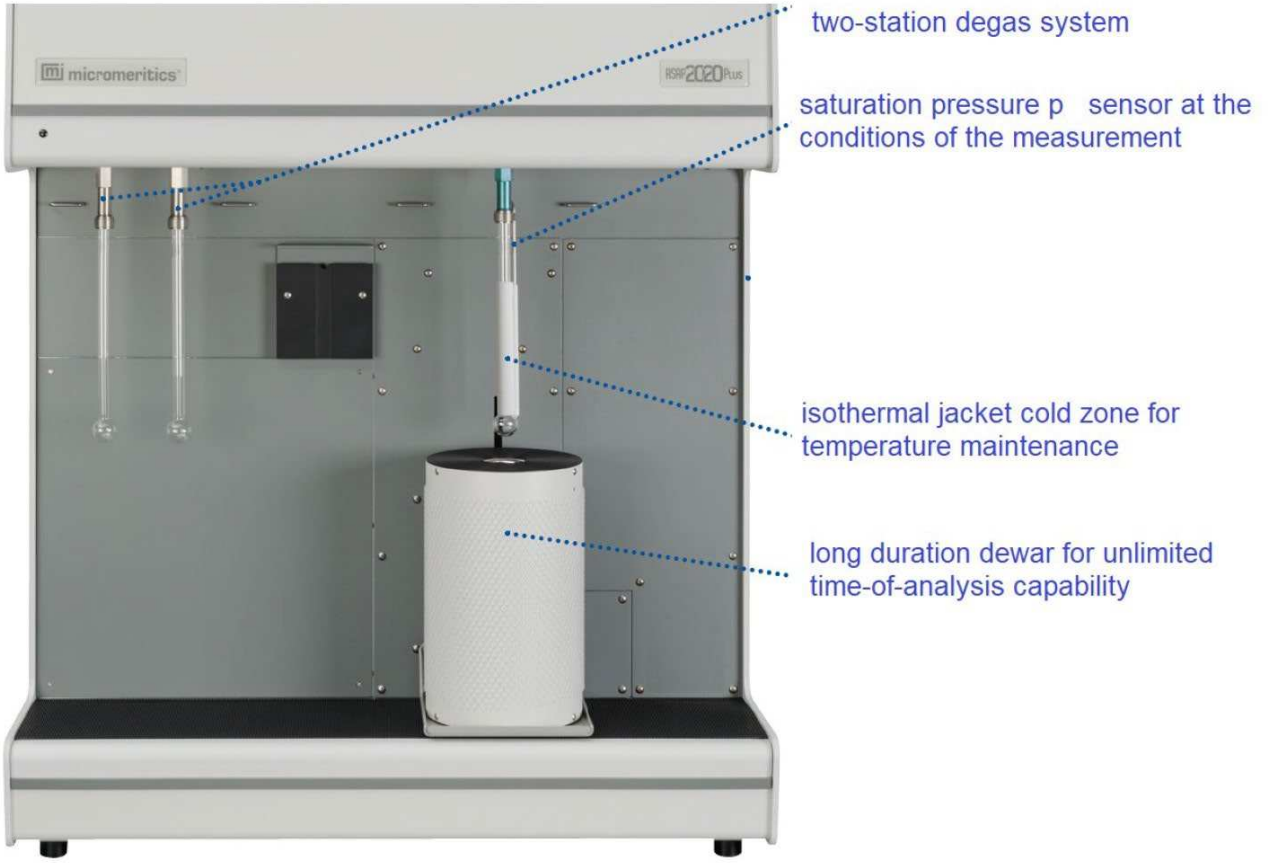

Figure 53. Front view of the ASAP 2020 Micromeritics showing the two-station degas system on left and the analysis station on right where the ampoule containing the sample is covered by an isothermal jacket for the temperature maintenance.

3.7 XRD INSTRUMENTATION

XRD measurements were performed using a Panalytical X'Pert Pro diffractometer equipped with a Co anode X-ray tube (40 kV, 40 mA), Bragg-Brentano optical module and X'Celerator detector (with a detecting length of 2.122° 2 theta). Diffraction patterns were collected in the 20 ° - 90 ° 2θ range, with 0.033° 2θ virtual step size, counting an equivalent time of 100 s per step. The average dimension of ordered crystalline domains (crystallite sizes) were estimated by line profile analysis using the Originlab software.

3.8 ICP-MS

3.8.1 Sample preparation

The platinum content was evaluated with ICP-MS. Platinum based material was digested in a mixture of HNO_3, HCl and H_2SO_4. Generally, 2g of HNO_3 69%, 6g of HCl 37% and 3g of H_2SO_4 96% were added to 5 mg of platinum on mesoporous carbon (considering a theoretical platinum loading of 25%). The strong oxidation mixture is mandatory to fulfill a total platinum and carbon oxidation. Furthermore, the carbon oxidation is important because platinum can be encapsulated in inaccessible carbon particles, thus the platinum loading could be underestimated. The mixture was digested at 220 °C for 10 minutes with a pressure of 100 psi and a medium stirring. After this treatment, the sample was diluted, filtered and finally analyzed in ICP-MS [98,99].

3.8.2 Instrumentation

A Microwave Digestion System (CEM EXPLORER SP-D PLUS) was used for the acid digestion. ICP-MS Agilent serie 7700x. (Agilent Technologies International Japan, Ltd., Tokyo, Japan). The instrument is equipped with an octupole collision cell operating in kinetic energy discrimination mode, which is useful for the removal of polyatomic interferences and argon-based interferences. RF power 1550 W, RF matching 1.8 V, Plasma gas flow rate 15 l min-1 Ar, Auxiliary gas flow rate 1.0 l min-1 Ar, Carrier gas flow rate 1.05 l min-1 Ar, Make-up gas flow rate 0.0 l min-1 Ar, He gas flow 4.3 ml/min, CeO+/Ce+ 0.902%, Ratio(2+) 70/140 0.944%, Nebuliser Microflow PFA nebuliser, Spray chamber Scott double-pass type at 2 °C and Torch Quartz glass torch.

3.8.3 Calibration

IMS-103. Multi-element calibration standard-3 (Ultra-scientific multi standard ICP-MS IMS-103), 100 mL: 10 mg/L. Sb, Au, Pt, Rh, Hf, Ru, Ir, Te, Pd and Sn; matrix 10% HCl / 1% HNO_3 COD: 8500-6948

Ag 1. Multi-element calibration standard-1, 100 mL: 10 mg/L of Ce, Dy, Er, Eu, Gd, Ho, La, Lu, Nd, Pr, Sc, Sm, Tb, Th, Tm, Y, Yb; matrix 5% HNO_3 N° 8500-6944.

4 EXPERIMENTAL PROCEDURE FOR THE SYNTHESIS OF THE CATALYSTS

In this chapter the preparation procedure of the whole $Pt/CeO_2/C$ catalysts was thoroughly described starting from the carbon support synthesis and thereafter moving to deposition of ceria and platinum. As regards the support, an innovative porous carbon materials were developed, and their properties were compared with those of commercial VulcanXC72 in this thesis. Porous carbons are widely employed in electrocatalysis owing to their huge surface area, porous structure, and good electrical conductivity. In the field of the development of heterogeneous supported electrocatalyst the suitable dimension is given by mesopores as they allow the growth of the active species (Pt nanoparticles) and facilitate the diffusion of reactants towards the active sites [100].

The synthesis of MCs is mainly accomplished by two methods: hard template and soft template [101], [102]. The former, schematically represented in Figure 54A, is widely adopted especially if combined with silica template since a high reproducibility is easily achievable. The template can be embedded in the carbon precursor (endo-template) or vice versa the latter is allowed to permeate into the pores of template (eso-template). Afterwards, a thermal treatment (pyrolysis) ensures the carbonization of the material and finally the template is leached out in alkaline solution thus generating a porous material with isolated or interconnected pores. Soft template method represents a more sustainable alternative to hard template. In fact, the use of a bifunctional copolymer as a template does not require an additional leaching step after the pyrolysis but the removal of the template is just accomplished during the thermal treatment. Therefore, only three steps can be accounted:

- the mixing of the carbon source and the template in an environment where they undergo a self-assembly process as a result of their intermolecular interactions
- the evaporation of the solvent, which ensures the growth of a three-dimensional interconnected structure
- the pyrolysis, which allows the removal of the template in a gas form.

The main steps of the soft template approach are illustrated in Figure 54B.

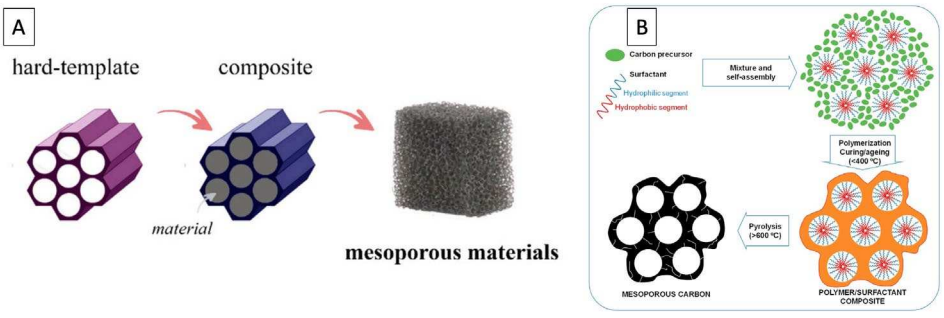

Figure 54.A) A simple sketch of the hard template synthetical approach showing that the final material results as a replication of the silica template. B) The main steps of soft template approach performed by block copolymers as template.

Block copolymers are the most promising candidate for soft template since they contain covalently bonded segments along the polymeric chain with different chemical characteristics. Owing to these chemical differences, blocks with identical properties (e.g. solubility) aggregate, whereas blocks with different chemical behavior repel. Consequently, a phase separation occurs inside the solution and this induces the formation of micelles or even more complex structures. These aggregates play a crucial role for the synthesis of many nanostructured material including mesoporous carbon. Block copolymers can be classified according to the segment which they contain, generally two or three and thus they are called diblock or triblock. Furthermore, some block copolymers can completely volatize during the pyrolysis, whereas others can partially volatize, i.e. one block volatizes (sacrificial block) generating pores while the other yields carbon residue which hereafter remains in the carbonized material (carbon block) [103].

Among the triblock, Pluronic copolymers are templates of great interest since they are relatively cheap. As a matter of fact, Pluronic is a family of PEO-PPO-PEO (i.e. polyethylene oxide - polypropylene oxide - polyethylene oxide) copolymers, which have been commercialized by BASF since 50s' [104]. They contain 2 hydrophilic segments, PEO, and one hydrophobic segment, PPO. Thus, these copolymers possess an amphiphilic behavior. Besides, according to the BASF notation, the first letter designates the physical state (i.e. P: Paste, F: Flake, L: Liquid), the first one or two numbers next to the letter refer to the molecular weight and the last number indicates the weight percent of the PEO block [105]. Pluronic F127, whose structure formula is reported in Figure 55A is one the most employed as a template in mesoporous carbon since it decomposes at a temperature of ca. 400 °C which is lower than those used for pyrolysis treatment of carbon [106]. Many works have combined it with thermosetting resins for instance resorcinol and phloroglucinol along with formaldehyde as a cross-linking agent [107,108]. However, Pluronic has recently been mixed with cheap biosources, including chitosan, which was used in this thesis together with agarose, as well [109,110]. Agarose and chitosan are both polysaccharides but with different chemical composition and water solubility. The former consists of β-1,3-linked D-galactose and α-1,4-linked 3,6-anhydro-α- L-galactose monomeric units (structure formula is depicted in Figure 55B and it is water-soluble polymer which can jellify upon cooling after being dissolved [111]. Chitosan, instead, is a polymer deriving from the deacetylation of chitin (up to 50%), a polysaccharide which can be found in the exoskeleton of arthropods, and its solubilization occurs in aqueous acidic media thanks to the deprotonation of the aminic NH_2 groups [112]. The chemical structure of chitosan is displayed in Figure 55C.

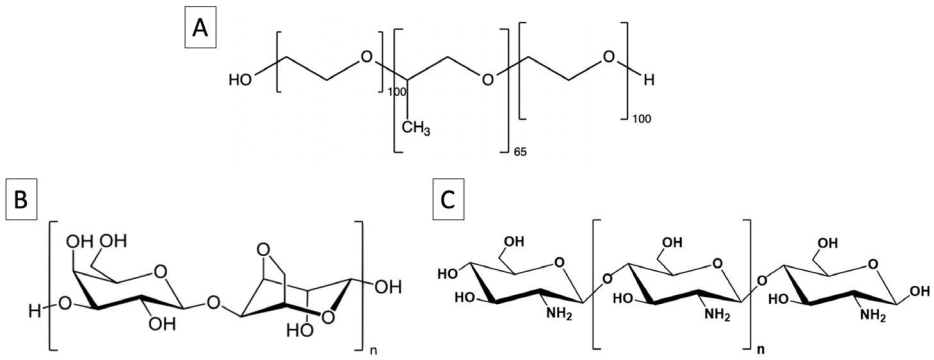

Figure 55. Chemical structure formula of A) Pluronic F127, B) Agarose, C) Chitosan.

As well as porosity, a certain degree of graphitization is desirable to guarantee an appreciable electronic conductivity and above all such a high stability against electrochemical corrosion, as explained in section 1.4.3.. Popular methods for the synthesis of graphitic carbon require temperature close to 3000°C to be graphitized. These temperatures are extremely high and it can be conducted on very expensive furnaces. Moreover, a large reduction of the surface area and pore volume generally result after treatment at such high temperatures [113]. However, it has been found that impregnating or mixing carbon with such transition metals, e.g. colbalt, nichel, iron, manganese, the temperature required for the graphitization of carbons can be lowered at temperature ≤ 1100 °C under mild reductive conditions with N_2 inert gas [114–117]. That occurs because these metals catalyze the formation of graphite inside the carbon matrix during the thermal treatment and therefore this phenomenon is known as catalytic graphitization. This process has extensively been studied since the last decades of the twentieth century by Oya e Marsh, who propose two complex mechanisms for catalytic graphitization of carbons [118].

The first is a dissolution and re-precipitation mechanism. Basically, upon the action of a graphitization catalyst at the mentioned temperatures, chemical bonds between the carbon atoms are broken and the catalyst continuously dissolves inside the amorphous carbon until it reaches the saturation inside the carbon matrix. During the cooling process, the solubility of the metal catalyst inside the carbon matrix decreases and carbon reprecipitates in the form of graphitic crystallites, since graphite is thermodynamically more stable than disordered amorphous carbon [119].

The second is a metal carbide formation and metal decomposition process. During the heat treatment metal catalyst can react with the solid carbon precursors to form metal carbides. By increasing the temperature the metal carbides can decompose to metal and graphite. The mechanism, schematically depicted in Figure 56 can be therefore represented as follows [119]:

$$M + C \rightarrow MC\ (carbide) \rightarrow\ M\ +\ graphitizable\ C \rightarrow\ M\ +\ graphite \qquad (4.1)$$

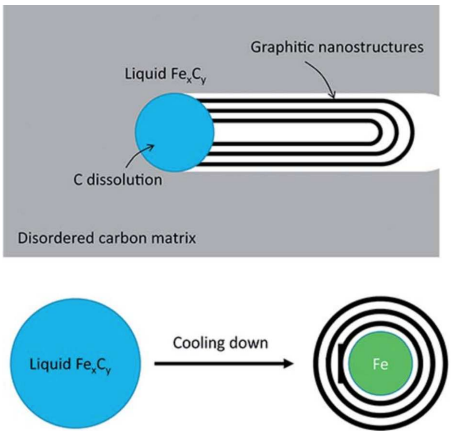

Figure 56. Iron carbide formation during the heat treatment and its decomposition upon cooling, which leads to the formation of graphitic shells surrounding metal iron nanoparticle.

As a consequence, dissolution-precipitation mechanism is controlled by the solubility of carbon in metal whereas metal carbide formation-decomposition mechanism is influenced by the formation of carbides and thermal stability of metal carbides [119]. In both cases, the final result is the same since nanoparticles of the transition metal (e.g. iron) surrounded by graphitic shells form inside the carbon matrix. As far as iron is concerned, different iron precursors have been impregnated with carbons and then treated at high temperature upon N_2 flux with the aim to graphitize carbon. Iron nitrate hexahydrated provided the best homogeneous graphitization since numerous small and uniformly distributed iron particles surrounded by graphitic shells formed inside the carbon matrix as depicted in Figure 57A and B [120]. Furthermore, it has recently been discovered that a high degree of graphitization can be reached by mixing a 2% molar of $FeCl_2$ with chitosan [81].

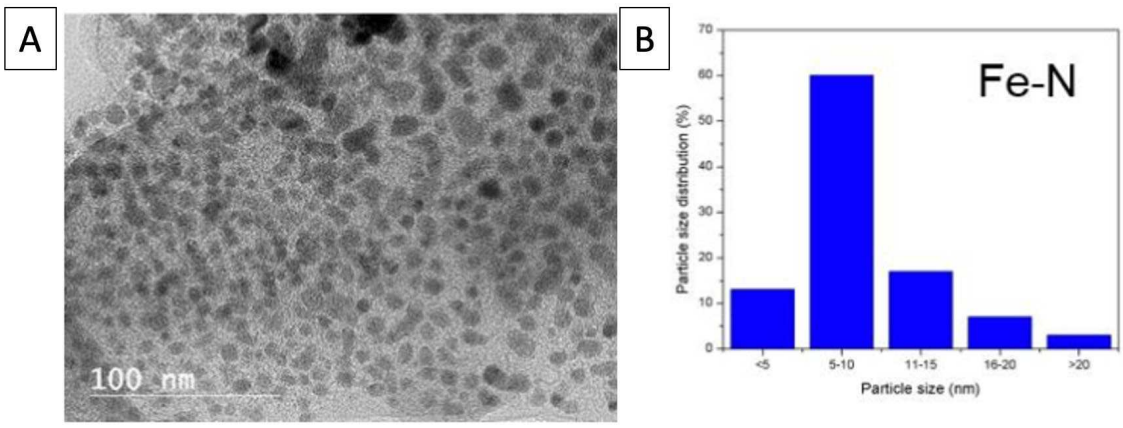

Figure 57. A) An example of TEM image showing iron nanoparticles embedded in a carbon matrix prepared by impregnating lignin with iron nitrate [120] *and the respective iron nanoparticles distribution.*

In this work, agarose and chitosan were used as different carbon sources and Pluronic as a template for the preparation of the home-made carbon supports. Additionally, two different iron salts, i.e. were introduced to study their influence on graphitization of carbon and on porosity. Since iron only serves

as graphitizing agent it was removed by an acid washing (1.5 M of H_2SO_4). It has been found that sulfuric and chloridric acid can selectively remove the iron nanoparticles leaving graphitic shells around them and thus the graphitization degree of carbon does not change. This aspect will be analyzed in this thesis, as well. The steps of the carbon support synthesis are illustrated in Figure 58. Afterwards, ceria and platinum were deposited on both a commercial carbon, Vulcan XC72 and two accurately chosen home-made carbons, according to a two-steps solid-state procedure as reported further ahead in section 4.3.1, or a one-pot solid-state deposition described in section 4.3.2. Cerium (III) nitrate hexahydrate $Ce(NO_3)_3 \cdot 6H_2O$ was employed as ceria precursor in the two-step approach whereas Ceria nanopowder furnished by the supplier company *Particular Materials* was used in the one-pot approach. Platinum acetil acetonate $Pt(acac)_2$ was used as platinum precursor and the deposition of the metal was performed by a solid-state reduction as described in section 4.3.1.2.

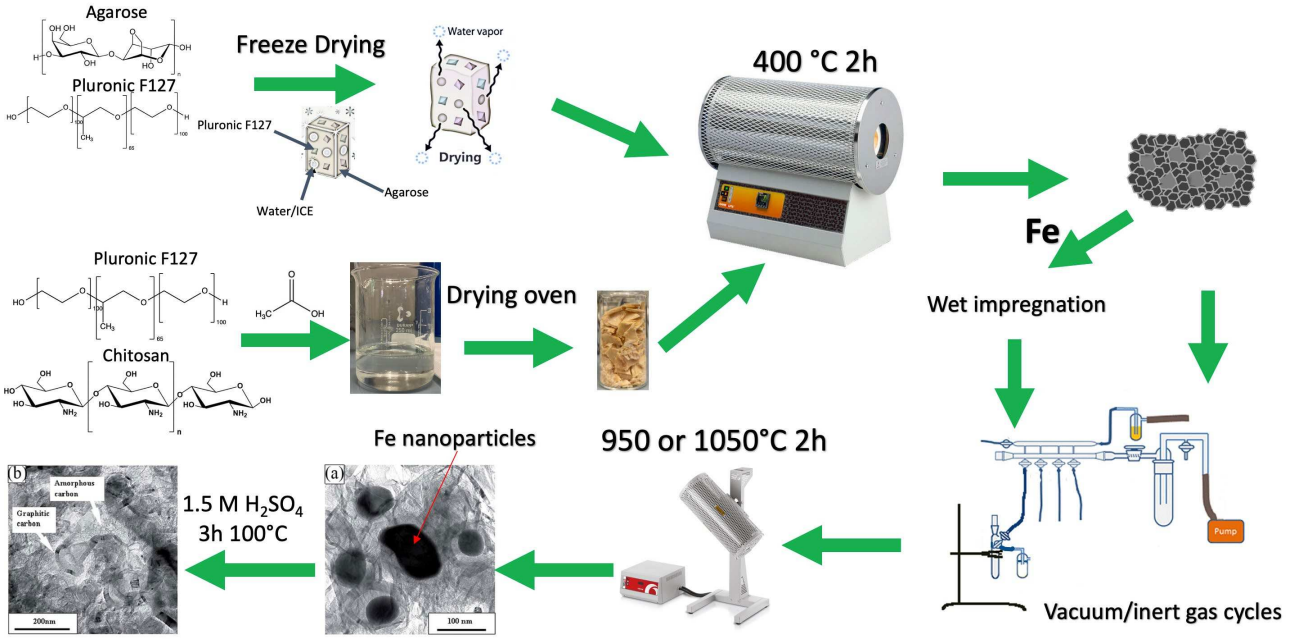

Figure 58. Scheme of the main steps for the preparation of home-made carbon supports: mixing of template, Pluronic F127, and carbon source, i.e. agarose and chitosan; desiccation of agarose-Pluronic hydrogel by freeze-drying and drying of chitosan-Pluronic gel; pyrolysis at 400°C; wet impregnation with iron precursors; vacuum/inert gas cycles; further heat treatment leading to the formation of iron nanoparticles surrounded by graphitic shells and iron removal.

4.1 CARBON SUPPORT SYNTHESIS

4.1.1 Preparation and desiccation of agarose and chitosan solution

1.8 g of Pluronic, as a template agent, was dissolved in (distillated) water at 100 °C. After its dissolution 0.9 g of agarose or chitosan were added to the solution as carbon sources for the agarose or chitosan-based carbon respectively. The mass ratio template/precursor, i.e. 2:1, was chosen by following a procedure reported in literature [109]. In the case of agarose, the solution was stirred and heated up until its boiling point and then let cool down to allow the jellification, which led to the formation of a compact and opaque hydrogel (Figure 59A). Conversely, for chitosan 400 µl of acetic acid was necessarily added to favor its dissolution and the solution was vigorously stirred until the complete dissolution. As far as the drying process is concerned, the solution of agarose was cut into small pieces and dried by means of freeze-drying whereas that of chitosan was left in an oven for some days at 80 °C. In fact, unlike the agarose solution, the chitosan one did not form a compact hydrogel but a transparent viscous solution (Figure 59B), which cannot be desiccated by freeze-drying.

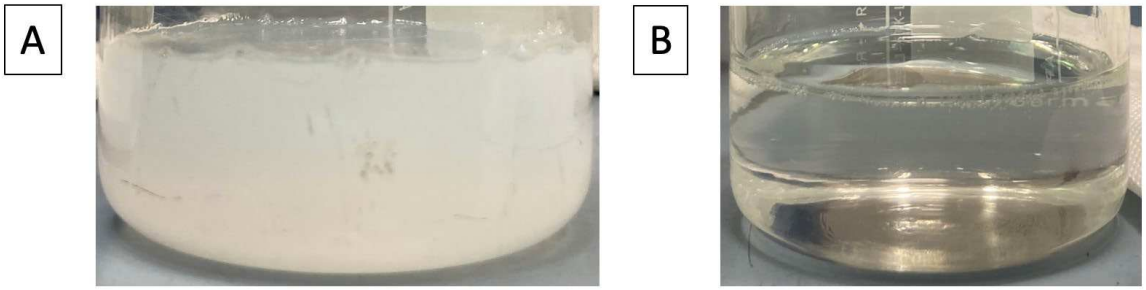

Figure 59. A) Agarose-Pluronic F127 compact and opaque hydrogel and B) chitosan-Pluronic F127 transparent gel.

Freeze-drying is employed as a drying technique in vacuum environment by alternating cycles of freezing and defrosting (unfreezing). Vacuum is essential to remove the water which sublimizes from the frozen sample when the unfreezing process is occurring. Figure 61 reports the freeze-drying set-up used in laboratory. An oil pump performing 10^{-3} mbar of vacuum was coupled with a trap immersed in liquid nitrogen, which was introduced to capture water in liquid form and thus to avoid the entrance of the liquid in the pump chamber. The obtained hydrogel was cut into small pieces, which were poured inside a flask. To perform the freeze-drying cycles the flask containing the sample was firstly submerged in liquid nitrogen (to freeze) and secondly immersed in a siliconic oil bath to unfreeze the sample. While the process was going on, the sample desiccated and after completing the drying process the sample became fluffy (Figure 60A).

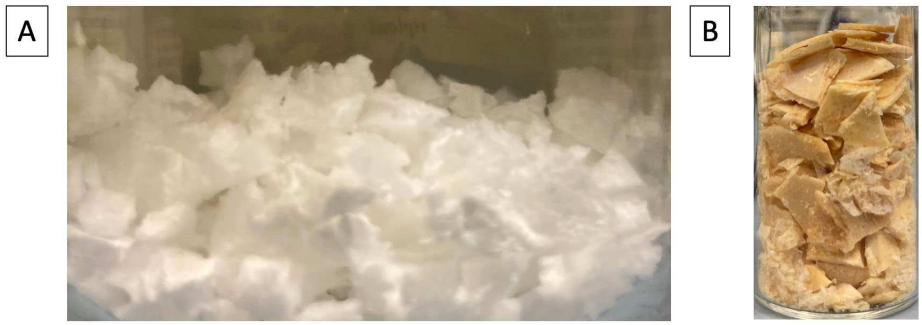

Figure 60. A) Dried agarose-Pluronic F127 hydrogel obtained after freeze-drying B) dried gel of chitosan-Pluronic F127 obtained after drying in an oven at 80 °C.

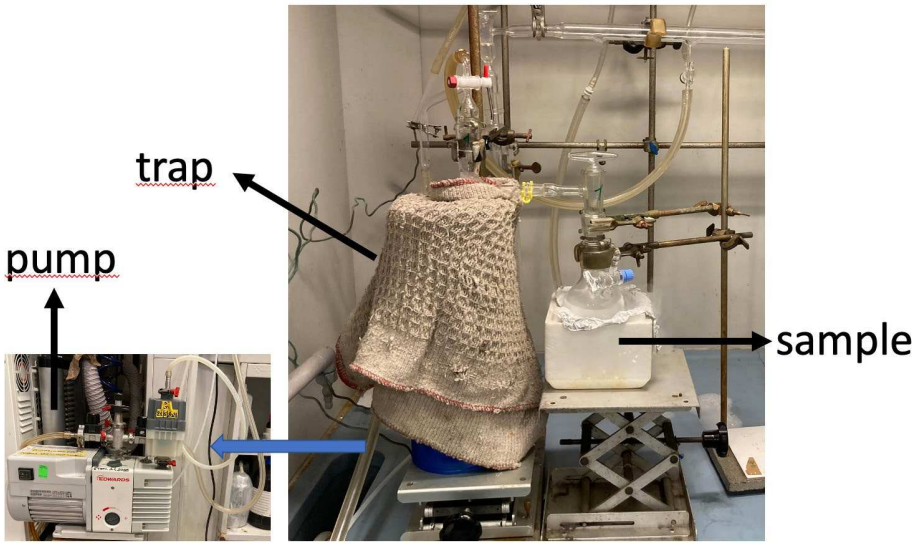

Figure 61. Freeze-drying set-up showing the main components, a pump, a trap immersed in liquid nitrogen and a flask containing the sample immersed in liquid nitrogen.

4.1.2 Pyrolysis at 400 °C

The dried samples were weighted and put in a quartz boat, which was introduced in a furnace (Carbolite MTF 10/25/130) for the carbon pyrolysis at 400 °C for 2 hours upon nitrogen flux at 100 sccm. The sample was firstly left in nitrogen atmosphere for 2 hours at room temperature. Secondly, it undergoes a rate of 10 °C/min up to 140 °C, which was maintained for 1 hour. This dwelling step is important to allow the elimination of the residual water in the sample and thus avoid a possible burn-off of the sample, which could occur if the sample was directly led to the final target temperature (i.e. 400°C). Afterwards, a second rate of 5 °C/min up to 400 °C permits the achievement of 400 °C, which was dwelled for 2 h of dwelling leads to the complete removal of the template, whose degradation temperature is around 400 °C and pyrolyze the sample.

After the pyrolysis the samples containing agarose or chitosan were ground in an agate mortar and the agarose-based carbon was labeled as CA4 whereas the chitosan-based carbon as CC4.

4.1.3 Addition of iron and further treatments

In order to improve the properties of the support, especially the graphitization of carbon, CA4 and CC4 was directly treated at high temperature, 950 °C, or, alternatively, a small amount of iron (i.e. 2 % molar with respect to the carbon support) was introduced in the carbon matrix by wet impregnation method. Thus, 0.232 g of iron dichloride tetrahydrate, $FeCl_2 \cdot 4H_2O$, or 0.471 g of iron nitrate nonahydrate, $Fe(NO_3)_3 \cdot 9H_2O$, were dissolved in 50 ml of water. Afterwards, 0.7 g of CA4 or CC4 were suspended in the iron solution and the solution was stirred for 3 hours ca. to ensure a better adsorption of iron on carbon. Afterwards, the solution was heated up and stirred at 100 °C to make the solvent evaporate and finally dried in an oven for 24 h.

The dried powder was ground and was poured inside a quartz test tube, which was in turn inserted in a long quartz tube for the thermal treatment at high temperature. Before doing the heat treatment, a pretreatment was performed by alternating vacuum and nitrogen cycles with a Schlenk line in order to remove the residual water and the oxygen adsorbed on the surface of the sample. At the end of the last cycle, the sample was left in nitrogen atmosphere. The quartz tube was put inside a vertical furnace (Carbolite MTF 10/25/130) where the sample was subject to a thermal treatment at 1050 °C or 950 °C for 2 hours upon nitrogen flux 25 sccm. The first target temperature was chosen for the samples containing iron to ensure an effective and homogeneous graphitization whereas the latter was decided for those without iron. After the pyrolysis all the samples containing agarose or chitosan were ground in an agate mortar. Table 1 reports the prepared sample containing iron and their synthesis conditions whereas Figure 62 displays the vacuum/inert apparatus (A) and the furnace for the thermal treatment (B).

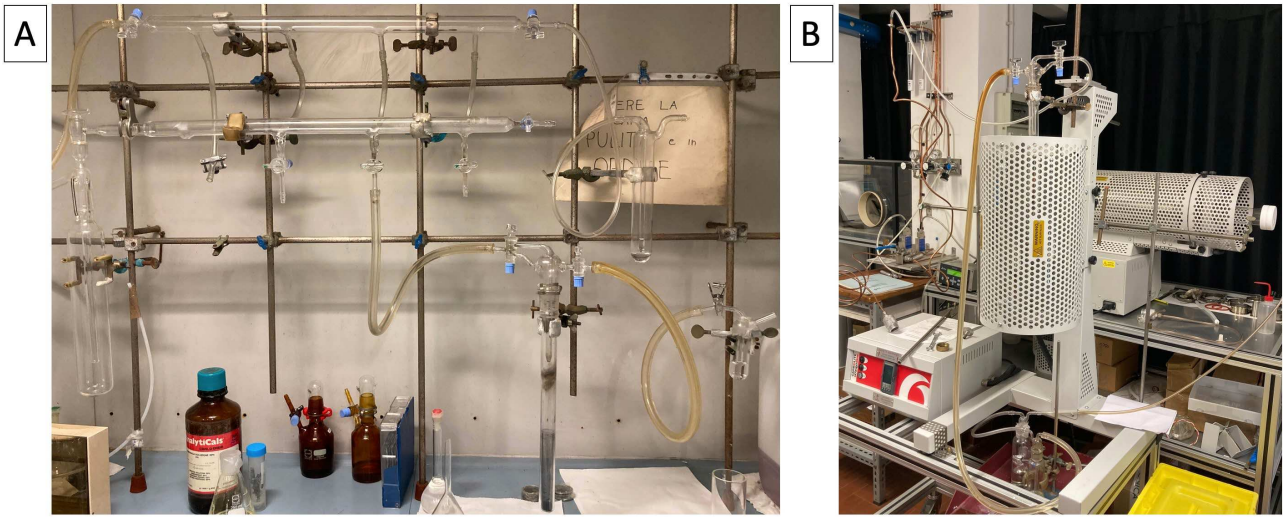

Figure 62. A) Vacuum/inert pretreatment apparatus and B) thermal treatment set-up.

Table 1: Final carbon supports prepared treated at high temperature (i.e. 950 °C for samples without iron and 1050 °C for those with iron) with the starting reactants and respective conditions.

Sample	***Carbon source***	***Fe precursor***		***Thermal Treatment***	***Time***
				°C	h
CA9	CA4	-	-	950	2
Fe_CA10	CA4	$FeCl_2 \cdot 4H_2O$	2% mol	1050	2
FeN_CA10	CA4	$Fe(NO_3)_3 \cdot 9H_2O$	2% mol	1050	2
CC9	CC4	-	-	950	2
Fe_CC10	CC4	$FeCl_2 \cdot 4H_2O$	2% mol	1050	2
FeN_CC10	CC4	$Fe(NO_3)_3 \cdot 9H_2O$	2% mol	1050	2

Since iron only serves as graphitizing agent and it is not important for the catalytic performances of the final catalyst, it was removed from the sample by an acid washing in an H_2SO_4 1.5 M solution at 100 °C held for 3 h. The washed samples were labeled by adding a "w" after Fe or FeN, i.e. Few_CA10, FeNw_CA10, Few_CC10 and FeNw_CC10.

4.2 DEPOSITION OF CERIA AND PLATINUM

4.2.1 Two-step deposition approach

4.2.1.1 Ceria deposition

Once the carbon supports were prepared, ceria nanoparticles were deposited according to a procedure reported in literature [121]. Unlike the usual deposition procedure of ceria, in this work no bases were required. 300 mg of carbon were dispersed in 100 ml of milliQ water and sonicated for 4 hours. Then, 47 mg of cerium nitrate hexahydrate ($Ce(NO_3)_3 \cdot 6H_2O$) were added to the solution, which was stirred for several hours and left to stand for one day. This rest allows to favor the adsorption of Ce^{3+} onto the carbon surface, as reported by the authors [121]. The next day the solvent was made evaporated under vigorous stirring at 100 °C and dried in an oven at 80 °C all night. Hence, the desiccated sample was collected in a quartz boat, which was put inside a horizontal quartz tubular furnace. Here the sample was flushed with nitrogen at low flux (75 sccm) to remove the residual O_2, brought with a 10 °C/min ramp to 140 °C maintained for 1 h and finally lead to the target temperature held for 15 or 30 minutes. After that, the furnace was let cooled down until the room temperature and the sample removed from the quartz boat to be ground in an agata mortar. Ceria was deposited both on a commercial carbon, Vulcan XC72 (denoted as C in the sample nomenclature) by varying the target temperature, i.e. 750 °C and 950 °C. The dwelling time at 750 °C was set to 15 or 30 minutes whereas for 950 °C only 15 minutes was set. Afterwards, ceria was deposited at 750 °C and 15 minutes on 2 home-made carbons, i.e. Few_CA10 and Few_CC10, whose nomenclature was abbreviated to CA and CC for simplicity. The samples prepared by depositing ceria are reported in Table 1 with the respective conditions and the ceria content in wt% estimated by the authors of the reference work for ceria deposition [121].

Table 1. Samples prepared via ceria deposition on different carbon types with the respective conditions for solid-state deposition of CeO_2, i.e. target temperature and dwelling time at the respective temperature, and the ceria content in wt% estimated in the reference work [121].

Sample	***Carbon source***	***Temperature***	***Time***	***CeO_2***
		° C	min	t.%
CeO_2 _750_30/C	Vulcan	750	30	6
CeO_2 _750_15/C	Vulcan	750	15	6
CeO_2 _950_15/C	Vulcan	950	15	6
CeO_2 _750_15/CC	Few_CC10	750	15	6
CeO_2 _750_15/CA	Few_CA10	750	15	6

4.2.1.2 Platinum deposition

The platinum (II) acetylacetonate was mixed with acetone and after 30 minutes the CeO_2/C support was added to the solution. Generally, for obtaining 130 mg of final Pt/CeO_2/C catalyst with a metal loading of 25 wt% and oxide loading of 5 wt%, 65.5 mg of $Pt(acac)_2$ are weight with 97.5 mg of supporting materials. The slurry precursor was maintained under vigorous agitation for 3h, at the end the solution was dried at 80 °C overnight and after finely ground in an agata mortar. After that, the mixture was heat-treated in a tubular furnace (Carbolite, UK) at a suitable temperature under a H_2/N_2 flow of 6/69 sccm. Before starting the heat treatment, the quartz tube was purged with N_2 (75 sccm) for 1 h at room temperature (r.t.) to remove O_2 [122]. The removal of water and oxygen impurities are crucial because can act as oxidation agents against platinum. Then, the temperature was raised to 100 °C and kept constant for 1 h to desorb as much H_2O as possible; at the same time H_2 was gradually fluxed into the quartz tube to the desired ratio (8%). Finally, the temperature was allowed to increase to 300 °C and kept constant for 3 h, after which the furnace was cooled down to r.t., while the H_2 flow was switched off, allowing only N_2 to flow inside the reactor [123,124]. The obtained catalyst was then removed from the quartz boat, ground in an agate mortar, and recovered in a glass vial. Figure 63 depicts a scheme of the deposition of ceria platinum by the two-step solid-state approach while Table 2 reports the nomenclature of the prepared samples containing a theoretical amount of 25 and 5 wt% of platinum and ceria respectively and the parameters used for the deposition of ceria and platinum, i.e. temperature and time.

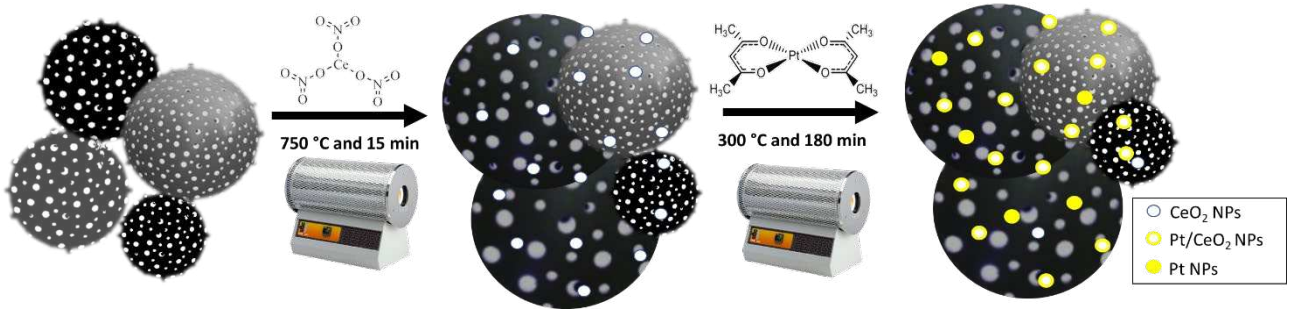

Figure 63. Deposition of platinum and ceria by two-step solid-state synthesis by using cerium nitrate as ceria precursor deposited in the first solid-state step and platinum acetyl acetonate as platinum precursor for the second pyrolysis step.

Table 2. Samples prepared by two-step solid-state synthesis with the different carbon source (C source), ceria and platinum deposition conditions, i.e. temperature and time. All the sample contain a theoretical amount of 25 and 5 wt% of platinum and ceria respectively.

Samples	*C source*	*CeO_2 deposition*	*Platinum deposition*
Pt_3h/CeO_2_750_15/C	Vulcan XC72	750 °C - 15 min	300 °C - 3 h
Pt_3h/CeO_2_ 750_30/C	Vulcan XC72	750 °C - 30 min	300 °C - 3 h
Pt_3h/CeO_2_950_15/C	Vulcan XC72	950 °C - 15 min	300 °C - 3 h
Pt_3h/CeO_2_750_15/CC	CC	750 °C - 15 min	300 °C - 3 h
Pt_3h/CeO_2_750_15/CA	CA	750 °C - 15 min	300 °C - 3 h

4.2.2 One-pot deposition of ceria and platinum

To obtain a ceria loading of 5 % within the catalyst, 175 mg of carbon were mixed with 12.5 mg of ceria furnished by *Particular Materials* thanks to ball milling. To obtain an optimal mixing of the two components, the vibration frequency was firstly set to 15 Hz maintained for 30 minutes and it was secondly enhanced to 20 Hz maintained for 30 minutes. Meanwhile, to obtain a platinum loading of 25 % in the catalyst, 126 mg of platinum acetylacetonate, $Pt(acac)_2$, were dissolved in 20 ml of acetone. After the ball milling, the carbon-ceria powder was added to the $Pt(acac)_2$ solution. Hence, the mixture was firstly stirred for ca. 30 minutes, secondly sonicated for 1 h and finally dried in an oven at 80 °C for 12 h. Subsequently, the sample was heat-treated in a tubular furnace in vertical configuration for the deposition of platinum following the same procedure described above in section 4.2.1.2 but varying the time used for the dwelling at 300°C, i.e. 3, 1, 0.5 h with the aim of reducing the platinum crystallographic domains. The samples synthesized by one-pot synthesis theoretically containing 25 % of platinum and 5 % of ceria are labeled by adding (PM) after CeO_2 and their respective nomenclature, carbon source and platinum deposition conditions are reported in Table 3.

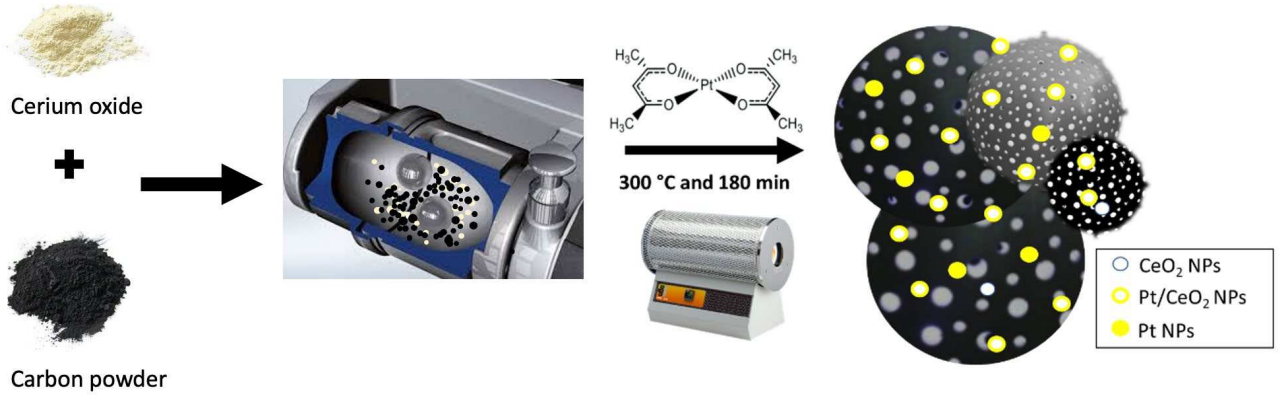

Figure 64. One-pot solid-state deposition of ceria and platinum performed by ball milling mixing of ceria nanopowder supplied by Particular materials and platinum acetyl acetonate as platinum precursor.

Table 3. Samples prepared by one-pot solid-state synthesis with the different carbon source (C source), ceria nanopowder of Particular Materials and platinum deposited with different conditions, i.e. temperature and time. All the samples contain a theoretical amount of 25 and 5 wt% of platinum and ceria respectively.

Samples	***C source***	***Platinum deposition***
Pt_3h/CeO_2(PM)/CC	CC	300 °C - 3 h
Pt_3h/CeO_2(PM)/CA	CA	300 °C - 3 h
Pt_3h/CeO_2(PM)/C	Vulcan XC72	300 °C - 3 h
Pt_1h/CeO_2(PM)/C	Vulcan XC72	300 °C - 1 h
Pt_0.5h/CeO_2(PM)/C	Vulcan XC72	300 °C – 0.5 h

4.3 INSTRUMENTATION USED FOR SYNTHESIS

Two tubular furnaces were employed in the heating treatments: Carbolite MTF 10/25/130 in horizontal or vertical configuration.

The Mass Flow Controller Broukhorst High-Tech El-Frow Select and GENius TH500 were used for the nitrogen and hydrogen flux regulation respectively.

4.4 CHEMICALS USED DURING THE SYNTHESIS OF THE CATALYSTS

Platinum (II) acetylacetonate ($Pt(acac)_2$, MM= 393.39 g mol^{-1}, Sigma-Aldrich, >97%), Cerium (III) nitrate hexahydrate ($Ce(NO_3)_3 \cdot 6H_2O$, MM=434.22 g mol^{-1}, Sigma-Aldrich, >99.99%), Vulcan XC72 (V or XC-72, MM=12.001 g mol^{-1}, Fuel Cell Store), Acetone (CH_3COCH_3, Fluka, HPLC grade), Pluronic F127 (Sigma-Aldrich), Agarose (Sigma-Aldrich), Chitosan (Sigma-Aldrich), Iron nitrate nonahydrate ($Fe(NO_3)_3 \cdot 9H_2O$, MM= 403.95 g mol^{-1}, Sigma-Aldrich, >99.0%), Iron chloride tetrahydrate ($FeCl_2 \cdot 4H_2O$ MM=196.81, Sigma-Aldrich, >99.0%).

5 PHYSICAL CHEMICAL RESULTS

5.1 MORPHOLOGICAL CHARACTERISTICS OF THE SYNTHETIZED CARBON SUPPORT

When a synthesis of a carbonaceous material is carried out, yield is the most important result since it is indicative of how much performing is the synthesis. Achieving high yields are desirable especially if a synthesis is designed for industrial purposes, so for large scale production. In this work the overall yield is 10 % for CC9 and CA9 whereas for the sample where iron was added as a graphitizing agent and subsequently removed 7% of yield was obtained. These very low values are mainly due to the loss of material in the first pyrolysis performed at 400 °C. In fact, after the pyrolysis at 400 °C a 14 % of yield was calculated, which means that a huge amount of material was lost. This can be due to the development of gases during the carbonization process which can mainly arise from the template removed during the dwelling of 2 hours at 400 °C. In this thesis no thermogravimetrical analysis (TGA) were conducted. However, the TGA results of a study where chitosan was mixed with Pluronic F127 reveal that after a dwelling of 2 h at 410 °C the template was completely removed [125].

5.1.1 Elemental analysis

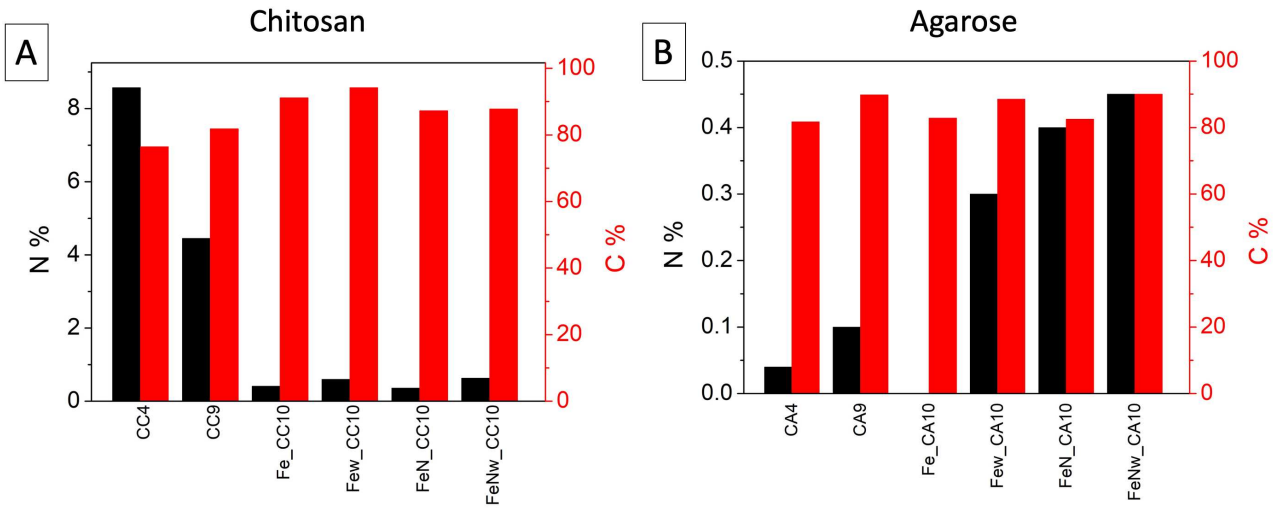

Figure 65. Amount of nitrogen and carbon in wt%. from elemental analysis of A) chitosan and B) agarose-based supports.

Table 4. Elemental analysis of the C, H, N, S in wt% in the prepared samples.

	C%	*H%*	*N%*	*S%*	*Residue*
CA4	81.73	4.11	0.04	0.00	14.12
CA9	89.78	0.52	0.10	0.00	9.60
Fe_CA10	82.84	0.26	0.00	0.00	16.90
Few_CA10	88.51	0.31	0.30	0.16	10.72
FeN_CA10	82.49	0.29	0.40	0.07	16.75
FeNw_CA10	90.04	0.3	0.45	0.10	9.11
CC4	76.44	3.78	8.57	0.00	11.21
CC9	81.83	0.95	4.45	0.00	12.77
Fe_CC10	91.16	0.15	0.41	0.00	8.28
Few_CC10	94.17	0.24	0.60	0.28	4.71
FeN_CC10	87.28	0.15	0.36	0.00	12.21
FeNw_CC10	87.8	0.28	0.63	0.25	11.04

Table 4 reports the percentual content of C, H, N and S. As depicted in the histograms of Figure 65 and in Table 4, the chitosan-based carbons show a higher N content compared to that of the agarose-based supports. The residue of the analysis corresponds to oxygen content in samples where iron is absent, whereas in the iron-containing samples the residue is given by sum of oxygen and iron content. For washed samples, no ICP-MS analysis were performed to determine the iron content. However, previous studies where iron was added after the first pyrolysis at 400 °C shown that the iron content decreased below 1 wt% after the acid washing with 2 M solution of H_2SO_4 at 100 °C for 2 h (almost the same condition used in this thesis) [81]. Therefore, it may be supposed that the washed samples of this thesis have a residue represented by mainly O. It is clearly visible that the second treatment at high temperature (i.e. 950 °C for CA9 and CC9 and 1050 °C for the other samples) decreases the H content for both agarose and chitosan and the nitrogen content for chitosan-based carbons, which switch from 8 wt% to 4 wt% for the sample without iron whereas it declines up to values < 1 wt% when iron is added (Figure 65). Meanwhile, the C content increases for both chitosan and agarose carbon and for iron-containing samples this value was further enhances by approaching 90 wt% or even overtaking 90 wt% in the case of FeNw_CA10 and Few_CC10 (Table 4). This fact proves that the heat treatment at high temperature was essential to fully carbonize the materials by removing heteroatoms such as N and O. The acid washing has a little effect on the chemical properties of carbon as it introduces S which is completely absent in the other samples.

5.2 N_2 ADSORPTION/DESORPTION ANALYSIS

Since porosity is an essential feature for catalytic supports, N_2 adsorption/desorption analysis was performed for all the supports prepared (apart from CA4 and CC4). The discussion starts with the agarose and chitosan-based carbon pyrolyzed at 950 °C without the addition of iron, thus evidencing the different porosity obtained by varying the carbon source (agarose or chitosan). Afterwards, the effect of the addition of iron on CA4 and CC4 was investigated by comparing the use of the two iron precursors $FeCl_2$ and $Fe(NO_3)_3$ on both chitosan and agarose carbons. Finally, the impact of washing acid on the morphological properties of carbons was discussed.

5.2.1 Chitosan and agarose after treatment at 950 °C

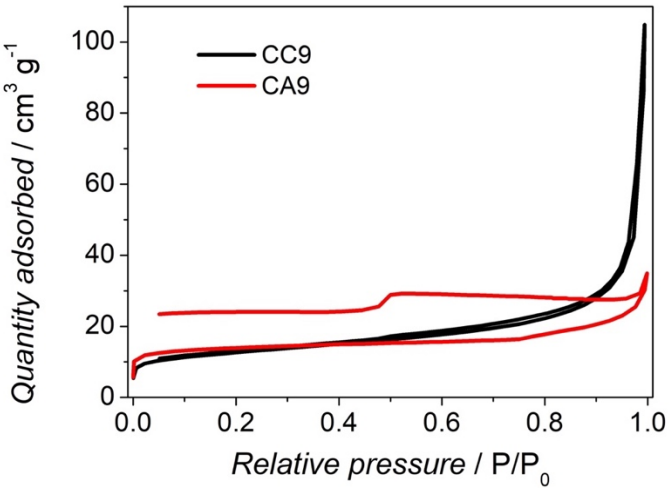

Figure 66. Isotherm of CA9 and CC9. The relative pressure was referred to the vapor tension of N_2 at 77K.

Table 5. Micro, meso, macro and total pore volume and micro, meso and total surface area values obtained from N_2 adsorption/desorption analysis by using slit/cylindrical QSDFT (quenched solid density functional theory) model. Additionally hierarchical factor (HF) was introduced.

	V_{micro}	V_{meso}	V_{macro}	V_{tot}	SA_{micro}	SA_{meso}	SA_{tot}	HF
	$cm^3\ g^{-1}$	$cm^3\ g^{-1}$	$cm^3\ g^{-1}$	$cm^3\ g^{-1}$	$m^2\ g^{-1}$	$m^2\ g^{-1}$	$m^2\ g^{-1}$	
CA9	0.017	0.019	0.018	0.054	50.5	0.019	50.5	0.0001
CC9	0.010	0.053	0.121	0.162	22.5	18.7	41.2	0.028

The samples prepared at 950 °C are not highly porous material as witnessed by the low total surface area which is 50.5 $m^2\ g^{-1}$ and 41.2 $m^2\ g^{-1}$ for agarose and chitosan respectively (Table 5). The two samples exhibit quite different isotherms and hysteresis loop, as shown in Figure 66. CA9 present an open hysteresis, which means that the desorption branch does not overlap that of adsorption. This can be due to the pore shape which hinders the outgassing of nitrogen and a higher equilibrium delay during the desorption should be necessary. The isotherm of CA9 is of II type and show a H4+H2(b) mixed hysteresis with a cavitation at 0.5 P/P_0. The presence of cavitation is an indication of ink-bottle shaped pore and therefore a slit/cylindrical QSDFT adsorption model was used for this sample, to calculate the respective data and determine the pore size distribution. In spite of the low surface area,

this sample has a certain microporosity as witnessed by the V_{micro}, which is similar to the V_{meso} value (Table 5) and the low contribution of the mesoporosity to the total surface area lowers the hierarchical factor (*HF*) value to 0.001.

The chitosan-based sample, i.e. CC9, present a close H3 type hysteresis which is hardly visible. The isotherm is of III type, which is assigned to a macroporosity materials. The macroporosity of this material is witnessed by the steep uptake at high relative pressure and by the fact that total pore volume (V_{tot}) is mainly due to macropores (V_{macro}) contributes for 75 % to the total pore volume (V_{tot}). The low value of V_{micro} strongly affects the value of *HF* which is below 0.05, thus indicating that this material is mainly meso-macroporous [126].

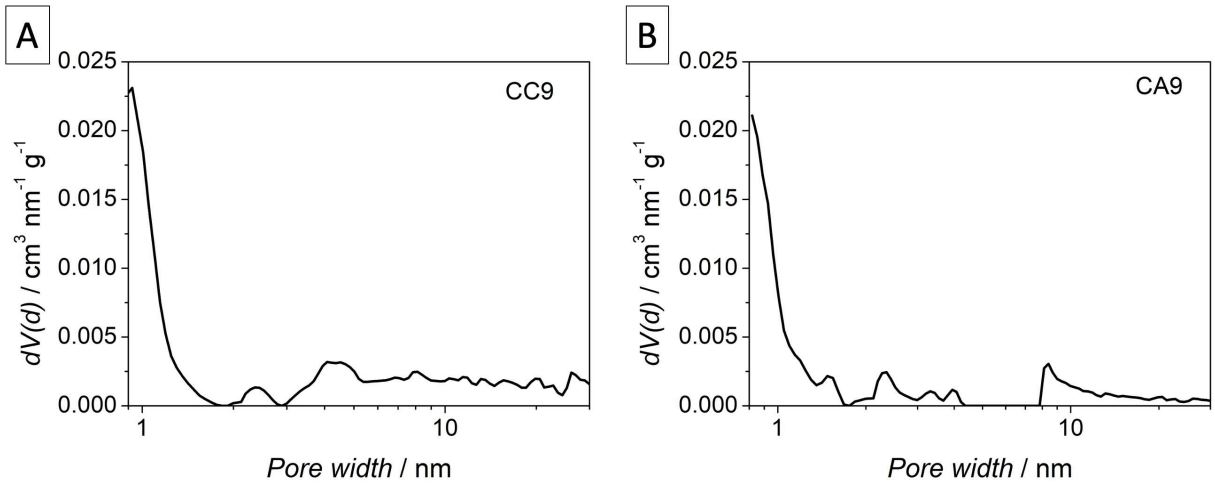

Figure 67. Pore size distribution of A) CC9 and B) CA9. In the vertical axis dV(d) represent the derivative of the volume with respect to the pore width (d), whose values lay on horizontal axis.

Figure 67A and B shows the pore size distribution of CA9 and CC9 respectively. Considering the value of the derivative of the volume with respect to the pore width (*dV(d)*), it is possible to deduce that the two materials have a low porosity. The oscillations appearing on the distribution are a clear indication that the porosity is not uniform, i.e. there is not a sharp intense peak at such a value of the pore width. Moreover, it is worthy to underline that these pore size distributions are determined in the range of micro and mesopores since the analysis of porosity was performed by using N_2 as adsorptive. As already declared in section 2.6, N_2 adsorption/desorption cannot provide any information about the macroporosity. Since CC9 is preferentially macroporous rather than micro and mesoporous, it should be expected that the hypothetical peak of the pore size distribution can be found in the range of macropores. However, to obtain a pore size distribution in the macropores region a mercury intrusion analysis should be used [127]. The formation of macropores for both samples could have arisen from the elimination of water during the drying step which was performed in oven in the case of chitosan and in the freeze-drying apparatus in the case of agarose. The resulting mesoporosity could be due to the removal of the template in the first pyrolysis step (at 400 °C) whereas the microporosity could be caused by the development of gases throughout the two-step pyrolysis.

5.2.2 Effect of the iron precursor

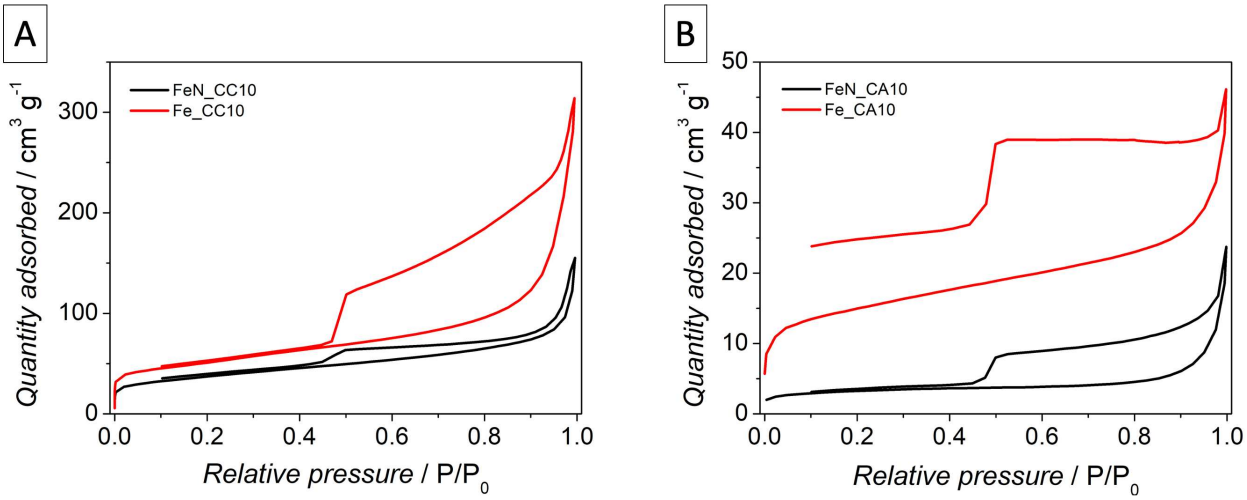

Figure 68. Isotherm of A) chitosan-based carbons FeN_CC10 and Fe_CC10; B) isotherms of agarose-based carbons FeN_CA10 and Fe_CA10 The relative pressure was referred to the vapor tension of N_2 at 77K.

Table 6. Micro, meso, macro and total pore volume and micro, meso and total surface area values obtained from N_2 adsorption/desorption analysis by using slit/cylindrical QSDFT (quenched solid density functional theory) model. Additionally hierarchical factor (HF) was introduced.

	V_{micro}	V_{meso}	V_{macro}	V_{tot}	SA_{micro}	SA_{meso}	SA_{tot}	*HF*
	$cm^3\ g^{-1}$	$cm^3\ g^{-1}$	$cm^3\ g^{-1}$	$cm^3\ g^{-1}$	$m^2\ g^{-1}$	$m^2\ g^{-1}$	$m^2\ g^{-1}$	
FeN_CC10	0.028	0.110	0.103	0.240	72.0	57.0	129	0.051
FeN_CA10	0.004	0.013	0.021	0.037	10.0	2.82	12.8	0.021
Fe_CC10	0.033	0.253	0.220	0.446	91.6	80.7	172	0.034
Fe_CA10	0.013	0.034	0.025	0.071	29.4	18.9	48.3	0.071

The addition of iron enormously affects the morphological properties of chitosan and agarose. Figure 68 represents the isotherm of chitosan- (A) and agarose-based (B) samples mixed with two precursor of iron ($FeCl_2$ and $Fe(NO_3)_3$) and treated at 1050 °C. In the case of chitosan, the addition of iron and the heat treatment at 1050 °C creates an additional microporosity, which is almost absent in CC9. This is deduced by the high uptake at lower relative pressure, by the calculated micropore volume (V_{micro}) and the surface area due to micropores (SA_{micro}), shown in Table 6, which are higher than those of CC9 (Table 5). Like microporosity, also mesoporosity enhances and even overtakes the contribute of macropores so that FeN_CC10 and Fe_CC10 result to be mainly micro/mesoporous materials. The additional micro and mesoporosity changes the isotherm, which belongs mostly to a II type rather than a III type and mesoporosity is supposed to "expand" the hysteresis loop which arose from the capillary condensation of nitrogen inside the mesopores during the analysis. A mixed H4+H2(b) with cavitation induced effect could be assigned for both FeN_CC10 and Fe_CC10. The H4 is associated to narrow slit pores, whereas the H2(b) witnesses the ink-bottle shape of pores (see section 2.6 for explanations). Therefore, a slit/cylindrical QSDFT model was used to calculate the respective data and determine the respective pore size distribution. The higher microporosity of these

samples compared to CC9 is also reflected in *HF* value which increases from 0.02 of CC9 to 0.05 of FeN_C10 and 0.03 of Fe_CC10 [126].

After this discussion, it can be concluded that both iron nitrate and iron (II) chloride act as activating agents for porosity. The activating capability of $FeCl_2$ has been already reported in literature [128], whereas the use of $Fe(NO_3)_3$ as an activating agent has never been documented. Fu et al. prepared activated carbons at different pyrolysis temperatures by using a tomato stem and $FeCl_2$ as an activating agent. By comparing TGA and N_2 adsorption/desorption analysis it was found that the SA_{micro} and V_{micro} significantly increased beyond 600°C because of the development of CO gas during the reaction between the Fe_3O_4 and the amorphous carbon [129]. In this reaction, carbon is oxidized to CO whereas Fe_3O_4 is reduced to iron:

$$Fe_3O_4 + C \rightarrow Fe + CO$$

However, the activation effect of $FeCl_2$ and $Fe(NO_3)_3$ did not work for agarose-based samples. That could be due to a possible pore collapse, especially of micropores, during the heat treatment which could have led to pore closure and thus the formation of materials with low porosity. FeN_CA10 is mainly a macroporous material due to the higher V_{macro} with respect to V_{micro} and V_{meso} and the steep uptake at high relative pressure, > 0.8, and it is the least porous material as it has only 12.8 $m^2\ g^{-1}$ and 0.037 $cm^3\ g^{-1}$ as total surface area (SA_{tot}) and total pore volume V_{tot} (Table 6). Conversely, Fe_CA10 is mainly mesoporous but it shows anyway low SA_{tot} and V_{tot} compared to those of chitosan-based samples containing iron (Table 6).

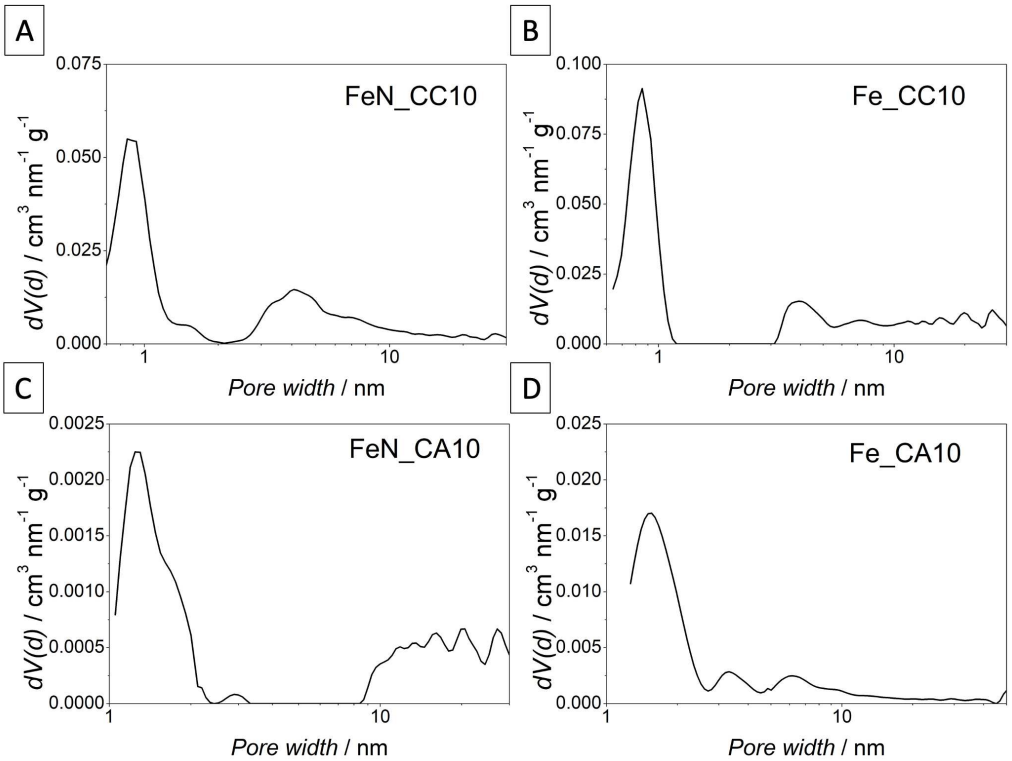

Figure 69. Pore size distribution of A) FeN_CC10, B) Fe_CC10, C) FeN_CA10 and D) Fe_CA10. In the vertical axis dV(d) represent the derivative of the volume with respect to the pore width (d), whose values lay on horizontal axis.

Figure 69 depicts the pore size distributions of FeN_CC10 (A), FeCC10 (B), FeN_CA10 (C) and Fe_CA10 (D). Unlike those of CA9 and CC9, the pore size distributions present a sharp intense peak at value lower than 1 nm for the chitosan-based carbons (i.e. FeN_CC10, Fe_CC10) and greater than 1 nm for the agarose-based carbons (i.e. FeN_CA10 and Fe_CA10). FeN_CC10 presents a broad peak centered at ca. 4 nm. Similarly, a less broad peak is detected for Fe_CC10 at the same value but some oscillations appear at value beyond 5 nm. Moving to agarose-based samples, FeN_CA10 a little intense peak is visible at 3 nm, as well as the already mentioned peak at 1.5 nm, and at value beyond 10 nm the *dV(d)* rises in intensity also showing some oscillations. Fe_CA10 shows two additional peaks centered at ca. 3.5 and 6 nm, along with already mentioned peak at ca. 1.5 nm.

5.2.3 Effect of the acid washing

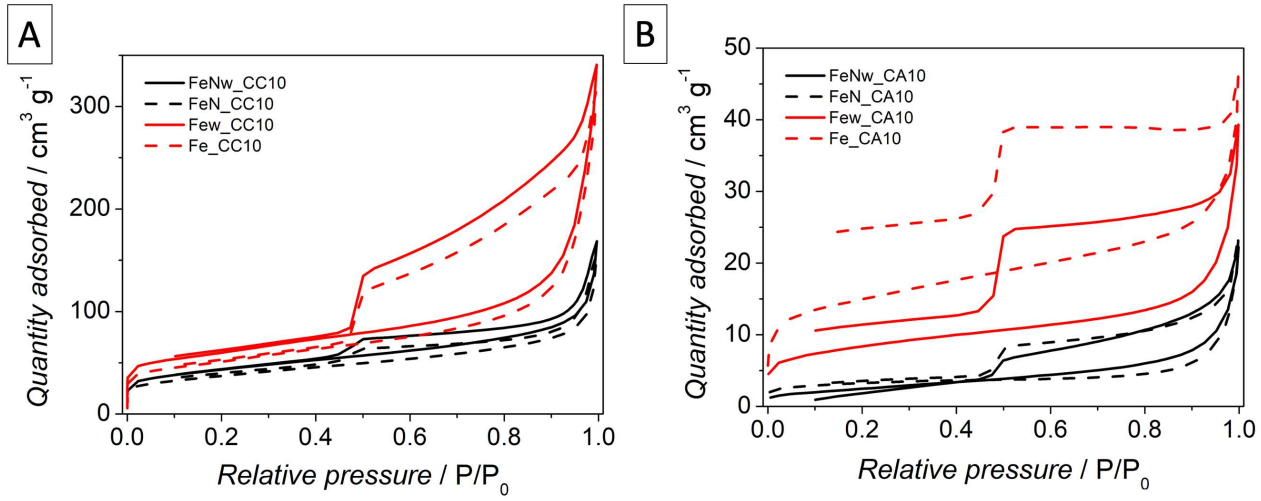

Figure 70. Comparison between the unwashed and washed samples of A) chitosan-based carbon and B) agarose-based carbon.

Table 7. Micro, meso, macro and total pore volume and micro, meso and total surface area values obtained from N_2 adsorption/desorption analysis by using slit/cylindrical QSDFT (quenched solid density functional theory) model. Additionally hierarchical factor (HF) was introduced.

	V_{micro}	V_{meso}	V_{macro}	V_{tot}	SA_{micro}	SA_{meso}	SA_{tot}	HF
	$cm^3\ g^{-1}$	$cm^3\ g^{-1}$	$cm^3\ g^{-1}$	$cm^3\ g^{-1}$	$m^2\ g^{-1}$	$m^2\ g^{-1}$	$m^2\ g^{-1}$	
FeNw_CC10	0.034	0.122	0.104	0.261	89.5	62.9	152	0.054
FeNw_CA10	0.0001	0.018	0.016	0.034	0.817	6.91	7.725	0.012
Few_CC10	0.047	0.261	0.219	0.527	139	75.0	214	0.031
Few_CA10	0.006	0.028	0.026	0.061	15.6	12.6	28.1	0.046

The acid washing is aimed at removing the iron from the carbon matrix. As shown in Figure 70, the shape of the isotherm and hysteresis loop and the pore size distribution do not change, all in all, which leads to hypothesize that the pore shape still remains the same after the acid washing. By comparing the results of Table 6 and Table 7 the total surface area and pore volume increase due to an increase of micro and mesoporosity whereas macroporosity remains the same as witnessed by the same value

of V_{macro} obtained before and after acid washing. Thus, also the acid treatment has an activation effect, even if it results to be smaller than that induced by the iron precursors.

In the case of agarose-based carbon the effect of the acid washing is the opposite, but this is due to the fact that this samples are scarcely porous or almost non-porous as in the case of FeN_CA10. Even if no TEM images were acquired for the carbon support samples in this thesis, it is well documented in literature that, after the impregnation of the iron in the carbon support, the heat treatment at such high temperatures (i.e. 1050 °C) gives rise to the nucleation of iron nanoparticles inside the carbon matrix [114]. While the gases developed upon heat treatment provide an additional micro and mesoporosity in the case of chitosan (as explained in the previous section), for agarose almost no porosity was created during the heat treatment. Due to the lack of development of porosity, the iron particles could have preferentially nucleated on the external surface rather than the internal one. A nucleation on the external surface means that the surface area is determined by the carbon surface and the nucleated iron nanoparticles. Therefore, when iron nanoparticles are removed, the surface area decreaseses. This could be a possible explanation for Fe_CA10, whose surface area changes significantly after washing. In the case of FeN_CA10 the surface area does not change significantly after the acid washing but at present we have any clear explanation for justifying this.

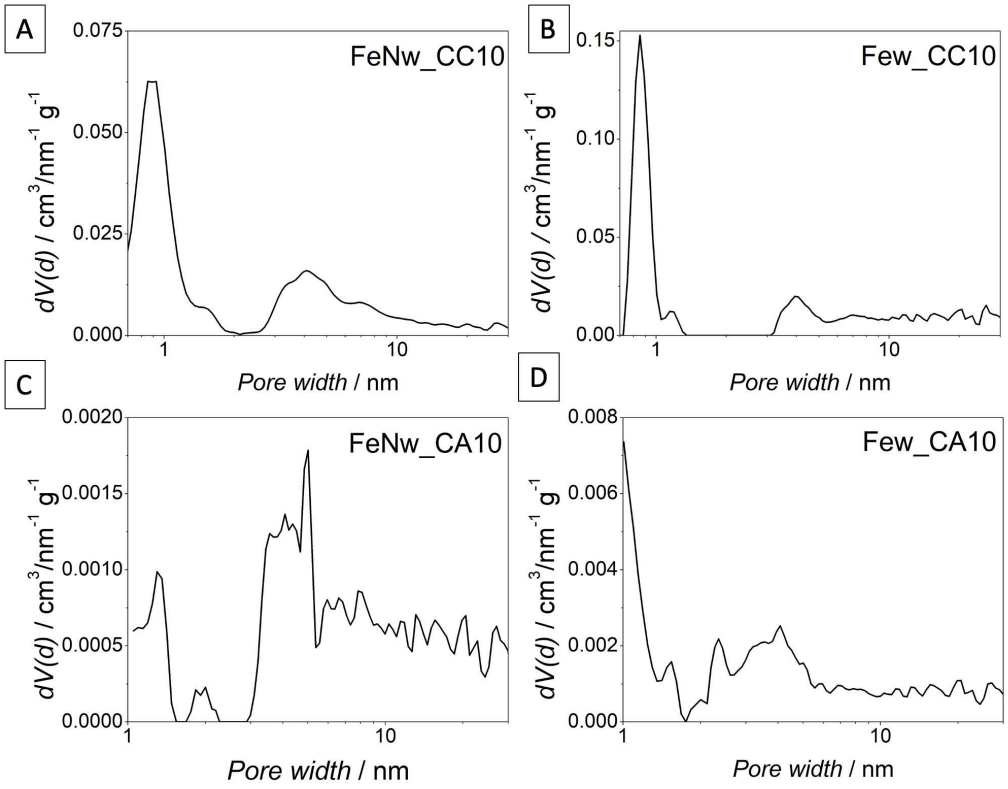

Figure 71. Pore size distribution of A) FeNw_CC10, B) Few_CC10, C) FeNw_CA10 and D) Few_CA10. In the vertical axis dV(d) represent the derivative of the volume with respect to the pore width (d), whose values lay on horizontal axis.

As regards the pore size distribution illustrated in Figure 71, similar trends are all in all observed for the chitosan-based samples after the acid washing (i.e. for FeNw_CC10 and Few_CC10 in Figure

71A and B). Conversely, the agarose-based samples (Figure 71C and D) exhibit a not well-defined pore size distribution after the acid washing. A lot of oscillations arise in the distribution especially in the mesoporous range (beyond 2 nm). Additionally, the low values of the pore volume derivative *dV(d)* of the agarose-based carbons are almost negligible with respect to those of the chitosan-based carbons and this is a further clear indication of the scarce porosity of the agarose-based carbons.

5.3 RAMAN CHARACTERIZATION FOR THE GRAPHITIZATION EVALUATION

In this section the graphitization of the synthetized carbons was evaluated by Raman spectroscopy. 5.3.1 and 5.3.2 sections compare the spectra obtained in the case of samples pyrolyzed at 950 °C without the addition of iron and those obtained with the addition of iron after the pyrolysis at 1050 °C. Instead, in the last section 5.3.3 the effect of the acid washing will be examined.

5.3.1 Evaluation of graphitization for chitosan-based carbons

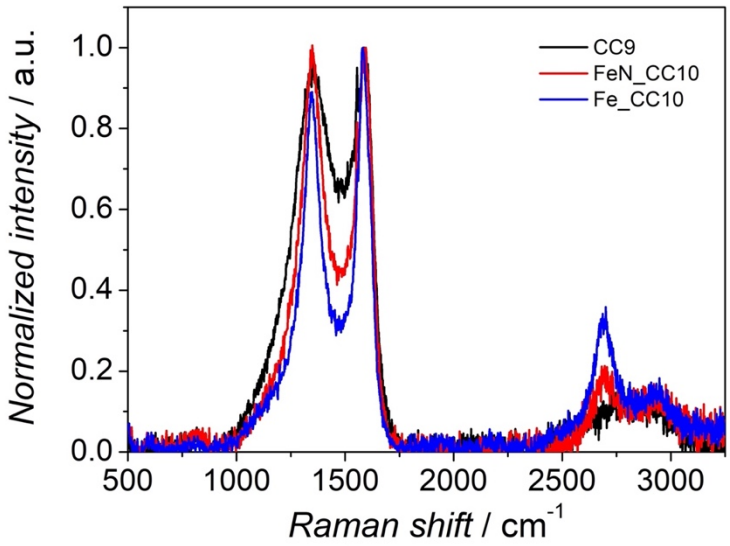

Figure 72. Raman spectra of CC9, FeN_CC10 and Fe_CC10.

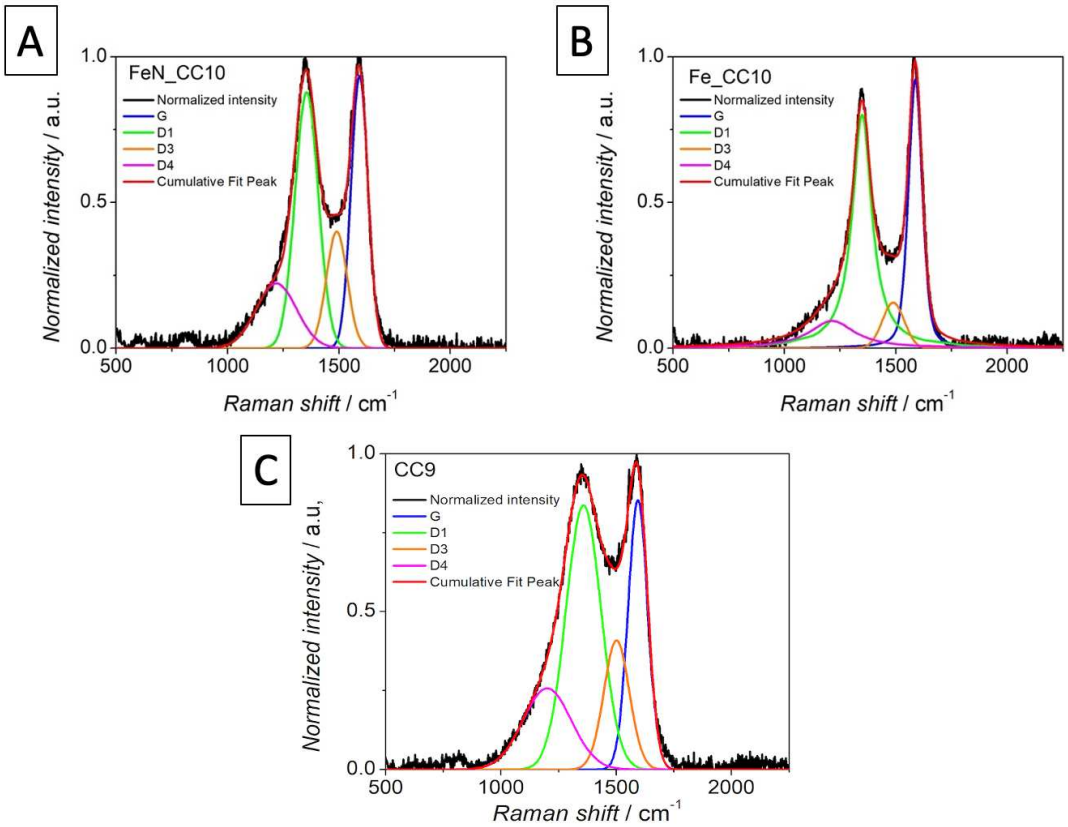

Figure 73. Deconvolution of the first order spectra of A) FeN_CC10, B) Fe_CC10 and C) CC9 showing the G, D1, D3 and D4 bands centered at ca. 1600, 1350, 1500 and 1200 cm^{-1} respectively.

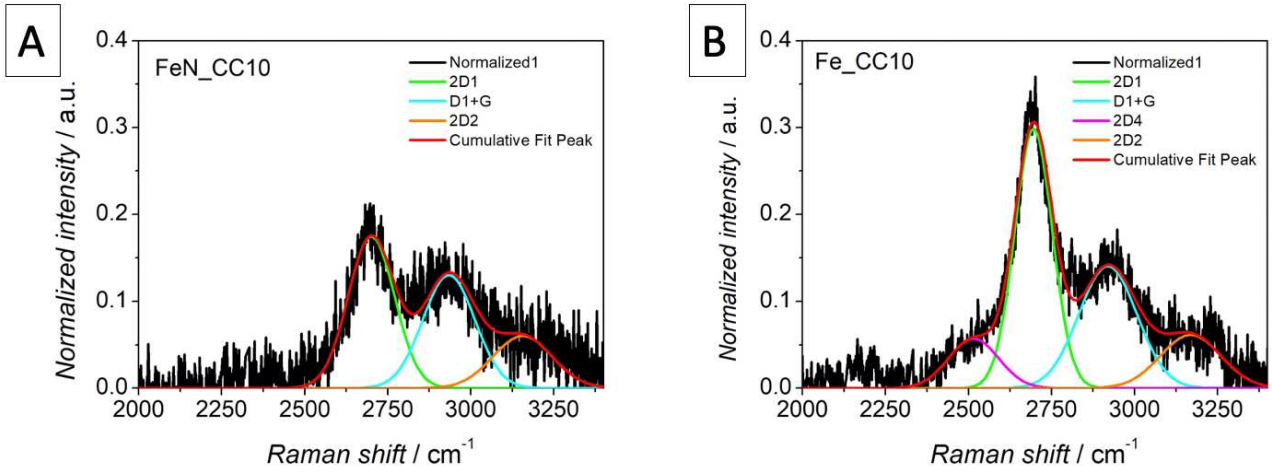

Figure 74. Fitting of the second order spectra of A) FeN_CC10 and B) Fe_CC10 showing the 2D1, D1+G, 2D2 and 2D4 bands centered at ca. 2700, 2900, 3150 and 2500 cm^{-1}.

Table 8. Values of I_{D1}/I_G, I_{D3}/I_G, I_{2D1}/I_G, D3 area, L_a^{TK}, L_a^{FR} and R2 of CC9, FeN_CC10 and Fe_CC10 obtained after deconvoluting the first and second order Raman spectra.

	I_{D1}/I_G	I_{D3}/I_G	I_{2D1}/I_G	D3 Area	L_a^{TK}	L_a^{FR}	R2
					nm	nm	
CC9	0.98	0.48	n.a.	56.67	5.05	1.26	0.50
Fe_CC10	0.87	0.17	0.32	19.30	5.71	1.18	0.46
FeN_CC10	0.94	0.43	0.16	46.81	5.28	1.23	0.48

Figure 72 compares the spectra of the chitosan-based samples obtained after the pyrolysis at 950 °C, i.e. CC9, with FeN_CC10 and Fe_CC10 obtained by the additions of the two iron precursors, i.e. $Fe(NO_3)_3$ and $FeCl_2$, respectively, and subsequently pyrolyzed at 1050 °C. Instead, Figure 73 and Figure 74 illustrate the deconvolution of the first order and the second order spectra respectively of CC9 (C), FeN_CC10 (A) and Fe_CC10 (B). The fit was performed by using a mixed Gaussian and Lorentzian functions thanks to Originlab software. Starting from graph represented in Figure 72, it is noticeable that the samples containing iron show a lower intense valley between the D1 and the G band at ca. 1500 cm^{-1} compared to CC9, whose intensity is governed by the height of the D3 band as shown by the fitted spectra of Figure 74., where the D3 is represented in orange at ca. 1500 cm^{-1}. This result is confirmed by the values obtained for the I_{D3}/I_G intensity ratio and the D3 area reported in Table 8, both of which decrease in the following order, CC9 > FeN_CC10 > Fe_CC10. Remaining in the first-order spectrum, the D1 band at 1350 cm^{-1}, which is represented by the green curve in the fit of Figure 73, follows the same trend of the D3 band as confirmed by the I_{D3}/I_G ratio reported in Table 8. The R2 ratio (see section 2.9 for explanation) was calculated by using the D1 and G band intensity, whereas the D2 value was put to 0 since the D2 band did not appear in the first order spectrum deconvolution. The R2 value of CC9 is equal to 0.5 whereas it is slightly < 0.5 for Fe_CC10 and FeN_CC10, which means that the iron containing samples have a well-ordered structure. By looking at the second order spectra (Figure 72 and Figure 74), the 2D1 band and D1+G band, which

cannot be distinguished in CC9, show a relatively high intensity for the iron-based samples, especially for Fe_CC10. In this case, the intensity of the second order spectrum is so high that even four bands can be used to deconvolute the spectrum. The weaker intense band appearing at 2500 and 3150 cm^{-1} are named as 2D4 and 2D2 (Figure 74B), respectively and they can be observed only in highly graphitized carbon such as graphene-based materials and carbon nanotubes [130]. In the case of FeN_CC10 (Figure 74A), the second order spectrum is deconvoluted in three bands since only the 2D2 appears as well as the 2D1 and the D1+G bands. The intensity of 2D1 follows the opposite trend compared to that of the D3 and D1 bands, as confirmed by the I_{2D1}/I_G intensity ratio, which decreases in the following order, Fe_CC10 > FeN_CC10 (Table 8).

Another important parameter which can be calculating by considering the I_{D1}/I_G ratio is the graphitic crystallite size, L_a. However, his determination depends on the considered stage of the amorphous trajectory proposed by Ferrari et al., as discussed in section 2.9 [83]. By considering the positions of the G and D1 bands and the I_{D1}/I_G intensity ratio the synthetized carbons can be placed between the first and the second stage of the amorphous trajectory prosed by Ferrari et al. (see section 2.9). Since it is not possible to attribute a specific stage, both the Tuinstra-Koening (TK) and Ferrari-Robertson (FR) formula (see section 2.9) were applied to calculate L_a. The TK gives values between 5.05 and 5.71 nm whereas the FR gives values between 1.18 and 1.26 nm (Table 8). In the absence of XRD characterizations for these carbons, it is not possible to assess which relationship gives the most real value. That is why both results were reported.

5.3.2 Evaluation of graphitization for agarose-based carbons

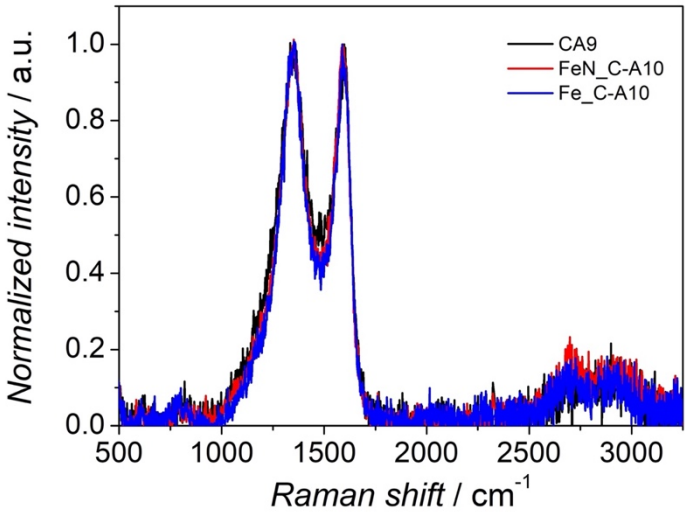

Figure 75. Raman spectra of CA9, FeN_CA10 and Fe_CA10.

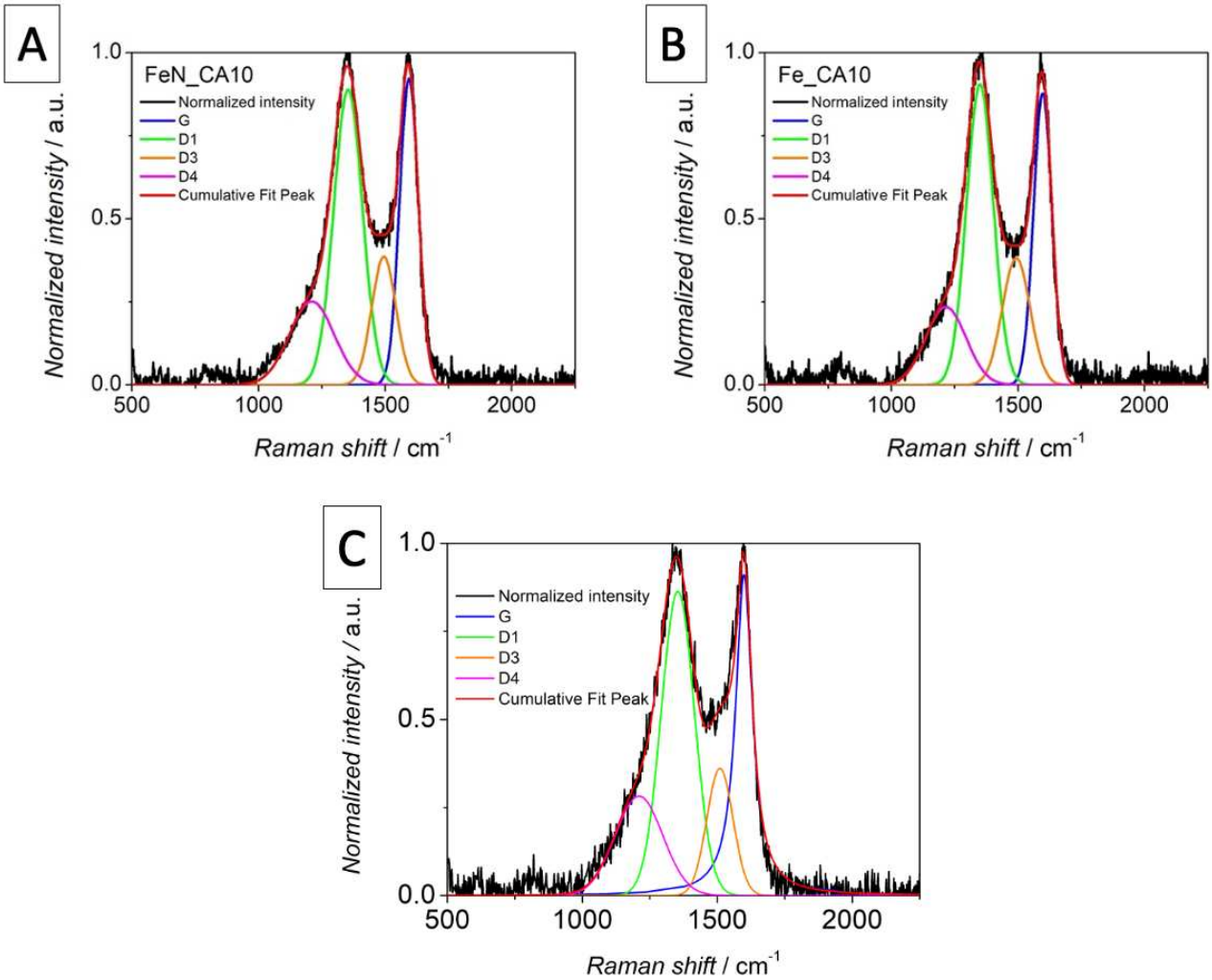

Figure 76. Deconvolution of the first order spectra of A) FeN_C10, B) Fe_CC10 and C) CC9 showing the G, D1, D3 and D4 bands centered at ca. 1600, 1350, 1500 and 1200 cm^{-1} respectively.

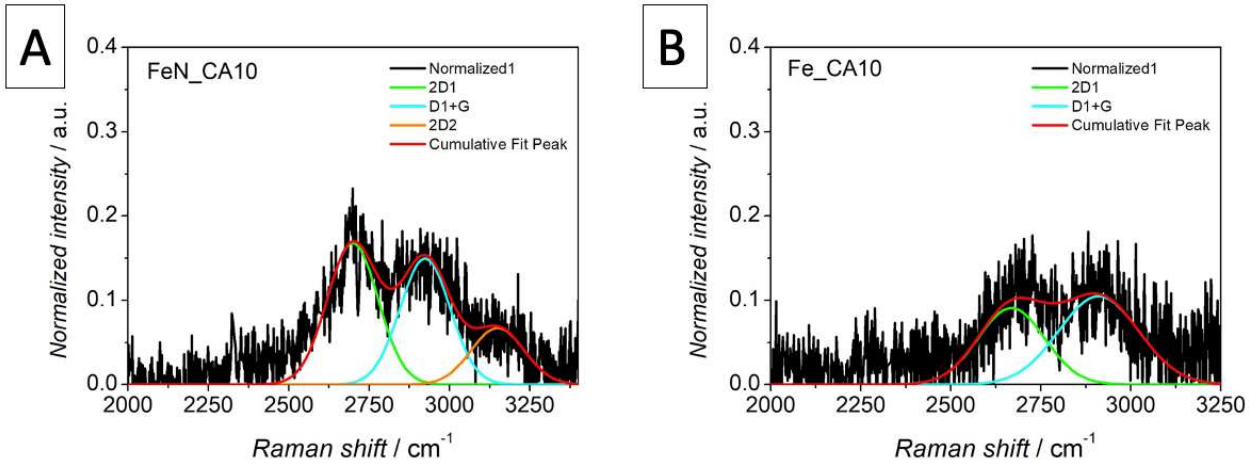

Figure 77. Fitting of the second order spectra of A) FeN_CA10 and B) Fe_CA10 showing the 2D1, D1+G, 2D2 and 2D4 bands centered at ca. 2700, 2900, 3150 and 2500 cm^{-1}, respectively

Table 9. Values of I_{D1}/I_G, I_{D3}/I_G, I_{2D1}/I_G, D3 area, L_a^{TK}, L_a^{FR} and R2 of CC9, FeN_CC10 and Fe_CC10 obtained after deconvoluting the first and second order Raman spectra.

	I_{D1}/I_G	I_{D3}/I_G	I_{2D1}/I_G	D3 Area	L_a^{TK}	L_a^{FR}	R2
					nm	nm	
CA9	0.95	0.40	n.a.	43.9	5.22	1.24	0.49
Fe_CA10	1.03	0.44	0.10	52.7	4.80	1.29	0.51
FeN_CA10	0.96	0.42	0.18	46.2	5.14	1.25	0.49

Figure 75 compares the spectra of the agarose-based samples obtained after the pyrolysis at 950 °C, i.e. CC9, with those obtained by the additions of the two iron precursors, i.e. $Fe(NO_3)_3$ and $FeCl_2$, and subsequently pyrolyzed at 1050 °C. Instead, Figure 76 and Figure 77 illustrate the deconvolution of first and second order spectra of CC9, FeN_CC10 and Fe_CC10. The fit was performed by using a mixed Gaussian and Lorentzian functions thanks to Originlab software. By firstly focusing on Figure 75, the valley between the D1 and G bands decreases moving from CA9 to FeN_CA10 and Fe_CA10 but not as significantly as shown in the set of chitosan-based carbons. In fact, I_{D3}/I_G ratio (reported in Table 9) and the D3 area seem to be quite similar to each other. Also the R2 values are similar among the three carbons, which means that they have basically the same graphitization degree. Regarding the second-order spectra, the 2D1 band follows this trend in decrescent order, FeN_CA10 > Fe_CA10. As for CC9, the CA9 does not show the 2D1 and D1+G overtones but a small modulating bump from 2400 to 3100 cm^{-1}. As in the case of chitosan-based carbon, by considering the positions of the G and D1 band and the I_{D1}/I_G intensity ratio the agarose-based carbons can be placed between the first and the second stage of the amorphous trajectory prosed by Ferrari et al. (see section 2.9). Since it is not possible to attribute a specific stage, both the Tuinstra-Koening (TK) and the Ferrari-Robertson (FR) formula (see section 2.9) were applied to calculate L_a. The TK gives values between 4.78 and 5.22 nm whereas the FR values between 1.24 and 1.29 nm.

5.3.3 Effect of the acid washing on graphitization

Figure 78 depicts the comparison between the washed (red) and unwashed (blue) of agarose and chitosan-based carbon mixed with $FeCl_2$ or $Fe(NO_3)_3$. It can be noticed that the acid washing does not affect so much the Raman spectrum. Some little differences can be individuated by looking closer in the graph A), where D1 band intensity slightly decreases as shown by the I_{D1}/I_G values which downshifts from 1.03 to 0.99. For instance, the comparison in graph C) shows a little decrease of 2D1 intensity band, as confirmed in the Table 10. Since the 2D1 band is sensitive to the ordered stacking of graphite sheets, a decrease of the intensity of this band may be due to a loss of the order of the stacking of graphite sheets caused by the acid treatment. The loss of order can be confirmed by the R2 ratio which is lower for Fe_CC10. However, the decrease of I_{2D1}/I_G is very small (only 0.04 in the I_{2D1}/I_G), which means that that the acid treatment selectively removes the iron particle whereas the graphitic shell, which develops around the iron nanoparticle, maintain its integrity. This result has been previously obtained by other authors which found that the acid treatment specifically removes the iron nanoparticles leaving the graphitic shell and thus forming a bamboo like as the structure reported in Figure 79 [131]. It can be therefore concluded that the acid washing has almost a negligible effect on the carbon graphitization.

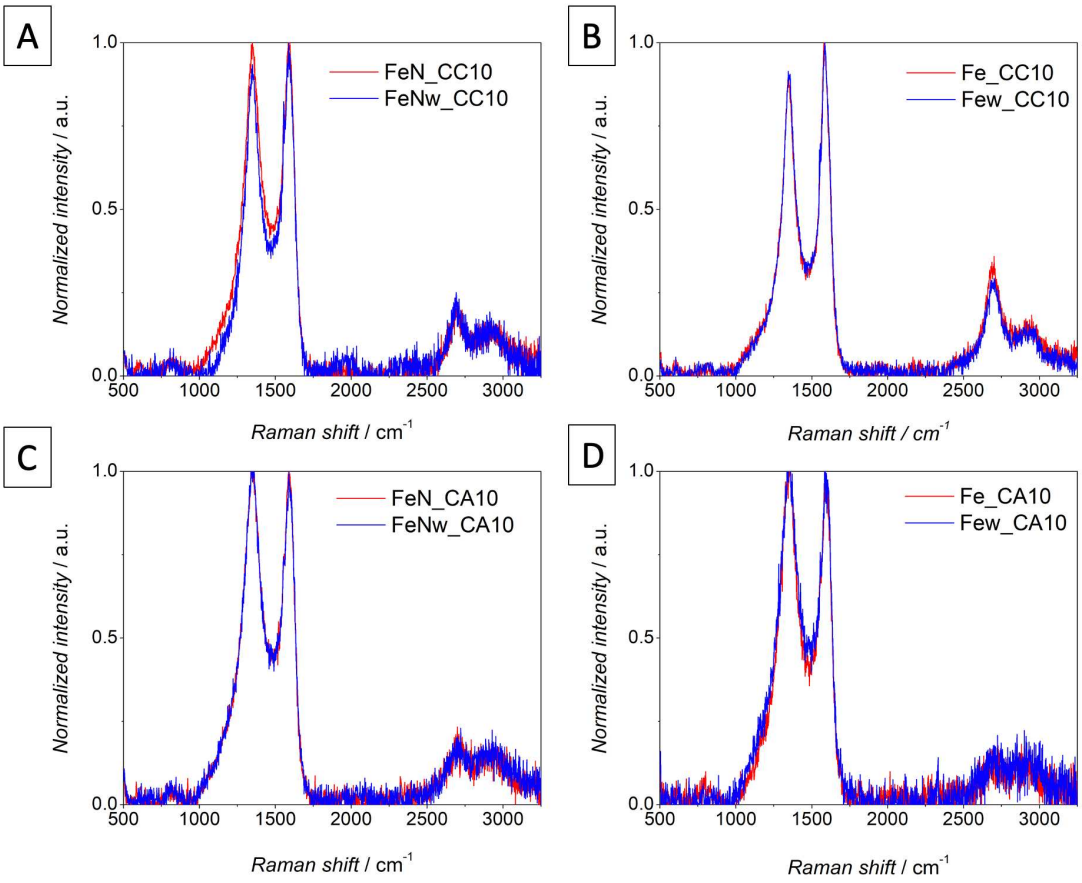

Figure 78. Comparison between washed and unwashed samples: A) FeN_CC10 and FeNw_CC10 spectra; B) Fe_CC10 and Few_CC10; C) FeN_CA10 and FeNw_CA10 and D) Fe_CA10 and Few_CA10

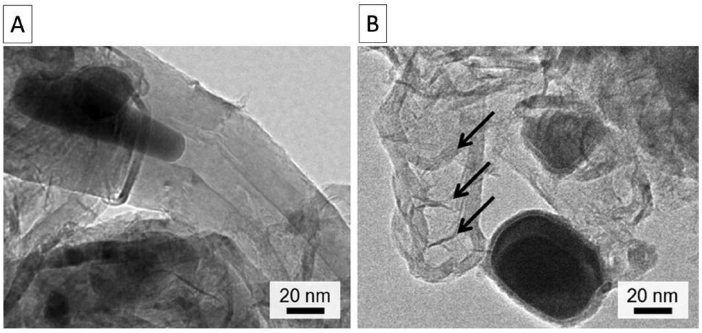

Figure 79. TEM images showing the effect of acid washing. A) Morphology of the sample synthesized according to before acid washing and B) after acid washing. The black arrows mark the presence of graphitic shells. [131].

Table 10. Values of I_{D1}/I_G, I_{D3}/I_G, I_{2D1}/I_G, D3 area, L_a^{TK}, L_a^{FR} and R2 for all the unwashed and washed samples obtained after deconvoluting the first and second order Raman spectra.

	I_{D1}/I_G	I_{D3}/I_G	I_{2D1}/I_G	D3 Area	L_a^{TK} (nm)	L_a^{FR} (nm)	R2
Few_CA10	1.04	0.47	0.11	50.95	4.76	1.30	0.51
Fe_CA10	1.03	0.44	0.10	52.69	4.80	1.29	0.51
FeNw_CA10	0.99	0.44	0.17	45.84	4.99	1.27	0.50
Fe_CA10	1.03	0.44	0.10	52.69	4.80	1.29	0.51
Few_CC10	0.91	0.18	0.28	19.92	5.42	1.21	0.48
Fe_CC10	0.87	0.17	0.32	19.30	5.71	1.18	0.46
FeNw_CC10	0.94	0.40	0.18	45.74	5.30	1.23	0.48
FeN_CC10	0.94	0.43	0.16	46.81	5.28	1.23	0.48

5.3.4 Summary

After commenting the Raman and BET results, Few_CC10, which was synthesized by mixing CC4 with $FeCl_2$, treated at 1050 °C and finally washed with H_2SO_4, is the most suitable carbon for catalytic purposes since it meets all the requirements needed for a stable catalytic support on which the nanoparticles of CeO_2 and Pt can be nucleate:

- sufficiently high surface area of 214 $m^2\ g^{-1}$, which approaches that of VulcanXC72 (256 $m^2\ g^{-1}$) [132];
- a high volume of mesopores of 0.261 $cm^3\ g^{-1}$, which contributes for 50 % to the total pore volume (0.561 $cm^3\ g^{-1}$) and provide a better nucleation of ceria and platinum nanoparticles compared to micropores;
- high degree of graphitization provided by an intense 2D with I_{2D1}/I_G = 0.28 almost similar to that of multiwalled carbon nanotubes [133], which are widely used as durable carbon supports for stabilizing ceria and platinum nanoparticles.

Therefore, Few_CC10 was chosen as a support for the deposition of ceria and platinum nanoparticles and the electrochemical performance of the final catalyst was compared to that of Vulcan XC72. At this purpose, Few_CA10 was used for further comparison aiming to highlight the influence of the chemical and morphological properties on electrochemical behavior. Henceforth, the names Few_CC10 and Few_CA10 were abbreviated as CC and CA, respectively.

5.4 CERIA DEPOSITION

After discussing the morphological properties of the synthesized carbon supports, the subsequent sections deal with the characterization attesting the successful deposition of ceria and platinum on commercial and home-made supports. Sections 5.4.1 and 5.4.2 report the XRD and Raman spectra of the composite obtained after depositing ceria on carbon Vulcan XC72 by varying temperature (750 or 950 °C) and dwelling time (15 or 30 min) at 750 °C.

5.4.1 XRD analysis

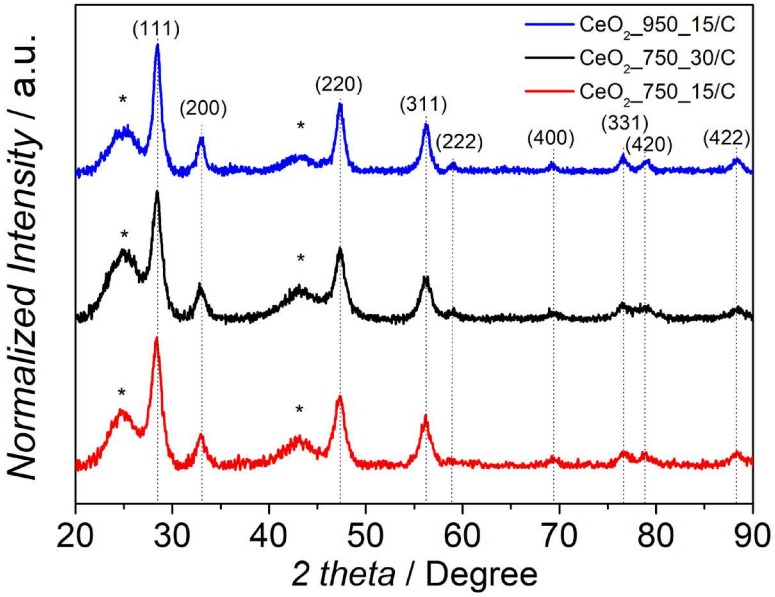

Figure 80. XRD spectra of CeO_2_750_15/C, CeO_2_750_30/C and CeO_2_950_15/C with the Miller indexes of ceria crystallographic planes. The peaks identified by star at 25 ° and 43.1 ° refer to the carbon support (002) and (101) reflections respectively.

XRD spectra were performed with the aim of evaluating the crystallographic properties of ceria deposited on carbon, in particular the crystallite size. Figure 80 compares the CeO_2 on carbon Vulcan XC72 samples synthetized at 750 °C (15 or 30 minutes of dwelling) with the sample kept for 15 minutes at 950 °C.

The reflections at 28.4, 33, 47.5, 56.3, 59.1, 69.4, 76.7, 79.1 and 87.9 ° indicate the presence of CeO_2 with a face-centered-cubic structure with Miller indices of (111), (200), (220), (311), (222), (400), (331), (420), (422) respectively. The peaks appearing at 25 ° and 43.1 ° correspond to the (002) and (101) crystallographic planes of the carbon support [134].

By observing the diffraction spectra, it is possible to notice that there is no shift of peaks, which means that no changes in the crystallographic interplanar distance occur by varying the used conditions for the solid-state synthesis. It is worthy to remind that the intensity is strictly correlated to the full width at half maximum of the peak (FWHM). A more intense peak results from a smaller FWHM. In Figure 80, the temperature seems to have a visible effect on the FWHM. The sample synthesized at 950 °C shows more sharp and intense peaks with respect to the other samples. This

means that the FWHM is smaller, and this is indicative of crystallite with higher dimensions. By exploiting the Sherrer's equation it is possible to obtain the crystallite dimensions from the FWHM as explained in section 2.5. The average crystallite size of the synthesized samples was determined by calculating the arithmetic average of the crystallite size obtained from the most intense peaks (111), (220) and (311). CeO_2_950_15/C has an average crystallite size of 9.3 ± 0.6 nm, which is ca. 3 nm larger than CeO_2_750_15/C (whose average crystallite size is 5.9 ± 0.3 nm). By comparing the samples synthesized at 750 °C but with two different dwelling time, the average crystallite size of CeO_2_750_30/C and CeO_2_750_15/C results to be 6.8 ± 0.2 nm and 5.9 ± 0.3 nm, respectively. Hence, a little influence of the dwelling time on the crystal growth is observable.

As a result, it can be concluded that both temperature and dwelling time are variables that affect the ceria deposition from the crystallographic point of view by leading to the nucleation of crystallite having dimensions which increase with time and temperature.

5.4.2 Raman analysis

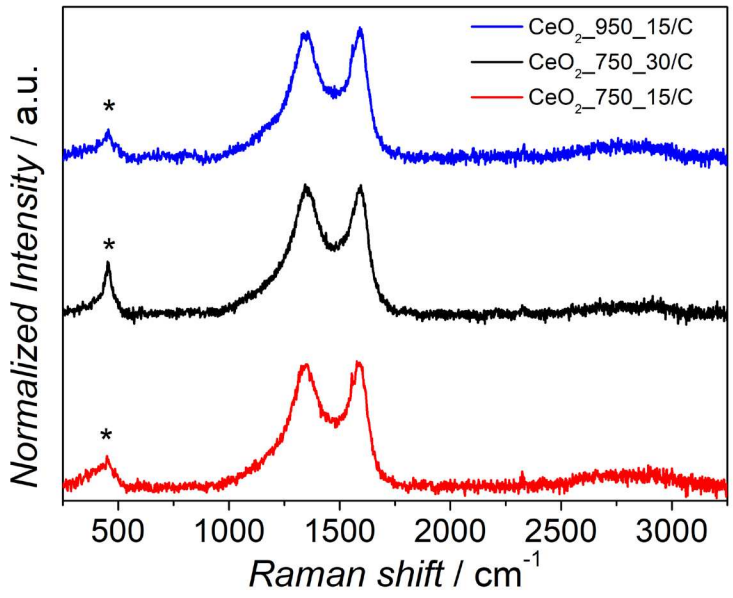

Figure 81. Raman spectra of CeO_2_750_15/C, CeO_2_750_30/C and CeO_2_950_15/C.

Moving to the Raman spectrum of the ceria on Vulcan XC72 samples synthetized by solid-state approach, displayed in Figure 81, it is possible to observe the D1 and G bands of the carbon support at 1350 and 1600 cm^{-1} respectively and an additional less intense peak marked with a star at 450 cm^{-1} ca. relates to the F_{2g} vibrational mode of the cubic fluoritic lattice of ceria, as discussed in section 2.9.

Usually, the F_{2g} peak for bulk ceria is placed at 460 cm^{-1} whereas those reported in these spectra results to be shifted to 451 and 453 cm^{-1}. The presence of broadness along with a red-shift of the bulk CeO_2 peak are size-dependent phenomena, which could be ascribed to the inhomogeneous strain

broadening related to crystallite mean size and to phonon confinement. The strong asymmetry of the F_{2g} band can be due to the distortion in the ceria lattice, as well [135].

The ceria peak at 450 cm^{-1} is more intense for CeO_2_750_30/C compared to that observed for CeO_2_950_15/C and CeO_2_750_15/C. As already mentioned in section 2.9, Graham et al. found a relationship between the half-width peak at 450 cm^{-1} of the Raman spectra of ceria and the crystallite size obtained from the XRD analysis [90]. If the crystallite size decreases the ceria peak becomes broader. For the shown spectra it was not possible to fit the peak at 450 cm^{-1} owing to its asymmetrical shape and low intensity. Therefore, it was not possible to extrapolate the crystallite size value by the linear trend proposed by Graham. By considering the difference in the broadness (and intensity) of the ceria peak among the three samples, i.e. CeO_2_750_30/C, CeO_2_950_15/C and CeO_2_750_15/C, and by comparing this observation with the XRD results, it cannot be concluded that the crystallite size of ceria is the factor affecting the broadness of Raman peak. In fact, the trend observed for the broadness of ceria Raman peak is not coherent with the results obtained with XRD, according to which an increase of time and temperature lead to a decrease of the half-width peak and therefore larger crystallites. It might be possible that the difference of the intensity between the CeO_2_750_30/C and the CeO_2_750_15/C is due to a different amount of the deposited ceria on the samples. However, this hypothesis cannot be confirmed since any quantitative analysis of the ceria content was done.

5.5 PLATINUM DEPOSITION

Sections 5.5.1, 5.5.2 and 5.5.3 show the results of the ICP-MS, XRD and TEM characterizations confirming the successful deposition of platinum on ceria/carbon hybrid supports obtained after depositing ceria via solid-state approach or by mixing ceria with carbon as described in section 4.2.2.

5.5.1 ICP-MS results

In Table 11 the quantitative analysis results of the Pt and Ce content in $Pt/CeO_2/C$ samples are compared with the supposed theoretical value.

Table 11. Theoretical and experimental platinum and ceria content obtained by ICP-MS analysis. Reduction yield was calculated by using the equation (5.1).

	Pt_{ICP-MS}	Pt_{theor}	Ce_{ICP-MS}	Ce_{theor}	*Reduction Yield*
	wt%	wt%	wt%	wt%	%
Pt/CeO2_950_15/C	22	25	3.1	4	88
Pt_3h/CeO2/C	23.6	25	3	4	94
Pt_3h/CeO2/CC	21.5	25	2.2	4	86
Pt/CeO2_750_15/C	22.9	25	3.3	4	92

The values obtained thanks to ICP-MS analysis are quite similar to those expected. In this thesis, the platinum deposition on carbon was performed by reducing $Pt(acac)_2$ to Pt at 300 °C for 3 h. According to B.J. Levecque, who performed the same solid-state reduction under similar conditions (i.e. 350 °C, 2h), it is possible to estimate the yield of the reduction process by calculating the ratio (5.1) between the empirical value of Pt content and the theoretical one [136]:

$$Reduction\ Yield = \frac{Pt_{ICP-MS}}{Pt_{theor.}} \qquad (5.1)$$

The yield values range between 88 and 94 %, which means that the solid-state reduction was successful. The remaining Pt could have been deposited on the furnace wall [136].

5.5.2 XRD spectra

The crystallinity of platinum strongly determines the electrochemical behavior of a Pt/C catalyst. In fact, as already mentioned, the intensity of the hydrogen adsorption and desorption peaks depend on the crystallinity of the sample. The higher the latter the more intense the corresponding peaks. Moreover, both the activity and stability are also influenced. The stability of a highly crystallographic sample is larger than an amorphous one. As regards the activity, the dimension of crystallites has a strongly impact on the activity similarly to that explained for nanoparticles size. The smaller the crystallites the higher will be the resultant activity. The technique which allows to determine the crystallography of platinum is XRD. In this section the impact of the ceria deposited by solid-state approach on platinum deposition, the effect of the different carbon support and the effect of the reduction time for platinum deposition will be analyzed.

5.5.2.1 Effect of ceria deposition

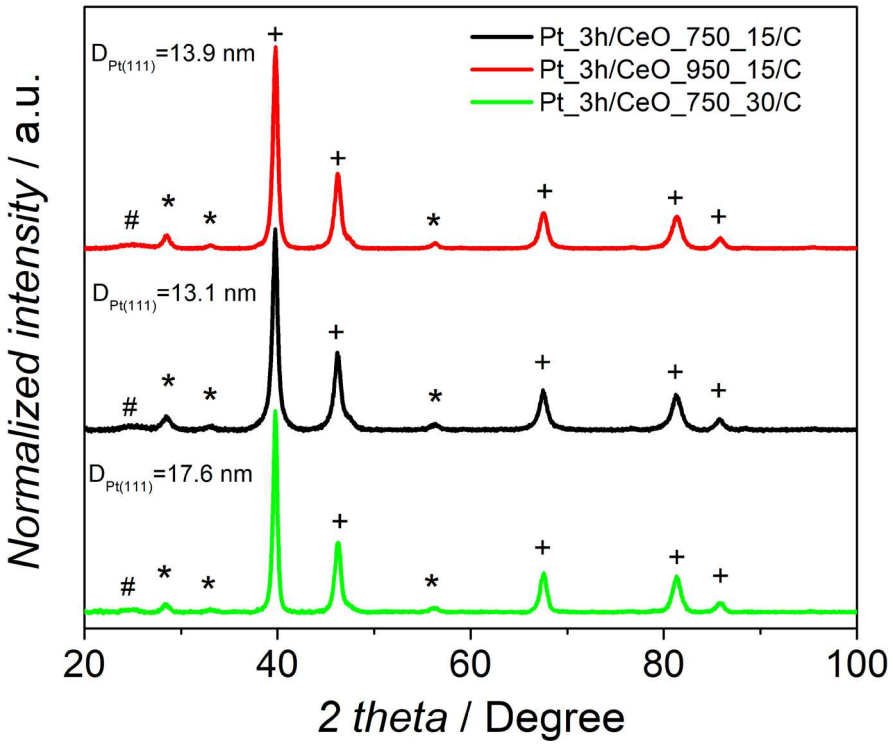

*Figure 82. XRD spectra of Pt_3h/CeO_2_750_30/C, Pt_3h/CeO_2_750_15/C and Pt_3h/CeO_2_950_15/C with the respective crystallite dimension of Platinum (111) facets. The + symbols refer to the platinum peaks, the * are related to ceria and finally # is associated to the broad peak of (002) graphite peak.*

Table 12. Peak center position of the reflection (111), (200), (220), (311) and (222) belonging to platinum (on left) and ceria (311), (200), (111) reflections (on right) as determined from the XRD spectra.

Pt	x_c	**CeO_2**	x_c
	°		°
(111)	39.7	**(311)**	28.4
(200)	46.2	**(200)**	32.8
(220)	67.4	**(111)**	56.0
(311)	81.4		
(222)	85.8		

Figure 82 compares the XRD spectra recorded for the Vulcan XC72 samples on which ceria was deposited with different temperature, i.e. 750 °C or 950 °C, and dwelling time, i.e. 15 or 30 minutes, whereas platinum was deposited maintaining the very same conditions (i.e. 3 h at 300°C). The presence of the metal is confirmed by the intense peaks marked by + at 39.7, 46.2, 67.4, 81.4 and 85.8 °, corresponding to the respective reflections (111), (200), (220), (311) and (222) which are consistent with a face cubic center structure of platinum [137]. Meanwhile, the less intense peaks at 28.4, 33, 56.3 ° marked by * are related to the corresponding (111), (200), (311) reflections of CeO_2. Additionally, the platinum (200) peak at 46.2 2 theta presents a shoulder which surely arises from the superimposition with the (220) reflection of ceria at 47.5 ° visible in the XRD spectra of the respective sample without Pt (see section 5.4.1). A broad peak appearing at ca. 25 ° refers to the reflection of

(002) peak of carbon Vulcan XC72 support. The broadness of the peak is a clear confirmation that Vulcan XC72 is an amorphous carbon [138]. The elevated intensity of platinum peaks proves that the platinum deposited is highly crystalline and the crystallites are quite large, as clearly observable by the crystallite size reported in Figure 82 obtained from the half width peak of (111) reflection. Pt_3h/CeO_2_750_30/C exhibits the largest crystallite size, i.e. 17.6 nm, which is much higher than those of the two other sample, i.e. 13.1 nm for Pt_3h/CeO_2_750_15/C and 13.9 nm for Pt_3h/CeO_2_950_15/C. This huge difference could be attributed by the higher dimension of ceria nanoparticles deposited at high temperature which is expected to stabilize Pt particles of bigger dimensions.

5.5.2.2 Effect of the different carbon support

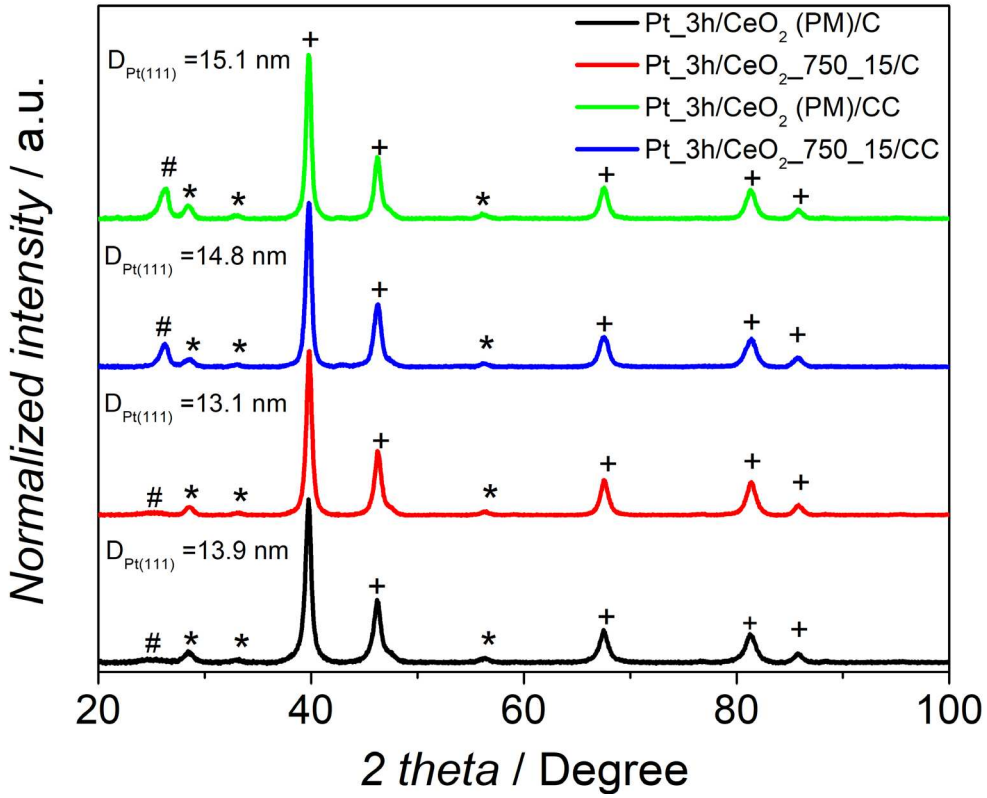

*Figure 83. XRD spectra of Pt_3h/CeO_2_750_15/C, Pt_3h/CeO_2_750_15/CC, Pt_3h/CeO_2(PM)/C and Pt_3h/CeO_2(PM)/CC with the respective crystallite dimension of Platinum (111) facets. The + symbols refer to the platinum peaks, the * are related to ceria and finally # is associated to the broad peak of (002) graphite peak.*

The purpose of Figure 83 is comparing the effect of the carbon support (Vulcan XC72 and Few_CC10 abbreviated as CC) and ceria types (home-made and commercial, Particular Materials) on platinum deposition. The appearance of an intense peak at 26.2 °, referred to the (002) reflection of carbon, distinguish the catalysts where CC is present as a carbon support from those where Vulcan XC72 is used as support. The elevated intensity of (002) peak is a further confirmation of the high graphitization degree of the most graphitized sample, i.e. Few_CC10, here abbreviated as CC. The graphitic crystallites have a size of 9.44 and 9.77 nm in Pt_3h/CeO_2(PM)/CC and

Pt_3h/CeO_2_750_15/CC, respectively which is higher, but fairly consistent, than that determined by Tuinstra-Koening equation in the Raman section, i.e. 5.76 nm, for Few_CC10. Anyway, the platinum crystallite size ($D_{Pt(111)}$) is larger for the samples where CC is adopted as support, 15.1 nm and 14.82 nm for Pt_3h/CeO_2(PM)/CC and Pt_3h/CeO_2_750_15/CC, respectively if compared to 13.87 nm and 13.09 nm for Pt_3h/CeO_2(PM)/C and Pt_3h/CeO_2_750_15/C, respectively (samples containing Vulcan XC72). This could be attributed to the higher graphitization of chitosan-based carbon which can induce a less nucleation of nanoparticles. Therefore, few nuclei grow giving rise to the formation of larger crystallites with dimensions higher than 15 nm.

As regards the different type of ceria (home-made and PM) the crystallite size was estimated by the FHWM of (111) reflection at 28.4 °. The crystallites of PM ceria are larger than those of ceria deposited at 750 °C for both chitosan and Vulcan XC72 support, as reported in Table 13. As regards the Vulcan XC72-based sample, it can be observed that as the ceria crystallite increases, the platinum crystallite increases, as well. Therefore, a possible effect of ceria could be considered. However, for chitosan-based samples this effect is much less pronounced, since the platinum crystallite size do not exhibit a high increase at the growing of ceria crystallite size, as it was in the case of VulcanXC72. This observation leads to conclude that ceria has a less pronounced effect with respect to that of the carbon support on the platinum crystallite size (maybe because the loading of ceria is very low, 5 wt%).

Table 13. Crystallite size of ceria and platinum determined from (111) peaks of ceria and platinum by Scherrer's equation.

	$D_{CeO2(111)}$	$D_{Pt(111)}$
	nm	nm
Pt_3h /CeO_2_750_15 / CC	8.5	14.8
Pt_3h / CeO_2(PM)/CC	11.1	15.1
Pt_3h / CeO_2 (PM)/ C 3h	11.0	13.8
Pt_3h /CeO_2_750_15 / C	8.7	13.1

5.5.2.3 Effect of the time deposition of platinum

Since the crystallite size obtained from XRD spectra is very high compared to those required for catalytic purposes [139], some attempts of decreasing platinum crystallite size were performed by lowering the dwelling time from 3 h, to 1 h or even 30 min at the deposition temperature (300 °C). Therefore, Vulcan XC72 was mixed with ceria of Particular Materials as described in section 4.2.2 and subsequently platinum was deposited at 300 °C maintained for 1 h or 30 min instead of 3 h, and the obtained samples were named as Pt_1h/CeO_2(PM)/C and Pt_0.5h/CeO_2(PM)/C, respectively. The XRD of these samples were acquired and compared in Figure 84 with the sample prepared by following the same procedure but with a 3 h of deposition, i.e. Pt_3h/CeO_2(PM)/C.

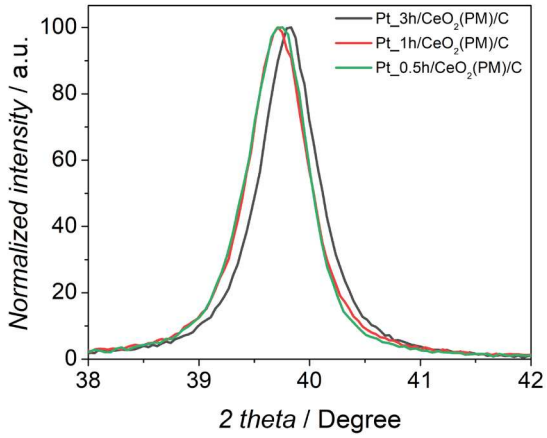

Figure 84. Graph comparing the (111) peak of the XRD spectra for the samples prepared by varying the time deposition, i.e. Pt_3h/CeO_2(PM)/C, Pt_1h/CeO_2(PM)/C and Pt_0.5h/CeO_2(PM)/C.

Table 14. Peak center of (111) peak (x_c), the (111) crystallite size (D_{111}) and the respective interplanar distance (d_{Pt111}).

	x_c	$D_{Pt(111)}$	$d_{Pt(111)}$ spacing
	°	nm	Ang.
Pt_3h/CeO_2(PM)/C	39.81	13.8	2.406
Pt_1h/CeO_2(PM)/C	39.71	13.4	2.411
Pt_0.5h/CeO_2(PM)/C	39.71	13.2	2.411

It was expected that by lowering the deposition time the crystallite size decreases. Nevertheless, a reduction of time deposition does not lead to a sensitive decrease of crystallite dimension, which remains almost unaltered: 13.8 nm for Pt_3h/CeO_2(PM)/C, 13.4 and 13.2 nm for Pt_1h/CeO_2(PM)/C and Pt_0.5h/CeO_2(PM)/C, respectively. Instead, an interesting effect was the slight shift of 0.1 ° for the (111) reflection belonging to Pt_1h/CeO_2(PM)/C and Pt_0.5h/CeO_2(PM)/C towards lower diffraction angles. This shift is associated with a little strain effect of crystallographic planes (as confirmed from the data reported in Table 14) which are more distanced for the samples on which platinum was deposited at 1 h and 0.5 h. Instead, by varying time from 1 h and 0.5 h the interplanar distance for (111) planes remains constant. The data reported in the graph were calculated by using Bragg's law and fixing the diffraction order n at 1.

5.5.3 TEM images

Evaluating the samples morphology is of great importance as the ORR starts with the adsorption of O_2 molecule on the active sites of platinum nanoparticles.

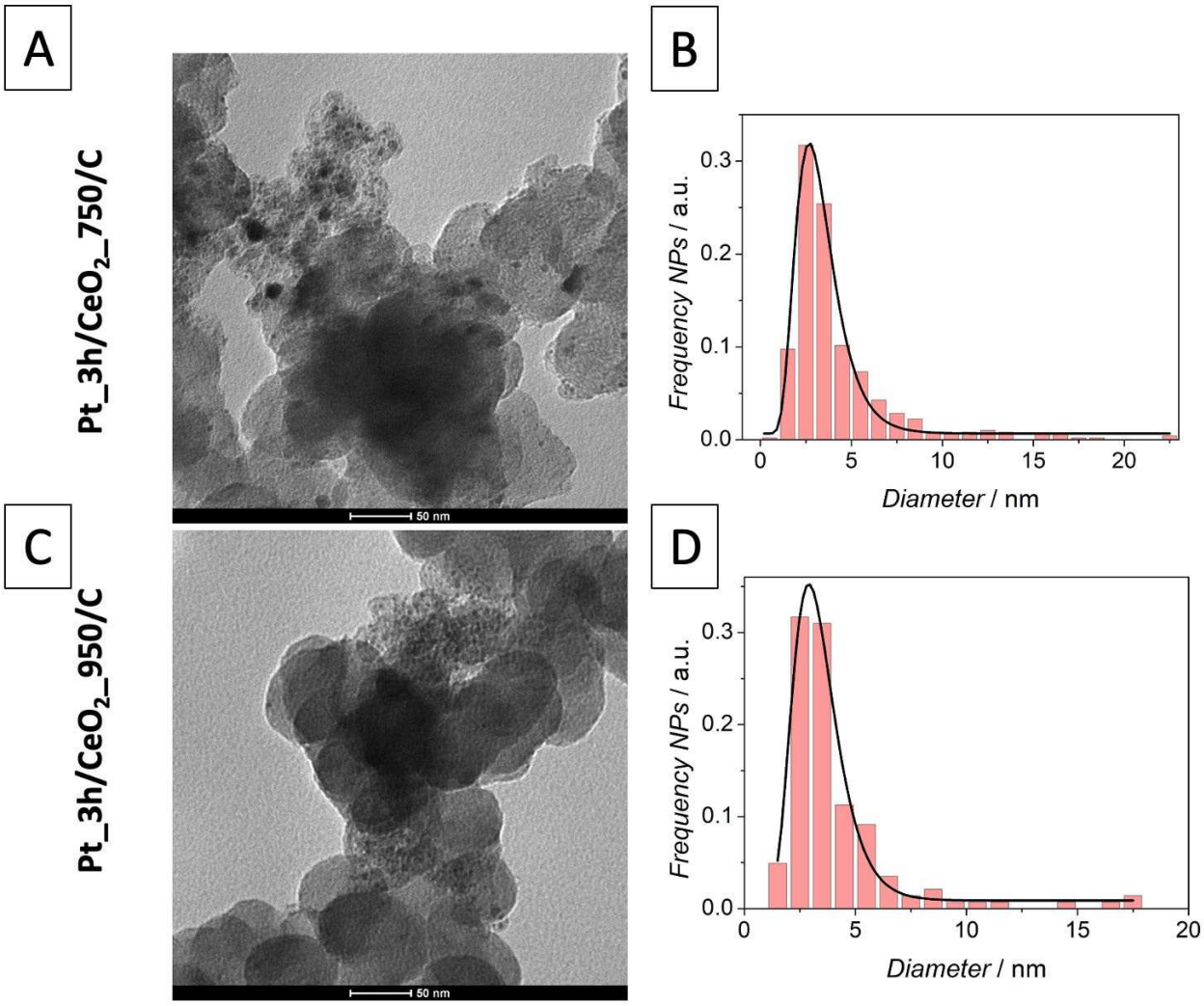

Figure 85. TEM images of A) Pt_3h/CeO_2_750/C and C) Pt_3h/CeO_2_750/C with the respective size distribution B) and D).

In this section the TEM images of Pt/CeO_2_750_15/C and Pt/CeO_2_950_15/C are displayed in Figure 85 A e C. In the case of Pt/CeO_2_750_15/C, numerous small nanoparticles (represented by black dots in the images) are clearly visible and homogeneously distributed throughout the sample. On the contrary, Pt/CeO_2_950_15/C does not show a homogeneous distribution on the sample since the nanoparticles are preferentially localized in some areas whereas other zones do not present nucleated nanoparticles at all. Notwithstanding, the size distribution of the two samples is asymmetric, sharp and centered at similar values for both the samples, i.e. 3.08 ± 0.04 nm for Pt/CeO_2_750_15/C and 3.22 ± 0.05 nm for Pt/CeO_2_950_15/C. On the other hand, some larger nanoparticles, probably resulting from agglomeration/aggregation phenomena, are observed. Nanoparticles exhibit a large variety of shapes, among which spherical, hexagonal, and squared are the most spread.

By considering the high electrondensity of Ce and Pt and the relative low resolution of the images, it is not possible to distinguish between platinum and ceria nanoparticles from the acquired TEM images. Therefore, the size distributions can surely include both platinum and ceria nanoparticles. However, by comparing the amount of Pt and CeO_2 loading (i.e. 25 wt%. and 5 wt%), it is quite obvious that the majority of counted nanoparticles are made of Pt. A clear distinction between Pt and CeO_2 images should be accomplished by a high resolution TEM which allows to recognize the crystallographic planes belonging to platinum or ceria.

Results obtained by TEM analysis seem to contrast with the XRD data since the crystallite size is much larger than the average nanoparticle size. This discrepancy arises from the fact that XRD is a bulk technique giving the average size across an entire sample whereas TEM provides particle size analysis form individual particles observed only in localized area where the images are obtained [140].

6 ELECTROCHEMICAL PERFORMANCE FOR OXYGEN REDUCTION REACTION

The last two chapter of the thesis deal with the electrochemical performance determined via RDE and GDE techniques. In this chapter the electrochemical behavior and the activity of the synthesized catalysts determined by cyclic voltammetry in Ar saturated solution at 50 mV s^{-1} and linear sweep voltammetry (LSV) recorded at 1600 rpm and 50 mV s^{-1} will be discussed. Since this thesis is focused on ceria, first of all, the influence of a little amount of ceria (5 wt%) on the electrochemical behavior of a Pt/C commercial standard containing up to Pt 30 wt% will be investigated. Then the discussion moves to the comparison between the intrinsic activity of ceria and platinum. Afterwards, the effects of the parameters used for depositing platinum and ceria will be considered. For platinum, a comparison of the catalytic performance obtaining by varying platinum time deposition in solid state synthesis and in a reduction atmosphere, i.e. 3, 1, 0.5 h, will be shown. While for ceria deposition, the effect of temperature deposition, i.e. 750 and 950 °C will be discussed (the influence of time will be reported in chapter 7). It will be also discussed the influence of other factors such as the type of support (Vulcan, chitosan-based, agarose-based carbon) and the ceria deposited (home-made and that of Particular Materials) on the activity of the synthesized catalysts. The chapter will end with the comparison between the most active catalyst synthesized in this work and the Pt/C standard used for comparison. The values of kinetic current, mass activity and surface activity determined from LSV were calculated by considering the current density at 0.85 V.

6.1 CERIA ON PLATINUM STANDARD CATALYSTS

In literature the effect of the loading of ceria is not well understood so far. In fact, several works use different amount of the oxide in $Pt/CeO_2/C$ catalysts and therefore is not clear which is the optimal quantity of ceria to achieve the best performance in terms of activity [65], [64], [141]. In this thesis, a low loading of ceria, namely 5 wt%, was adopted since a drastic drop of the electronic conductivity it is expected at higher loading. The addition of ceria on commercial Pt/C standard was conducted by suspending carbon together with ceria in water and sonicating for 6 h. Subsequently, the mixture was dried in oven at 80 °C all night. Once dried, the sample was ground in an agata mortar and afterwards used for the ink preparation following the procedure reported in 3.2.2 section.

6.1.1 Electrochemical surface area

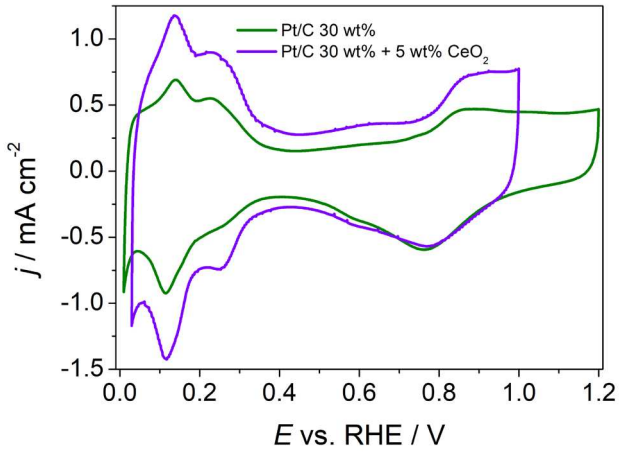

Figure 86. Voltammetry of Pt/C 30 wt% and Pt/C 30 wt%+5 wt% CeO_2 recorded at 50 mV s^{-1} in Ar saturated solution 0.1 M of $HClO_4$. The current density was normalized by the geometrical area of the electrode (0.196 cm^2).

Table 15. EPSA and ECSA values of both adsorption and desorption of hydrogen in the H_{upd} region.

	$EPSA_{ads}$	$EPSA_{des}$	$ECSA_{ads}$	$ECSA_{des}$
	cm^2	cm^2	$m^2\ g^{-1}$	$m^2\ g^{-1}$
Pt/C 30 wt%	2.3 ± 0.1	1.9 ± 0.2	80 ± 5	63 ± 6
Pt/C 30 wt% + 5 wt% Ceria	3.1 ± 0.2	3.0 ±0.2	106 ± 5	103 ± 5

Figure 86 depicts the cyclic voltammetry at 50 mV s^{-1}obtained for standard Pt/C and Pt/C with the addition of 5 wt% of CeO_2. In literature, it has been reported that the presence of an oxide can cause an enhancement on the capacitive current due to the insulant behavior of oxides [142]. Thus, many authors tend to carry out electrochemical experiments where oxides are introduced in Pt/C catalysts in more concentrated solution, such as 1 M of $HClO_4$ or 0.5 M of H_2SO_4 since the higher proton concentration enhances the conductivity of the electrolyte thus decreasing the double layer capacitance [65], [143]. In this thesis 0.1 M solution of $HClO_4$ was employed and as a consequence the effect of the insulant behavior of cerium oxide is clearly more pronounced in the double layer region of the voltammogram (0.3-0.5 V).

Despite that, the peaks of the platinum butterfly related to the adsorption on Pt(111) and Pt(110) surface at 0.250 and 0.115 V vs. RHE respectively and those of desorption on Pt(111) and Pt(110) V vs. RHE at 0.226 and 0.139 V vs. RHE respectively, are still observable, without any peak shift compared to those of Pt/C standard. The electrochemical surface area, obtained after subtracting the capacitive current in the hydrogen underpotential deposition region (H_{upd}), is higher in the case of Pt/C 30 wt% + 5 wt% CeO_2 compared to Pt/C 30 wt%. By reminding that H_2 can be adsorb in different way on the platinum surface, i.e bridge and on top, as seen in 3.1.1.1 section, it might be supposed that ceria could modify the selectivity of the adsorption of hydrogen on the platinum sites favoring the one-to-one type of adsorption (i.e. one atom of platinum adsorb one hydrogen molecule)

compared to the case where ceria is absent. However, this hypothesis does not find any confirmation in literature. The value of $ECSA_{des}$ and $ECSA_{ads}$ are comparable within the error range in the case of Pt/C 30 wt% + 5 wt% CeO_2 and almost similar for the standard but not comparable within the error range.

6.1.2 Catalitic activity vs. the ORR

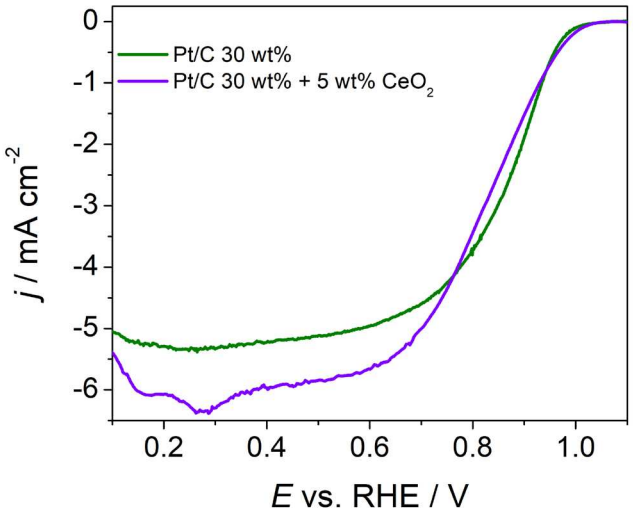

Figure 87. Linear sweep voltammetry of Pt/C 30 wt% and Pt/C 30 wt% +5 wt% CeO_2 recorded at 1600 rpm and 50 mV s^{-1} in O_2 saturated solution, 0.1 M of $HClO_4$. The current density was normalized by the geometrical area of the electrode.

Table 16. LSV results of Pt/C 30%$_w$ and Pt/C 30 wt% +5 wt% CeO_2: limiting current density (j_L) , onset potential(E_{on}), half wave potential($E_{1/2}$) , kinetic current (j_k) determined at 0.85 V, mass activity (MA) determined at 0.85 V and surface activity (SA) determined at 0.85 V.

	j_L	E_{on}	$E_{1/2}$	j_k	*MA*	*SA*
	mA cm^{-2}	V vs. RHE	V vs. RHE	mA cm^{-2}	A g^{-1}	µA cm^{-2}
Pt/C 30 wt%	5.4 ± 0.1	0.958± 0.003	0.90 ± 0.01	5.7 ± 0.2	1940 ± 80	600 ± 70
Pt/C 30 wt% + 5 wt% CeO_2	5.9 ± 0.1	1.008 ± 0.004	0.831 ± 0.004	4.4 ± 0.2	1500 ± 60	290 ±20

Figure 87 compares the LSV recorded at 1600 rpm and 50 mV s^{-1} obtained for the standard Pt/C (30 wt% of Pt) and the standard Pt/C with the addition of 5 wt% of ceria. The activity results to be enhanced in terms of limiting current and onset potential, which are higher for the sample containing ceria. Instead, the half wave potential results to be slightly lower ($\Delta E_{1/2}$ = 39mV) for the sample containing ceria. The presence of a higher E_{on} but a lower $E_{1/2}$ for the sample containing ceria could mean that the kinetic process results to be slowed down for the sample containing ceria since the limiting current reaches a diffusion controlled condition only at less negative potential if compared with Pt/C. Notwithstanding, the higher limiting current observed in the sample containing ceria could be attributed, to an higher intrinsic activity due to the higher availability of oxygen near the platinum active sites probably associated to the high oxygen storage capacity of ceria as reported in literature [64].

6.2 INTRINSIC ACTIVITY OF CERIA

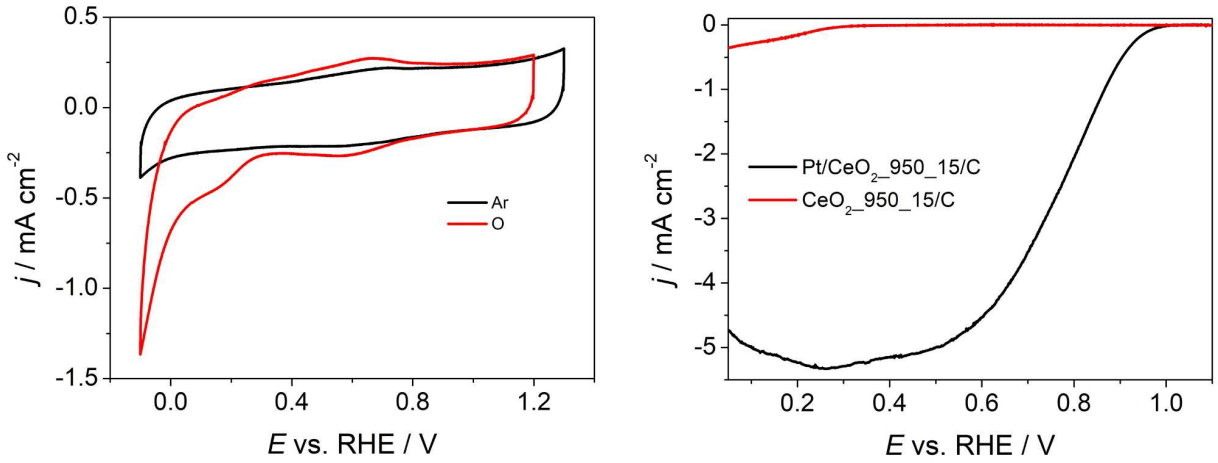

Figure 88. A) Voltammetry of CeO_2 recorded at 200 mV s^{-1} in Ar and O_2 saturated solution respectively. B) Comparison between the linear sweep voltammetry of CeO_2_950_15/C and Pt/CeO_2_950_15/C

The Figure 88A depicts the voltammogram of CeO_2_950_15/C recorded in Ar saturated solution (black line) and O_2 saturated solution (red line) at 200 mV s^{-1} in the potential range of -0.01 – 1.2 V vs. RHE and -0.01 – 1.3 V vs. RHE respectively. The black voltammogram (Ar saturated solution) does not show any peak in the reported potential window, whereas in the red one some peaks are visible at medium potentials (0.6-0.7 V vs. RHE) and at low potentials (< 0.2 V vs. RHE).

The peaks observable at between 0.6 - 0.7 V in the cathodic and anodic scan of the voltammogram acquired in O_2 saturated solutions could be assigned to the quinone/hydroquinone redox couple of the carbon Vulcan XC72 support [144]. The same peaks have been observed in a voltammogram of CeO_2/C recorded at 10 mV s^{-1} in N_2 purged 0.1 M $HClO_4$ solution by G. Sun et al. [144]. The two peaks are visible also in the inert gas purged 0.1 M $HClO_4$ solution, even though to a minor extend.

Another difference between the voltammogram recorded in Ar and O_2 saturated solutions (Figure 88A) is the presence of a broad peak at 0.167 V in the cathodic scan of the red voltammogram, which can be associated with the oxygen reduction reaction. This assignment has not been found in literature but its absence in the Ar purged voltammogram suggests that this peak arises from the oxygen reduction reaction of the CeO_2/C material in solution. However, moving to the LSV carried out on RDE at 1600 rpm and 50 mV s^{-1} (Figure 88B) it is clearly noticeable that CeO_2_950_15/C (red line) does not manifest a catalytic behavior towards the ORR since the developed current is practically negligible with respect to that developed by platinum containing sample (black line).

6.3 EFFECT OF THE Pt REDUCTION TIME ON CeO_2/C SUPPORT CATALYST

In the XRD section it has been discussed the effect of the Pt reduction time on the crystallographic properties of platinum, namely a slight shift for the Pt(111) peak for Pt_1h/CeO_2(PM)/C and compared to Pt_3h/CeO_2(PM)/C and only a little decrease of the crystallite size, i.e. 0.4 nm by switching from 3 to 1 h and 0.6 nm if the time is decreased to 0.5 h. This effect has been associated to the narrowing of the interplanar distance by enhancing the deposition time from 1h to 3h. A comparison will be done in order to see if this strain has an impact or not on the activity.

6.3.1 Cyclic voltammetry in Argon Atmosphere

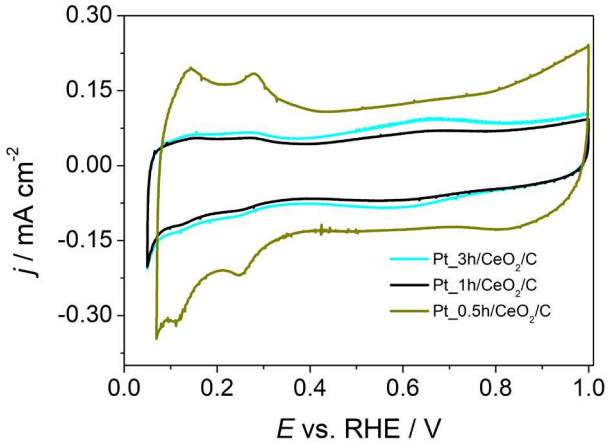

Figure 89. Voltammetry of Pt_3h/CeO_2(PM)/C, Pt_1h/CeO_2(PM)/C and Pt_0.5h/CeO_2(PM)/C recorded at 50 mV s^{-1} in Ar saturated solution 0.1 M of $HClO_4$. The current density was normalized by the geometrical area of the electrode.

Table 17. EPSA and ECSA values of both adsorption and desorption of hydrogen in the H_{upd} region for Pt_0.5h/CeO_2(PM)/C.

	$EPSA_{ads}$	$EPSA_{des}$	$ECSA_{ads}$	$ECSA_{des}$
	cm^2	cm^2	$m^2\ g^{-1}$	$m^2\ g^{-1}$
Pt_0.5h/CeO_2(PM)/C	0.46 ± 0.07	0.30 ± 0.03	16 ± 2	10 ± 1

Figure 89 displays the voltammogram of Pt_3h/CeO_2(PM)/C, Pt_1h/CeO_2(PM)/C and Pt_0.5h/CeO_2(PM)/C recorded in Ar saturated solution of 0.1 M of $HClO_4$. It can be observed that by increasing the deposition time from 30 min to 1 h the capacitive current decreases. Conversely, by switching from 1 to 3 h the capacitive current remains the same all in all and the peaks assigned to the quinone/hydroquinone couple in the range between 0.6 and 0.7 V become more intense. The decreasing of the capacitive current could be related to an increase of the Pt reduction efficiency (more platinum deposited on the surface of the support is supposed to enhance the electronic conductivity). Pt_0.5h/CeO_2(PM)/C presents a sharp hydrogen adsorption and desorption peaks due to the high crystallinity of platinum (confirmed by the XRD spectrum) whereas they are almost no observable in the other samples due to high capacitive current. For Pt_0.5h/CeO_2(PM)/C the value of ECSA and EPSA desorption ($ECSA_{des}$ and $EPSA_{des}$ respectively) reported in Table 17 is larger than that of desorption since the latter present an additional contribution to the area due to the hydrogen

evolution. The ECSA and EPSA results of the other samples was not reported since the values are so low (below 7 m^2 g^{-1} for ECSA and below 0.2 cm^{-2} for EPSA) that they are clearly underestimated with respect the real value by the high capacitive current.

6.3.2 ORR activity

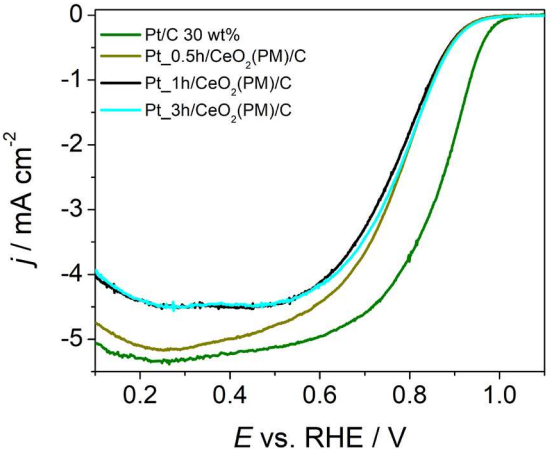

Figure 90. Linear sweep voltammetry of Pt_3h/CeO_2(PM)/C, Pt_1h/CeO_2(PM)/C and Pt_0.5h/CeO_2(PM)/C recorded at 1600 rpm and 50 mV s^{-1} in O_2 saturated solution, 0.1 M of $HClO_4$. The current density was normalized by the geometrical area.

Table 18. LSV results of Pt_3h/CeO_2(PM)/C, Pt_1h/CeO_2(PM)/C and Pt_0.5h/CeO_2(PM)/C: limiting current density (j_L), onset potential (E_{on}), half wave potential ($E_{1/2}$) , kinetic current (j_k) determined at 0.85 V vs. RHE, mass activity (MA) determined at 0.85 V vs. RHE and surface activity (SA) determined at 0.85 V vs. RHE.

	j_L	E_{on}	$E_{1/2}$	j_k	*MA*	*SA*
	mA cm^{-2}	V vs. RHE	V vs. RHE	mA cm^{-2}	A g^{-1}	µA cm^{-2}
Pt_0.5h/CeO_2(PM)/C	5.2 ± 0.09	0.886 ± 0.002	0.775 ± 0.007	1.24 ± 0.07	420 ± 20	820 ± 40
Pt_1h/CeO_2(PM)/C	4.5 ± 0.1	0.943 ± 0.006	0.760 ± 0.02	1.1 ± 0.2	370 ± 80	500 ± 100
Pt_3h/CeO_2(PM)/C	4.4 ± 0.1	0.890 ± 0.009	0.799 ± 0.006	1.4 ± 0.1	470 ± 40	4000 ± 1000

Figure 90 reports the LSV at 1600 rpm and 50 mV s^{-1} obtained after depositing platinum for 0.5, 1, 3 h and Table 18 the data acquired for the standard Pt/C. By considering the LSV trend and the kinetic parameters it is possible to observe that in the kinetic regime Pt_0.5h/CeO_2(PM)/C and Pt_3h/CeO_2(PM)/C show the same performance but at potential below than $E_{1/2}$ Pt_0.5/CeO_2(PM)/C develops highest current at equal potential compared to the other catalysts. In the diffusive regime (below 0.6 V vs. RHE) the limiting current reached for Pt_0.5h/CeO_2(PM)/C is ca. 0.5 mA cm^{-2} larger with respect to the other samples. The highest ORR performance for 0.5 h can be probably related to the smaller crystallites of platinum nanoparticles compared to the other samples containing ceria shown in the graph calculated from the XRD spectra. Notwithstanding, it can be noticed that Pt_0.5/CeO_2(PM)/C reaches the limiting current at lower potential value compared to the other ceria containing catalysts (0.3 V vs. RHE VS ca. 0.5 V vs. RHE) and a formation of a *tilt* can be observed in the potential range of 0.3-0.6 V. This phenomenon has been already detected in ORR LSV measurements at the same rotation rate (i.e. 1600 rpm) and in the same potential range (i.e. 0.3-0.6

V) for Pt supported on defective titania support by Geppert et al. [145]. In their work they deposited platinum nanoparticle by atomic layer deposition on a defective titania film. They prepared different sample by varying the number of cycle of atomic layer deposition (10, 30 and 50 cycles) and they observed the formation of a thin TiO_x film (whose thickness was much smaller compared to that of the support) that they attributed to the strong metal support interaction between the oxide and the metal (Figure 91A).

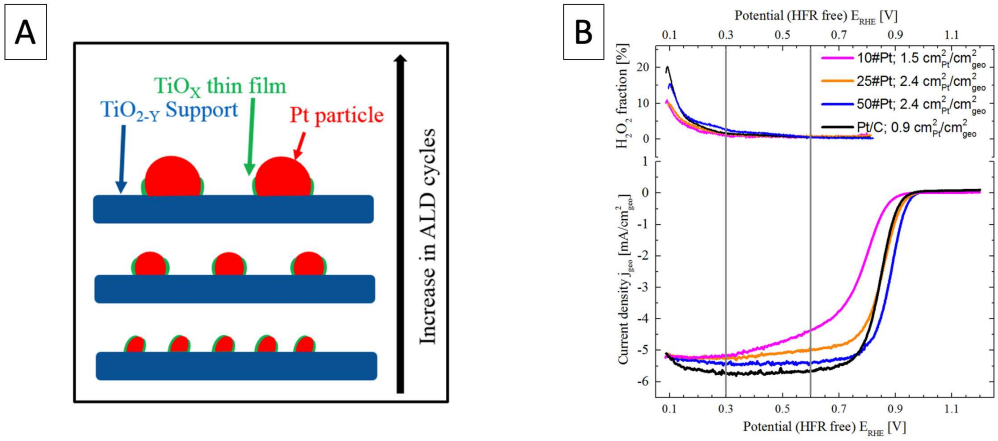

Figure 91. A) From Geppert et al., representation of the Pt nanoparticles deposited on a defective titania substrate (TiO_{2-y}) by atomic layer deposition (ALD) by varying number of cycles, i.e. 10, 25 and 50 cycles. It is highlighted the influence of the number of cycles on platinum nanoparticles size and the formation of a thin film partially covering nanoparticles especially the smallest ones. B) LSV results obtaining via RRDE by Geppert al. for 10#Pt (10 cycles of deposition), 25#Pt (25 cycles of deposition) and 50#Pt cycles of deposition (50 cycles of deposition).

This film covered the active sites of platinum especially at low number of cycles whereas at high ALD cycles the Pt nanoparticle increase in size and the fraction of the uncovered platinum atoms increases. The formation of this film covering the platinum active sites hindered the access of oxygenated species of the ORR from to/from the platinum surface and therefore led to the appearance of a tilted polarization curve (as shown in Figure 91B) due to the poor reactant accessibility to active sites (and not to the formation of hydrogen peroxide that they initially had supposed in the article) [145]. In this thesis, a defective oxide (i.e. ceria) was mixed with carbon. Thus, a comparison with the mentioned study can be done by hypothesizing that, during the heat treatment employed for platinum deposition, the high temperature activated the diffusion of cerium and oxygen atoms, which could probably lead to the formation of an oxide thin film partially covering the platinum nanoparticle surface. The formation of this hypothetical thin oxide film, arising from the strong metal support interaction, could have affected the electrochemical performance by generating the *tilt* visible for Pt_0.5/CeO_2(PM)/C caused by limited accessibility of oxygenated species to the active sites of platinum surface. Anyway, the comparison with the LSV of Pt/C standard shows that the electrochemical performance of the catalysts depicted in Figure 90 does not reach that of Pt/C standard due to the limited ORR kinetics provided by these catalysts.

6.4 EFFECT OF THE TEMPERATURE DEPOSITION OF CERIA

6.4.1 Cyclic voltammetry in Argon Atmosphere

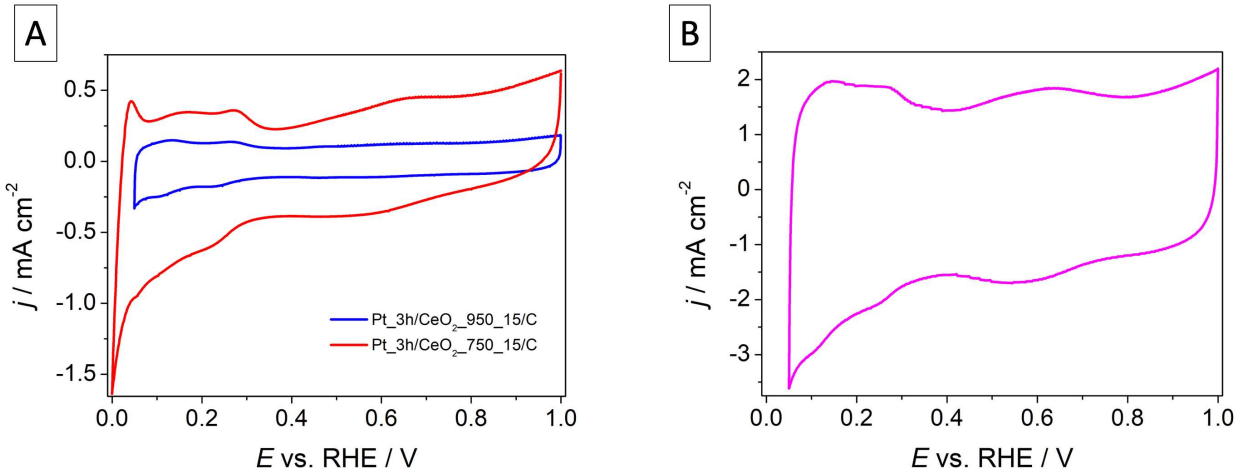

Figure 92.A) Voltammetry of Pt_3h/CeO₂_750_15/C, Pt_3h/CeO₂_950_15/C and B) Pt_3h/CeO₂_750_15/CC recorded at 50 mV s^{-1} in Ar saturated solution 0.1 M of $HClO_4$. The current density was normalized by the geometrical area of the electrode.

Table 19.EPSA and ECSA values of both adsorption and desorption of hydrogen in the H_{upd} region of Pt_3h/CeO₂_750_15/C and Pt_3h/CeO₂_750_15/CC.

	$EPSA_{ads}$	$EPSA_{des}$	$ECSA_{ads}$	$ECSA_{des}$
	cm^2	cm^2	$m^2\ g^{-1}$	$m^2\ g^{-1}$
Pt_3h/CeO₂_750_15/CC	1.90 ± 0.05	1.7 ± 0.2	65 ± 2	59 ± 5
Pt_3h/CeO₂_750_15/C	2.3 ± 0.1	0.62 ± 0.08	126 ± 7	33 ± 2
Pt_3h/CeO₂_950_15/C	0.432 ± 006	0.181 ± 0.006	14.70 ± 0.02	6.2 ± 0.2

The effect of ceria temperature deposition on electrochemical properties of Pt/CeO₂/C catalysts is reported in Figure 92A where Pt_3h/CeO₂_750_15/C and Pt/CeO₂_950_15/C voltammograms on Ar saturated solution are compared. Noticeably, the capacitive current of Pt_3h/CeO₂_750_15/C is higher but focusing on the ECSA values of hydrogen adsorption and desorption in the H_{upd} region the values of Pt_3h/CeO₂_750_15/C are much larger compared to those obtained for Pt/CeO₂_950_15/C (one order of magnitude) as shown in Table 19. In the case of Pt_3h/CeO₂_750_15/C, the huge difference between the adsorption and desorption is related to the contribution of hydrogen evolution discharge at 0 V vs. RHE. This explains the higher value obtained for $ECSA_{ads}$ and $EPSA_{ads}$ with respect to $ECSA_{des}$ and $EPSA_{des}$. $ECSA_{des}$ and $EPSA_{des}$ of Pt_3h/CeO₂_750_15/C remain lower than those of the standard Pt/C due to the high capacitive current induced by the presence of the oxide (compare Table 15). Compared to the other samples, Pt/CeO₂_950_15/C exhibit much lower values of ECSA and EPSA especially for desorption, whose value is probably underestimated by the high capacitive current. Anyway, the difference of ECSA values for Pt_3h/CeO₂_750_15/C and Pt/CeO₂_950_15/C could be explained by the observation done for the TEM images (section 5.5.3), which show a bad dispersion of platinum nanoparticles together with the presence of large agglomerates for Pt/CeO₂_950_15/C. Since ECSA and EPSA are related to surface active area, a

sample with a higher active surface is likely to perform better in electrocatalytic reactions. Therefore, 750 °C was chosen as the optimal temperature for depositing ceria on the home-made chitosan-derived carbon, whose voltammetry is depicted separately in Figure 92B since it exhibit a high capacitive current but an appreciable high ECSA for both adsorption and desorption (64.52 m^2 g^{-1} and 58.94 m^2 g^{-1} respectively), which is not so far from those values determined for standard Pt/C as reported in Table 15.

6.4.2 ORR activity

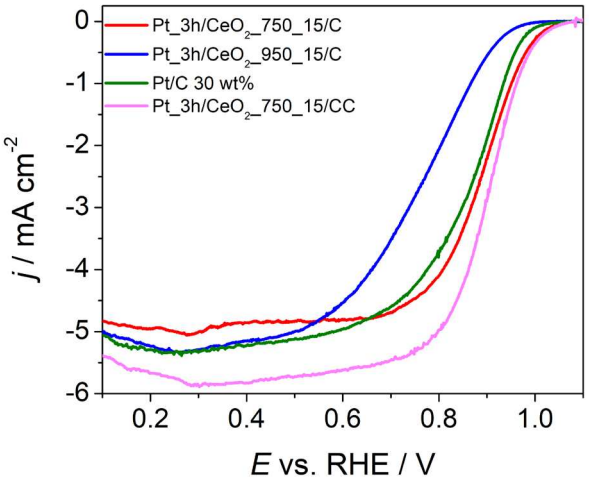

Figure 93. Linear sweep voltammetry of Pt_3h/CeO_2_750_15/C, Pt_3h/CeO_2_950_15/C and Pt_3h/CeO_2_750_15/CC recorded at 1600 rpm and 50 mV s^{-1} in O_2 saturated solution, 0.1 M of $HClO_4$. The current density was normalized by the geometrical area.

Table 20. LSV results of Pt_3h/CeO_2_750_15/C, Pt_3h/CeO_2_950_15/C and Pt_3h/CeO_2_750_15/CC limiting current density (j_L), onset potential (E_{on}), half wave potential ($E_{1/2}$), kinetic current (j_k) determined at 0.85 V vs. RHE, mass activity (MA) determined at 0.85 V vs. RHE and surface activity (SA) determined at 0.85 V vs. RHE.

	j_L	E_{on}	$E_{1/2}$	j_k	*MA*	*SA*
	mA cm^{-2}	V vs. RHE	V vs. RHE	mA cm^{-2}	A g^{-1}	µA cm^{-2}
Pt/C 30%w	5.4 ± 0.1	0.958 ± 0.003	0.90 ± 0.01	5.7 ± 0.2	1940 ± 80	600 ± 70
Pt_3h/CeO_2_750_15/CC	6.0 ± 0.1	1.10 ± 0.01	0.90 ± 0.003	15.2 ± 0.9	5200 ± 300	1720 ± 60
Pt_3h/CeO_2_750_15/C	4.84 ± 0.08	1.032 ± 0.002	0.889 ± 0.003	10.7 ± 0.4	1190 ± 40	1500 ± 80
Pt_3h/CeO_2_950_15/C	5.36 ± 0.04	0.757 ± 0.001	0.963 ± 0.001	1.58 ± 0.01	119.5 ± 0.6	100 ± 1

The influence of the deposition temperature of ceria on the electrochemical performance is analyzed in the graph of Figure 93. By focusing on Pt_3h/CeO_2_750_15/C and Pt/CeO_2_950_15/C, it is clearly observable that the variation in temperature strongly affects the activity in terms of onset potential and half wave potential. The half wave potential of Pt_3h/CeO_2_750_15/C is extremely higher than that of Pt_3h/CeO_2_950_15/C (0.889 V vs. RHE against 0.757 V vs. RHE) and the same can be stated for the onset potential (1.032 V vs. RHE and 0.963 V vs. RHE). Similar consideration can be done by watching the j_k, *MA* and *SA* values of Pt_3h/CeO_2_750_15/C, which are practically one order of magnitude higher compared to those of Pt_3h/CeO_2_950_15/C. By considering the result obtained from TEM, the lower activity of Pt_3h/CeO_2_950_15/C could be attributed to a not uniform

deposition of platinum nanoparticles compared to that achieved for Pt_3h/CeO_2_750_15/C. For this reason, 750 °C was chosen as optimal temperature for depositing ceria on chitosan-based carbon (CC). The results for Pt_3h/CeO_2_750_15/CC are even better than the Pt_3h/CeO_2_750_15/C on Vulcan since $E_{1/2}$, E_{on}, the kinetic current, mass activity, surface activity and limiting current determined for Pt_3h/CeO_2_750_15/CC are higher than those determined for Pt_3h/CeO_2_750_15/C as observable in Table 20. On the top of that, the performance of both Pt_3h/CeO_2_750_15/C and Pt_3h/CeO_2_750_15/CC exceed that of Pt/C standard.

6.5 EFFECT OF THE CERIA DEPOSITED

6.5.1 Cyclic voltammetry in Argon Atmosphere

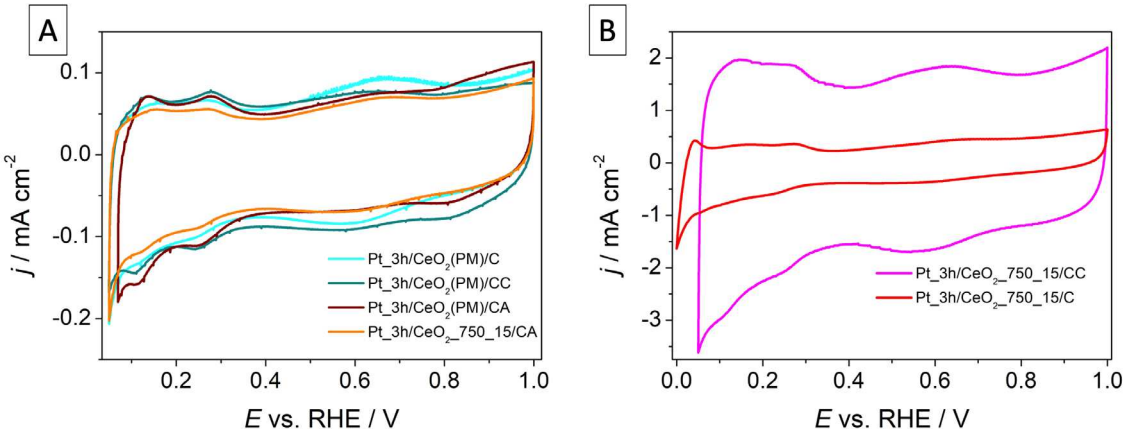

Figure 94. A) Cyclic voltammetries of Pt_3h/CeO_2(PM)/C, Pt_3h/CeO_2(PM)/CC, Pt_3h/CeO_2(PM)/CA and Pt_3h/CeO_2_750_15/CA recorded at 50 mV s^{-1} in Ar saturated solution 0.1 M of $HClO_4$. The current density was normalized by the geometrical area of the electrode; B) Cyclic voltammetries of Pt_3h/CeO_2_750_15/CC and Pt_3h/CeO_2_750_15/C recorded at 50 mV s^{-1} in Ar saturated solution 0.1 M of $HClO_4$. The current density was normalized by the geometrical area of the electrode.

Figure 94A and B compare the voltammetry of the sample where ceria was deposited by solid-state approach or mixed with carbon through ball milling. In addition to chitosan, agarose-based support is introduced in this graph and the effect of different type of ceria is here evaluated. Except for the catalyst where agarose-based carbon was used as support, the voltammograms of the sample where ceria was deposited by means of solid-state approach show a high capacitive current, whereas those where ceria of Particular Materials was used are less capacitive. This difference could be explained as follows.

When ceria is deposited as nanoparticles on the carbon support two phases form in the material: an insulant phase given by the oxide and an electronic conductive phase given by carbon. On the contrary, ball milling mixing with carbon ceria does not lead to phase separation between carbon and oxide. Thus, it might be supposed that the resultant electronic resistivity when a phase separation process occurs could be larger since phase separation could mean the formation of grain borders between the carbon and the oxide which can be seen as further source of conductivity drop. Moreover,

when oxide and carbon are mixed (no separation phase) these boundaries zone are not likely to form and therefore the resultant material resistivity is less than the sum between the oxide and carbon resistivity. Some investigation with spectroscopic impedance should be done in order to better clarify the difference in conductivity of hybrid ceria-carbon support prepared in the two different ways adopted in this thesis. Despite that, the ECSA and EPSA values of the sample where ceria was deposited by solid state are much higher than those where ceria was mixed with carbon, except for CA. These results could be explained by the formation of platinum aggregates on sample where ceria was mixed with carbon (see the following section), since aggregates could lead to the decrease of the available active sites for adsorption of hydrogen atoms.

6.5.2 ORR activity

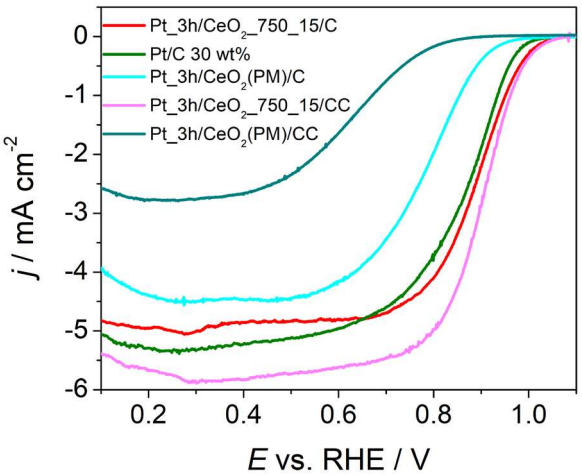

Figure 95. Linear sweep voltammetry of Pt_3h/CeO2(PM)/C, Pt_3h/CeO2(PM)/CC, Pt_3h/CeO2_750_15/CC, Pt_3h/CeO2_750_15/C and Pt/C 30 wt% recorded at 1600 rpm and 50 mV s^{-1} in O_2 saturated solution, 0.1 M of $HClO_4$. The current density was normalized by the geometrical area.

From Figure 95, it can be easily noticed that the results of the samples where ceria of Particular Materials was used are worse than that obtain for the samples where ceria was deposited by solid-state approach. This difference is particularly amplified for the sample with chitosan-based support since Pt_3h/CeO2(PM)/C is the least active catalyst whereas Pt_3h/CeO2_750_15/CC is the most active in this thesis. This substantial difference could be explained as follows. Ball milling technique provide a loose bond of ceria on carbon whereas the deposition of ceria by solid state approach leads to a stronger anchoring of ceria on carbon matrix with the formation of nanoparticles on the surface of carbon as confirmed by the reference article chosen for ceria deposition [121]. When platinum was deposited on a ceria-carbon support prepared by ball milling a weak interaction between the metal and the support could favor the migration of platinum nanoparticles and therefore the formation of aggregates which could not form when ceria was deposited via solid state.

In most works ceria has been deposited via the formation of nanoparticles on carbon support rather than mixing the oxide and when ceria and platinum NPs are homogeneously and randomly dispersed

on the carbon support a possible contact between them could arise. The contact between a ceria and a platinum nanoparticle allows a possible interaction between them which benefits the performance of the ORR. In fact, according to the redox properties of ceria, CeO_2 NPs can easily store oxygen and feed the near Pt nanoparticles with oxygen especially when oxygen partial pressure decreases [64]. In fact, oxygen on the surface of the CeO_2 is released to the closed Pt active sites when CeO_2 changes to Ce_2O_3, which increases the local oxygen concentration. Afterwards, Ce_2O_3 quickly changes to CeO_2 when the oxygen concentration increases in the cathode atmosphere [64,141]. The oxygen supplier ability at the interface between Pt and ceria which was called oxygen spillover from ceria to platinum in the introduction it is believed to be the reason of high performance for ORR [65]. A possible explanation of this mechanism is provided by Figure 96 reported below where it is possible to appreciate the promotional donation of oxygen by ceria arising when platinum and ceria are in contact.

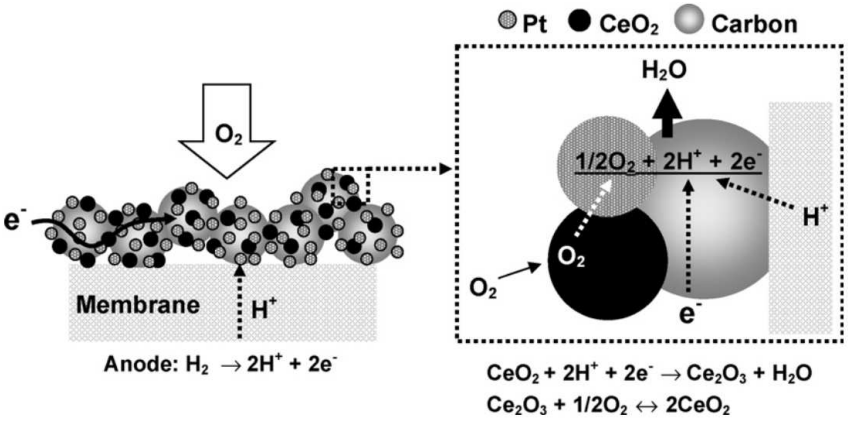

Figure 96. Possible mechanism of ORR arising from the synergystic effect between ceria and platinum.

This mechanism could explain the enhanced activity of Pt_3h/CeO_2_750_15/C and Pt_3h/CeO_2_750_15/CC compared to that of the standard. The difference in ORR performance between Pt_3h/CeO_2_750_15/C, Pt_3h/CeO_2_750_15/CC and Pt_3h/CeO_2_750_15/CA could be attributed to the support (as explained in the following section).

Therefore, it can be concluded that depositing ceria by solid state method led to a possible formation of nanoparticles (randomly dispersed) which could probably interact with the nearest Pt nanoparticles (if a contact forms) whereas the mixing of ceria with carbon could leads to aggregation phenomena causing a sluggish ORR kinetics.

6.6 EFFECT OF THE CARBON SUPPORT

6.6.1 Cyclic voltammetry in Argon Atmosphere

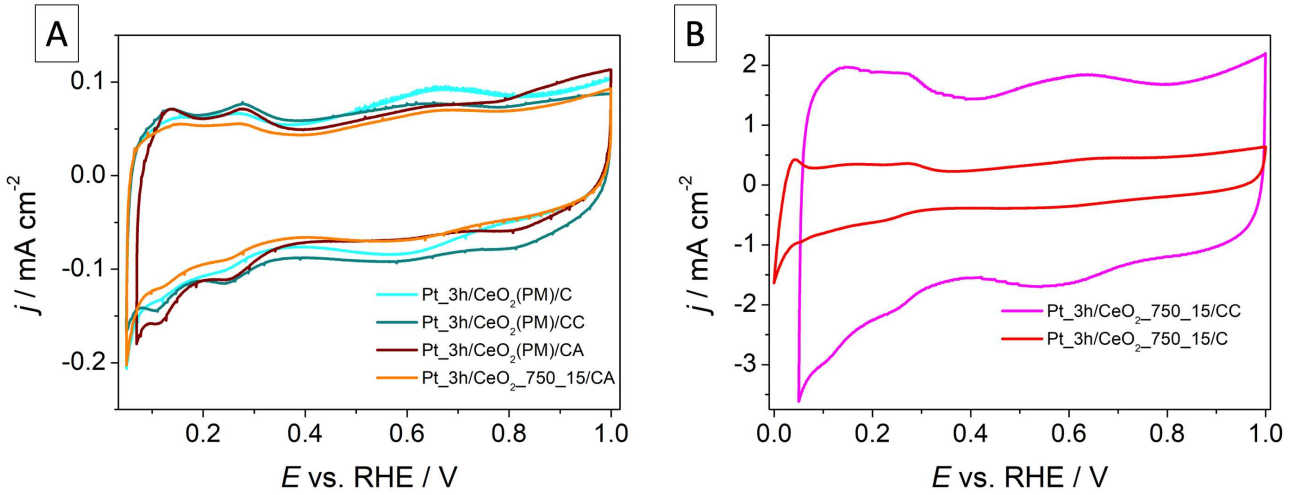

Figure 97. A) Cyclic voltammetries of Pt_3h/CeO2(PM)/C, Pt_3h/CeO2(PM)/CC, Pt_3h/CeO2(PM)/CA and Pt_3h/CeO2_750_15/CA recorded at 50 mV s^{-1} in Ar saturated solution 0.1 M of $HClO_4$. The current density was normalized by the geometrical area of the electrode; B) Cyclic voltammetries of Pt_3h/CeO2_750_15/CC and Pt_3h/CeO2_750_15/C recorded at 50 mV s^{-1} in Ar saturated solution 0.1 M of $HClO_4$. The current density was normalized by the geometrical area of the electrode.

The purpose of this section is showing the influence of the carbon support on the electrochemical behavior and catalytic activity of Pt/CeO2/C catalyst. That is why agarose-based carbon (Few_CA10, abbreviated as CA) was introduce in this section along with chitosan and Vulcan XC72. Figure 97A reports the cyclic voltammetry obtained for Pt_3h/CeO2(PM)/C, Pt_3h/CeO2(PM)/CC, Pt_3h/CeO2(PM)/CA and Pt_3h/CeO2_750_15/CA whereas B show the cyclic voltammetry of Pt_3h/CeO2_750_15/CC and Pt_3h/CeO2_750_15/C. The voltammetry of Figure 97A are comparable apart from the more pronounced quinone/hydroquinone peaks of Pt_3h/CeO2(PM)/C and they exhibit such a high capacitive current that the ECSA and EPSA values results to be very low, i.e. below 5 m^2 g^{-1}. Thus, they are heavily underestimated and that is why they were not reported. For samples where ceria was mixed with carbon no sensitive changes are observed in the voltammetries, which almost overlap each other. Instead, by comparing the samples where ceria was deposited by solid state approach, i.e. Pt_3h/CeO2_750_15/C, Pt_3h/CeO2_750_15/CC and Pt_3h/CeO2_750_15/CA, the carbon support seems to contribute together with ceria to the capacitive current, giving rise to a synergistic effect. The most capacitive carbon is represented by Pt_3h/CeO2_750_15/CC whereas the least capacitive is given by Pt_3h/CeO2_750_15/CA. This could be attributed by the carbon support, i.e. the presence of defects, such as heteroatoms and how the support can interact with ceria. The absence of changes in the capacitive current for samples where PM ceria was used could means that mixing via ball milling gives rise to ceria-carbon hybrid support with similar morphological characteristics. Conversely, when ceria was deposited by solid state approach it might be supposed the carbon support can influence the growth of ceria nanoparticles leading to the formation of carbon-ceria composites with different textural characteristics features,

which in turns can be reflected on the voltametric features, such as the capacitive current. Thus, it might be concluded that the carbon support has a strong impact on the capacitive current when ceria is deposited rather than mixing due to the different interactions created when ceria is deposited on different carbon supports.

6.6.2 ORR activity

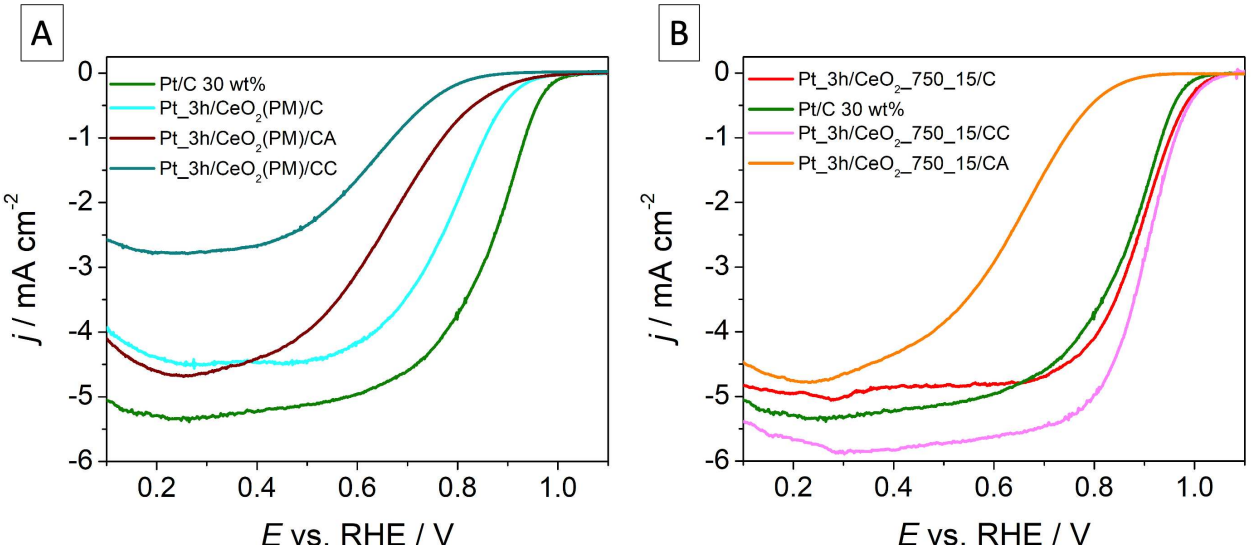

Figure 98. A) Linear sweep voltammetry of Pt_3h/CeO_2(PM)/C, Pt_3h/CeO_2(PM)/CA and Pt_3h/CeO_2(PM)/CC and Pt/C 30 wt% recorded at 1600 rpm and 50 mV s^{-1} in O_2 saturated solution, 0.1 M of $HClO_4$. The current density was normalized by the geometrical area. B) Pt_3h/CeO_2_750_15/CC, Pt_3h/CeO_2_750_15/C, Pt_3h/CeO_2_750_15/CA and Pt/C 30%w recorded at 1600 rpm and 50 mV s^{-1} in O_2 saturated solution, 0.1 M of $HClO_4$. The current density was normalized by the geometrical area.

Table 21. LSV results of *Pt_3h/CeO_2_750_15/CC, Pt_3h/CeO_2_750_15/C and Pt_3h/CeO_2_750_15/CA : limiting current density (j_L) , onset potential(E_{on}), half wave potential($E_{1/2}$) , kinetic current (j_k) determined at 0.85 V vs. RHE, mass activity (MA) determined at 0.85 V vs. RHE and surface activity (SA) determined at 0.85 V vs. RHE.*

	j_L	E_{on}	$E_{1/2}$	j_k	*MA*	*SA*
	mA cm^{-2}	V vs. RHE	V vs. RHE	mA cm^{-2}	A g^{-1}	µA cm^{-2}
Pt/C 30 wt%	5.4 ± 0.1	0.958 ± 0.003	0.87 ± 0.01	5.7 ± 0.2	1940 ± 80	600 ± 70
Pt_3h/CeO_2_750_15/CC	6.0 ± 0.1	1.10 ± 0.01	0.90 ± 0.003	15.2 ± 0.9	5200 ± 300	1720 ± 60
Pt_3h/CeO_2_750_15/C	4.84 ± 0.08	1.032 ± 0.002	0.889 ± 0.003	10.7 ± 0.4	1190 ± 40	1500 ± 80
Pt_3h/CeO_2_750_15/CA	4.8 ± 0.1	0.926 ± 0.003	0.636 ± 0.005	0.19 ± 0.02	64 ± 7	2000 ± 200

Table 22. LSV results of Pt_3h/CeO_2(PM)/CC, Pt_3h/CeO_2(PM)/CA and Pt_3h/CeO_2(PM)/C: limiting current density (j_L), onset potential (E_{on}), half wave potential ($E_{1/2}$) , kinetic current (j_k) determined at 0.85 V vs. RHE, mass activity (MA) determined at 0.85 V vs. RHE and surface activity (SA) determined at 0.85 V vs. RHE.

	j_L	E_{on}	$E_{1/2}$	j_k	*MA*	*SA*
	mA cm^{-2}	V vs. RHE	V vs. RHE	mA cm^{-2}	A g^{-1}	µA cm^{-2}
Pt_3h/CeO_2(PM)/ CC	2.86 ± 0.04	0.86 ± 0.02	0.627 ± 0.008	0.11 ±0.03	8 ± 2	n.a.
Pt_3h/CeO_2(PM)/ C	4.4 ± 0.1	0.890 ± 0.009	0.799± 0.006	1.4 ± 0.1	470 ± 40	4000 ± 1000
Pt_3h/CeO_2(PM)/ CA	4.9 ± 0.1	0.971 ± 0.005	0.666 ± 0.008	0.748 ± 0.07	250 ± 20	1900 ± 200

Figure 98A depicts the effects of the carbon support on the ORR activity for samples containing ceria of Particular Materials whereas B illustrates the different LSV for the samples where ceria was deposited by solid state approach. In graph A the best performing catalyst is Pt_3h/CeO_2(PM)/C

where Vulcan XC-72 was used as support whereas in Figure B the more active catalyst is Pt_3h/CeO_2_750_15/CC. The activity in terms of E_{on}, $E_{1/2}$, j_k, *MA* decreases following this order Pt_3h/CeO_2_750_15/CC > Pt_3h/CeO_2_750_15/C >> Pt_3h/CeO_2_750_15/C for graph B (see also Table 21) and this observable trend is surely attributed to the different morphological properties of CC, CA and Vulcan XC-72. The values of *SA* do not follow this trend since it could be possible that the underestimation of EPSA, caused by the higher capacitive current of the sample containing ceria, leads to misleading results. Therefore, *SA* is for sure overestimated. Chitosan-based carbon (CC) has a surface area comparable to Vulcan whereas CA possesses the lowest surface area. The low surface area could ease the aggregation of platinum nanoparticles on the carbon surface. This could be a possible reason explaining the bad performance when this support is used. The lack of porosity of this carbon leads to cancel the effect explained in the previous section, i.e. the deposition of ceria rather than mixing ceria with carbon, and thus Pt_3h/CeO_2_750_15/CA and Pt_3h/CeO_2(PM)/ CA show similar performance (see Figure 99B) in terms of $E_{1/2}$ whereas the other kinetic parameters are higher in the case of Pt_3h/CeO_2_750_15/CA.

It could be possible that ceria nanoparticles aggregated during the deposition (due to the lack of surface area) or they did not deposited at all. This fact could have an impact on platinum nanoparticles nucleation and growth, thus facilitating the aggregation or the formation of large nanoparticles rather than the distancing between nanoparticles or the formation of small nanoparticles.

Instead, chitosan possesses a higher surface area (200 m^2 g^{-1}), shows the highest graphitization degree compared to the other carbons and present more nitrogen atoms than the agarose-based support and Vulcan (see elemental analysis). The presence of a high porosity allows a uniform dispersion of ceria and platinum nanoparticles thus avoiding aggregation phenomena which can occur during the synthesis whereas nitrogen atoms in the chitosan-based support can strengthen the interaction between platinum nanoparticles and the support, as already declared in the introduction. In fact, due to the low amount of ceria deposited, it might be possible platinum nanoparticles can interact with the nitrogen atoms present on its surface. This interaction is known to change the electronic structure of platinum assigned to a shift of the *d-band* center position, as proven by DFT calculation in several studies. This electronic modification can in turn lower the energy dissociation of O_2 molecule and weaken the OH adsorption energy on platinum surface, thus enhancing the electrochemical activity. To assess this hypothesis X-rays photoelectron spectroscopy (XPS), X-rays adsorption (XAS) techniques are needed. Anyway, the presence of nitrogen atoms on chitosan-based support (which are absent in Vulcan XC-72) could explained the enhanced activity of Pt_3h/CeO_2_750_15/CC compared to that of Pt_3h/CeO_2_750_15/C where Vulcan XC-72 was employed as support. The possibility for platinum nanoparticles to nucleate inside the numerous available pores of chitosan-

based carbon can explain the huge difference in activity between Pt_3h/CeO_2_750_15/CC and Pt_3h/CeO_2_750_15/CA where the absence of porosity limits the nucleation of metal nanoparticles on the external surface thus facilitating aggregation phenomena.

Nevertheless, the aforementioned hypothesis related to the presence of high porosity and nitrogen atoms in chitosan-based supports seem to fail when ceria of Particular Materials is used since the activity of Pt_3h/CeO_2(PM)/CC is worse than Pt_3h/CeO_2(PM)/CA and Pt_3h/CeO_2(PM)/C (Figure 98A). The very low values of E_{on}, $E_{1/2}$, j_k, *MA* of Pt_3h/CeO_2(PM)/CC (Table 22) indicate an enormous kinetic hindrance since they are much lower than those of the other catalysts. This could be due to the formation of many aggregates of platinum nanoparticles, which not only could explain the lower activity of this carbon but also the lower ECSA (< 6 m^2 g^{-1}) with respect to that of Pt_3h/CeO_2_750_15/CC which is similar to that of the standard. The formation of aggregates can also explain such a low value of j_L, since it indicates a strong limitation in oxygen mass transport due to the lack of active sites on the surface of the catalyst. Anyway, apart from *SA* (which is surely overestimated for the reasons explained above in the text), the values of kinetic parameters and the limiting current of Pt_3h/CeO_2(PM)/CA and Pt_3h/CeO_2(PM)/C remains much lower than those of the standard Pt/C.

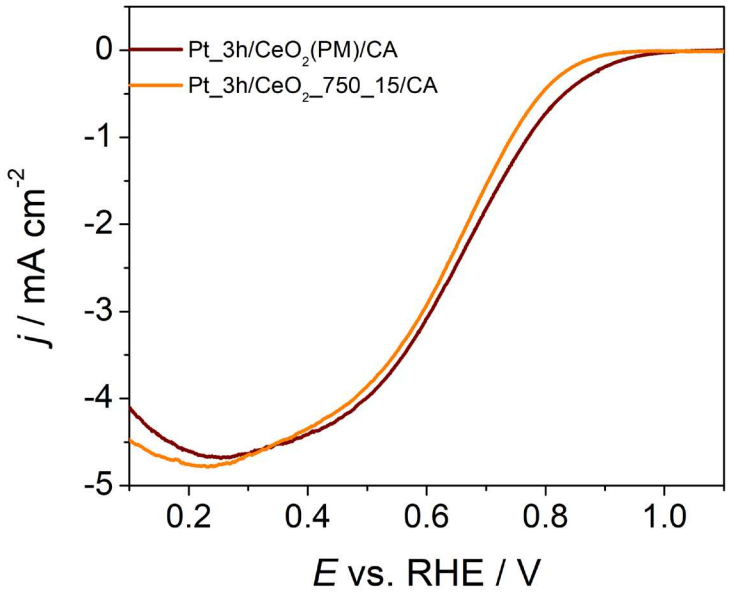

Figure 99. Linear sweep voltammetry of Pt_3h/CeO_2(PM)/CA and Pt_3h/CeO_2_750_15/CA recorded at 1600 rpm and 50 mV s^{-1} in O_2 saturated solution, 0.1 M of $HClO_4$. The current density was normalized by the geometrical area.

6.7 COMPARISON BETWEEN THE BEST CATALYSTS

After this long discussion, which has tried to figure out the main effects on the catalytic activity, it could be concluded that the best catalysts overcoming the performance of the standard Pt/C are Pt_3h/CeO_2_750_15/CC and Pt_3h/CeO_2_750_15/C so the samples where ceria was deposited via solid state deposition at 750 °C for 15 minutes on support having a high surface area (> 200 m^2 g^{-1}). The higher performance can be evidenced by the $E_{1/2}$ shift (shown in Figure 100) of 19 mV and 30 mV for Pt_3h/CeO_2_750_15/C and Pt_3h/CeO_2_750_15/CC, respectively, compared to the standard, which indicates a better kinetics. Other indicators of better performance are the onset potential, which result to be higher for Pt_3h/CeO_2_750_15/CC and Pt_3h/CeO_2_750_15/C meaning an anticipation of the ORR starting point (less overpotential required), the kinetic current determined at 0.85 V the *SA* and the *MA*. However, it can be observed that *SA* determined for the sample containing ceria is overestimated due to the high capacitive current and the higher value of *MA* of Pt/C with respect to that of Pt_3h/CeO_2_750_15/C could be attributed to the higher content of platinum, i.e. 30 wt% of Pt/C standard vs. value of 22.9 wt% of Pt_3h/CeO_2_750_15/C obtained form ICP-MS. Moreover, a higher limiting current value for Pt_3h/CeO_2_750_15/CC with respect to that of the standard indicates an improved number of active sites or turn over frequency that can be associated to the presence of ceria which acts as an oxygen buffer, enriching platinum active sites with O_2 molecules.

Table 23. LSV results of Pt_3h/CeO_2_750_15/CC, Pt_3h/CeO_2_750_15/C and Pt/C 30%w : limiting current density (j_L), onset potential (E_{on}), half wave potential($E_{1/2}$) , kinetic current (j_k) determined at 0.85 V, mass activity (MA) determined at 0.85 V and surface activity (SA) determined at 0.85 V.

	j_L	E_{on}	$E_{1/2}$	j_k	*MA*	*SA*
	mA cm^{-2}	V vs. RHE	V vs. RHE	mA cm^{-2}	A g^{-1}	µA cm^{-2}
Pt/C 30 wt%	5.4 ± 0.1	0.958 ± 0.003	0.87 ± 0.01	5.7 ± 0.2	1940 ± 80	600 ± 70
Pt_3h/CeO_2_750_15/CC	6.0 ± 0.1	1.10 ± 0.01	0.90 ± 0.003	15.2 ± 0.9	5200 ± 300	1720 ± 60
Pt_3h/CeO_2_750_15/C	4.84 ± 0.08	1.032 ± 0.002	0.889 ± 0.003	10.7 ± 0.4	1190 ± 40	1500 ± 80

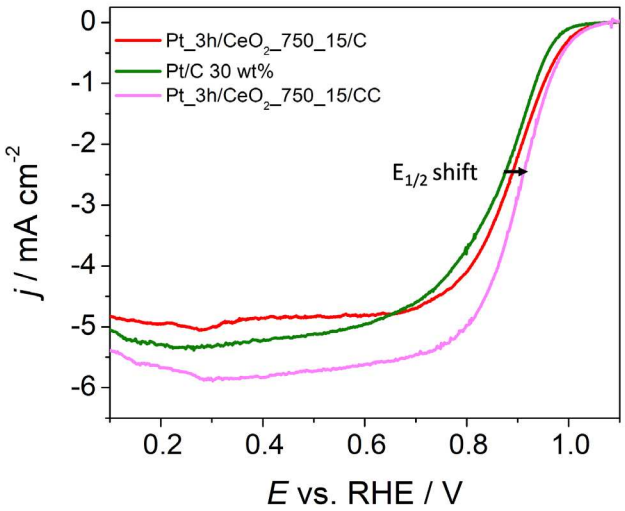

Figure 100. Linear sweep voltammetry of Pt_3h/CeO_2_750_15/C, Pt_3h/CeO_2_750_15/CC and Pt/C 30 wt% recorded at 1600 rpm and 50 mV s^{-1} in O_2 saturated solution, 0.1 M of $HClO_4$. The current density was normalized by the geometrical area.

7 GDE: MEASUREMENTS OF STABILITY

In this chapter, the electrochemical measurements acquired by means of gas diffusion electrode (GDE) will be reported and the difference between RDE and GDE results will be highlighted. As already declared, GDE allows testing catalysts performance in terms of activity and durability upon current densities and potentials similar to those used in fuel cells without mass-transport limitation which arises during RDE measurements. Differently from RDE, the deposition was carried out by spray coating technique and with a catalyst loading of 10 μg_{Pt} cm^{-2} (for sake of comparison the RDE measurement was recorded using a loading of 15 μg_{Pt} cm^{-2}). The ink fabrication was performed by considering a platinum content of 22 % wt for each sample. Two kinds of plot will be shown, namely a linear sweep voltammetry recorded in the 1 - 0 V potential window at 20 mV s^{-1} and a Tafel plot (potential plotted against the decimal logarithm of the current density). The effect of two types of key parameters for $Pt/CeO_2/C$ synthesis on the electrochemical activity and stability will be considered, i.e. time for depositing platinum at the same temperature for sample synthesized following one-pot procedure and both temperature and time for the deposition of ceria in the case of samples synthesized by two-step deposition approach.

Since one of the main purposes of GDE is to determine the stability of catalysts, a comparison between the results obtained before and after the accelerated durability test (ADT) will be emphasized. The results obtained for the synthesized $Pt/CeO_2/C$ catalysts will be compared with that of Pt/C (TKK) standard, which contains up to 50 wt% of Pt.

7.1 EFFECT PLATINUM TIME DEPOSITION

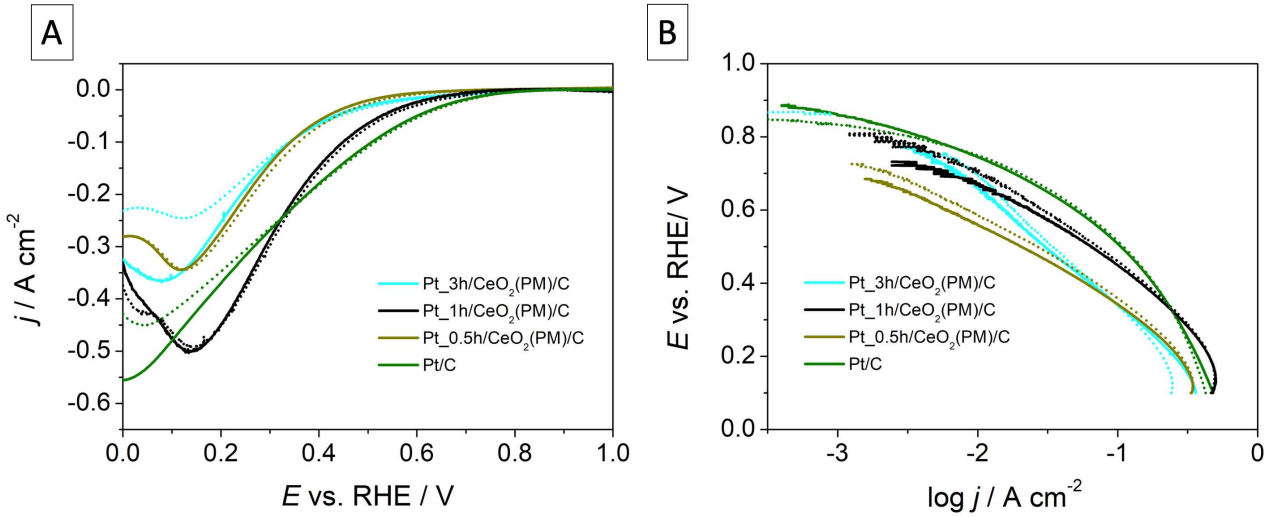

Figure 101. A) Linear sweep voltammetry of Pt_3h/CeO_2(PM)/C, Pt_1h/CeO_2(PM)/C and Pt_0.5h/CeO_2(PM)/C and Pt/C before ADT (straight line) and after ADT (dotted line) in gas diffusion electrode recorded at 20 mV s^{-1} in GDE and B)Tafel plot of Pt_3h/CeO_2(PM)/C, Pt_1h/CeO_2(PM)/C and Pt_0.5h/CeO_2(PM)/C and Pt/C. The current was normalized by the geometric area of the electrode.

Table 24. Onset potential before ADT (E^i_{on}), final onset potential after ADT (E^f_{on}), and stability efficiency of Pt_3h/CeO_2(PM)/C, Pt_1h/CeO_2(PM)/C and Pt_0.5h/CeO_2(PM)/C and Pt/C determined by LSV.

Sample	E^i_{on}	E^f_{on}	Stability efficiency
	V vs. RHE	V vs. RHE	%
Pt_3h/CeO_2(PM)/C	-0.340	-0.230	67
Pt_1h/CeO_2(PM)/C	-0.390	-0.420	98
Pt_0.5/CeO_2(PM)/C	-0.280	-0.280	100
Pt/C	-0.550	-0.450	81

In this section, the influence of platinum time deposition on activity and stability is shown in the Figure 101A and B. The solid lines refer to the results obtained for the pristine material before ADT whereas the dotted ones were obtained after ADT and the catalytic performance of ceria containing catalysts is compared with that of standard Pt/C (TKK), which is abbreviated as Pt/C. By focusing firstly on Figure 101A, a kinetic and a mass transport-controlled zone can be identified at lower and higher current densities respectively, as for RDE. However, the limiting current plateau observable in RDE LSVs is never visible in GDE LSVs. The current densities in the range between 0 and 0.05 A cm^{-2} identify a kinetic regime while the minimum appearing at higher current identify the peak of the oxygen reduction reaction. For comparing activity through GDE analysis a not well-defined protocol has been reported in literature, so far. In this thesis, the activity of the catalyst was determined by individuating the potential at 0.025 A cm^{-2} which can be assimilated to the onset potential determined by RDE analysis. For comparing the catalyst stability from the kinetic point of view the values of onset potential obtained before and after ADT (called E^i_{on} and E^f_{on} respectively) are compared in Table 24. Instead, for comparing the overall stability, stability efficiency, a parameter

describing how much the material degraded after ADT, can be calculated as the ratio between the final current peak value (j_p^f), the initial peak value (j_p^i):

$$stability\ efficiency = \frac{j_p^f}{j_p^i}$$

Among the catalyst containing CeO_2, the most active catalyst before and after ADT is represented by Pt_1h/CeO_2(PM)/C since it shows the highest E^i_{on} and E^f_{on}, -0.390 and -0.420 V respectively, but in general it develops more current at equal potential compared to the other catalysts. Nevertheless, its performance does not reach that of Pt/C, whose E^i_{on} and E^f_{on} are -0.550 V and -0.450 V. According to the GDE analysis, the most active catalysts is Pt_1h/CeO_2(PM)/C whereas in RDE the best performance was obtained for Pt_0.5/CeO_2(PM)/C. However, in RDE section this conclusion was based on the limiting current of Pt_0.5/CeO_2(PM)/C as discriminating factor, since the parameters used for determining activity (i.e. $E_{1/2}$, j_k, *MA* and *SA*) were much similar in values (in the limit of the error range see section). Since GDE technique is not affected by the mass transport limitations of RDE some discrepancies could arise as in this case.

Moving to stability description, the superimposition between the solid and the dotted line at low current densities demonstrates that the kinetic of reaction remains stable upon the accelerated stress test for all catalyst, particularly for the standard Pt/C and Pt_3h/CeO_2(PM)/C. High variation can be conversely detected near the peak region for Pt_3h/CeO_2(PM)/C and Pt_0.5/CeO_2(PM)/C catalyst, whose stability efficiency is 67 and 81 % respectively. This loss of performance can be attributed to degradation process, such as particle detachment and sintering, which might be assessed by comparing TEM images before and after ADT. Moreover, an ORR peak shift of 0.05 and 0.044 V toward more positive potential is observable for Pt_3h/CeO2(PM)/C and Pt/C TKK respectively. This could be attributed to morphological changes of the active species (i.e. Pt) such as variation of crystallinity after ADT or of particle dimension. Conversely, Pt_0.5/CeO_2(PM)/C and Pt_1h/CeO_2(PM)/C shows the best stability efficiency, 100 and 98 %, without any peak shift.

By watching the Tafel plots of Figure 101B, in the log j range reported it can be observed that the standard shows the highest kinetic current at a selected potential. As regards the CeO_2 containing catalysts, before ADT, Pt_3h/CeO_2(PM)/C and Pt_1h/CeO_2(PM)/C shows the same current at values > 0.6 V, whereas at potential values less positive, Pt_3h/CeO_2(PM)/C exhibits lower current density values, which are similar to those recorded for Pt_0.5h/CeO_2(PM)/C. Concerning the current density recorded before and after ADT, it can be noticed changes are observed both at high potential value for every catalyst but at low potential the current remains the same for both Pt_1h/CeO_2(PM)/C and Pt_0.5h/CeO_2(PM)/C and varies for Pt_3h/CeO_2(PM)/C. The stability of current density at low current values for Pt_0.5h/CeO_2(PM)/C could be related to what discussed regarding the formation

of a tilt at low potential in RDE in section 6.3.2, caused by the formation of an insulating thin oxide layer partially covering platinum nanoparticles. The formation of this layer probability arising during the heat treatment for platinum reduction could lead to a strong metal-support interaction (SMSI) between platinum and ceria, which prevents the platinum nanoparticles sintering and detachment in the case of Pt_0.5h/CeO_2(PM)/C and Pt_1h/CeO_2(PM)/C as reported in literature [146]. The lower stability of Pt_3h/CeO_2(PM)/C at lower potentials could be assigned to the formation of larger platinum nanoparticles which are not protected by the formation of a thin oxide layer. By reminding Figure 91 it can be observed that large Pt nanoparticles are not as covered as the small ones and thus sintering, and detachment of Pt NPs are more likely to occur for large NPs consequently causing a loss in performance.

By weighing up activity and stability results obtained by LSV and Tafel plot from GDE, it can be concluded that the best condition for depositing platinum at 300 °C is 1 h.

7.2 EFFECT OF CERIA DEPOSITION TEMPERATURE

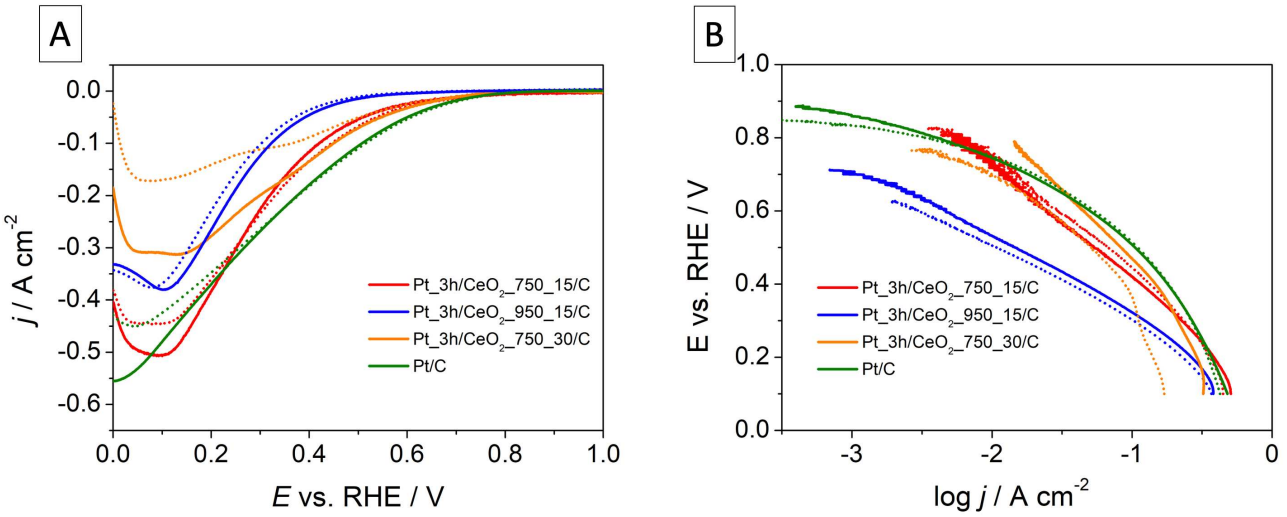

Figure 102. A) Linear sweep voltammetry of Pt_3h/CeO_2_750_15/C, Pt_3h/CeO_2_750_30/C and Pt_3h/CeO_2_950_15/C and Pt/C before ADT (straight line) and after ADT (dotted line) in gas diffusion electrode recorded at 20 mV s^{-1} in GDE and B)Tafel plot of Pt_3h/CeO_2_750_15/C, Pt_3h/CeO_2_750_30/C and Pt_3h/CeO_2_950_15/C and Pt/C. The current was normalized by the geometric area of the electrode.

Table 25. Onset potential before ADT (E^i_{on}), final onset potential after ADT (E^f_{on}) and stability efficiency of Pt_3h/CeO_2_750_15/C, Pt_3h/CeO_2_750_30/C and Pt_3h/CeO_2_950_15/C and Pt/C determined by LSV.

Sample	E^i_{on}	E^f_{on}	Stability efficiency
	V vs. RHE	V vs. RHE	%
Pt_3h/CeO_2_750_15/C	-0.30	-0.43	88
Pt_3h/CeO_2_750_30/C	-0.28	-0.14	55
Pt_3h/CeO_2_950_15/C	-0.35	-0.34	99
Pt/C	-0.55	-0.45	81

Figure 102A reports the LSV of Pt_3h/CeO_2_750_15/C, Pt_3h/CeO_2_750_30/C and Pt_3h/CeO_2_950_15/C. Despite the highest stability efficiency, Pt_3h/CeO_2_950_15/C shows a slight shift of the onset potential toward lower values after the stress test and this phenomenon can be rated as a degradation of the material. In the case of Pt_3h/CeO_2_750_30/C, a heavy degradation can be detected since the onset potential halves after the stress test (as seen from Table 25) and the current density largely shift toward lower potential. The stability efficiency is very low for this sample (i.e. 55%) and this could be attributed with no doubt to a heavy aggregation or to particle detachment from the support. Another feature supporting such an elevated degradation is provided by the change of the peak shape before and after degradation. In fact, the two bumps observable in the pristine material (solid line) disappear after ADT (dotted line) and this is probably due to a high variation of the catalyst morphology. As regards Pt_3h/CeO_2_750_15/C, the onset potential is very similar to that of Pt_3h/CeO_2_750_30/C, -0.3 V vs. 0.28 V respectively. These values are much higher than that of Pt_3h/CeO_2_750_30/C thus proving that the 750 °C is the best condition for obtaining a highly active catalyst. However, the current values obtained for Pt_3h/CeO_2_750_15/C below 0.4 V are much

higher than that of Pt_3h/CeO_2_750_30/C. Although the ORR peak of Pt_3h/CeO_2_750_15/C shows a current upshift after ADT, which gives a stability efficiency of 88%, no potential shift is observed, unlike Pt_3h/CeO_2_950_15/C. This means that the degradation of Pt_3h/CeO_2_750_15/C material does not degrade as Pt_3h/CeO_2_950_15/C but it loses the performance efficiency during ADT.

Moving to Tafel plot, similar consideration as LSV can be done. The least active catalyst is represented by Pt_3h/CeO_2_950_15/C whereas the most active but the least stable catalyst is Pt_3h/CeO_2_750_30/C since a huge potential shift towards lower current values is observed along the whole curve. Pt_3h/CeO_2_750_15/C is less active than Pt_3h/CeO_2_750_30/C at high potential but more active at low potentials. On top of that, Pt_3h/CeO_2_750_15/C is much more stable compared to Pt_3h/CeO_2_750_30/C and Pt_3h/CeO_2_950_15/C since the current remains almost constant after ADT along the entire potential range.

In conclusion, the best conditions for depositing ceria are 750 °C and 15 minutes, which give rise to a catalyst showing an activity almost comparable to that of standard Pt/C (TKK) but a higher stability. This is a remarkable result if we consider that the TKK benchmark has a Pt content up to 50% conversely to the home-made catalysts in which Pt is below 25 %.

8 CONCLUSION

In this thesis the effect of CeO_2 on Pt NPs activity and stability versus oxygen reduction reaction was considered. Pt/CeO_2/C was successfully synthesized by following two different ways: a two-step solid-state approach, which consists of a thermochemical deposition of ceria and platinum on a commercial Vulcan XC72 or on two home-mode carbons with different morphological and chemical properties (CA and CC). The one-pot approach consists in the mixing of commercially available ceria NPs with carbon and afterwards depositing platinum in furnace at 300 °C by varying deposition time (3h, 1h, 0.5h). RDE characterization shows that catalysts prepared by the in-situ synthesis of CeO_2 NPs are by far more stable and active than catalysts with the sole addition of ceria. The best active catalyst is Pt_3h/CeO_2_750_15/CC synthesized by firstly depositing ceria at 750 °C for 15 min and subsequently platinum at 300 °C for 3h on a highly graphitized and porous chitosan-based carbon. The chitosan derived mesoporous carbon was in turn prepared by mixing a pretreated chitosan/pluronic carbon with $FeCl_2$, and pyrolyzing at 1050°C for 2 h. The performances of Pt_3h/CeO_2_750_15/CC and Pt_3h/CeO_2_750_15/C, as determined by RDE analysis, overtake those of Pt/C standard showing a $E_{1/2}$ shift of 19 and 30 mV towards more positive potential with respect to Pt benchmark. GDE results shows a higher activity and stability of Pt_3h/CeO_2_750_15/C with respect to the catalyst prepared by varying the temperature and time deposition of ceria. Moreover, Pt_3h/CeO_2_750_15/C almost equalizes the activity of Pt/C TKK standard but it shows better stability. Although this target has been well-accomplished for the samples where ceria was deposited at 750 °C for 15 min on Vulcan and CC, when the same conditions was adopted for depositing on CA (agarose-based) carbon the electrochemical performance worsen probably due to the low porosity of the carbon support. Mixing ceria with carbon has not been revealed a suitable route for obtaining active catalyst probably due to the possible formation of aggregates caused by a loosing bond of ceria on carbon, differently from what happened in solid-state deposition of ceria. In general, for all catalysts the capacitive current is very high and some improvement at the platinum/ceria interface should be done to reduce the capacitance. The crystallites size of platinum is believed to partially limit the activity performance of the synthesized catalyst (too big with respect the optimal size of 2-3 nm) and although some attempts were performed to reduce the NPs size by reducing the dwelling time at 300 °C further investigation should be done, searching for more suitable synthetic conditions. Notwithstanding, lowering platinum time deposition improves the stability of the catalyst probably associated to a strong metal support interactions arising through the formation of a film oxide layer between ceria and platinum.

9 BIBLIOGRAPHY

[1] Global Energy Review 2021, Glob. Energy Rev. 2019. (2020). https://doi.org/10.1787/90c8c125-en.

[2] A. Khodadoust, D. Miller, M. Politovich, W. Vaughan, Atmospheric environment, Elsevier B.V., 2001. https://doi.org/10.1539/sangyoeisei.kj00001989963.

[3] A.G. Olabi, T. Wilberforce, M.A. Abdelkareem, Fuel cell application in the automotive industry and future perspective, Energy. 214 (2021) 118955. https://doi.org/10.1016/j.energy.2020.118955.

[4] J.M. Andújar, F. Segura, Fuel cells: History and updating. A walk along two centuries, Renew. Sustain. Energy Rev. 13 (2009) 2309–2322. https://doi.org/10.1016/j.rser.2009.03.015.

[5] E. Ogungbemi, O. Ijaodola, F.N. Khatib, T. Wilberforce, Z. El Hassan, J. Thompson, M. Ramadan, A.G. Olabi, Fuel cell membranes – Pros and cons, Energy. 172 (2019) 155–172. https://doi.org/10.1016/j.energy.2019.01.034.

[6] D.M. Fadzillah, M.I. Rosli, M.Z.M. Talib, S.K. Kamarudin, W.R.W. Daud, Review on microstructure modelling of a gas diffusion layer for proton exchange membrane fuel cells, Renew. Sustain. Energy Rev. 77 (2017) 1001–1009. https://doi.org/10.1016/j.rser.2016.11.235.

[7] Y. Li, Q. Li, H. Wang, L. Zhang, D.P. Wilkinson, J. Zhang, Recent Progresses in Oxygen Reduction Reaction Electrocatalysts for Electrochemical Energy Applications, Electrochem. Energy Rev. 2 (2019) 518–538. https://doi.org/10.1007/s41918-019-00052-4.

[8] P.C. Okonkwo, I. Ben Belgacem, W. Emori, P.C. Uzoma, Nafion degradation mechanisms in proton exchange membrane fuel cell (PEMFC) system: A review, Int. J. Hydrogen Energy. 46 (2021) 27956–27973. https://doi.org/10.1016/j.ijhydene.2021.06.032.

[9] L. Khotseng, Fuel Cell Thermodynamics, Thermodyn. Energy Eng. (2020) 1–17. https://doi.org/10.5772/intechopen.90141.

[10] Y.R. Luo, Comprehensive handbook of chemical bond energies, Compr. Handb. Chem. Bond Energies. (2007) 1–1656. https://doi.org/10.1201/9781420007282.

[11] L. Osmieri, Q. Meyer, Recent advances in integrating platinum group metal-free catalysts in proton exchange membrane fuel cells, Curr. Opin. Electrochem. 31 (2022) 100847. https://doi.org/10.1016/j.coelec.2021.100847.

[12] L. Khotseng, Oxygen Reduction Reaction, Electrocatal. Fuel Cells Hydrog. Evol. - Theory to Des. (2018). https://doi.org/10.5772/intechopen.79098.

[13] C. Li, H. Tan, J. Lin, X. Luo, S. Wang, J. You, Y.M. Kang, Y. Bando, Y. Yamauchi, J. Kim, Emerging Pt-based electrocatalysts with highly open nanoarchitectures for boosting oxygen reduction reaction, Nano Today. 21 (2018) 91–105. https://doi.org/10.1016/j.nantod.2018.06.005.

[14] Y. Wang, D. Wang, Y. Li, A fundamental comprehension and recent progress in advanced Pt-based ORR nanocatalysts, SmartMat. 2 (2021) 56–75. https://doi.org/10.1002/smm2.1023.

[15] A. Panchenko, M.T.M. Koper, T.E. Shubina, S.J. Mitchell, E. Roduner, Ab Initio Calculations of Intermediates of Oxygen Reduction on Low-Index Platinum Surfaces, J. Electrochem. Soc. 151 (2004) A2016. https://doi.org/10.1149/1.1809586.

[16] H. Cruz-Martínez, H. Rojas-Chávez, P.T. Matadamas-Ortiz, J.C. Ortiz-Herrera, E. López-Chávez, O. Solorza-Feria, D.I. Medina, Current progress of Pt-based ORR electrocatalysts for PEMFCs: An integrated view combining theory and experiment, Mater. Today Phys. 19 (2021). https://doi.org/10.1016/j.mtphys.2021.100406.

[17] J.C. Dong, X.G. Zhang, V. Briega-Martos, X. Jin, J. Yang, S. Chen, Z.L. Yang, D.Y. Wu, J.M. Feliu, C.T. Williams, Z.Q. Tian, J.F. Li, In situ Raman spectroscopic evidence for oxygen reduction reaction intermediates at platinum single-crystal surfaces, Nat. Energy. 4 (2019) 60–67. https://doi.org/10.1038/s41560-018-0292-z.

[18] M. Shao, A. Peles, K. Shoemaker, Electrocatalysis on platinum nanoparticles: Particle size effect on oxygen reduction reaction activity, Nano Lett. 11 (2011) 3714–3719. https://doi.org/10.1021/nl2017459.
[19] J. Quinson, M. Inaba, S. Neumann, A.A. Swane, J. Bucher, S.B. Simonsen, L. Theil Kuhn, J.J.K. Kirkensgaard, K.M. Jensen, M. Oezaslan, S. Kunz, M. Arenz, Investigating Particle Size Effects in Catalysis by Applying a Size-Controlled and Surfactant-Free Synthesis of Colloidal Nanoparticles in Alkaline Ethylene Glycol: Case Study of the Oxygen Reduction Reaction on Pt, ACS Catal. 8 (2018) 6627–6635. https://doi.org/10.1021/acscatal.8b00694.
[20] M. Inaba, A. Zana, J. Quinson, F. Bizzotto, C. Dosche, A. Dworzak, M. Oezaslan, S.B. Simonsen, L.T. Kuhn, M. Arenz, The Oxygen Reduction Reaction on Pt: Why Particle Size and Interparticle Distance Matter, ACS Catal. 11 (2021) 7144–7153. https://doi.org/10.1021/acscatal.1c00652.
[21] Y.J. Wang, N. Zhao, B. Fang, H. Li, X.T. Bi, H. Wang, Carbon-Supported Pt-Based Alloy Electrocatalysts for the Oxygen Reduction Reaction in Polymer Electrolyte Membrane Fuel Cells: Particle Size, Shape, and Composition Manipulation and Their Impact to Activity, Chem. Rev. 115 (2015) 3433–3467. https://doi.org/10.1021/cr500519c.
[22] S. Jayabal, G. Saranya, D. Geng, L.Y. Lin, X. Meng, Insight into the correlation of Pt-support interactions with electrocatalytic activity and durability in fuel cells, J. Mater. Chem. A. 8 (2020) 9420–9446. https://doi.org/10.1039/d0ta01530j.
[23] N. Zhang, R. Jiang, Interfacial Engineering of Metal/Metal Oxide Heterojunctions toward Oxygen Reduction and Evolution Reactions, Chempluschem. 86 (2021) 1586–1601. https://doi.org/10.1002/cplu.202100466.
[24] M.A. Molina-García, N. V. Rees, Effect of catalyst carbon supports on the oxygen reduction reaction in alkaline media: A comparative study, RSC Adv. 6 (2016) 94669–94681. https://doi.org/10.1039/c6ra18894j.
[25] M.H. Seo, S.M. Choi, E.J. Lim, I.H. Kwon, J.K. Seo, S.H. Noh, W.B. Kim, B. Han, Toward New Fuel Cell Support Materials: A Theoretical and Experimental Study of Nitrogen-Doped Graphene, ChemSusChem. 7 (2014) 2609–2620. https://doi.org/10.1002/cssc.201402258.
[26] J. Ma, A. Habrioux, Y. Luo, G. Ramos-Sanchez, L. Calvillo, G. Granozzi, P.B. Balbuena, N. Alonso-Vante, Electronic interaction between platinum nanoparticles and nitrogen-doped reduced graphene oxide: Effect on the oxygen reduction reaction, J. Mater. Chem. A. 3 (2015) 11891–11904. https://doi.org/10.1039/c5ta01285f.
[27] R. Martínez-Hincapié, V. Čolić, Electrocatalysts for the Oxygen Reduction Reaction: From Bimetallic Platinum Alloys to Complex Solid Solutions, ChemEngineering. 6 (2022) 1–18. https://doi.org/10.3390/chemengineering6010019.
[28] J. Gu, G.-M. Zhang, R. Yao, T. Yu, M.-F. Han, R.-S. Huang, High Oxygen Reduction Activity of Pt-Ni Alloy Catalyst for Proton Exchange Membrane Fuel Cells, Catalysts. 12 (2022) 250. https://doi.org/10.3390/catal12030250.
[29] V.R. Stamenkovic, B.S. Mun, M. Arenz, K.J.J. Mayrhofer, C.A. Lucas, G. Wang, P.N. Ross, N.M. Markovic, Trends in electrocatalysis on extended and nanoscale Pt-bimetallic alloy surfaces, Nat. Mater. 6 (2007) 241–247. https://doi.org/10.1038/nmat1840.
[30] F.D. Sanij, P. Balakrishnan, P. Leung, A. Shah, H. Su, Q. Xu, Advanced Pd-based nanomaterials for electro-catalytic oxygen reduction in fuel cells: A review, Int. J. Hydrogen Energy. 46 (2021) 14596–14627. https://doi.org/10.1016/j.ijhydene.2021.01.185.
[31] Y. He, G. Wu, PGM-Free Oxygen-Reduction Catalyst Development for Proton-Exchange Membrane Fuel Cells: Challenges, Solutions, and Promises, Accounts Mater. Res. 3 (2022) 224–236. https://doi.org/10.1021/accountsmr.1c00226.
[32] L. Du, V. Prabhakaran, X. Xie, S. Park, Y. Wang, Y. Shao, Low-PGM and PGM-Free Catalysts for Proton Exchange Membrane Fuel Cells: Stability Challenges and Material Solutions, Adv. Mater. 33 (2021) 1–18. https://doi.org/10.1002/adma.201908232.
[33] V.P. Glibin, M. Cherif, F. Vidal, J.-P. Dodelet, G. Zhang, S. Sun, Non-PGM Electrocatalysts

for PEM Fuel Cells: Thermodynamic Stability and DFT Evaluation of Fluorinated FeN 4 - Based ORR Catalysts , J. Electrochem. Soc. 166 (2019) F3277–F3286. https://doi.org/10.1149/2.0341907jes.
[34] J. Zhang, Y. Yuan, L. Gao, G. Zeng, M. Li, H. Huang, Stabilizing Pt-Based Electrocatalysts for Oxygen Reduction Reaction: Fundamental Understanding and Design Strategies, Adv. Mater. 33 (2021) 1–23. https://doi.org/10.1002/adma.202006494.
[35] S. Cherevko, N. Kulyk, K.J.J. Mayrhofer, Durability of platinum-based fuel cell electrocatalysts: Dissolution of bulk and nanoscale platinum, Nano Energy. 29 (2016) 275–298. https://doi.org/10.1016/j.nanoen.2016.03.005.
[36] P. Parthasarathy, A. V. Virkar, Electrochemical Ostwald ripening of Pt and Ag catalysts supported on carbon, J. Power Sources. 234 (2013) 82–90. https://doi.org/10.1016/j.jpowsour.2013.01.115.
[37] J.C. Meier, C. Galeano, I. Katsounaros, J. Witte, H.J. Bongard, A.A. Topalov, C. Baldizzone, S. Mezzavilla, F. Schüth, K.J.J. Mayrhofer, Design criteria for stable Pt/C fuel cell catalysts, Beilstein J. Nanotechnol. 5 (2014) 44–67. https://doi.org/10.3762/bjnano.5.5.
[38] P.C. Okonkwo, O.O. Ige, E.M. Barhoumi, P.C. Uzoma, W. Emori, A. Benamor, A.M. Abdullah, Platinum degradation mechanisms in proton exchange membrane fuel cell (PEMFC) system: A review, Int. J. Hydrogen Energy. 46 (2021) 15850–15865. https://doi.org/10.1016/j.ijhydene.2021.02.078.
[39] J. Zhao, Z. Tu, S.H. Chan, Carbon corrosion mechanism and mitigation strategies in a proton exchange membrane fuel cell (PEMFC): A review, J. Power Sources. 488 (2021) 229434. https://doi.org/10.1016/j.jpowsour.2020.229434.
[40] F. Maillard, A. Bonnefont, F. Micoud, An EC-FTIR study on the catalytic role of Pt in carbon corrosion, Electrochem. Commun. 13 (2011) 1109–1111. https://doi.org/10.1016/j.elecom.2011.07.011.
[41] L. Castanheira, L. Dubau, M. Mermoux, G. Berthomé, N. Caqué, E. Rossinot, M. Chatenet, F. Maillard, Carbon corrosion in proton-exchange membrane fuel cells: From model experiments to real-life operation in membrane electrode assemblies, ACS Catal. 4 (2014) 2258–2267. https://doi.org/10.1021/cs500449q.
[42] L. Zhao, J. Zhu, Y. Zheng, M. Xiao, R. Gao, Z. Zhang, G. Wen, H. Dou, Y.P. Deng, A. Yu, Z. Wang, Z. Chen, Materials Engineering toward Durable Electrocatalysts for Proton Exchange Membrane Fuel Cells, Adv. Energy Mater. 12 (2022) 1–27. https://doi.org/10.1002/aenm.202102665.
[43] H. Liu, J. Li, X. Xu, F. Wang, J. Liu, Z. Li, J. Ji, Highly graphitic carbon black-supported platinum nanoparticle catalyst and its enhanced electrocatalytic activity for the oxygen reduction reaction in acidic medium, Electrochim. Acta. 93 (2013) 25–31. https://doi.org/10.1016/j.electacta.2013.01.090.
[44] Y. Li, Y. Li, E. Zhu, T. McLouth, C.Y. Chiu, X. Huang, Y. Huang, Stabilization of high-performance oxygen reduction reaction Pt electrocatalyst supported on reduced graphene oxide/carbon black composite, J. Am. Chem. Soc. 134 (2012) 12326–12329. https://doi.org/10.1021/ja3031449.
[45] S.Y. Huang, P. Ganesan, S. Park, B.N. Popov, Development of a titanium dioxide-supported platinum catalyst with ultrahigh stability for polymer electrolyte membrane fuel cell applications, J. Am. Chem. Soc. 131 (2009) 13898–13899. https://doi.org/10.1021/ja904810h.
[46] Y. Takabatake, Z. Noda, S.M. Lyth, A. Hayashi, K. Sasaki, Cycle durability of metal oxide supports for PEFC electrocatalysts, Int. J. Hydrogen Energy. 39 (2014) 5074–5082. https://doi.org/10.1016/j.ijhydene.2014.01.094.
[47] Q. Jia, S. Ghoshal, J. Li, W. Liang, G. Meng, H. Che, S. Zhang, Z.F. Ma, S. Mukerjee, Metal and Metal Oxide Interactions and Their Catalytic Consequences for Oxygen Reduction Reaction, J. Am. Chem. Soc. 139 (2017) 7893–7903. https://doi.org/10.1021/jacs.7b02378.

[48] J.H. Kim, G. Kwon, H. Lim, C. Zhu, H. You, Y.T. Kim, Effects of transition metal doping in Pt/M-TiO2 (M = V, Cr, and Nb) on oxygen reduction reaction activity, J. Power Sources. 320 (2016) 188–195. https://doi.org/10.1016/j.jpowsour.2016.04.019.
[49] C. He, S. Sankarasubramanian, A. Ells, J. Parrondo, C. Gumeci, M. Kodali, I. Matanovic, A.K. Yadav, K. Bhattacharyya, N. Dale, P. Atanassov, V.K. Ramani, Self-Anchored Platinum-Decorated Antimony-Doped-Tin Oxide as a Durable Oxygen Reduction Electrocatalyst, ACS Catal. 11 (2021) 7006–7017. https://doi.org/10.1021/acscatal.1c00963.
[50] Y. Qin, X. Yang, R. Li, S. Chen, Y. Wang, Z. Yu, Y. Wang, X. Liu, X. Tong, Carbon nanoparticle coated by silicon dioxide supported platinum nanoparticles towards oxygen reduction reaction, Mater. Res. Bull. 139 (2021) 111268. https://doi.org/10.1016/j.materresbull.2021.111268.
[51] H. Lv, N. Cheng, T. Peng, M. Pan, S. Mu, High stability platinum electrocatalysts with zirconia-carbon hybrid supports, J. Mater. Chem. 22 (2012) 1135–1141. https://doi.org/10.1039/c1jm14076k.
[52] S. Armini, J. De Messemaeker, C.M. Whelan, M. Moinpour, K. Maex, Composite Polymer Core–Ceria Shell Abrasive Particles during Oxide CMP: A Defectivity Study, J. Electrochem. Soc. 155 (2008) H653. https://doi.org/10.1149/1.2949085.
[53] N. Jaiswal, K. Tanwar, R. Suman, D. Kumar, S. Uppadhya, O. Parkash, A brief review on ceria based solid electrolytes for solid oxide fuel cells, J. Alloys Compd. 781 (2019) 984–1005. https://doi.org/10.1016/j.jallcom.2018.12.015.
[54] N.S. Priya, C. Somayaji, S. Kanagaraj, Optimization of ceria-zirconia solid solution based on OSC measurement by cyclic heating process, Procedia Eng. 64 (2013) 1235–1241. https://doi.org/10.1016/j.proeng.2013.09.203.
[55] Y. Ma, W. Gao, Z. Zhang, S. Zhang, Z. Tian, Y. Liu, J.C. Ho, Y. Qu, Regulating the surface of nanoceria and its applications in heterogeneous catalysis, Surf. Sci. Rep. 73 (2018) 1–36. https://doi.org/10.1016/j.surfrep.2018.02.001.
[56] G.N. Vayssilov, Y. Lykhach, A. Migani, T. Staudt, G.P. Petrova, N. Tsud, T. Skála, A. Bruix, F. Illas, K.C. Prince, V. Matolín, K.M. Neyman, J. Libuda, Support nanostructure boosts oxygen transfer to catalytically active platinum nanoparticles, Nat. Mater. 10 (2011) 310–315. https://doi.org/10.1038/nmat2976.
[57] H. Matsui, S. Takao, K. Higashi, T. Kaneko, G. Samjeské, T. Uruga, M. Tada, Y. Iwasawa, Operando Imaging of Ce Radical Scavengers in a Practical Polymer Electrolyte Fuel Cell by 3D Fluorescence CT-XAFS and Depth-Profiling Nano-XAFS-SEM/EDS Techniques, ACS Appl. Mater. Interfaces. 14 (2022) 6762–6776. https://doi.org/10.1021/acsami.1c22336.
[58] A. Kostuch, I.A. Rutkowska, B. Dembinska, A. Wadas, E. Negro, K. Vezzù, V. Di Noto, P.J. Kulesza, Enhancement of activity and development of low pt content electrocatalysts for oxygen reduction reaction in acid media, Molecules. 26 (2021) 1–19. https://doi.org/10.3390/molecules26175147.
[59] P. Valk, J. Nerut, R. Kanarbik, I. Tallo, J. Aruväli, E. Lust, Synthesis and Characterization of Platinum-Cerium Oxide Nanocatalysts for Methanol Oxidation, J. Electrochem. Soc. 165 (2018) F315–F323. https://doi.org/10.1149/2.0781805jes.
[60] G. qing Li, P. kang Wen, C. qiang Gao, T. yi Zhang, J. yang Hu, Y. hao Zhang, S. you Guan, Q. feng Li, B. Li, Effects of CeO2 pre-calcined at different temperatures on the performance of Pt/CeO2-C electrocatalyst for methanol oxidation reaction, Int. J. Miner. Metall. Mater. 28 (2021) 1224–1232. https://doi.org/10.1007/s12613-020-2076-2.
[61] Y. Luo, L. Calvillo, C. Daiguebonne, M.K. Daletou, G. Granozzi, N. Alonso-Vante, A highly efficient and stable oxygen reduction reaction on Pt/CeOx/C electrocatalyst obtained via a sacrificial precursor based on a metal-organic framework, Appl. Catal. B Environ. 189 (2016) 39–50. https://doi.org/10.1016/j.apcatb.2016.02.028.
[62] K.H. Lee, K. Kwon, V. Roev, D.Y. Yoo, H. Chang, D. Seung, Synthesis and characterization of nanostructured PtCo-CeOx/C for oxygen reduction reaction, J. Power Sources. 185 (2008)

871–875. https://doi.org/10.1016/j.jpowsour.2008.09.029.
[63] C. Du, X. Gao, C. Cheng, Z. Zhuang, X. Li, W. Chen, Metal organic framework for the fabrication of mutually interacted Pt–CeO2–C ternary nanostructure: advanced electrocatalyst for oxygen reduction reaction, Electrochim. Acta. 266 (2018) 348–356. https://doi.org/10.1016/j.electacta.2018.02.035.
[64] D.H. Lim, W.D. Lee, D.H. Choi, H.I. Lee, Effect of ceria nanoparticles into the Pt/C catalyst as cathode material on the electrocatalytic activity and durability for low-temperature fuel cell, Appl. Catal. B Environ. 94 (2010) 85–96. https://doi.org/10.1016/j.apcatb.2009.10.024.
[65] F. Xu, D. Wang, B. Sa, Y. Yu, S. Mu, One-pot synthesis of Pt/CeO2/C catalyst for improving the ORR activity and durability of PEMFC, Int. J. Hydrogen Energy. 42 (2017) 13011–13019. https://doi.org/10.1016/j.ijhydene.2017.04.039.
[66] K.R. Yoon, J.M. Kim, K.A. Lee, C.K. Hwang, S.G. Akpe, Y.J. Lee, J.P. Singh, K.H. Chae, S.S. Jang, H.C. Ham, J.Y. Kim, Activity-stability benefits of Pt/C fuel cell electrocatalysts prepared via remote CeO2 interfacial doping, J. Power Sources. 496 (2021) 229798. https://doi.org/10.1016/j.jpowsour.2021.229798.
[67] D.R. Ou, T. Mori, K. Fugane, H. Togasaki, F. Ye, J. Drennan, Stability of ceria supports in Pt-CeOx/C catalysts, J. Phys. Chem. C. 115 (2011) 19239–19245. https://doi.org/10.1021/jp205640k.
[68] K. Fugane, T. Mori, D.R. Ou, P. Yan, F. Ye, H. Yoshikawa, J. Drennan, Improvement of cathode performance on Pt-CeOx by optimization of electrochemical pretreatment condition for PEFC application, Langmuir. 28 (2012) 16692–16700. https://doi.org/10.1021/la302912r.
[69] K. Ehelebe, N. Schmitt, G. Sievers, A.W. Jensen, A. Hrnjić, P. Collantes Jiménez, P. Kaiser, M. Geuß, Y.P. Ku, P. Jovanovič, K.J.J. Mayrhofer, B. Etzold, N. Hodnik, M. Escudero-Escribano, M. Arenz, S. Cherevko, Benchmarking Fuel Cell Electrocatalysts Using Gas Diffusion Electrodes: Inter-lab Comparison and Best Practices, ACS Energy Lett. 7 (2022) 816–826. https://doi.org/10.1021/acsenergylett.1c02659.
[70] G.W. Sievers, A.W. Jensen, V. Brüser, M. Arenz, M. Escudero-Escribano, Sputtered Platinum Thin-films for Oxygen Reduction in Gas Diffusion Electrodes: A Model System for Studies under Realistic Reaction Conditions, Surfaces. 2 (2019) 336–348. https://doi.org/10.3390/surfaces2020025.
[71] M. Thommes, K. Kaneko, A. V. Neimark, J.P. Olivier, F. Rodriguez-Reinoso, J. Rouquerol, K.S.W. Sing, Physisorption of gases, with special reference to the evaluation of surface area and pore size distribution (IUPAC Technical Report), Pure Appl. Chem. 87 (2015) 1051–1069. https://doi.org/10.1515/pac-2014-1117.
[72] K.J. Ko, S. Jin, H. Lee, K.M. Kim, M. Mofarahi, C.H. Lee, Role of Ultra-micropores in CO2Adsorption on Highly Durable Resin-Based Activated Carbon Beads by Potassium Hydroxide Activation, Ind. Eng. Chem. Res. 60 (2021) 14547–14563. https://doi.org/10.1021/acs.iecr.1c02430.
[73] K.A. Cychosz, R. Guillet-Nicolas, J. García-Martínez, M. Thommes, Recent advances in the textural characterization of hierarchically structured nanoporous materials, Chem. Soc. Rev. 46 (2017) 389–414. https://doi.org/10.1039/c6cs00391e.
[74] K. Liu, N. Zakharova, A. Adeyilola, L. Zeng, Experimental Study on the Pore Shape Damage of Shale Samples during the Crushing Process, Energy and Fuels. 35 (2021) 2183–2191. https://doi.org/10.1021/acs.energyfuels.0c03297.
[75] P. Maziarka, C. Wurzer, P.J. Arauzo, A. Dieguez-Alonso, O. Mašek, F. Ronsse, Do you BET on routine? The reliability of N2 physisorption for the quantitative assessment of biochar's surface area, Chem. Eng. J. 418 (2021). https://doi.org/10.1016/j.cej.2021.129234.
[76] J. Landers, G.Y. Gor, A. V. Neimark, Density functional theory methods for characterization of porous materials, Colloids Surfaces A Physicochem. Eng. Asp. 437 (2013) 3–32. https://doi.org/10.1016/j.colsurfa.2013.01.007.
[77] A. V. Neimark, Y. Lin, P.I. Ravikovitch, M. Thommes, Quenched solid density functional

theory and pore size analysis of micro-mesoporous carbons, Carbon N. Y. 47 (2009) 1617–1628. https://doi.org/10.1016/j.carbon.2009.01.050.
[78] V. Hoffmann, D. Jung, J. Zimmermann, C.R. Correa, A. Elleuch, K. Halouani, A. Kruse, Conductive carbon materials from the hydrothermal carbonization of vineyard residues for the application in electrochemical double-layer capacitors (EDLCs) and direct carbon fuel cells (DCFCs), Materials (Basel). 12 (2019). https://doi.org/10.3390/MA12101703.
[79] T.A. Saleh, I. Ali, Synthesis of polyamide grafted carbon microspheres for removal of rhodamine B dye and heavy metals, J. Environ. Chem. Eng. 6 (2018) 5361–5368. https://doi.org/10.1016/j.jece.2018.08.033.
[80] G. Daniel, M. Mazzucato, R. Brandiele, L. De Lazzari, D. Badocco, P. Pastore, T. Kosmala, G. Granozzi, C. Durante, Sulfur Doping versus Hierarchical Pore Structure: The Dominating Effect on the Fe-N-C Site Density, Activity, and Selectivity in Oxygen Reduction Reaction Electrocatalysis, ACS Appl. Mater. Interfaces. (2021). https://doi.org/10.1021/acsami.1c09659.
[81] G. Daniel, T. Kosmala, F. Brombin, M. Mazzucato, A. Facchin, M.C. Dalconi, D. Badocco, P. Pastore, G. Granozzi, C. Durante, Chitosan Hydrogel Frameworks, (2021) 1–16.
[82] X. Tan, J. Koch, D. Günther, E. Reusser, B. Hattendorf, In situ element analysis of spodumenes by fs-LA-ICPMS with non-matrix-matched calibration: Signal beat and accuracy, Chem. Geol. 583 (2021) 120463. https://doi.org/10.1016/j.chemgeo.2021.120463.
[83] A. Ferrari, J. Robertson, Interpretation of Raman spectra of disordered and amorphous carbon, Phys. Rev. B - Condens. Matter Mater. Phys. 61 (2000) 14095–14107. https://doi.org/10.1103/PhysRevB.61.14095.
[84] F. Tuinstra, J.L. Koenig, Raman Spectrum of Graphite Raman Spectrum of Graphite, 1126 (1970). https://doi.org/10.1063/1.1674108.
[85] M.J. Matthews, M.A. Pimenta, G. Dresselhaus, M.S. Dresselhaus, M. Endo, Origin of dispersive effects of the Raman D band in carbon materials, Phys. Rev. B - Condens. Matter Mater. Phys. 59 (1999) 6585–6588. https://doi.org/10.1103/physrevb.59.r6585.
[86] A. Sadezky, Raman microspectroscopy of soot and related carbonaceous materials : Spectral analysis and structural information, 43 (2005) 1731–1742. https://doi.org/10.1016/j.carbon.2005.02.018.
[87] O. Beyssac, B. Goffé, J.P. Petitet, E. Froigneux, M. Moreau, J.N. Rouzaud, On the characterization of disordered and heterogeneous carbonaceous materials by Raman spectroscopy, Spectrochim. Acta - Part A Mol. Biomol. Spectrosc. 59 (2003) 2267–2276. https://doi.org/10.1016/S1386-1425(03)00070-2.
[88] N. Pongpichayakul, S. Themsirimongkon, S. Maturost, K. Wangkawong, L. Fang, B. Inceesungvorn, P. Waenkaew, S. Saipanya, Cerium oxide-modified surfaces of several carbons as supports for a platinum-based anode electrode for methanol electro-oxidation, Int. J. Hydrogen Energy. 46 (2021) 2905–2916. https://doi.org/10.1016/j.ijhydene.2020.06.196.
[89] Y. Xu, F. Wang, X. Liu, Y. Liu, M. Luo, B. Teng, M. Fan, X. Liu, Resolving a Decade-Long Question of Oxygen Defects in Raman Spectra of Ceria-Based Catalysts at Atomic Level, J. Phys. Chem. C. 123 (2019) 18889–18894. https://doi.org/10.1021/acs.jpcc.9b00633.
[90] G.W. Graham, W.H. Weber, C.R. Peters, R. Usmen, Empirical method for determining CeO2-particle size in catalysts by raman spectroscopy, J. Catal. 130 (1991) 310–313. https://doi.org/10.1016/0021-9517(91)90113-I.
[91] G. Papatheodorou, P. Ntzoufra, E. Hapeshi, J. Vakros, D. Mantzavinos, Hybrid Biochar / Ceria Nanomaterials : Synthesis , Characterization and Activity Assessment for the Persulfate-Induced Degradation of Antibiotic Sulfamethoxazole, (2022).
[92] Z. Zhang, Y. Wang, M. Wang, J. Lü, L. Li, Z. Zhang, M. Li, J. Jiang, F. Wang, An investigation of the effects of CeO2 crystal planes on the aerobic oxidative synthesis of imines from alcohols and amines, Cuihua Xuebao/Chinese J. Catal. 36 (2015) 1623–1630. https://doi.org/10.1016/S1872-2067(15)60869-5.

[93] 3 Zlatko Meić Mladen Žini ć Snežzana Miljanić, Leo Frkanec, Tomislav Biljan, Recent Advances in linear and nonlinear Raman spectroscopy I, J. Raman Spectrosc. 38 (2007) 1538–1553. https://doi.org/10.1002/jrs.
[94] Y. Yu, J. Yang, C. Hao, X. Zhao, Z. Wang, The adsorption, vibration and diffusion of hydrogen atoms on platinum low-index surfaces, J. Comput. Theor. Nanosci. 6 (2009) 439–448. https://doi.org/10.1166/jctn.2009.1054.
[95] K. Shinozaki, J.W. Zack, S. Pylypenko, B.S. Pivovar, S.S. Kocha, Oxygen Reduction Reaction Measurements on Platinum Electrocatalysts Utilizing Rotating Disk Electrode Technique, J. Electrochem. Soc. 162 (2015) F1384–F1396. https://doi.org/10.1149/2.0551512jes.
[96] Y. Garsany, O.A. Baturina, K.E. Swider-Lyons, S.S. Kocha, Experimental methods for quantifying the activity of platinum electrocatalysts for the oxygen reduction reaction, Anal. Chem. 82 (2010) 6321–6328. https://doi.org/10.1021/ac100306c.
[97] S. Alinejad, M. Inaba, J. Schröder, J. Du, J. Quinson, A. Zana, M. Arenz, Testing fuel cell catalysts under more realistic reaction conditions: accelerated stress tests in a gas diffusion electrode setup, JPhys Energy. 2 (2020). https://doi.org/10.1088/2515-7655/ab67e2.
[98] M. Riisom, B. Gammelgaard, I.H. Lambert, S. Stürup, Development and validation of an ICP-MS method for quantification of total carbon and platinum in cell samples and comparison of open-vessel and microwave-assisted acid digestion methods, J. Pharm. Biomed. Anal. 158 (2018) 144–150. https://doi.org/10.1016/j.jpba.2018.05.038.
[99] Y. Pei, B. Zhang, R. V. Maligal-Ganesh, P.J. Naik, T.W. Goh, H.L. MacMurdo, Z. Qi, M. Chen, R.K. Behera, I.I. Slowing, W. Huang, Catalytic properties of intermetallic platinum-tin nanoparticles with non-stoichiometric compositions, J. Catal. 374 (2019) 136–142. https://doi.org/10.1016/j.jcat.2019.04.013.
[100] C. Liang, Z. Li, S. Dai, Mesoporous carbon materials: Synthesis and modification, Angew. Chemie - Int. Ed. 47 (2008) 3696–3717. https://doi.org/10.1002/anie.200702046.
[101] N. Díez, M. Sevilla, A.B. Fuertes, Synthesis strategies of templated porous carbons beyond the silica nanocasting technique, Carbon N. Y. 178 (2021) 451–476. https://doi.org/10.1016/j.carbon.2021.03.029.
[102] R. Chakraborty, V. K, M. Pradhan, A.K. Nayak, Recent Advancement of Biomass-derived Porous Carbon Based Materials for Energy and Environmental Remediation Applications, J. Mater. Chem. A. (2022). https://doi.org/10.1039/d1ta10269a.
[103] T. Liu, G. Liu, Block copolymer-based porous carbons for supercapacitors, J. Mater. Chem. A. 7 (2019) 23476–23488. https://doi.org/10.1039/c9ta07770g.
[104] P. Alexandridis, Poly(ethylene oxide)/poly(propylene oxide) block copolymer surfactants, Curr. Opin. Colloid Interface Sci. 2 (1997) 478–489. https://doi.org/10.1016/S1359-0294(97)80095-7.
[105] A.M. Bodratti, P. Alexandridis, Formulation of poloxamers for drug delivery, J. Funct. Biomater. 9 (2018). https://doi.org/10.3390/jfb9010011.
[106] Y. Meng, D. Gu, F. Zhang, Y. Shi, L. Cheng, D. Feng, Z. Wu, Z. Chen, Y. Wan, A. Stein, D. Zhao, A family of highly ordered mesoporous polymer resin and carbon structures from organic-organic self-assembly, Chem. Mater. 18 (2006) 4447–4464. https://doi.org/10.1021/cm060921u.
[107] J. Jiao, Y. Cai, P. Liu, P. Liu, Influence of template on the structure of mesoporous carbon prepared with novalac resin as carbon precursor, J. Porous Mater. 20 (2013) 1247–1255. https://doi.org/10.1007/s10934-013-9709-z.
[108] U.B. Suryavanshi, T. Ijima, A. Hayashi, Y. Hayashi, M. Tanemura, Simple methods for tuning the pore diameter of mesoporous carbon, Chem. Commun. 47 (2011) 10758–10760. https://doi.org/10.1039/c1cc13471j.
[109] C. Matei Ghimbeu, V.A. Luchnikov, Hierarchical porous nitrogen-doped carbon beads derived from biosourced chitosan polymer, Microporous Mesoporous Mater. 263 (2018) 42–

52. https://doi.org/10.1016/j.micromeso.2017.12.001.
[110] L. Peng, Y. Peng, A. Primo, H. García, Porous Graphitic Carbons Containing Nitrogen by Structuration of Chitosan with Pluronic P123, ACS Appl. Mater. Interfaces. (2021). https://doi.org/10.1021/acsami.0c19463.
[111] D. Nordqvist, T.A. Vilgis, Rheological Study of the Gelation Process of Agarose-Based Solutions, Food Biophys. 6 (2011) 450–460. https://doi.org/10.1007/s11483-011-9225-0.
[112] M. Rinaudo, Chitin and chitosan: Properties and applications, Prog. Polym. Sci. 31 (2006) 603–632. https://doi.org/10.1016/j.progpolymsci.2006.06.001.
[113] C. Wang, D. Ma, X. Bao, Transformation of biomass into porous graphitic carbon nanostructures by microwave irradiation, J. Phys. Chem. C. 112 (2008) 17596–17602. https://doi.org/10.1021/jp805113y.
[114] J. Hoekstra, A.M. Beale, F. Soulimani, M. Versluijs-Helder, D. Van De Kleut, J.M. Koelewijn, J.W. Geus, L.W. Jenneskens, The effect of iron catalyzed graphitization on the textural properties of carbonized cellulose: Magnetically separable graphitic carbon bodies for catalysis and remediation, Carbon N. Y. 107 (2016) 248–260. https://doi.org/10.1016/j.carbon.2016.05.065.
[115] S.J. Goldie, S. Jiang, K.S. Coleman, Cobalt nanoparticle catalysed graphitization and the effect of metal precursor decomposition temperature, Mater. Adv. 2 (2021) 3353–3361. https://doi.org/10.1039/d1ma00125f.
[116] Z. Qiao, S. Hwang, X. Li, C. Wang, W. Samarakoon, S. Karakalos, D. Li, M. Chen, Y. He, M. Wang, Z. Liu, G. Wang, H. Zhou, Z. Feng, D. Su, J.S. Spendelow, G. Wu, 3D porous graphitic nanocarbon for enhancing the performance and durability of Pt catalysts: A balance between graphitization and hierarchical porosity, Energy Environ. Sci. 12 (2019) 2830–2841. https://doi.org/10.1039/c9ee01899a.
[117] M. Sevilla, A.B. Fuertes, Catalytic graphitization of templated mesoporous carbons, Carbon N. Y. 44 (2006) 468–474. https://doi.org/10.1016/j.carbon.2005.08.019.
[118] A. Ōya, H. Marsh, Phenomena of catalytic graphitization, J. Mater. Sci. 17 (1982) 309–322. https://doi.org/10.1007/BF00591464.
[119] Q. Yan, J. Li, X. Zhang, E.B. Hassan, C. Wang, J. Zhang, Z. Cai, Catalytic graphitization of kraft lignin to graphene-based structures with four different transitional metals, J. Nanoparticle Res. 20 (2018). https://doi.org/10.1007/s11051-018-4317-0.
[120] Q. Yan, J. Li, X. Zhang, J. Zhang, Z. Cai, Synthetic bio-graphene based nanomaterials through different Iron catalysts, Nanomaterials. 8 (2018). https://doi.org/10.3390/nano8100840.
[121] W. Peng, L. Zhao, C. Zhang, Y. Yan, Y. Xian, Controlled growth cerium oxide nanoparticles on reduced graphene oxide for oxygen catalytic reduction, Electrochim. Acta. 191 (2016) 669–676. https://doi.org/10.1016/j.electacta.2016.01.129.
[122] R. Brandiele, C. Durante, E. Grądzka, G.A. Rizzi, J. Zheng, D. Badocco, P. Centomo, P. Pastore, G. Granozzi, A. Gennaro, One step forward to a scalable synthesis of platinum–yttrium alloy nanoparticles on mesoporous carbon for the oxygen reduction reaction, J. Mater. Chem. A. 4 (2016) 12232–12240. https://doi.org/10.1039/C6TA04498K.
[123] V. Perazzolo, R. Brandiele, C. Durante, M. Zerbetto, V. Causin, G.A. Rizzi, I. Cerri, G. Granozzi, A. Gennaro, Density Functional Theory (DFT) and Experimental Evidences of Metal–Support Interaction in Platinum Nanoparticles Supported on Nitrogen- and Sulfur-Doped Mesoporous Carbons: Synthesis, Activity, and Stability, ACS Catal. 8 (2018) 1122–1137. https://doi.org/10.1021/acscatal.7b03942.
[124] R. Brandiele, M. Zerbetto, M.C. Dalconi, G.A. Rizzi, A.A. Isse, C. Durante, A. Gennaro, Mesoporous Carbon with Different Density of Thiophenic-Like Functional Groups and Their Effect on Oxygen Reduction, ChemSusChem. 12 (2019) 4229–4239. https://doi.org/10.1002/cssc.201901568.
[125] S. Jia, C. Li, H. Pan, M. Wang, X. Wang, Q. Lin, Preparation and pore-forming mechanism

of hydrogen bond and ionic bond double-driven chitosan-based mesoporous carbon, Int. J. Biol. Macromol. 179 (2021) 519–531. https://doi.org/10.1016/j.ijbiomac.2021.03.024.
[126] J. Peréz-Ramírez, D. Verboekend, A. Bonilla, S. Abelló, Zeolite catalysts with tunable hierarchy factor by pore-growth moderators, Adv. Funct. Mater. 19 (2009) 3972–3979. https://doi.org/10.1002/adfm.200901394.
[127] C. Schlumberger, M. Thommes, Characterization of Hierarchically Ordered Porous Materials by Physisorption and Mercury Porosimetry—A Tutorial Review, Adv. Mater. Interfaces. 8 (2021). https://doi.org/10.1002/admi.202002181.
[128] K. Fu, Q. Yue, B. Gao, Y. Sun, Y. Wang, Q. Li, P. Zhao, S. Chen, Physicochemical and adsorptive properties of activated carbons from Arundo donax Linn utilizing different iron salts as activating agents, J. Taiwan Inst. Chem. Eng. 45 (2014) 3007–3015. https://doi.org/10.1016/j.jtice.2014.08.026.
[129] K. Fu, Q. Yue, B. Gao, Y. Wang, Q. Li, Activated carbon from tomato stem by chemical activation with FeCl2, Colloids Surfaces A Physicochem. Eng. Asp. 529 (2017) 842–849. https://doi.org/10.1016/j.colsurfa.2017.06.064.
[130] A.C. Ferrari, D.M. Basko, studying the properties of graphene, Nat. Publ. Gr. 8 (2013) 235–246. https://doi.org/10.1038/nnano.2013.46.
[131] E. Thompson, A.E. Danks, L. Bourgeois, Z. Schnepp, Iron-catalyzed graphitization of biomass, Green Chem. 17 (2015) 551–556. https://doi.org/10.1039/c4gc01673d.
[132] J. Yu, W. Du, F. Zhao, B. Zeng, High sensitive simultaneous determination of catechol and hydroquinone at mesoporous carbon CMK-3 electrode in comparison with multi-walled carbon nanotubes and Vulcan XC-72 carbon electrodes, Electrochim. Acta. 54 (2009) 984–988. https://doi.org/10.1016/j.electacta.2008.08.029.
[133] L. Bokobza, J.-L. Bruneel, M. Couzi, Raman Spectra of Carbon-Based Materials (from Graphite to Carbon Black) and of Some Silicone Composites, C. 1 (2015) 77–94. https://doi.org/10.3390/c1010077.
[134] M. Todica, T. Stefan, S. Simon, I. Balasz, L. Daraban, UV-Vis and XRD investigation of graphite-doped poly(acrylic) acid membranes, Turkish J. Phys. 38 (2014) 261–267. https://doi.org/10.3906/fiz-1305-16.
[135] X. Garcia, L. Soler, A. Casanovas, C. Escudero, J. Llorca, X-ray photoelectron and Raman spectroscopy of nanostructured ceria in soot oxidation under operando conditions, Carbon N. Y. 178 (2021) 164–180. https://doi.org/10.1016/j.carbon.2021.03.009.
[136] C. Jackson, G.T. Smith, N. Mpofu, J.M.S. Dawson, T. Khoza, C. September, S.M. Taylor, D.W. Inwood, A.S. Leach, D. Kramer, A.E. Russell, A.R.J. Kucernak, P.B.J. Levecque, A quick and versatile one step metal-organic chemical deposition method for supported Pt and Pt-alloy catalysts, RSC Adv. 10 (2020) 19982–19996. https://doi.org/10.1039/d0ra03001e.
[137] M.A. Shah, Growth of uniform nanoparticles of platinum by an economical approach at relatively low temperature, Sci. Iran. 19 (2012) 964–966. https://doi.org/10.1016/j.scient.2012.02.027.
[138] Y. Ma, H. Wang, S. Ji, J. Goh, H. Feng, R. Wang, Highly active Vulcan carbon composite for oxygen reduction reaction in alkaline medium, Electrochim. Acta. 133 (2014) 391–398. https://doi.org/10.1016/j.electacta.2014.04.080.
[139] M.M. Magalhães, J.F. Gomes, G. Tremiliosi-Filho, P.B.S. de Figueiredo, R.B. de Lima, F. Colmati, Ethanol electro-oxidation on carbon-supported Pt3Sn/C, Pt3Cu/C and PtSnCu/C catalysts: CV and in situ FTIR study, J. Appl. Electrochem. 51 (2021) 173–181. https://doi.org/10.1007/s10800-020-01491-4.
[140] J.M. Oh, J. Park, A. Kumbhar, D. Smith, S. Creager, Electrochemical oxygen reduction at platinum/mesoporous carbon/zirconia/ionomer thin-film composite electrodes, Electrochim. Acta. 138 (2014) 278–287. https://doi.org/10.1016/j.electacta.2014.06.111.
[141] D.H. Lim, W.D. Lee, D.H. Choi, H.H. Kwon, H.I. Lee, The effect of cerium oxide nanoparticles on a Pt/C electrocatalyst synthesized by a continuous two-step process for low-

temperature fuel cell, Electrochem. Commun. 10 (2008) 592–596. https://doi.org/10.1016/j.elecom.2008.02.001.
[142] G.R. Mirshekari, C.A. Rice, Effects of support particle size and Pt content on catalytic activity and durability of Pt/TiO2 catalyst for oxygen reduction reaction in proton exchange membrane fuel cells environment, J. Power Sources. 396 (2018) 606–614. https://doi.org/10.1016/j.jpowsour.2018.06.061.
[143] M. Eckardt, C. Gebauer, Z. Jusys, M. Wassner, N. Hüsing, R.J. Behm, Oxygen reduction reaction activity and long-term stability of platinum nanoparticles supported on titania and titania-carbon nanotube composites, J. Power Sources. 400 (2018) 580–591. https://doi.org/10.1016/j.jpowsour.2018.08.036.
[144] Y. Li, X. Zhang, S. Wang, G. Sun, Durable Platinum-Based Electrocatalyst Supported by Multiwall Carbon Nanotubes Modified with CeO2, ChemElectroChem. 5 (2018) 2442–2448. https://doi.org/10.1002/celc.201800483.
[145] T.N. Geppert, M. Bosund, M. Putkonen, B.M. Stühmeier, A.T. Pasanen, P. Heikkilä, H.A. Gasteiger, H.A. El-Sayed, HOR Activity of Pt-TiO 2-Y at Unconventionally High Potentials Explained: The Influence of SMSI on the Electrochemical Behavior of Pt , J. Electrochem. Soc. 167 (2020) 084517. https://doi.org/10.1149/1945-7111/ab90ae.
[146] X. Liu, J. Chen, G. Liu, L. Zhang, H. Zhang, B. Yi, Enhanced long-term durability of proton exchange membrane fuel cell cathode by employing Pt/TiO2/C catalysts, J. Power Sources. 195 (2010) 4098–4103. https://doi.org/10.1016/j.jpowsour.2010.01.077.